

UNIVERSITY OF CAMBRIDGE

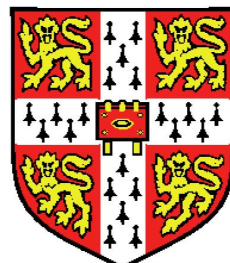
Towards Predictive Eddy Resolving Simulations for Gas Turbine Compressors

A dissertation submitted for the degree of Doctor of Philosophy

by

Ashley Duncan Scillitoe
Downing College

Cambridge Centre for Computational Aerodynamics and Aeroacoustics
Department of Engineering



Supported by:



December 7, 2017

Preface

I, Ashley D. SCILLITOE, declare that this thesis titled, 'Towards Predictive Eddy Resolving Simulations for Gas Turbine Compressors' and the work presented in it are my own. I confirm that:

- This dissertation is the result of my own work and includes nothing which is the outcome of work done in collaboration except as declared in the Preface and specified in the text.
- It is not substantially the same as any that I have submitted, or, is being concurrently submitted for a degree or diploma or other qualification at the University of Cambridge or any other University or similar institution except as declared in the Preface and specified in the text.
- This thesis comprises of 7 chapters and 2 appendices, with a total of approximately 55,000 words and 123 figures. It does not exceed the prescribed word limit for the Engineering Degree Committee.

Signed:

Date:

The work contained within this thesis has, to date, produced the following conference proceedings and journal publications:

Scillitoe AD, Tucker PG, Adami P. Evaluation of RANS and ZDES Methods for the Prediction of Three-Dimensional Separation in Axial Flow Compressors. In: *Proc. ASME Turbo Expo 2015*.

Scillitoe AD, Tucker PG, Adami P. Numerical Investigation of Three-Dimensional Separation in an Axial Flow Compressor: The Influence of Free-Stream Turbulence Intensity and Endwall Boundary Layer State. In: *Proc. ASME Turbo Expo 2016*.

Scillitoe AD, Tucker PG, Adami P. Numerical Investigation of Three-Dimensional Separation in an Axial Flow Compressor: The Influence of Freestream Turbulence Intensity and Endwall Boundary Layer State. In: *J. Turbomach. 139.2 (2016)*.

UNIVERSITY OF CAMBRIDGE

Abstract

Department of Engineering

A dissertation submitted for the degree of Doctor of Philosophy

Towards Predictive Eddy Resolving Simulations for Gas Turbine Compressors

by Ashley D. SCILLITOE

This thesis aims to explore the potential for using large eddy simulation (LES) as a predictive tool for gas-turbine compressor flows. The term “predictive tool” is used to describe a tool (or method) that can give accurate predictions of flows without the need for regular calibration with a priori data. Compressors present a significant challenge for the Reynolds Averaged Navier-Stokes (RANS) based CFD methods commonly used in industry. RANS models require extensive calibration to experimental data, and thus cannot be used predictively. This thesis explores how LES can offer a more predictive alternative, by exploring the sensitivity of LES to sources of uncertainty. Specifically, the importance of the numerical scheme, the Sub-Grid Scale (SGS) model, and the correct specification of inflow turbulence is examined.

The sensitivity of LES to the numerical scheme is explored using the Taylor-Green vortex test case. The numerical smoothing, controlled by a user defined smoothing constant, is found to be important. To avoid tuning the numerical scheme, a locally adaptive smoothing (LAS) scheme is implemented. But, this is found to perform poorly in a forced isotropic turbulence test case, due to the intermittency of the dispersive error. A novel scheme, the LAS with windowing (LASW) scheme, is thus introduced. The LASW scheme is shown to be more suitable for predictive LES, as it does not require tuning to a known solution.

The LASW scheme is used to perform LES on a compressor cascade, and results are found to be in close agreement with direct numerical simulations. Complex transition mechanisms, combining characteristics of both natural and bypass modes, are observed on the pressure surface. These mechanisms are found to be sensitive to numerical smoothing, emphasising the importance of the LASW scheme, which returns only the minimum smoothing required to prevent dispersion. On the suction surface, separation induced transition occurs. The flow here is seen to be relatively insensitive to numerical

smoothing and the choice of SGS model, as long as the Smagorinsky-Lilly SGS model is not used. These findings are encouraging, as they show that, with the LASW scheme and a suitable SGS model, LES can be used predictively in compressor flows. In order to be predictive, the accurate specification of inflow conditions was shown to be just as important as the numerics. For example, both free-stream turbulence intensity (T_i) and periodically incoming wakes are shown to have a significant impact on the transition mechanisms.

RANS models are shown to over-predict the extent of the three dimensional separation in the endwall - suction surface corner. LES is used to examine the challenges for RANS in this region. The LES shows that it is important to accurately capture the suction surface transition location, with early transition leading to a larger endwall separation. Large scale aperiodic unsteadiness is also observed in the endwall region. Additionally, turbulent anisotropy in the endwall - suction surface corner is found to be important. Adding a non-linear term to the RANS model leads to turbulent stresses that are in better agreement with the LES. This results in a stronger corner vortex which is thought to delay the corner separation. The addition of a corner fillet reduces the importance of anisotropy, thereby reducing the uncertainty in the RANS prediction.

Acknowledgements

First of all, I would like to sincerely thank my supervisor, Prof. Paul G. Tucker for all his guidance and support during my PhD. I am deeply grateful for his approachability and eagerness to help. His patience and continual encouragement, especially while writing up, was invaluable. I am also thankful to my advisor, Dr Liping Xu, for his useful comments on my work. The staff in the department of engineering have also been incredibly helpful. Special thanks to Peter Benie for his computing expertise, and Wendy Raymond for her help organising sall orts of things, even when I'd left it to the last minute.

To the members of my research group, your friendship and assistance have been crucial. In particular; special thanks to Dr Jiahuan Cui for providing his incompressible version of the HYDRA CFD code, Dr Ifthekar Naqavi for his help in generating a turbulent boundary layer dataset, Dr Nagabhushana Rao Vadlamani for his advice with running the wake simulation, and Bryn Ubald for his help with mesh generation. Also, many thanks to Drs Rob Watson and James Tyacke for their their assistance with the HYDRA code, and the many useful discussions on my project.

Without the funding provided by an EPSRC/Rolls-Royce studentship, I would not have been able to pursue this project in an area of particular interest to me. My gratitude goes to both organisations for this. In particular, thanks to Paolo Adami for his interest and support. Many of the computations in this thesis were run using UK Turbulence Consortium computing time (EPSRC grant EP/L000261/1) on the UK high-performance computing service ARCHER, and this is gratefully acknowledged.

To all my friends, you have been an incredible source of support and entertainment. To Hardeep, thank you for putting up with copious amounts of cheese and the trips to Hot Numbers. Camille, thank you for the amusing cat drama and other gossip. Mus and Ross, thanks for accompanying me on my morning bike rides, even when it was cold and dark. Thanks to Sanjeev for sharing our footballing woes together, and to Audrey for her encouragement, including the timely supply of excellent chocolate brownies. Thanks to Andrea for lovely Italian food, and to Bryn for our weekly squash games.

Finally, I am deeply grateful to my parents and brother for their love, encouragement and support. To Cindy, thank you for your love and understanding, and for helping in so many ways.

Contents

| | |
|--|----------|
| Preface | ii |
| Abstract | iv |
| Acknowledgements | vii |
| List of Figures | xiii |
| List of Tables | xix |
| Abbreviations | xxi |
| Nomenclature | xxiii |
| 1 Introduction | 1 |
| 1.1 Motivation - The need for predictive CFD | 1 |
| 1.2 Turbulence modelling for turbo-machinery | 2 |
| 1.3 Objectives of research | 4 |
| 1.4 Outline of thesis | 5 |
| I Literature and Numerical Methods | 7 |
| 2 Literature Review | 9 |
| 2.1 Flow physics in compressors | 9 |
| 2.1.1 Boundary layer transition | 9 |
| 2.1.2 Multi-stage effects | 13 |
| 2.1.3 Endwall flows | 15 |
| 2.2 The use of RANS modelling in compressors | 20 |
| 2.2.1 The Navier-Stokes equations | 20 |
| 2.2.2 Direct Numerical Simulation | 20 |
| 2.2.3 Reynolds averaged turbulence modelling | 21 |
| 2.2.4 Challenges for RANS in compressors | 22 |
| 2.3 Large eddy simulation | 24 |
| 2.3.1 The filtering operation | 25 |
| 2.3.2 Sub-grid scale modelling | 26 |
| 2.3.3 Meshing for LES | 27 |

| | | |
|-----------|---|-----------|
| 2.4 | Previous LES compressor studies | 29 |
| 2.4.1 | Numerical schemes for LES | 32 |
| 2.4.2 | Representation of compressor flows | 34 |
| 2.5 | Concluding remarks | 36 |
| 3 | Numerical Methods | 39 |
| 3.1 | The solver | 39 |
| 3.1.1 | Spatial discretisation | 39 |
| 3.1.2 | Conversion to an incompressible solver | 42 |
| 3.1.3 | Temporal discretisation | 43 |
| 3.1.4 | High performance computing | 43 |
| 3.1.5 | Turbulence treatments | 44 |
| 3.2 | Unsteady boundary conditions | 46 |
| 3.2.1 | Turbulent boundary layers | 47 |
| 3.2.2 | Unsteady wakes | 48 |
| 3.2.3 | Free-stream turbulence | 49 |
| 3.2.4 | Enforcing periodicity | 51 |
| 3.3 | Vortex identification methods | 52 |
| II | Results | 53 |
| 4 | A Robust Numerical Scheme for Eddy Resolving Simulations | 55 |
| 4.1 | Numerical challenges for eddy resolving simulations | 55 |
| 4.1.1 | The Taylor-Green vortex | 57 |
| 4.2 | Locally adaptive smoothing schemes | 63 |
| 4.2.1 | Forced isotropic turbulence test case | 66 |
| 4.2.2 | Appraisal of existing LAS scheme | 68 |
| 4.3 | A locally adaptive smoothing scheme with windowing | 72 |
| 4.3.1 | The windowing procedure | 73 |
| 4.3.2 | Modification for small target values | 75 |
| 4.3.3 | Extrapolation using gradients | 76 |
| 4.3.4 | The final LASW scheme | 76 |
| 4.3.5 | Performance of the LASW scheme | 78 |
| 4.4 | Concluding remarks | 81 |
| 5 | Boundary Layer Transition in Compressors | 83 |
| 5.1 | The V103 compressor cascade | 83 |
| 5.1.1 | Case set-up | 84 |
| 5.1.2 | LASW scheme | 87 |
| 5.2 | Pressure surface transition mechanisms | 89 |
| 5.2.1 | Moderate free-stream turbulence intensity | 90 |
| 5.2.2 | High free-stream turbulence intensity | 93 |
| 5.3 | Suction surface transition mechanisms | 97 |
| 5.3.1 | Moderate free-stream turbulence intensity | 98 |
| 5.3.2 | High free-stream turbulence intensity | 99 |
| 5.4 | An assessment of sensitivities | 102 |
| 5.4.1 | Specification of inflow turbulence | 102 |

| | | |
|------------|--|------------|
| 5.4.2 | Sub-grid scale modelling | 103 |
| 5.4.3 | Numerical scheme | 111 |
| 5.5 | Concluding Remarks | 113 |
| 6 | Towards Engine Representative Compressor Flows | 115 |
| 6.1 | The PVD compressor cascade | 115 |
| 6.1.1 | Case set-up | 116 |
| 6.1.2 | Mid-span cases | 118 |
| 6.1.3 | Endwall cases | 119 |
| 6.2 | Periodically varying inflow conditions | 120 |
| 6.2.1 | Transition mechanisms without wakes present | 121 |
| 6.2.2 | Transition mechanisms with wakes present | 123 |
| 6.3 | The endwall flow | 129 |
| 6.3.1 | Effect of inflow turbulence | 131 |
| 6.3.2 | Challenges for lower fidelity modelling approaches | 139 |
| 6.3.3 | Addition of an endwall fillet | 149 |
| 6.4 | Concluding Remarks | 151 |
| III | Conclusions and Future Outlook | 155 |
| 7 | Conclusions and Recommendations for Future Work | 157 |
| 7.1 | Flow physics perspective | 158 |
| 7.1.1 | The effect of free-stream turbulence on transition | 158 |
| 7.1.2 | Wake induced transition | 158 |
| 7.1.3 | The endwall flow region | 159 |
| 7.2 | Engineering perspective | 161 |
| 7.2.1 | Specification of turbulent inflow conditions | 161 |
| 7.2.2 | Compressor performance | 161 |
| 7.2.3 | RANS modelling | 161 |
| A | Additional Information on Turbulence Treatments | 165 |
| A.1 | Additional challenges faced by RANS models | 165 |
| A.1.1 | Compressive/Extensive strain | 165 |
| A.1.2 | Curvature and rotation | 166 |
| A.2 | Baseline RANS models | 167 |
| A.2.1 | Spalart-Allmaras model | 167 |
| A.2.2 | Shear-Stress Transport model | 168 |
| A.3 | RANS model extensions added to HYDRA | 169 |
| A.3.1 | SA with Quadratic Constitutive Relation (SA-QCR) | 169 |
| A.3.2 | Strain Adaptive formulation of SA model (SALSA) | 170 |
| A.3.3 | SA with Rotation/Curvature correction (SA-RC) | 170 |
| A.4 | SGS models with additional filtering | 171 |
| A.4.1 | Dynamic Smagorinsky model | 171 |
| A.4.2 | Variational Multiscale method | 172 |
| A.4.3 | Shear-Improved Smagorinsky model | 173 |

| | |
|--|----------------|
| B Reformulation of the Synthetic Turbulence Method | 175 |
| B.1 The synthetic turbulence method | 175 |
| B.2 Enforcing mass conservation on a staggered grid | 176 |
| B.3 Enforcing mass conservation on a collocated grid | 177 |
| Bibliography | 179 |

List of Figures

| | | |
|------|---|----|
| 1.1 | A modern gas-turbine aero engine | 1 |
| 1.2 | A hierarchy of the main turbulence treatments | 3 |
| 2.1 | Schematic showing natural boundary layer transition | 10 |
| 2.2 | Contours of stream-wise fluctuating velocity, illustrating the concept of shear-sheltering | 11 |
| 2.3 | Schematic of a laminar separation bubble | 12 |
| 2.4 | Sketch of a typical axial compressor | 14 |
| 2.5 | Sketch of a typical axial compressor | 14 |
| 2.6 | Simple schematic of endwall flow in a compressor | 16 |
| 2.7 | Sketch of the endwall separation topology | 18 |
| 2.8 | Lei's diffusion parameter and stall indicator map | 18 |
| 2.9 | Overview of unsteady flow phenomena in turbo-machinery, and the turbulence treatments capable of addressing them | 23 |
| 2.10 | Spectral gap required for theoretically valid URANS | 23 |
| 2.11 | Reynolds number variation through a medium-sized gas turbine engine, along with Hybrid RANS/LES and LES grid requirements | 29 |
| 2.12 | Solution to the 1D advection equation showing the effect of finite difference errors | 33 |
| 3.1 | HYDRA dual control volumes for interior and boundary nodes | 40 |
| 3.2 | Time taken for HYDRA to write a 16GB file on ARCHER. | 44 |
| 3.3 | Inflow turbulence box appended to compressor cascade. | 47 |
| 3.4 | Velocity and stress profiles of TBL generated with Lund recycling | 48 |
| 3.5 | Velocity and stress profiles of wake data. | 49 |
| 3.6 | Isotropic turbulence from synthetic method. | 50 |
| 3.7 | Velocity and stress profiles of inflow box with TBL + FST blended together. | 50 |
| 3.8 | Gaussian-like filtering applied to inflow turbulence box | 52 |
| 4.1 | Iso-surfaces of Q-criterion for LES of compressor endwall flow showing excessive dispersive errors | 56 |
| 4.2 | Iso-surfaces of Q-criterion for TGV | 59 |
| 4.3 | Effect of ϵ_2 on temporal evolution of TGV | 60 |
| 4.4 | Iso-lines of non-dimensional vorticity on a subset of the periodic face $x = -\pi L$ | 61 |
| 4.5 | Effect of mesh resolution on temporal evolution of TGV | 62 |
| 4.6 | Resolved, numerical and SGS contribution to energy dissipation. σ SGS model. | 63 |
| 4.7 | Four-point stencil for LAS scheme | 64 |

| | | |
|------|---|----|
| 4.8 | Two examples of signals ϕ with and without wiggles | 65 |
| 4.9 | Energy spectra of stationary state of FIT on 32^3 grid | 67 |
| 4.10 | Temporal evolution of FIT on 32^3 grid | 68 |
| 4.11 | Iso-surfaces of Q-criterion for FIT | 69 |
| 4.12 | Temporal history of volume averaged ϵ_2 and θ for 32^3 FIT case with LAS and FS schemes. | 70 |
| 4.13 | Temporal history of wiggle magnitude θ_1 at a single computational edge, for two different LES cases (with FS). | 71 |
| 4.14 | Time history of wiggle magnitude θ and ϵ_2 at a single computational edge, for 32^3 FIT case with LAS | 71 |
| 4.15 | Histogram showing frequency of ϵ_2 and θ values occurring at a single edge for 32^3 FIT case. | 72 |
| 4.16 | Window averaging applied to the θ signal measured at a single edge in the 32^3 FIT case | 74 |
| 4.17 | Normalized root-mean-square deviation of windowed signals for various windowing methods and window lengths | 74 |
| 4.18 | Modification to LASW control equation for cases with small θ_t | 76 |
| 4.19 | Error of extrapolation using cell centred gradients | 77 |
| 4.20 | Temporal history of volume averaged ϵ_2 and θ for 32^3 FIT case with LASW scheme and different θ_t values | 78 |
| 4.21 | Temporal history of volume averaged ϵ_2 and θ for 32^3 FIT case with LASW scheme and different θ_t values | 79 |
| 4.22 | Contours and line plot of ϵ_2 field at a given instance in time for the 32^3 FIT with LASW | 79 |
| 4.23 | Effect of FIT grid resolution on volume averaged θ for different ϵ_2 values with the FS scheme | 80 |
| 4.24 | Comparison of volume averaged θ and ϵ_2 relationship for the FS and LASW schemes | 80 |
| 5.1 | Computational grid used for LES of V103 compressor cascade | 85 |
| 5.2 | Turbulence intensity at mid-pitch for a selection of the V103 LES and DNS cases | 87 |
| 5.3 | Convergence history of domain averaged smoothing constant with LASW scheme | 88 |
| 5.4 | Converged smoothing field for compressor LES case with LASW scheme | 88 |
| 5.5 | Pressure and skin friction coefficients on the pressure surface, at various free-stream turbulence intensities | 90 |
| 5.6 | Momentum thickness Reynolds number and Görtler number on the pressure surface | 91 |
| 5.7 | Contours of the tangential velocity perturbations on a plane inside the pressure surface boundary layer, at a moderate free-stream turbulence intensity | 91 |
| 5.8 | Close-up of the two types of vortical structures that occur on the pressure surface | 92 |
| 5.9 | Contours of the normal velocity perturbations on a plane inside the pressure surface boundary layer, at a moderate free-stream turbulence intensity | 94 |
| 5.10 | Contours of the tangential velocity perturbations on an xy-plane bisecting a Λ -structure | 95 |

| | | |
|------|--|-----|
| 5.11 | Contours of the normal velocity perturbations on a plane inside the pressure surface boundary layer, at another time instance | 96 |
| 5.12 | Contours of the tangential velocity perturbations on a plane inside the pressure surface boundary layer, at another time instance | 97 |
| 5.13 | Contours of the tangential velocity perturbations on an xy-plane bisecting the overlap mode hairpin structures | 97 |
| 5.14 | Pressure and skin friction coefficients on the suction surface, at various free-stream turbulence intensities | 98 |
| 5.15 | Contours of the tangential velocity perturbations on a plane inside the suction surface boundary layer, at a moderate free-stream turbulence intensity | 99 |
| 5.16 | Contours of the tangential velocity perturbations on a plane inside the suction surface boundary layer, at a high free-stream turbulence intensity | 100 |
| 5.17 | Contours of the normal velocity perturbations on a plane inside the suction surface boundary layer, at a high free-stream turbulence intensity . | 101 |
| 5.18 | Contours of the tangential velocity perturbations on an xy-plane bisecting a turbulent spot | 102 |
| 5.19 | Sensitivity of the suction and pressure surface skin friction coefficient to inflow turbulent length scale | 103 |
| 5.20 | Maximum of tangential and spanwise velocity fluctuations in the pressure and suction surface boundary layers | 104 |
| 5.21 | Sensitivity of the suction and pressure surface skin friction coefficient to the SGS model | 104 |
| 5.22 | Contours of the modelled turbulent kinetic energy | 105 |
| 5.23 | Contours of the resolved turbulent kinetic energy | 106 |
| 5.24 | Profiles of $u'_n \partial \bar{u}_t / \partial x_n$ on the suction surface | 106 |
| 5.25 | Profiles of the mean tangential velocity on the suction surface | 107 |
| 5.26 | Profiles of \bar{u}_t and $u'_n \partial \bar{u}_t / \partial x_n$ within the separation bubble | 107 |
| 5.27 | Maximum level of velocity fluctuations across the suction surface boundary layer | 108 |
| 5.28 | Profiles of the tangential and shear components of the Reynolds stresses on the suction surface, showing the resolved and modelled contributions . | 109 |
| 5.29 | Profiles of SGS model viscosity and velocity gradients in the suction surface laminar boundary layer | 110 |
| 5.30 | Profiles of the $\overline{S_{ij}S_{ij}}$ term on the suction surface | 110 |
| 5.31 | Sensitivity of the suction and pressure surface skin friction coefficient to the numerical smoothing | 111 |
| 5.32 | Contours of the tangential velocity perturbations on a plane inside the pressure surface boundary layer, with a large amount of artificial smoothing | 112 |
| 5.33 | Contours of the tangential velocity perturbations on a plane inside the suction surface boundary layer, with no artificial smoothing | 112 |
| 6.1 | The computational domain for the PVD compressor cascade case with endwall included | 117 |
| 6.2 | Smoothing field for 3D endwall compressor LES case with LASW scheme | 118 |
| 6.3 | Time-averaged momentum thickness Reynolds number and shape factor of the incoming endwall boundary layer | 119 |

| | | |
|------|---|-----|
| 6.4 | Endwall boundary layer profiles of time-averaged velocity and turbulence intensity at the inflow ($x = -0.7C_x$) | 120 |
| 6.5 | Time-averaged skin friction coefficient with and without wakes | 121 |
| 6.6 | Contours of the tangential velocity perturbations on a plane inside the suction surface boundary layer, at a low free-stream turbulence intensity . | 122 |
| 6.7 | Contours of the tangential velocity perturbations on a plane inside the pressure surface boundary layer, at a low free-stream turbulence intensity | 122 |
| 6.8 | Phase-averaged friction coefficients on suction and pressure surfaces . . | 124 |
| 6.9 | Phase-averaged and time-averaged friction coefficient on suction and pressure surfaces | 125 |
| 6.10 | Phase-averaged space-time plot of the suction surface skin friction distributions | 126 |
| 6.11 | Contours of the tangential velocity perturbations on a plane inside the suction surface boundary layer, as a wake passes | 127 |
| 6.12 | Contours of the normal velocity perturbations on a plane inside the suction surface boundary layer, as a wake passes | 128 |
| 6.13 | Phase-averaged space-time plots of the suction surface boundary layer momentum thickness and shape factor | 128 |
| 6.14 | Instantaneous iso-surfaces of Q-criterion coloured by axial vorticity, showing the endwall flow | 129 |
| 6.15 | Time-averaged skin friction lines from LES flow compared to the experimental oilflow in the suction surface-endwall corner region | 130 |
| 6.16 | Lei's diffusion parameter and stall indicator map, with the PVD cascade operating point indicated | 130 |
| 6.17 | Time-averaged pressure coefficient at two span-wise locations | 131 |
| 6.18 | Time-averaged loss coefficient and exit angle versus span, downstream of the trailing edge | 132 |
| 6.19 | Time-averaged skin friction lines on endwall, with two different boundary layer states | 133 |
| 6.20 | Time-averaged (for $4T^*$) iso-surfaces of vorticity magnitude $ \bar{\omega} $ coloured by u_{rms} | 133 |
| 6.21 | Iso-contours of Q-criterion on suction surface before and after boundary layer trip added. | 134 |
| 6.22 | Skin friction coefficient and boundary layer displacement thickness with and without boundary layer trip applied | 135 |
| 6.23 | Time-averaged skin friction lines on the suction surface, with and without a boundary layer trip applied | 136 |
| 6.24 | Area-averaged viscous dissipation and turbulent dissipation through the blade passage | 137 |
| 6.25 | Contours of turbulent dissipation and loss coefficient in endwall region, showing effect of endwall boundary layer state | 139 |
| 6.26 | Cumulative integral of area-averaged total dissipation through the blade passage | 140 |
| 6.27 | Predicted pressure coefficient distribution and mass averaged exit angle for a number of RANS models | 140 |
| 6.28 | Time-averaged streamlines near the endwall and suction surface, showing the probes used | 141 |
| 6.29 | Power spectral density of velocity fluctuations | 142 |

| | | |
|------|--|-----|
| 6.30 | Integral length-scales of turbulence across the blade span | 142 |
| 6.31 | Probability density function of the axial velocity at two locations | 143 |
| 6.32 | Contours of time-averaged resolved turbulent kinetic energy in the pressure surface - endwall corner | 144 |
| 6.33 | Cumulative integral of area-averaged total dissipation through the blade passage | 144 |
| 6.34 | Skin friction lines and slices of axial velocity for RANS SST cases with and without QCR term | 146 |
| 6.35 | Reynolds stress in the endwall corner | 146 |
| 6.36 | Iso-surfaces of kinematic vorticity number identifying vortical structures . | 147 |
| 6.37 | Difference between span-wise and wall-normal Reynolds stresses in the endwall corner close to the leading edge | 148 |
| 6.38 | Reynolds stress in the endwall corner | 149 |
| 6.39 | Close-up of the blade leading edge with a fillet added to the endwall - blade corner | 149 |
| 6.40 | Time-averaged loss coefficient and exit angle versus span, downstream of the trailing edge, with and without corner fillet | 150 |
| 6.41 | Skin friction lines and slices of axial velocity for RANS SST cases with and without QCR term, with filleted corner | 151 |
| 6.42 | Difference between span-wise and wall-normal Reynolds stresses in the endwall corner close to the leading edge, with a corner fillet | 151 |
| 7.1 | Total time-averaged loss coefficient 50% chord downstream of the trailing edge, for a number of LES cases | 162 |
| A.1 | Schematic showing the concept of dynamic Smagorinsky and VMS . . . | 172 |

List of Tables

| | | |
|-----|--|-----|
| 1.1 | Summary of the main turbulence treatments | 3 |
| 2.1 | Near-wall grid requirements for DNS and LES | 27 |
| 2.2 | Overview of near-wall grid resolution parameters and their effect on the solution | 28 |
| 2.3 | Summary of published compressor LES studies | 30 |
| 3.1 | Properties of the Smagorinsky-Lilly, WALE and σ SGS models. | 45 |
| 3.2 | Parameters of unsteady turbulent wake. | 48 |
| 5.1 | Geometrical and inflow parameters for the V103 compressor cascade. . . . | 84 |
| 5.2 | LES cases run for V103 compressor cascade. | 86 |
| 6.1 | Comparision of geometrical and inflow parameters for the V103 and PVD compressor cascades. | 116 |
| 6.2 | Maximum non-dimensional wall spacings for LES PVD cascade mesh . . | 117 |
| 6.3 | LES cases for the PVD compressor cascade | 119 |

Abbreviations

| | |
|---------------|---|
| BL | Boundary Layer |
| CFD | Computational Fluid Dynamics |
| CFL | Courant Friedrichs Lewy conditions |
| CV | Corner Vortex |
| DNS | Direct Numerical Simulation |
| DSM | Dynamic Smagorinsky Model |
| ENO | Essentially Non-Oscillatory |
| FIT | Forced Isotropic Turbulence |
| FS | Fixed Smoothing |
| FST | Free-Stream Turbulence |
| HDT | Homogeneous Decaying Turbulence |
| HV | Horse-shoe Vortex |
| ILES | Implicit Large Eddy Simulation |
| KEP | Kinetic Energy Preserving |
| K-H | Kelvin-Helmholtz |
| LAPACK | Linear Algebra PACKage |
| LAS | Locally Adaptive Smoothing |
| LASW | Locally Adaptive Smoothing with Windowing |
| LBL | Laminar Boundary Layer |
| LES | Large Eddy Simulation |
| LKE | Laminar Kinetic Energy |

| | |
|--------------|---|
| MPI | Message Passing Interface |
| NRMSD | Normalised Root-Mean-Square Deviation |
| PDF | Probability Density Function |
| PID | Proportional-Integral-Derivative |
| PSD | Power Spectral Density |
| PVD | Prescribed Velocity Distribution |
| QCR | Quadratic Constitutive Relations |
| RANS | Reynolds Averaged Navier-Stokes |
| RK | Runge-Kutta |
| RSM | Reynolds Stress Model |
| SA | Spalart-Allmaras (model) |
| SALSA | Strain Adaptive formuLation of Spalart-Allmaras model |
| SA-RC | Spalart-Allmaras model with Rotation and Curvature correction |
| SFS | Sub-Filter Scale |
| SGS | Sub-Grid Scale |
| SISM | Shear-Improved Smagorinsky Model |
| SM | Smagorinsky-Lilly Model |
| SST | Shear Stress Transport |
| TBL | Turbulent Boundary Layer |
| TGV | Taylor Green Vortex |
| Ti | Turbulence intensity (usually free-stream) |
| T-S | Tollmien-Schlichting |
| TVD | Total Variation Diminishing |
| URANS | Unsteady Reynolds Averaged Navier-Stokes |
| VMS | Variational Multi-Scale |
| WALE | Wall-Adapting-Local-Eddy viscosity model |

Nomenclature

Latin

| | |
|------------------|--|
| A | Forcing constant for FIT |
| A_{ij} | Edge weight of the e_{ij} edge |
| b | Wake half-width |
| c | Blade chord length |
| C_x | Blade axial (x-direction) chord length |
| $C_{s,w,\sigma}$ | Model constant for the Smagorinsky/WALE/Sigma SGS models |
| C_p | Static pressure coefficient |
| C_f | Skin friction coefficient |
| C_D | Drag coefficient |
| d | Distance from nearest wall |
| $D_{w/\sigma}$ | Differential operator for the WALE/Sigma SGS models |
| D | Vector of primitive variables, or vertical separation of wakes |
| e_{ij} | Edge linking nodes i and j |
| E_i | Set linking all the nodes connected to node i via an edge |
| E | Total energy, or turbulent kinetic energy |
| fr | Reducing frequency of wake |
| F | Flux |
| F_{trip} | Force per unit volume of boundary layer trip |
| f | Frequency |

| | |
|--------------|--|
| G | Gain parameter of FIT, or Görtler number |
| h | Grid spacing, or blade height (span) |
| H | Boundary layer shape factor |
| i | Incidence angle |
| k | Turbulent kinetic energy |
| l | Turbulent length-scale corresponding to κ |
| L | Turbulent integral length-scale, or reference length for TGV |
| L_i | Laplacian operator for node i |
| L_{ii} | Integral length-scale in the i-direction |
| Ma | Mach number |
| n_{ij} | Unit vector of the e_{ij} edge |
| N_{wig} | Number of wiggles detected during LASW scheme's window |
| p | Static pressure |
| P | Exact production term of turbulent kinetic energy |
| Pe | Peclet number |
| q_i | Heat flux |
| Q | Vector of conservative variables |
| r | Radial coordinate |
| R | Radius of curvature, or specific gas constant |
| Re_\square | Reynolds number, $Re = \frac{\rho U \square}{\mu}$, based on the length-scale \square |
| $R(Q)$ | Residual vector of the spatial discretisation |
| S_{ij} | Rate-of-Strain tensor , $S_{ij} = (\partial u_i / \partial x_j + \partial u_j / \partial x_i)$ |
| S | Magnitude of Rate-of-strain tensor, $S = \sqrt{2S_{ij}S_{ij}}$ |
| S_r | Velocity skewness derivative |
| S | Blade pitch |
| t | Time or blade thickness |
| t_w | Time through LASW scheme's window |
| T_w | LASW scheme's window length |

| | |
|----------------------|--|
| T^* | Flow-through time |
| u_e | Velocity at the boundary layer edge |
| u, v, w | Instantaneous velocity components in the x,y,z directions |
| $\bar{u}_{wake,max}$ | Mean velocity deficit of wake |
| U_{cyc} | Wake cycle velocity |
| U | Magnitude of velocity, $U = \sqrt{u^2 + v^2 + w^2}$ |
| V_0 | Reference velocity for TGV |
| V_i | Volume of the i^{th} cell |
| \mathbf{x} | Position vector |
| x, y, z | Standard Cartesian coordinate system |
| $x_t/x_n/z$ | Coordinate system tangential/normal/span-wise to blade surface |
| $w_i^{(k)}$ | Filter weights for inflow filter |
| W_{LE} | Leading edge of wake |
| W_{TE} | Trailing edge of wake |
| Y_p | Total pressure loss coefficient |
| X_s | Start of transition region |
| X_e | End of transition region |
| x_s | Time-averaged separation location |
| x_r | Time-averaged reattachment location |

Greek

| | |
|---------------|---|
| α_1 | Inlet flow angle |
| α_2 | Exit flow angle |
| β | Artificial compressibility constant |
| γ | Smoothing function for LASW scheme |
| Γ | Diffusion coefficient |
| δ_{ij} | Kronecker delta, $\delta_{ij} = 1$ if $i = j$ and $\delta_{ij} = 0$ otherwise |
| δ^* | Boundary layer displacement thickness |

| | |
|--------------------------------|---|
| δ^x | Boundary layer thickness where $U = (x/100)U_{FS}$ |
| Δ | Filter width |
| $\Delta x, \Delta y, \Delta z$ | Grid spacing in the x,y,z directions |
| Δ_{vol} | Filter width based on cubed root of cell volume |
| ε_{tot} | Total turbulent kinetic energy dissipation rate |
| ε_{res} | Resolved turbulent kinetic energy dissipation rate |
| ε_{SGS} | Turbulent kinetic energy dissipation rate due to SGS model |
| ε_{num} | Turbulent kinetic energy dissipation rate due to numerical scheme |
| ϵ_2 | Smoothing constant scaling upwinding for the Roe scheme |
| θ | Boundary layer momentum thickness, or wiggle magnitude |
| θ_t | Target wiggle magnitude |
| θ_{max} | Maximum wiggle magnitude during LASW scheme's window |
| θ_{w2} | Average wiggle magnitude during LASW scheme's window |
| κ | Von Kármán costant ($\kappa = 0.41$) or wave number ($\kappa = 2\pi/l$) |
| κ_e | Wave number of maximum energy |
| κ_p | $\kappa_p = \sqrt{12/5}\kappa_e$ |
| κ_η | Kolmogorov wave number |
| λ | Taylor micro-scale |
| μ | Dynamic viscosity |
| μ_t | Turbulent viscosity |
| μ_{SGS} | Sub-grid scale viscosity |
| ν | Kinematic viscosity, $\nu = \mu/\rho$ |
| $\xi/\eta/\zeta$ | Vorticity of the mean flow in the $x_t/x_n/z$ co-ordinate system |
| ρ | Density |
| $\sigma_{1/2/3}$ | Singular values of the resolved velocity gradient tensor |
| σ | Cascade blade solidity, c/S |
| τ_{au_w} | Wall shear stress |
| τ_{ij} | Reynolds stress tensor |

| | |
|---------------|---|
| τ_{ij}^h | Numerical stress |
| τ_{ij}^r | Modelled stress |
| τ | Pseudo time |
| τ_w | Wake passing period |
| τ_c | Characteristic convective time of TGV |
| τ_l | Integral time-scale of FIT |
| ϕ | Any of the primitive variables, i.e. u, v, w, p, ρ |
| Φ_{ii} | Power spectral density of velocity u_i |
| $\psi_{t/v}$ | Turbulent/Viscous dissipation |
| Ψ_{tot} | Cumulative integral of $(\psi_t + \psi_v)$ in x-direction |
| ω | Vorticity vector, or specific turbulent dissipation rate |
| Ω_{ij} | Vorticity tensor, $\Omega_{ij} = (\partial u_i / \partial x_j - \partial u_j / \partial x_i)$ |
| Ω | Magnitude of vorticity tensor, $\Omega = \sqrt{2\Omega_{ij}\Omega_{ij}}$ |

Superscripts

| | |
|-----|---|
| $+$ | Non-dimensional distance, given by $\square^+ = \frac{\square}{\nu} \sqrt{\tau_w / \rho}$ |
| $'$ | Fluctuating quantity |
| I | Inviscid contribution |
| V | Viscous contribution |

Subscripts

| | |
|-----------|---|
| 0 | Stagnation conditions or initial conditions |
| 1 | Inflow conditions |
| $1, 2, 3$ | Correspond to x,y,z directions |
| FS | Free-stream conditions |
| i, j, k | Standard unit vector notation, or i^{th} and j^{th} nodes |
| TE | Trailing edge conditions |
| r | Contribution from resolved fluctuations |

SGS

Contribution from SGS model

Other

- Time-averaged quantity
- ^ Filtered quantity, or periodic perturbation
- $\langle \rangle$ Box average or phase average
- { } Spatial averaging

Chapter 1

Introduction

1.1 Motivation - The need for predictive CFD

After many years of optimisation, the design of even more efficient gas turbine engines presents a significant challenge. It is necessary to understand complex unsteady flows in individual engine components and their interactions, in order to further improve engine performance. Compressors, like those labelled in Figure 1.1, are critical to the performance of the engine. Due to the adverse pressure gradients a compressor experiences, it is subject to surge and rotating stall, which can lead to mechanical failure. These flow instabilities impose strict constraints on the design and thus dictate the engine's performance. Increasing the efficiency of compressors, and in doing so the entire engine, thus requires a detailed understanding of the complex flow physics.

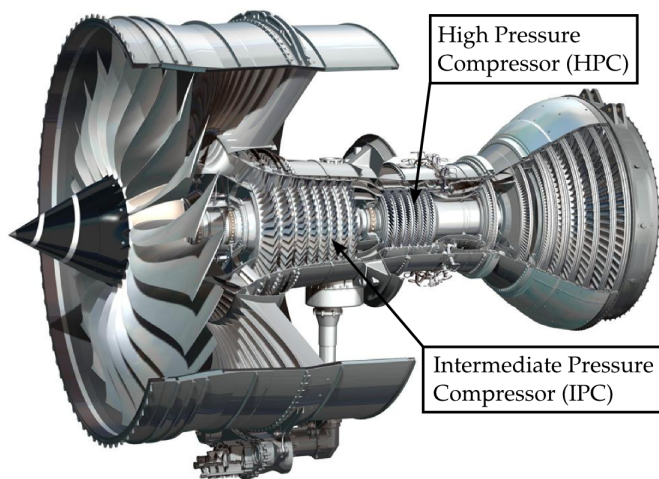


FIGURE 1.1: A modern gas-turbine aero engine, the Trent XWB, with the intermediate and high pressure compressors labelled.

In addition to technical challenges, the development of a modern gas turbine engine is a long and expensive venture, with development costs in excess of 1 billion US dollars [1]. Much of this time and cost stems from the need to conduct a large number of experimental investigations throughout the design process. Such investigations can take several months to set up and are very costly. For example in the 1990's, the cost for a rig test for the high pressure compressor of the Rolls-Royce Trent engine amounted to around 1.5 million US dollars [2]. In order to reduce development time and costs, it is therefore desirable to minimise the number of experimental investigations. This requires quick yet accurate predictive tools.

The numerical simulation of flows, known as Computational Fluid Dynamics (CFD), is heavily used in the industrial design process to compliment experiments. CFD is used to predict and study flows in industrial compressors, and helps reduce the number of time consuming and expensive experiments required. High fidelity CFD simulations are still expensive, for example Tyacke et al. [3] estimate that a large eddy simulation (like those presented in this thesis) of a low pressure turbine may cost between £4-13k. However, with ever increasing computing power [4], such simulations are forecast to become cheaper.

1.2 Turbulence modelling for turbo-machinery

Throughout the design of a gas turbine engine, several CFD methods of varying complexity are used. These range from two dimensional throughflow methods where the flow is solved on an axisymmetric surface, to three dimensional multistage computations, where multiple stages and their interactions with each other are modelled. In most components of a gas turbine engine, the Reynolds numbers are sufficiently high for there to be substantial regions of turbulent flow. This turbulence generally plays a key role in drag generation, heat transfer, particle dispersion and scalar mixing, along with sound generation [5]. Hence, as noted by Denton [6], the accurate prediction of turbulence is essential for turbo-machinery design.

However, the prediction of turbulence is not easy; the Physics Nobel Laureate Richard Feynman wrote “*Turbulence is the last great unsolved problem in classical physics*”. There are various methods available which attempt this challenge and the main ones are presented in Figure 1.2.

At the top of Figure 1.2 lies the most computationally expensive but conceptually simple method, Direct Numerical Simulation (DNS). This method involves directly resolving all the turbulence down to the Kolmogorov length and time scales, representing the smallest

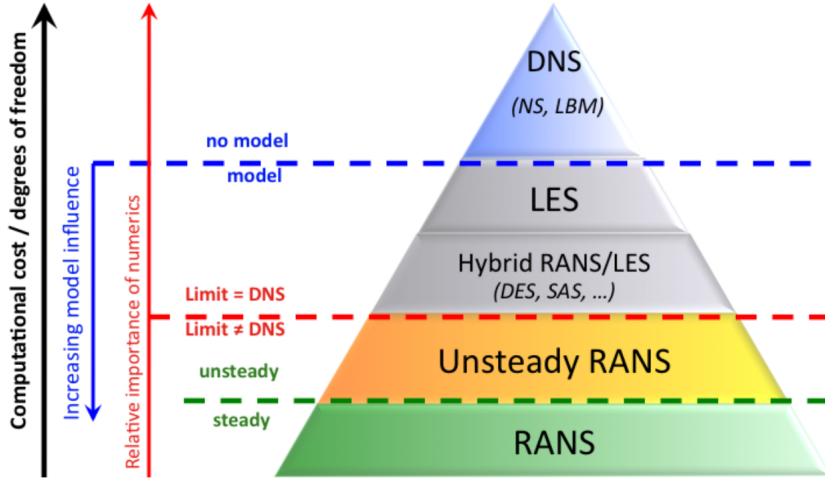


FIGURE 1.2: A hierarchy of the main turbulence treatments. From Sagaut et al. [7].

scales of turbulence within the flow. The Navier-Stokes equations are discretised and solved in their original form, with no modelling of the turbulence required, and it follows that this method is very accurate. Unfortunately, the computational expense required to fully resolve all the turbulence scales is vast. Hence, DNS will not be seen in an industrial setting for the foreseeable future, even as the available supercomputers move into the exascale realm.

| Method | Re-dependence | Empiricism | Grid points | Time-steps | Ready |
|-----------------|---------------|------------|-------------|------------|-------|
| 2D URANS | Weak | Strong | 10^5 | $10^{3.5}$ | 1980 |
| 3D RANS | Weak | Strong | 10^7 | 10^3 | 1990 |
| 3D URANS | Weak | Strong | 10^7 | $10^{3.5}$ | 1995 |
| Hybrid RANS/LES | Medium | Medium | 10^8 | 10^4 | 2000 |
| LES | Strong | Weak | $10^{11.5}$ | $10^{6.7}$ | 2045 |
| QDNS | V. Strong | Weak | 10^{15} | $10^{7.3}$ | 2070 |
| DNS | V. Strong | None | 10^{16} | $10^{7.7}$ | 2080 |

TABLE 1.1: Summary of the main turbulence treatments, modified from Spalart [8]. The cost estimates are based on common practice (Feb 2000). Readiness roughly means that a simulation is ready as a “Grand Challenge”, and is estimated by assuming that computer power increases by a factor of five every five years. These estimates are for the prediction of the flow over an airliner or a car, and would be different for a compressor. Nevertheless, the comparison serves to give an indication of the relative costs between the turbulence treatments.

On the other end of the fidelity spectrum are Reynolds-Averaged Navier-Stokes (RANS) approaches. The RANS equations are obtained by decomposing the instantaneous terms of the Navier-Stokes equations into fluctuating and time-averaged components. The equations are closed through the use of a turbulence model. As is apparent from Table 1.1, RANS methods do not require a high spatial or temporal resolution and are

therefore relatively cheap compared to DNS. This is why they are currently the workhorse for the aerothermal design of gas turbines. However, the models contain numerous tunable constants and are usually calibrated against simple canonical flows. There is no guarantee that different models will give the same results for more complex flows, such as those found in turbo-machinery. This means that RANS can not truly be called a predictive tool, as it requires validation and calibration to experimental data throughout the design process.

An alternative approach to RANS is large eddy simulation (LES), which lies between RANS and DNS on the fidelity scale. The principle of LES is that the larger three-dimensional turbulent scales are computed explicitly, while the effect of the smaller turbulent scales is accounted for with a sub-grid scale (SGS) model. DNS expends nearly all of its computational effort on resolving the smallest dissipative scales. By modelling these scales (which have, to some extent, a universal character), LES can be orders of magnitude cheaper than DNS. Since LES ideally only models about 10% of the turbulent energy of the flow, the empiricism in LES is far weaker than in RANS.

Due to the large cost of resolving very fine elongated streaks near the wall, LES is still computationally expensive. Despite this, LES can offer valuable insights into complex flow physics. A better understanding of the flow can lead to improvements in design, as well as feeding back to the further development of RANS methods.

1.3 Objectives of research

In order for LES to be used reliably, it is important that the method is predictive; it should not require regular calibration to experimental data. This thesis aims to examine the extent to which LES can be used predictively when used to simulate the flow through compressors. This will be done in three stages:

1. For LES to be predictive, it is important that it is not overly sensitive to the numerical scheme, or sources of uncertainty such as the inflow conditions. The first objective is therefore to identify and understand any areas of sensitivity in the simulation of compressor flows.
2. Once any sensitivities have been identified, the next objective is to explore how they can be reduced, so that the LES framework can be made more predictive.
3. The LES studies are expected to provide an improved understanding of the typical flow physics seen in a compressor. Therefore, the final objective is to use LES to highlight particular areas where RANS models could struggle. This might provide

useful information on how RANS models could be improved for application to compressor flows.

1.4 Outline of thesis

To begin this thesis, a review of the current literature is presented in Chapter 2. Important features of compressor flows are discussed, overviews of the RANS and LES approaches are presented, and previous compressor LES studies are summarised. In Chapter 3, an outline of the numerical methods is given.

Chapter 4 examines the sensitivity of LES to the numerics. Two canonical test cases are run, the Taylor-Green vortex and forced isotropic turbulence. A new robust numerical scheme, the locally adaptive smoothing with windowing (LASW) scheme, is introduced and tested.

In Chapter 5 the LES framework, including the LASW scheme and a number of sub-grid scale (SGS) models, is used to simulate a transitional compressor flow. The sensitivity to the numerical scheme, SGS models, and inflow conditions is studied.

The investigation moves towards more engine representative flows in Chapter 6. The effect of periodically incoming wakes is examined. The sensitivity of the endwall flow region to inflow conditions is determined. The endwall flow regions have a significant influence on the performance of a compressor, and RANS models perform poorly here. Therefore, the LES is used to offer an insight into areas of potential improvement for RANS models. Finally, conclusions are drawn and recommendations for future work are made in Chapter 7.

Part I

Literature and Numerical Methods

Chapter 2

Literature Review

In this chapter some of key flow features seen in compressors are discussed. The motivation for performing LES of compressors is then outlined, by summarising some of the limitations of RANS approaches. The principles of LES are introduced, and some of the notable previous LES studies of compressors are examined.

2.1 Flow physics in compressors

There is a large amount of literature on the flow physics of axial compressor flows. This section introduces three features of particular significance; the transitional behaviour of the boundary layers, the interactions between rotor/stator stages, and the three-dimensional separation that occurs near endwalls.

2.1.1 Boundary layer transition

2.1.1.1 Attached flow transition at low free-stream T_i

When the free-stream turbulence intensity (T_i) is low, the laminar boundary layer transitions to turbulence through a process referred to as “natural transition”. This process is shown in Figure 2.1. At a certain critical Reynolds number, the boundary layer becomes linearly unstable due to the amplification of small background disturbances, and two-dimensional T-S¹ waves form (region 1). As the T-S waves convect downstream the Reynolds number increases and the T-S waves are amplified. If the amplitude of

¹Tollmien-Schlichting

these waves reaches approximately 1% of the free-stream velocity¹, a secondary instability occurs (region 2). Klebanoff et al. [10] found that this secondary instability is three-dimensional in nature, and takes the form of span-wise periodic Λ patterns, which develop on top of the T-S waves. The arrangement from row to row can be aligned (K-type) due to fundamental resonance, or staggered (C-type and H-type) due to sub-harmonic resonance [9]. The Λ -vortices rapidly lead to a three-dimensional breakdown to turbulence (Region 3). Further breakdown leads to turbulent spots (Region 4), and by Region 5 the boundary layer is fully turbulent.

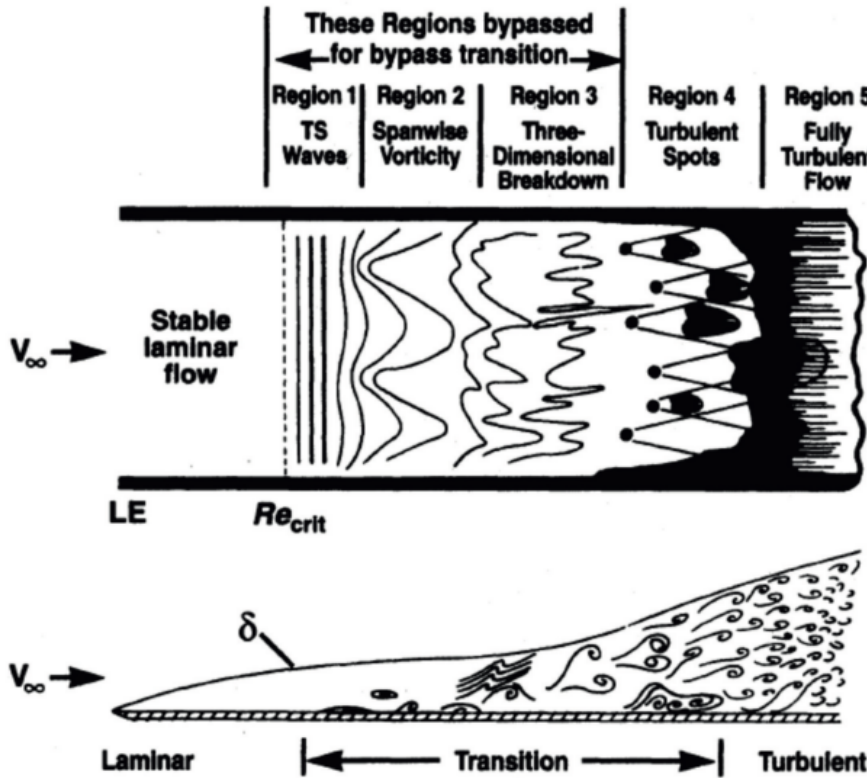


FIGURE 2.1: Schematic showing natural boundary layer transition, from White [11].

2.1.1.2 Attached flow transition at high free-stream T_i

Under high free-stream T_i the natural transition process seen in Regions 1 to 3 in Figure 2.1 is bypassed. In the absence of significant pressure gradient effects, this “bypass transition” occurs due to the amplification of Klebanoff distortions [10]. Klebanoff distortions, or streaks, are stream-wise elongated disturbances, characterised by high positive and negative perturbations of stream-wise velocity relative to the mean flow.

Jacobs et al. [12] describe how the Klebaonoff streaks are forced by the low-frequency component of the free-stream turbulence. Through a phenomenon called shear-sheltering,

¹If the Reynolds number crosses the upper branch of the stability curve before the amplitude reaches 1%, the linear stability waves will return to a stable state [9].

the boundary layer acts as a low-pass filter, only admitting low frequency perturbations from the free-stream. Within the boundary layer, shear causes the low frequency perturbations to be stretched, leading to the Klebanoff streaks. This can be seen in Figure 2.2; the flow is relatively isotropic in the free-stream, but within the boundary layer, the flow is dominated by streaks with a long stream-wise extent.

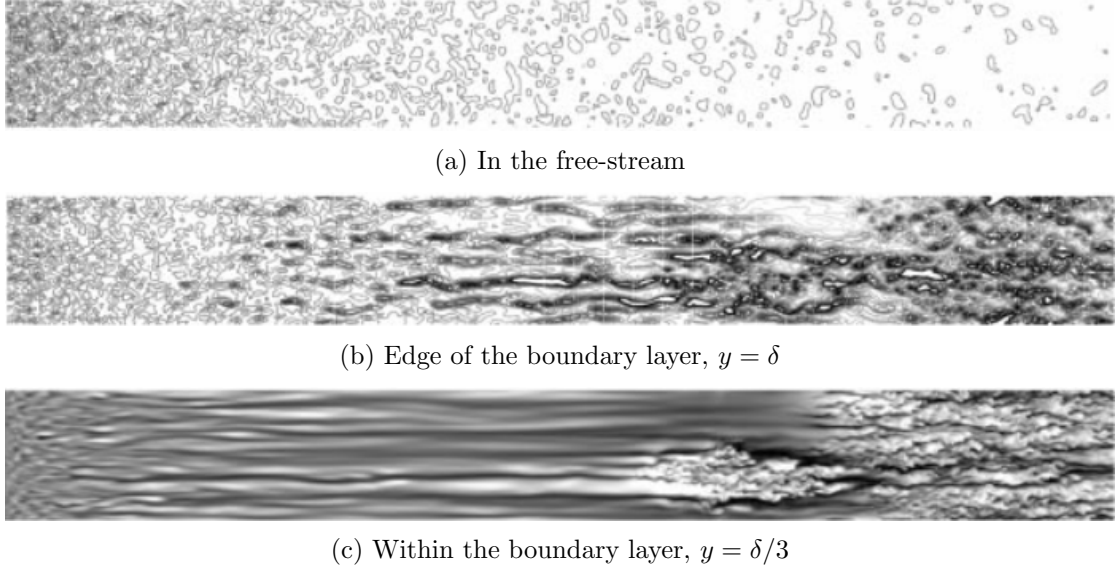


FIGURE 2.2: Contours of stream-wise fluctuating velocity u' from Jacobs et al. [12], illustrating the concept of shear-sheltering.

Jacobs et al. [12] describe how the low-speed Klebanoff streaks lift off from the surface, transporting low momentum fluid with them. These lifted shear layers have the appearance of backward jets. Higher frequencies in the free-stream, which penetrate only the upper part of the boundary layer, perturb the backward jets and trigger a local breakdown to turbulence. An example of this is the turbulent spot seen in Figure 2.2.

2.1.1.3 Separation induced transition

In highly adverse pressure gradients, a laminar boundary is at risk of separation. This is often followed by a rapid transition to turbulence when free-stream turbulence is present. The transition process causes an increase in the wall-normal mixing, leading to the flow reattaching to form a “separation bubble”, like that shown in Figure 2.3. Within the bubble is a region of “dead-air”, where the fluid is almost stagnant. This results in a plateau in the static pressure distribution.

The time-averaged flow shown in Figure 2.3 is in reality highly unsteady. The shear layer is inherently unstable due to its inflectional velocity profile, and it sheds span-wise

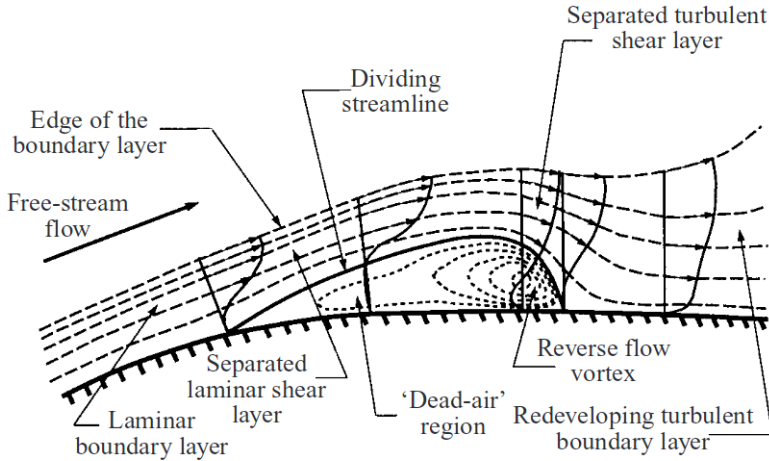


FIGURE 2.3: Schematic of a laminar separation bubble, from Horton [13].

K-H rolls¹. The rolls further breakdown due to secondary instabilities, and the flow undergoes transition.

Many studies, such as that of Spalart et al. [14], conclude that the inviscid instability of the free shear layer is the dominant transition mechanism in laminar separation bubbles. However, the DNS study of Alam et al. [15] finds that rather than undergoing an inviscid instability mechanism, a Λ -vortex-induced breakdown to turbulence occurs. The exact transition mechanisms in a separation bubble are clearly complicated, and this is examined in detail by Nagabhushana Rao [16]. The effects of free-stream turbulence are examined. It is found that the interaction of Klebanoff streaks with the separated shear layer can reduce the size of the separation bubble, or even suppress the separation completely.

2.1.1.4 Transition in compressors

Despite the high Reynolds numbers and free-stream T_i 's seen in gas-turbine compressors, significant extents of the boundary layers are still transitional. Steinert et al. [17] showed experimentally that, even at a relatively high Reynolds number of $Re_c = 8.4 \times 10^5$ and a free-stream turbulence intensity of 2.5%, the suction surface boundary layer remained laminar until peak suction over a wide range of incidences.

Furthermore, while focussing on the design of outlet guide vanes for a small turbofan engine, Schreiber et al. [18] found that laminar separation causes significant profile losses below a critical Reynolds number of 2×10^5 . This is below the range found in conventional aircraft engines ($Re_c \geq 6 \times 10^6$), but does show that transition is even more important in the design of smaller engines. The investigation is performed on a

¹Kelvin-Helmholtz

linear compressor cascade and lacks some real-engine loss sources, such as large endwall separations and rotor-stator interactions. The relative importance of transition may therefore be smaller in a real engine, but the study still highlights the sensitivity of profile losses to transition (and therefore Reynolds number).

Boundary layer transition is especially complicated in turbo-machinery because, as Mayle [19] shows, zones of forward transition (laminar to turbulent) and reverse transition (turbulent to laminar) can coexist. There are a number of routes/mechanisms to laminar-turbulent transition, elegantly presented by Coull et al. [20]. Zaki et al. [9] uses DNS to study the effect of free-stream turbulence on a transitional compressor flow. At a low free-stream turbulence intensity, Zaki et al. [9] observe separation induced transition on the suction and pressure surfaces of the compressor blade. At a moderate free-stream Ti of 3.25%, the pressure surface transition is bypassed. However, the mechanism here is not found to resemble the pure bypass mechanism discussed in Section 2.1.1.1, and instead shows similarities with the natural mechanisms discussed in Section 2.1.1.2. At higher free-stream Ti 's of 6% and above, the mechanism moves towards a more standard bypass type, and at $Ti = 10\%$ the separation is suppressed on both surfaces.

In addition to the free-stream turbulence and pressure gradient, transition is also influenced by the leading edge design. Nagarajan et al. [21] found that blunter leading edges severely stretch the vortices at the leading edge, leading to early transition. Goodhand et al. [22] also found that small changes in the compressor blade leading edge geometry can have a significant influence on the suction surface transition process, and hence a strong effect on the profile losses.

2.1.2 Multi-stage effects

It is important to remember that, as shown in Figure 2.4, an axial compressor is actually made up of multiple rows of rotor and stator stages. The interactions between stages are often important, and cannot be ignored in the design of a compressor. There is a large amount of literature covering the complex rotor-stator interactions that occur in an axial compressor, and this is well summarised by Ernst et al. [23]. Wakes from upstream stages have two significant effects on blades; firstly, they lead to large periodic fluctuations in incidence angle. Secondly, they directly influence the boundary layer transition.

As the incoming wake passes a blade, the boundary layer is locally accelerated at the front of the wake, and decelerated at the back. This perturbs the edge of the boundary layer. In the DNS studies of Wu et al. [25] it is shown that wake induced transition is similar to bypass transition. The wake disturbances are observed to rapidly evolve

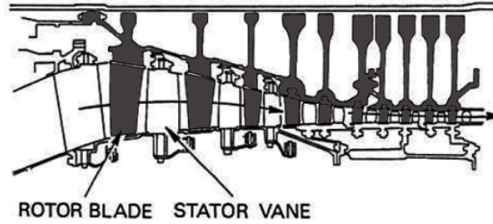


FIGURE 2.4: Sketch of a typical axial compressor, from [24].

into turbulent puffs, which are quickly stretched into streaky structures as they convect downstream. Coull et al. [20] find that these streaky structures are in-fact Klebanoff streaks. As Figure 2.5 shows, what happens next is dependent on the external forcing (and also the Reynolds number). Below a critical Reynolds number $Re_\theta = 200$ the streaks decay (Fig. 2.5(b)), although they still form young turbulent spots downstream if subject to forcing (Fig. 2.5(c)). However, if turbulence inside the wake impinges on the boundary layer, it can interact with its outer part. This leads to an intensification of the near-wall streaky structures, and the breakdown into young spots as shown in Figure. 2.5(a). The young spots then grow, eventually leading to a fully turbulent boundary layer.

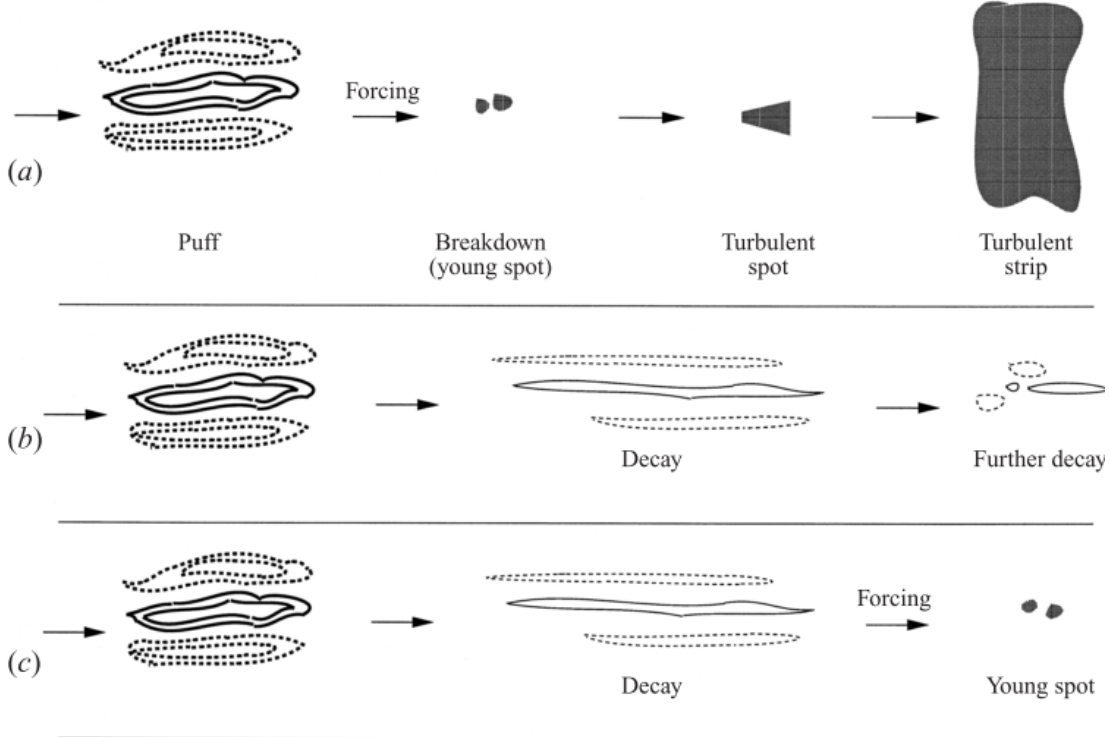


FIGURE 2.5: Wake-induced turbulent puffs stretching into streaks within the boundary layer. Under (a) strong forcing, (b) weak forcing and (c) strong forcing downstream. From Wu et al. [25].

There have also been many studies of wake-induced transition specific to compressors, and these are well summarised by Wheeler et al. [26]. Here it is also found that the

incoming wakes can cause a periodic increase of the boundary layer momentum thickness at the leading edge. This thickened laminar boundary layer then convects downstream, and turbulent spots are observed to form inside it. Following this, Wheeler et al. [27] show how this process is influenced by the leading edge geometry. With a circular leading edge, the wake/leading-edge interaction may contribute up to a 1.5% efficiency reduction. However, with an elliptical leading edge, this reduction is limited to 0.5%.

2.1.3 Endwall flows

The term “endwall flow” describes the viscosity affected boundary layer flow present at the hub and casing of axial turbo-machines. When combined with secondary flows in axial compressors and turbines, these result in highly unsteady and complex three-dimensional flow fields. Denton et al. [28] state that endwall flows typically account for about 30% of the loss in efficiency of an axial turbo-machine. In addition, endwall flows alter stage exit angles and cause blockage, which has further implications on the flow through downstream stages. Hence, it is critical that these flows are accurately predicted.

2.1.3.1 The corner vortex

In blade passages there is a pressure gradient acting from the pressure to the suction surface. This sets up a force balance as follows:

$$\frac{\partial p}{\partial r} = \rho \frac{U^2}{R} \quad (2.1)$$

where R is the radius of curvature of the streamlines, U is the velocity magnitude of the streamlines, and r is the direction perpendicular to the streamlines¹. The pressure gradient therefore causes the flow to be turned. In the boundary layer the velocity is smaller but the static pressure remains fairly constant, therefore the flow is turned more sharply (over-turned) close to the endwall.

This over-turning of the flow near the endwall causes the “corner vortex” to be created near the leading edge on the suction side, shown as V_{sLc} in Figure 2.6. Although there are some diffusive effects not accounted for in the above analysis, this process is primarily an inviscid process, involving the convection of existing vorticity.

¹All other symbols, such as p and ρ , have their usual meanings as defined in the nomenclature (where symbols are not explicitly defined, refer to the nomenclature).

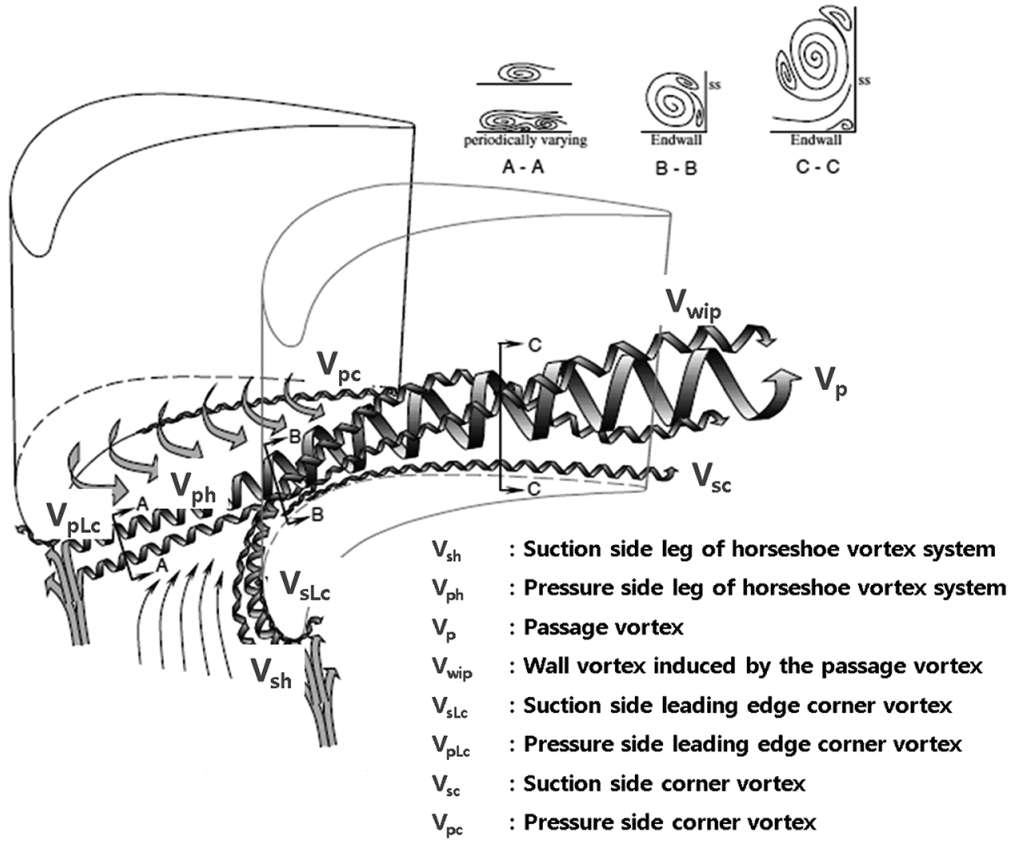


FIGURE 2.6: Simple schematic of endwall flow in a turbine, from Park et al. [29].

2.1.3.2 Leading edge horse-shoe vortex system

Upstream of the blade, a horse-shoe vortex system is formed due to the roll-up of vorticity in the endwall inlet boundary layer, which separates near the leading edge as shown in Figure 2.6. The separation occurs due to the adverse pressure gradient near the leading edge, and is characterised by a saddle point¹, from which the two legs of the horse-shoe vortex (V_{sh} and V_{ph}) propagate. The horse-shoe vortex system is associated with vicious effects on the wall, and its presence is shown in endwall oil-flow visualisations through the leading edge saddle point and its associated dividing skin friction lines.

The pressure side of the horse-shoe vortex (V_{ph}) is convected across the blade passage, when it reaches the suction surface of the next blade it interacts with the corner vortex, where it lifts off the endwall surface and induces another “wall vortex” V_{wip} . Due to the removal of the endwall boundary layer, a new thin boundary layer grows behind the lift-off line of the pressure leg. This boundary layer reveals laminar-like characteristics. Both the lifted-off pressure leg and the crossflow due to the secondary flow combine to form the passage vortex (V_p), which interacts with the suction surface boundary layer.

¹a stagnation point

2.1.3.3 Entropy generation

Denton et al. [28] provide an overview of the main entropy generation sources arising from an endwall flow:

- Entropy generation in the endwall boundary layer itself.
- Entropy generation due to mixing out of the upstream boundary layer within and downstream of the blade row.
- Entropy generation due to mixing out of the kinetic energy of the secondary vortex system.

2.1.3.4 Endwall separation

The above description has been for a turbine endwall flow, since these are more commonly studied. However, there are several differences between turbine and compressor endwall flows; the low blade turning angles of compressors mean that the magnitude of the secondary flow is decreased, and the endwall boundary layers tend to be thicker. This means that the amount of endwall fluid involved is higher.

Additionally, the adverse pressure gradient makes the endwall boundary layers prone to separation. This leads to a complex 3D separation, referred to as a endwall or corner separation, at the endwall - suction surface corner. One possible topology of the corner separation, proposed by Schulz et al. [30], is shown in Figure 2.7. The streamlines on the surface at points (a) and (b) represent the saddle points of a large ring vortex. The separation region is closed off from the main flow by limiting streamlines on the suction surface and endwall. There is however disagreement here. Other authors, such as Hah et al. [31] and Beselt et al. [32], propose alternative topologies.

As Lei et al. [33] explain, a corner separation can be considered to be in one of two states. In the first state, shown in the left in Figure 2.8, the reverse flow region on the endwall is very small. In this case, the flow blockage and loss caused by the corner separation are small. The first state tends to occur at high mass-flow-rate conditions. When the mass-flow-rate decreases (or incidence increases) the reverse flow region can expand abruptly. This state, shown on the right in Figure 2.8, results in significantly increased flow blockage and loss. The first state is often referred to as a “closed separation”, while the second is referred to as an “open separation” or a “corner/hub stall”.

In order to predict the occurrence of corner stall, Lei et al. [33] propose the use of stall indicator (S). This quantifies the extent of the separation region via the local blade

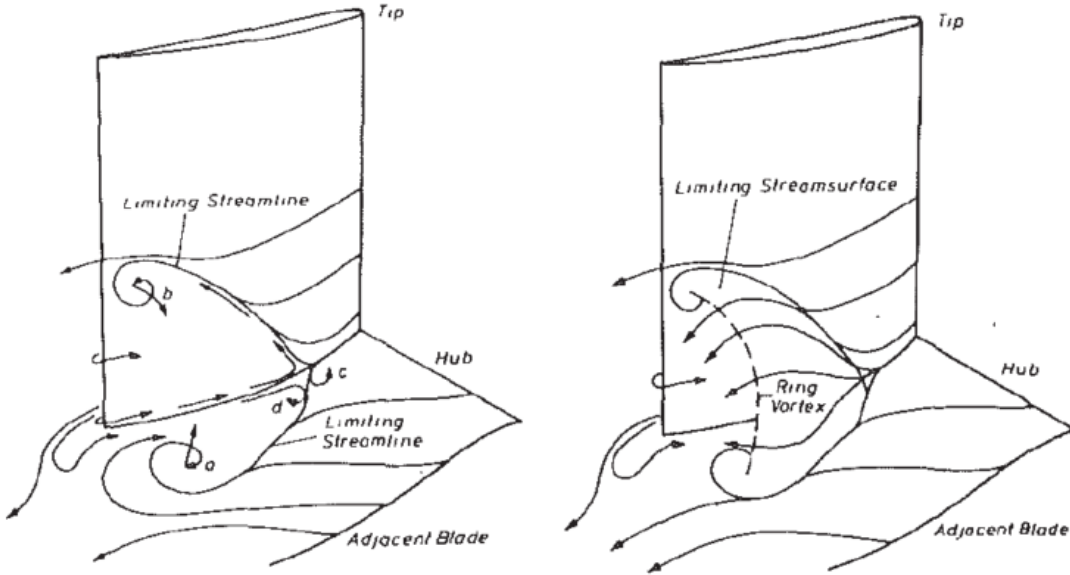


FIGURE 2.7: Sketch of the endwall separation topology proposed by Schulz et al. [30], from Schulz et al. [30].

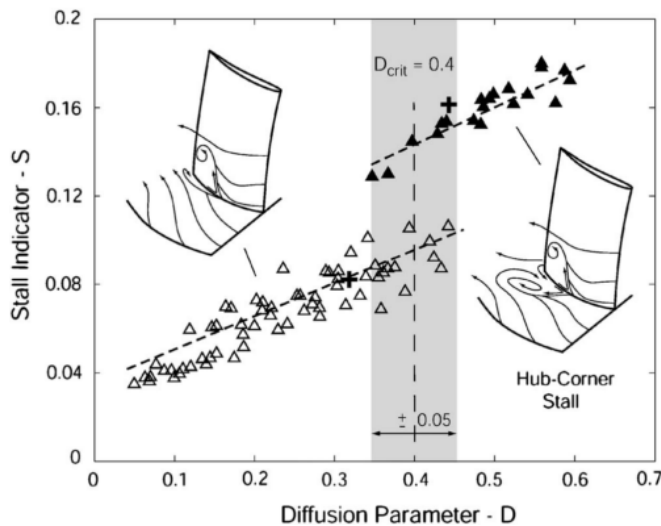


FIGURE 2.8: Lei's diffusion parameter and stall indicator map, from Lei et al. [33].

loading, and thus indicates whether a corner stall occurs. A diffusion parameter (D) is also defined, which can be readily obtained from the geometry and inflow conditions:

$$D = \frac{C_{p_i} \Delta\epsilon}{\sigma} \quad (2.2)$$

where C_{p_i} is the ideal static pressure rise coefficient, σ is the cascade solidity, and $\Delta\epsilon$ is the overall turning angle of the cascade. Figure 2.8 indicates that there is strong correlation between the extent of the corner separation (quantified by S) and the diffusion parameter D . However, there is a significant uncertainty (± 0.025) in the critical diffusion factor at which a corner stall is predicted to occur. Yu et al. [34] reduce the

uncertainty to ± 0.015 by accounting for the influence of blade aspect ratio. Although useful to the designer, both criterion suffer from uncertainty to their semi-empirical nature. They do not account for some of the influences discussed in Section 2.1.3.5, for example unsteady inflow conditions and real geometry features such as wakes.

2.1.3.5 Sensitivities

A number of studies have investigated the sensitivity of the endwall flow to various geometry and flow features. Some of the most important are listed below:

Incidence As mentioned above, an increase in incidence leads to an increase in the blade diffusion parameter and therefore increases the likelihood of endwall stall. Gbadebo [35] also shows that the span-wise and pitch-wise extents of the endwall separation increase with increasing incidence.

Inlet boundary layer thickness The influence of the inlet boundary layer thickness was studied by Gbadebo [35]. It was found that a thickened boundary layer induces a larger endwall separation. This leads to a reduction in blade loading, an increase in flow deviation, and an increase in loss near the endwall. Gbadebo [35] claims that the thickened boundary layer leads to additional entrainment of high momentum fluid from the free-stream into the boundary layer, which suppresses further growth of the endwall separation beyond a certain size.

Real geometry effects Surface roughness of a stator blade was bound to have an important effect on the endwall separation by Gbadebo et al. [36]. They found that increased roughness around the leading edge and peak-suction regions significantly increased the span-wise and pitch-wise extents of the endwall separation. Along similar lines, Goodhand et al. [37] found that the endwall separation is sensitive to small variations in the blade geometry. Leading edge roughness, leading edge fillet and blade-endwall corner fillet were all found to be important. Any geometry feature that causes the suction surface transition to move towards the leading edge (over the first 30% of the span) is found to increase the size of the endwall separation.

Unsteady inflow conditions Schulz et al. [30] found that an upstream rotor wake results in a smaller endwall separation compared to the no-wake case. Schulz et al. [30] hypothesise that the increase in turbulence level due to the wakes is responsible. However, detailed unsteady measurements are not taken here, so it is difficult to be certain. This appears to contradict the findings of Goodhand et al. [37], since incoming wakes (or increased free-stream turbulence intensity) might be

expected to bring the suction surface transition point forward, leading to a larger endwall separation.

2.2 The use of RANS modelling in compressors

As mentioned in Section 1.2, computational fluid dynamics (CFD) involves solving of the Navier-Stokes equations, introduced in Section 2.2.1. The flows encountered in turbomachinery are turbulent, and so the turbulent fluctuations must be accounted for. The two approaches at opposite ends of the turbulence treatment hierarchy, DNS and RANS, are introduced in Sections 2.2.2 and 2.2.3.

2.2.1 The Navier-Stokes equations

The Navier-Stokes equations are derived from a set of global conservation laws for mass, momentum and energy:

$$\frac{\partial \rho}{\partial t} + \frac{\partial \rho u_i}{\partial x_i} = 0 \quad (2.3)$$

$$\frac{\partial \rho u_i}{\partial t} + \frac{\partial u_i u_j}{\partial x_j} = -\frac{\partial p}{\partial x_i} + \frac{\partial \tau_{ij}}{\partial x_j} \quad (2.4)$$

$$\frac{\partial E}{\partial t} + \frac{\partial ((E + p)u_j)}{\partial x_j} = -\frac{\partial q_j}{\partial x_j} + \frac{\partial \tau_{ij} u_i}{\partial x_j} \quad (2.5)$$

with pressure and density being linked by the ideal gas equation:

$$p = \rho RT \quad (2.6)$$

It is the efficient and accurate solution of this set of equations over a range of flow regimes which drives the continued research into computational fluid dynamics.

2.2.2 Direct Numerical Simulation

The most conceptually simple method of solving the Navier-Stokes equations is Direct Numerical Simulation (DNS). This involves simulating the entire range of spatial and temporal scales of the turbulence. Therefore, the dissipation of energy is fully accounted for and there is no need for any additional form of turbulence closure.

However, the need to resolve such a large range of scales means that DNS is impractically expensive. Pope [38] demonstrates how the number of floating-point operations required to complete a DNS scales with Re^3 . This makes it impractical to perform even a single DNS of an industrial compressor flow. For example, the DNS of a turbine blade recently

performed by Wheeler et al. [39] required 6.45×10^8 grid points to compute only a 5% span-wise segment of the blade.

2.2.3 Reynolds averaged turbulence modelling

A far cheaper alternative to DNS is the Reynolds-Averaged Navier-Stokes (RANS) approach, which involves solving the RANS equations. The approach is based on the decomposition of the Navier-Stokes equations into time-averaged ($\bar{\phi}$) and fluctuating (ϕ') components:

$$\phi(\mathbf{x}, t) = \bar{\phi}(\mathbf{x}) + \phi'(\mathbf{x}, t) \quad (2.7)$$

Substituting Equation 2.7 into the full Navier-Stokes equations (with the time derivatives ignored) and Reynolds averaging gives the RANS continuity and momentum equations:

$$\frac{\partial \bar{\rho} \bar{u}_i}{\partial x_i} = 0 \quad (2.8)$$

$$\frac{\partial \bar{\rho} \bar{u}_i \bar{u}_j}{\partial x_j} = \frac{\partial}{\partial x_j} [-\bar{p} \delta_{ij} + 2\mu \bar{S}_{ij} - \tau_{ij}] \quad (2.9)$$

The final term in the RANS momentum equation (Equation 2.9), the Reynolds stress tensor τ_{ij} , is a result of the closure problem introduced by Reynolds averaging. By applying Reynolds averaging, the need to simulate the unsteady turbulent flow field in a time-accurate fashion has been removed. However, we now require a model to account for the effects of turbulence (the Reynolds stresses), which is the job of the RANS model.

The majority of RANS models use the Boussinesq hypothesis to link the Reynolds stresses to the strain of the time-averaged flow field:

$$\tau_{ij} = -\overline{\rho u'_i u'_j} = \underbrace{2\mu_t \left(S_{ij} - \frac{1}{3} \frac{\partial u_k}{\partial x_k} \delta_{ij} \right)}_{\text{Linear}} - \frac{2}{3} \rho k \delta_{ij} + \underbrace{f(S_{ij}, \Omega_{ij})}_{\text{Non-Linear}} \quad (2.10)$$

where S_{ij} and Ω_{ij} are the strain and vorticity tensors (defined in the nomenclature), and μ_t , the turbulent/eddy viscosity, must be calculated by the RANS model.

The two RANS models used in this thesis, the Spalart-Allmaras (SA) model and the shear-stress transport (SST) model, are described in Section A.2. These models are two of the most commonly used RANS models. They ignore non-linear terms in Equation 2.10, and are thus referred to as linear Eddy Viscosity Model's (EVM's).

2.2.4 Challenges for RANS in compressors

RANS approaches have an obvious cost benefit over other approaches such as DNS, but they struggle in the complex flows found in compressors. This prevents RANS from being used as a truly predictive method. Some of the main challenges faced by RANS models in compressors are discussed in the following sections. Some more generic challenges for RANS models are reviewed in Appendix A.1. A number of authors have proposed modelling extensions that are intended to improve RANS models in certain situations, such as the SA-RC correction [40] which sensitises the SA model [41] to rotation and curvature effects. A number of such extensions are introduced in Section A.3.

2.2.4.1 Unsteady flow phenomena

An overview of the unsteady flow phenomena found in turbo-machinery is shown in Figure 2.9. To some extent, periodic flows and transient running can be addressed with an unsteady RANS (URANS) approach. URANS methods are built upon the RANS procedure of dividing the flow into a mean and fluctuating component, but a time dependent component is also allowed in the mean:

$$\phi(\mathbf{x}, t) = \bar{\phi}(\mathbf{x}, t) + \phi'(\mathbf{x}, t) \quad (2.11)$$

For this approach to be theoretically valid, the scales of unsteadiness between the fluctuating mean and the turbulent motion must be distinct. In other words, there must be a “spectral gap” between the resolved and modelled scales, as shown in Figure 2.10.

But, as Tucker [5] discusses in detail, such spectral gaps are not always present in turbo-machinery. For example, in the wake flow of a compressor, all structures are turbulence. Hence, as he explains: “*the notion of having a RANS model to resolve them and unsteady modelling to pick up larger unsteady scales is double accounting*”. This does not mean URANS studies of compressors are not possible, and indeed many useful URANS studies of compressors have been performed [44–46], however it could potentially be a source of inaccuracy.

2.2.4.2 Predicting transition

Mayle [19] provides an overview of the methods available to model the complex transition mechanisms seen in Section 2.1.1. Most RANS models include a trip term to boost the eddy viscosity in some way at the desired transition location. However, this location is often not known, and must be estimated using experimental correlations such as that

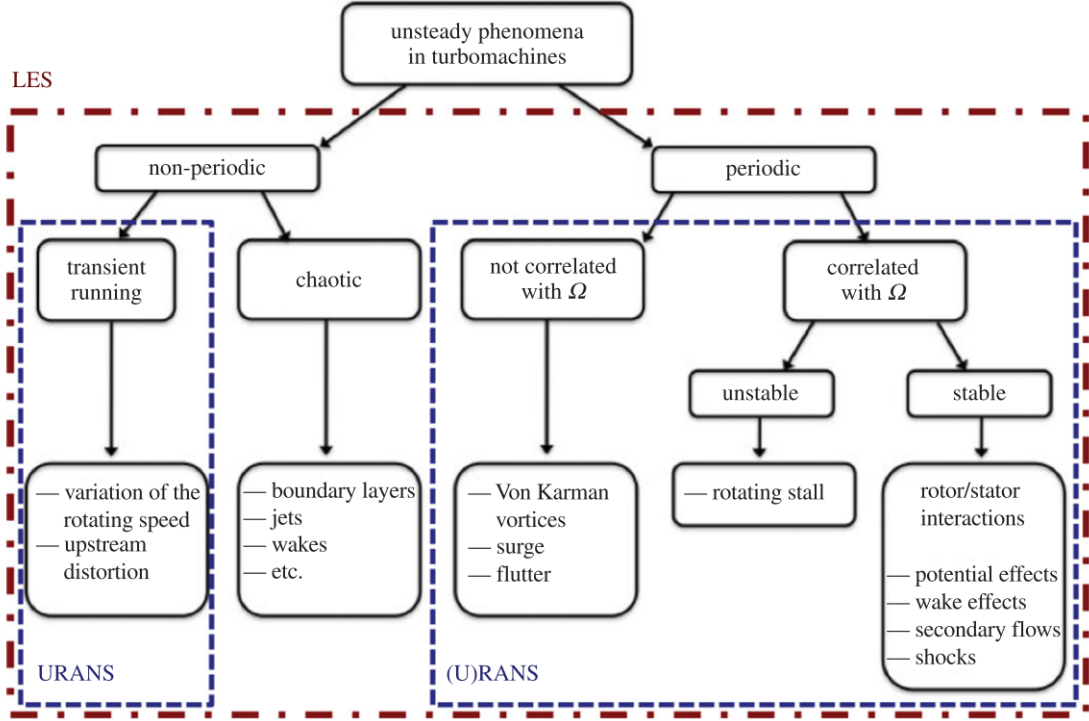


FIGURE 2.9: Overview of unsteady flow phenomena in turbo-machinery, and the turbulence treatments capable of addressing them. Taken from Gourdain et al. [4], originally from Hodson [42].

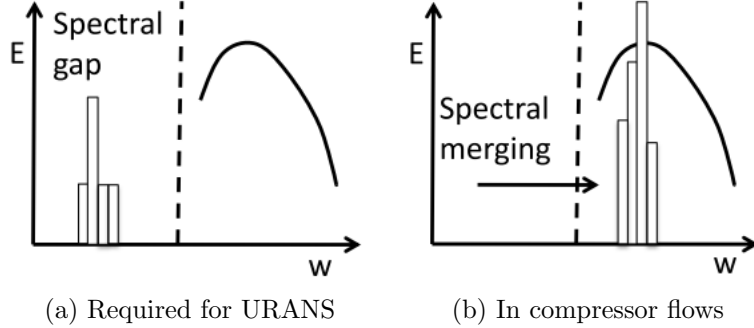


FIGURE 2.10: Spectral gap required for theoretically valid URANS, from Tucker [43].

of Abu-Ghannam et al. [47], or through experience. For example, using the “rule of thumb” that at low Reynolds numbers the transition location can be taken as just after the peak suction location on blades [5]. More advanced RANS treatments are available, such as the Laminar Kinetic Energy (LKE) model of Mayle et al. [48] and the transition model of Menter et al. [49], however these bring in additional empiricism.

2.2.4.3 Endwall flow regions

In 1998 a working group [50] tested the performance of a large number of CFD codes and RANS models on a compressor and a turbine cascade. They concluded that the

simple zero equation mixing length model was unsuitable for complex endwall flows (without significant tuning), and some kind of turbulence transport model was essential. However, even then they found that more complex RANS models were unable to predict the highly three-dimensional flows near the endwalls. In fact, no turbulence model was found which always provides good loss predictions for the endwall flow region. Along similar lines, Langston [51] and Holley et al. [52] both report errors of the order of 40% for the predicted loss with RANS computations of turbine endwall flows, and Marty et al. [53] and Wang et al. [54] report a significant over-prediction of the size of the three-dimensional separation in the endwall region. According to Langston [51] and Horlock et al. [55], a serious deficiency in RANS modelling of turbine flows is the inability to correctly simulate the thin laminar-like endwall boundary layer¹. This leads to inaccurate loss predictions in turbine endwall flows.

Additionally, in some of the above RANS studies the transition locations may be inaccurate. Goodhand et al. [37] showed experimentally that this can significantly affect the endwall separation. Finally, numerous studies (summarised by Rumsey et al. [56]) have found linear EVM's over-predict the corner separation in wing-junction flows. Most find that adding a non-linear term, such as the QCR (quadratic constitutive relation) term, gives significantly improved results. Bordji et al. [57] claim that the QCR returns a turbulent stress field that aids the growth of the corner vortex, which then prevents corner separation. On the other hand, Yamamoto et al. [58] claim that the QCR closure generates stress-induced vortices inside the corner boundary layer, which accelerate it and delay separation. It is unknown if these effects are also significant in compressor and turbine endwall flows.

2.3 Large eddy simulation

In large eddy simulation (LES), the larger three-dimensional turbulent scales are computed explicitly, while the effect of the smaller turbulent scales is modelled. The larger scales, which contain most of the energy and anisotropy, are usually far from universal. Directly resolving these can make LES more reliable than RANS methods. DNS expends nearly all of its computational effort on resolving the smallest dissipative scales. By modelling these scales (which have, to some extent, a universal character), LES can be orders of magnitude cheaper than DNS.

In order to distinguish between the resolved and modelled scales LES involves applying a filtering operation to the Navier-Stokes equations, such that any flow variable ϕ is

¹encountered downstream of the endwall separation line in turbine endwall separations

decomposed into a filtered (resolved) field $\langle \phi \rangle$ and a residual (unresolved) field $\hat{\phi}$:

$$\phi(\mathbf{x}, t) = \langle \phi \rangle(\mathbf{x}, t) + \hat{\phi}(\mathbf{x}, t) \quad (2.12)$$

This decomposition appears very similar to the Reynolds decomposition seen in Equation 2.7, however there are important differences. Firstly, whereas in the Reynolds decomposition the mean field is a statistical quantity generally independent of time, the resolved field in LES is a time-dependent random variable. Secondly, the time mean of the residual field is generally not zero i.e. $\bar{\hat{\phi}} \neq 0$. Substituting Equation 2.12 into the momentum equations (Equation 2.4) gives the filtered momentum equations:

$$\langle \rho \rangle \frac{\partial \langle u_i \rangle}{\partial t} + \langle \rho \rangle \frac{\partial \langle u_i \rangle \langle u_j \rangle}{\partial x_j} = \frac{\partial}{\partial x_j} [-\langle p \rangle \delta_{ij} + 2\mu \langle S_{ij} \rangle - \tau_{ij}^r] \quad (2.13)$$

The final term in Equation 2.13 is the residual stress tensor, which must be modelled. Clark et al. [59] split this term further:

$$\tau_{ij}^r = L_{ij} + R_{ij} + C_{ij} \quad (2.14)$$

where L_{ij} is the Leonard stress, representing uncaptured interactions between the resolved scales. R_{ij} is the Reynolds stress, representing the interactions between the unresolved scales. C_{ij} is the Clark stress, representing interactions between the resolved and unresolved scales.

2.3.1 The filtering operation

During the numerical solution of the filtered LES equations, various numerical errors are experienced, the most significant being the spatial truncation error. This can be thought of as an additional numerical stress, τ_{ij}^h , which is of order h^p (where p is the numerical order of the spatial discretisation).

There are two main schools of thought regarding the role of the numerical stress in LES. The first is that, quite simply, the filtered equations should be solved accurately. In practical terms this means that, the grid spacing h must be chosen to be sufficiently small such that the numerical stress is negligible compared to the modelled residual stress ($\tau_{ij}^h \ll \tau_{ij}^r$). If this is achieved then the filtering and modelling have been decoupled from the numerical method, and the influence of numerical errors on the solution is minimised.

However, Ghosal [60] shows that, when the filter width Δ is set equal to the grid spacing h , the modelled stress τ_{ij}^r scales similarly to the numerical stress τ_{ij}^h (when $p = 2$).

Therefore, simply refining the mesh doesn't decouple the modelling and numerics. One solution to this is to use an explicit filter width, $\Delta \geq 2h$. Now the mesh can be refined to reduce the numerical stress, without the modelled stress also being reduced, and $\tau_{ij}^h \ll \tau_{ij}^r$ can be achieved.

Despite the advantages of explicit filtering, it is rarely used in complex LES cases due to its cost. Even achieving a filter width of $\Delta = 2h$ requires $2^3 = 8$ times the number of grid points over $\Delta = h$. Hence it is more common to use implicit filtering, where the filter operation is implicitly performed by the grid ($\Delta = h$). It is then appropriate to use the terms "resolved" and "subgrid" instead of "filtered" and "residual".

An alternative approach, advocated by Boris et al. [61], is to accept that the numerical stress is significant ($\tau_{ij}^h \approx \tau_{ij}^r$). No explicit residual stress modelling is performed ($\tau_{ij}^r = 0$). Instead, the numerical stress is used to implicitly perform the filtering operation. This approach is termed Implicit LES (ILES).

2.3.2 Sub-grid scale modelling

The earliest and simplest approach to large eddy simulation is the Smagorinsky-Lilly sub-grid scale (SGS) model [62, 63]. The Leonard stress L_{ij} and the Clark stress C_{ij} are ignored, and the residual stress is then obtained from the Boussinesq approximation:

$$\tau_{ij}^r = 2\mu_{sgs} \left(S_{ij} - \frac{1}{3} \frac{\partial u_k}{\partial x_k} \delta_{ij} \right) \quad (2.15)$$

where the SGS viscosity is:

$$\mu_{sgs} = \rho(C_s \Delta_{vol})^2 S \quad (2.16)$$

and C_s is a model constant. S is the magnitude of the strain rate tensor S_{ij} ($S = \sqrt{2S_{ij}S_{ij}}$). The filter is an implicit filter determined from the cube root of the local median control volumes:

$$\Delta_{vol} = \sqrt[3]{h_x h_y h_z} \quad (2.17)$$

Even for a good quality LES mesh, moderately high aspect ratio cells are found close to viscous walls. Consequently Δ_{vol} remains large and excessively high μ_{sgs} values are found close to the wall. This problem can be mitigated by using ad-hoc wall limiting or damping. For example, Schumann [64] shows that limiting the Smagorinsky length scale $l_s = C_s \Delta_{vol}$ to the mixing length near the wall works well in a turbulent boundary layer:

$$C_s \Delta_{vol} = \min(C_s \Delta_{vol}, \kappa y) \quad (2.18)$$

Even with a wall limiter or damping, the Smagorinsky-Lilly SGS model suffers from a range of shortcomings. Various SGS models (explained further in Sect. A.4) have been proposed that use additional filtering in order to alleviate some of the Smagorinsky-Lilly models shortcomings. For example, Germano et al. [65] propose the dynamic Smagorinsky model. This uses a test filter to locally adjust C_s , allowing $C_s \approx 0$ in regions such as laminar boundary layers. Hughes et al. [66] propose the Variational Multiscale approach, where a test filter is used to prevent the modelled stress τ_{ij}^r from acting on the larger scales of turbulence.

The need for additional filtering adds complexity, and can be a significant complication in many compressor flows where there isn't an obvious homogeneous flow direction. As an alternative, the WALE and Sigma (σ) SGS models are proposed by Nicoud et al. [67, 68] for use in transitional flows. These models are explained further in Section 3.1.5.

2.3.3 Meshing for LES

As has been touched upon previously, LES requires the resolution of at least some of the turbulent flow scales, and is therefore considerably more expensive than RANS methods. Much of this cost is attributed to simulating the near wall region. As with RANS, applying a no-slip wall condition requires the resolution of steep velocity gradients at the wall. This necessitates a fine wall normal grid spacing with the first grid point placed at $y^+ \approx 1$, and ≈ 5 grid points in the viscous sub-layer [69].

Additionally, in the proximity of walls ($y^+ < 100$) energy-carrying turbulent structures are small, and flow is dominated by elongated coherent structures (streaks). These are responsible for most of the momentum transfer and production of turbulent energy close to a wall [38]. The streaks measure about 2000 wall units in the streamwise direction, have a width of about 20-80 wall units, and a spacing in the spanwise direction of about 100 wall units [70]. LES must, by definition, resolve most of these energy containing near wall streaks. This requires a fine grid spacing in all three spatial directions near the wall, in contrast to RANS where only a fine wall-normal resolution is required. Piomelli et al. [71] suggest the near-wall grid requirements given in Table 2.1 for LES. These are compared to the grid requirements suggested for DNS by Piomelli [72].

| Grid requirement | LES | DNS |
|--|------------------------|------------------|
| Location of first grid point from wall | $y^+ < 2$ | $y^+ < 1$ |
| Streamwise grid spacing | $x^+ \approx 50 - 100$ | $x^+ \approx 15$ |
| Spanwise grid spacing | $z^+ \approx 15 - 40$ | $z^+ \approx 5$ |

TABLE 2.1: Near-wall grid requirements for DNS and LES.

It may be tempting to use LES on coarser grids, but Table 2.2 shows that this can have a detrimental effect on the solution. Ferziger [73] explains that an under-resolved near-wall grid can lead to an under-prediction of turbulent production, and consequently a reduction of predicted Reynolds stresses and thus skin friction. Temmerman et al. [74] also showed that it can lead to an erroneous representation of the log-law and excessive anisotropy near the wall.

| Grid resolution parameters | Quality of LES | Effect on Solution |
|-----------------------------|-------------------|--|
| $x^+ \leq 50, z^+ \leq 12$ | High resolution | Generally good predictions of skin friction |
| $x^+ \leq 100, z^+ \leq 30$ | Medium resolution | Thicker and shorter streaks, error in skin friction prediction |
| $x^+ \geq 100, z^+ \geq 30$ | Poor resolution | Unrealistic streaks, larger error in skin friction prediction |

TABLE 2.2: Overview of near-wall grid resolution parameters and their effect on the solution, from Sagaut [75].

To make matters worse, the near wall streaks decrease in size as the Reynolds number is increased. As Chapman [76] showed, if it is assumed that wall spacings of $\Delta x^+ = 100$ and $\Delta z^+ = 20$ are sufficient to resolve the near wall streaks, then the number of grid points required to resolve the $y^+ < 100$ zone (about 1% of the boundary layer thickness) scales with $Re^{1.8}$ (or $Re^{1.86}$ according to Moin [77]). Chapman [76] then goes on to show that the number of grid points required to resolve the rest of the boundary layer ($100 < y^+ < \delta^+$) scales as $Re^{0.4}$. These correlations are important because, as Figure 2.11 demonstrates, the Reynolds number varies significantly through a gas turbine engine. This means that the cost of LES varies tremendously for different components.

Piomelli et al. [78] follows on from Chapman [76] to show that for flows with Reynolds number of the order of 10^6 , 99% of the grid points are used to resolve the viscosity affected near-wall region, whose thickness is less than 10% of the boundary layer. Therefore, one way to reduce cost is to model this grid-intensive near-wall region in some way. A common method is hybrid RANS-LES, where a RANS layer is used to model the near-wall turbulence. Figure 2.11 shows that this allows for cost savings of multiple orders of magnitude in some regions. However, the suitability of such methods for transitional flows is not well understood. Since one of the aims of this thesis is to examine the importance of transition in compressor flows, hybrid methods are not used.

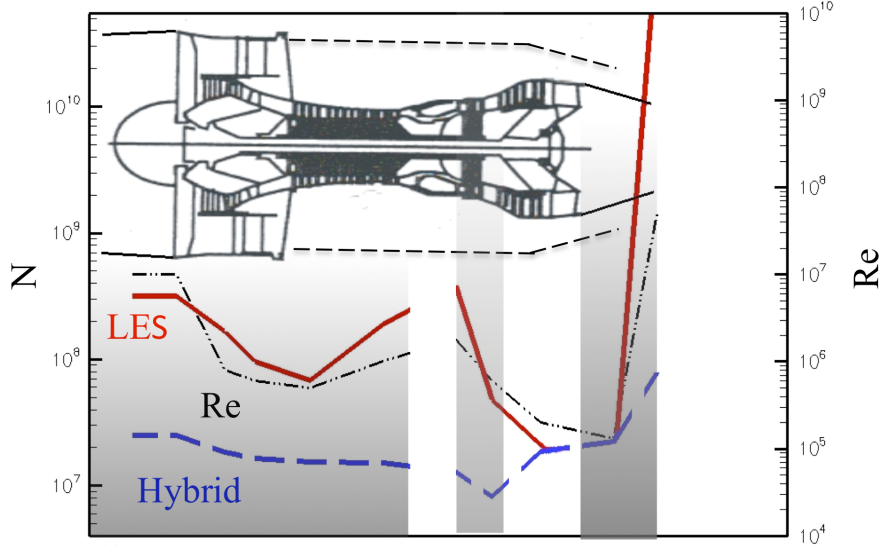


FIGURE 2.11: Re number variation through a medium-sized gas turbine engine, along with Hybrid RANS/LES and LES grid requirements. Taken from Tucker [5], originally extended from Mayle [19].

2.4 Previous LES compressor studies

In this section, an overview of some of the previous LES compressor studies is presented. Due to the higher Reynolds numbers found in compressors, LES studies of compressors used to be rare compared to those of turbines, however as the summary in Table 2.3 shows, compressor LES studies are becoming increasingly popular.

Some of the first compressor LES studies were performed by Klostermeier [83] and Eastwood et al. [84]. LES and hybrid RANS/LES were used to compute a compressor endwall flow. Both find that the 5 million grid point mesh is far too coarse to correctly support the turbulent endwall boundary layer upstream of the blade in the pure LES cases, causing premature endwall separation. Hence, both studies recommend the use of a RANS layer on the endwall of the domain. With the hybrid RANS/LES method, broadly encouraging agreement is found with time averaged experimental data. However, Klostermeier [83] finds that the results are sensitive to the thickness of the RANS layer.

Hah [85] uses LES to simulate the NASA rotor 37, a transonic axial compressor. The LES gives significantly more accurate performance predictions compared to previous RANS studies, with the compressor characteristic predicted to within 5% of experiments. The LES results suggest that the compressor stall inception can be strongly related to blade tip events. Hah et al. [45] take this further by using LES to investigate how circumferential-groove casing treatments can increase the compressor stall margin. Experiments show that this gain is due to complex unsteady flow effects, and previous RANS and URANS studies had significantly under-predicted the achievable increase in

| Year | Method (Spatial order, implicit or explicit in time) | SGS Model | Grid points [†] (10^6) | Reynolds no. (10^6) | Ref. |
|------|---|-------------|---|-------------------------------|------|
| 2005 | LES (6 th , imp) | - | 9.8 (x1) | 0.45 | [79] |
| 2006 | LES (2 nd , imp) | - | 0.8 (x6) | 0.15 | [80] |
| 2006 | LES (2 nd , imp) | DSM | 25.0 (x1) | 0.40 | [81] |
| 2007 | LES (4 th , exp) | SISM | 3.0 (x6) | 1.00 | [82] |
| 2008 | LES (2 nd , exp) | SM, WALE | 10.0 (x1) | 0.23 | [83] |
| 2008 | Hybrid (2 nd , exp) | - | 10.0 (x0.5) | 0.23 | [83] |
| 2009 | Hybrid (2 nd , exp) | - | 10.0 (x0.5) | 0.23 | [84] |
| 2009 | LES (2 nd , imp) | DSM | 13.8 (x1) | 1.20 | [85] |
| 2011 | LES (2 nd , imp) | DSM, VMS | 6.3 (x1) | 0.14 | [86] |
| 2011 | LES (3 rd , imp) | WALE | 100.0 (x1) | 1.20 | [87] |
| 2012 | LES (2 nd , imp) | ILES | 1.5 (x10) | 0.50 | [88] |
| 2012 | LES (2 nd , exp) | SM | 39.0 (x1) | 0.70 | [89] |
| 2012 | LES (2 nd , exp) | SM | 36.0 (x2) | 0.18 | [89] |
| 2012 | LES (2 nd , exp) | SM | 35.0 (x5) | 0.35 | [89] |
| 2012 | LES (2 nd , imp) | DSM | 5.0 (x1) | 1.20 | [45] |
| 2013 | LES (2 nd , exp) | - | 7.0 (x2) | 0.70 | [90] |
| 2013 | LES (3 rd , imp) | WALE | 122.0 (x7) | 0.70 | [91] |
| 2013 | Hybrid (2 nd , imp) | - | 44.0 (x2) | 1.00 | [92] |
| 2013 | Hybrid (2 nd , imp) | - | 4.5 (x1) | 0.38 | [93] |
| 2014 | LES (2 nd , exp) | Vreman [94] | 48.0 (x1) | 0.13 | [95] |
| 2015 | LES (4 th , exp) | SISM | 200.0 (x1) | 0.38 | [96] |
| 2016 | Hybrid (2 nd , imp) | - | 10.0 (x0.5) | 0.23 | [97] |
| 2016 | LES (4 th , exp) | WALE | 156.0 (x1) | 0.3 | [98] |
| 2016 | LES (2 nd , exp) | WALE | 30.0 (x1) | 0.25 | [99] |

[†] Grid points is per rotor/stator blade passage, coefficient in () is number of blade passages simulated.

* SM = Smagorinsky-Lilly Model. DSM = Dynamic Smagorinsky Model. ILES = Implicit LES. WALE = Wall-Adapting Local Eddy-viscosity Model. SISM = Shear-improved Smagorinsky Model.

TABLE 2.3: Summary of published works, since 2005, dealing with LES (or hybrid methods) for the simulation of compressor flows, modified and extended from [4].

stall mass flow rate. The LES results gave a much more accurate prediction of the stall margin, and also allowed for a superior understanding of the complex flow physics involved with the casing treatment.

Lardeau et al. [86] use two LES SGS¹ models to simulate the transitional flow over a

¹Sub-Grid Scale

low-pressure compressor blade, and compare the results to previous DNS studies by Zaki et al. [9, 100]. In the majority of studies in Table 2.3, it is found that the effect of the SGS is overshadowed by numerical errors and grid quality issues, and the choice of SGS model is not as important. However, for the transitional flows studied by Lardeau et al. [86] this appears to be less certain.

A number of different LES compressor studies are performed by McMullan et al. [89]. The first study compares two blades with differing spanwise extents, using inviscid walls for the span-wise boundaries. Both spanwise extents are quite small due to the computational cost associated with the high Reynolds number. The time-averaged surface pressure distributions are in close agreement with measurements, however the span-wise inviscid walls contaminate the predicted loss¹. It is also noted that although the laminar separation bubble on the suction surface is quite well predicted, even with a relatively large mesh ($\approx 40M$ grid points), the grid is thought to be too coarse for the LES to capture the natural boundary layer transition on the pressure surface.

The second study performed by McMullan et al. [89] is on a stator blade located in a multi-stage axial compressor test rig. It is demonstrated that the effect of wakes from upstream blade rows is significant, and must be considered for multi-stage compressors. A part of the upstream rotor blade row is added to the domain, however it is noted that the lack of an unsteady inflow for the rotor stage results in poor predictions of the flow at the casing endwall. To account for this, Lund recycling [101] is used to recycle the turbulence from the stator outflow onto the rotor inflow. This improves results, but is still not completely representative, as it implies an infinite number of stages. The overriding message here is that the higher fidelity of LES brings with it the need for higher fidelity inflow conditions.

Wang et al. [93] use a hybrid RANS/LES method to explore the endwall flow of a compressor at different incidences. Some grid sensitivity is observed, but mostly encouraging agreement is found with surface pressure measurements and downstream loss contours. This study highlights some of the physics which cause RANS models to struggle in the endwall flow region; there is substantial misalignment of the Reynolds stress with the shear strain, high turbulence anisotropy, turbulence non-equilibrium, energy backscatter, and strong resonant type interaction between the trailing edge vortices and the corner separation.

Perhaps the largest compressor LES study to date was performed by Gourdain [91]. He performed URANS and LES of a large scale compressor test rig. The mesh sizes ranged from 12.8 to 857 million. LES predictions of the compressor characteristic are not found

¹The capability to use multiple pairs of periodic boundaries has been added to HYDRA to prevent this issue in the present work.

to be noticeably better than the URANS predictions. However on a positive note, the LES elucidates the presence of a complex pulsation of the tip leakage flow not seen in the URANS studies. The lack of accuracy of the LES studies is perhaps partly due to the fact that the inflow turbulence intensity and length scales were not known, and had to be guessed.

In their recent LES study, Gao et al. [96] use LES to give important insights into the dynamics of a corner separator in a linear compressor cascade. Histograms of the velocity at the edge of the corner separation provide evidence that the separation switches between two different modes in an intermittent and aperiodic fashion. This bimodal behaviour was also observed in the experiment.

2.4.1 Numerical schemes for LES

Upon further examination of Table 2.3 it becomes apparent that the majority of the works so far have used second order accurate schemes. This is perhaps due to the fact that many LES studies use modified industrial RANS codes, where such schemes are common. The order of the numerical method arises from the spatial and temporal finite difference approximations used. As an example, the spatial derivative (at point i) in the 1D advection equation

$$\frac{\partial u}{\partial t} + c \frac{\partial u}{\partial x} = 0 \quad (2.19)$$

can be approximated using second order central differencing

$$\left. \frac{\partial u}{\partial x} \right|_i = \frac{u_{i+1} - u_{i-1}}{2\Delta x} + O((\Delta x)^2), \quad (2.20)$$

to give a second order accurate scheme. This approximation is obtained by subtracting the Taylor series expansions for u_{i+1} and u_{i-1} from each other, and ignoring the $\partial^3 u / \partial x^3$ and higher order terms. We are therefore left with a leading error term of:

$$O((\Delta x)^2) = \frac{(\Delta x)^2}{3!} \left. \frac{\partial^3 u}{\partial x^3} \right|_i \quad (2.21)$$

The influence of the numerical errors arising from finite difference approximations is shown in Figure 2.12. If the leading error term contains an even order derivative, then the numerical error will be dissipative (Fig. 2.12a). If the leading error term contains an odd order derivative, as is the case in Equation 2.20, then the numerical error will be dispersive (Fig. 2.12b).

Both these types of errors have a detrimental effect on the solution; dissipative errors cause smearing in the solution (amplitude errors), while dispersion causes wiggles (phase

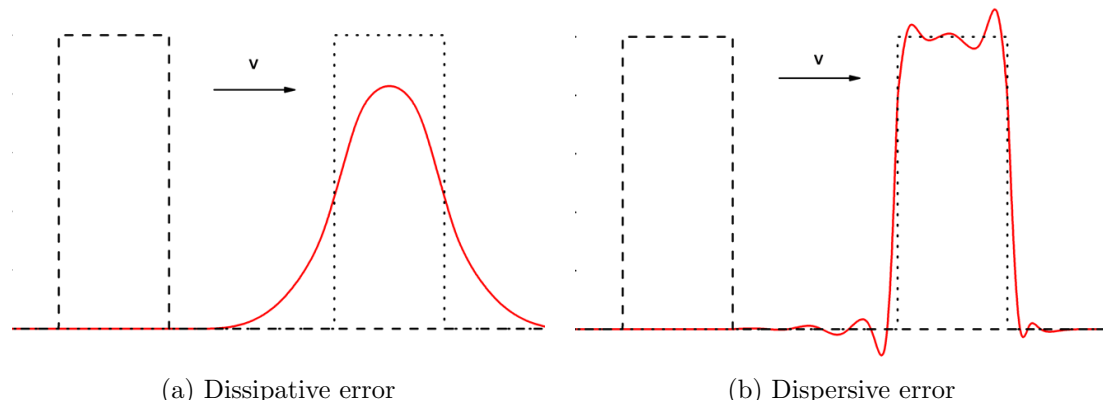


FIGURE 2.12: Solution to the 1D advection equation (eqn. 2.19) showing the effect of finite difference errors. Adapted from Kuzmin et al. [102].

errors). Ghosal [60] notes how the reliability of numerical simulations of turbulence depend on the our ability to control these errors. Many CFD codes, such as the HYDRA code discussed in Chapter 3, use a low dissipation central differencing scheme for spatial discretisation. Excessive dispersive errors are smoothed out by blending in a small amount of a more dissipative scheme, such as 1st order upwinding. This strategy works well for RANS computations, where the numerical dissipation aids convergence. However, for eddy resolving computations the smoothing can cause turbulent vortices to be dissipated too quickly [103]. To avoid this excessive numerical dissipation, fine grid resolutions are necessary.

One approach to reducing discretisation errors is to use a higher order scheme, where higher order derivatives than those in Equation 2.20 are included. Vreman et al. [104] performs a LES of a temporal mixing layer with a variety of numerical schemes, and finds that the low-order schemes exhibit larger discretisation errors, unless a finer grid resolution is used. Despite the increased computational cost of a higher order method for a given mesh resolution, Wang et al. [103] notes that higher order methods perform better based on error versus cost for 2D problems, and similar results are expected in three dimensions. However, even higher order schemes still require some smoothing. Meinke et al. [105] compare a 2nd and 6th order scheme on an LES turbulent jet case, and find both give comparable results. Thus it would seem the accuracy of advantages gained from higher order schemes are quite case specific.

Wang et al. [103] highlights a number of other issues preventing high order codes from impacting the industrial design process. For example; they have a high memory requirement if implicit time stepping is employed, robust high order mesh generators are not readily available, and high order accuracy is lost for problems with non-smooth solutions (e.g. shocks) or geometries. Additionally, due to the larger communication halos required by high-order methods, they are more challenging to efficiently parallelise.

In addition to (or instead of) increasing the order of accuracy of the numerical scheme, a number of alternative numerical approaches have been explored for use with LES:

- As discussed in Section 2.3.1, explicit filtering could be used. It is then possible to decouple filtering and modelling from the numerical method, but this requires dramatically increased grid sizes for a given filter scale.
- The ENO approach, first proposed by Harten et al. [106], uses a combination of stencils with different levels of upwind and downwind bias. When wiggles are detected, the least oscillatory member of the family of stencils is selected. Despite their promise, the experiences of using ENO type schemes for LES are mixed. A number of studies, such as Garnier et al. [107], have found the schemes are still overly dissipative at the small scales.
- Flux limiters, such as min-mod or superbee [108], can be implemented to enforce the Total Variation Diminishing (TVD) constraint. These flux limiters control a blending between a dissipative (usually first order) and higher order scheme, based on the local flow conditions. They are attractive as they can make use of existing differencing schemes within a code. However, Watson [109] implemented a number of flux limiters in HYDRA and found that results were strongly dependent on the flux limiter selected.
- The need to tune the numerical smoothing can be problematic when using CFD as a predictive tool. Locally adaptive smoothing (LAS) schemes, like that proposed by Tajallipour et al. [110], avoid the need for manual tuning by locally adapting the smoothing in response any detected wiggles in the solution. Kumar et al. [111] had success using this scheme for LES of a jet cross-flow.
- A kinetic energy preserving (KEP) scheme [112] was implemented in HYDRA by Watson [109]. By simply changing the order of averaging of the flux terms, kinetic energy is conserved (at the cost of conserving momentum). This approach offers substantial gains in stability, meaning that less artificial dissipation is required.

2.4.2 Representation of compressor flows

In order to use CFD to properly understand the flow in real gas-turbine compressors, the numerical test cases must properly represent the flow physics seen in a real engine. Due the high computational cost and complexity of simulating real engine compressor components, most of the LES studies listed in Table 2.3 have investigated significantly simplified geometries. It is important to appreciate how these simplified cases differ from a real gas-turbine compressor flow.

The first common simplification involves scaling down the operating conditions compared to a real engine. To reduce the computational cost the LES investigations are often performed at a lower Reynolds number (see Section 2.3.3). Hobson et al. [113] find that as the Reynolds number increases, the suction surface separation bubble on a compressor stator blade moves towards the leading edge. Eventually, if the Reynolds number were high enough, the flow would be fully turbulent. However, as noted in Section 2.1.1.4, even at the relatively high Reynolds found in gas-turbine compressors, there are still substantial regions where the boundary layers are laminar.

For a number of reasons¹, the Mach number of LES studies is also lower than in a real compressor. If the Mach number is high enough, then the shocks can become important [85]. Even at lower compressible Mach numbers, compressibility can have a significant impact. For example, Matsuura et al. [114] finds that pressure waves originating from the trailing edge in a compressible turbine flow becomes one of the dominant behaviours of the boundary layer when the free-stream turbulence intensity is low.

Due to the complexity and computation cost of simulating real compressor geometries, many LES studies are performed on more simple linear (2D) compressor cascades. These cascades also often have more experimental data available for comparison, since it is easier to take measurements within them. Real compressors have a number of important flow features that are not usually captured in linear compressor cascades:

Inlet boundary layer skewness The relative motion of adjacent blade rows generates an endwall boundary layer which is skewed relative to the downstream blade row.

The direction of the skew is such that, close to the hub and casing endwalls, the flow approaches the leading edge with at high positive incidence angles. Despite the increased loading near the endwalls, Bode et al. [115] finds that the interaction of the overturned endwall flow with the blade suction surface was reduced by the inlet skew. Additionally, the overall total pressure losses were found to be lower with inlet skew than without.

Rotation effects The rotation of rotor blade rows leads to a span-wise redistribution of fluid. Dring et al. [116] found that at a low rotating speed condition, low total pressure fluid accumulates at the blade hub corner due to the passage vortex, which leads to a large corner separation. However, at a high rotating speed condition, low energy fluid is centrifuged outwards, leading to a smaller corner separation.

¹For example; only having an incompressible LES/DNS code available, the original experiment being run at a low Mach number (for practical considerations such as power requirements), or to remove the added complexities of analysing a compressible flow (e.g. Favre averaging instead of Reynolds averaging).

This radial redistribution also results in non-uniform stagnation pressure and temperature profiles at the inlet to stages, something not often accounted for in linear cascade investigations.

Radial variations In an annular compressor there are relative speed differences between the tip and root of rotor blades. This causes radial variations in the swirl angles seen by both the rotor and stator rows. To account for these radial variations different blade cross-sections are often used at different radial locations, and the blades are twisted. Lei et al. [33] notes that this results in the overall pressure rise across the stage varying with radius.

Leakage flows According to Borello et al. [117], the vortex occurring as flow leaks through the gap between the rotor tip and casing is one of the major causes of loss in a compressor. Additionally, Wellborn et al. [118] show that the leakage that occurs between the hub and a shrouded stator also substantially degrades performance. On the other hand, Gbadebo et al. [119] shows that a clearance gap between a stator blade and the casing can be added to reduce loss, with the gap causing the corner separation to be inhibited.

2.5 Concluding remarks

The main aim of this thesis is to explore the predictive capability of CFD for use in the design of gas-turbine compressors. In Section 2.2 some of the challenges faced by RANS approaches in compressors are explored. The uncertainty here means that RANS cannot be considered predictive. The review of previous LES studies in Section 2.4 highlights the potential for using LES in such flows. For example; the LES results of Hah [85] give a much more accurate prediction of the stall margin. Additionally, studies such as those of Hah [85] and Gao et al. [96] allow for a superior understanding of the complex flow physics.

However, the review of compressor LES literature has also touched upon some of the possible sensitivities that may prevent LES being used in a predictive sense. One of the main aims of this thesis is to explore these sensitivities further. More specifically:

1. Lardeau et al. [86] find that the boundary layer transition mechanisms are influenced by the SGS model. As Table 2.3 shows, many different SGS models are being used by the LES community. The models used by Lardeau et al. [86] require additional filtering and averaging operations¹ which limit their applicability

¹see Section 2.3.2

to industrial compressor LES. Therefore, it is important to determine the sensitivity of compressor flows to more practical models currently in use, such as the Smagorinsky-Lilly and WALE SGS models.

2. The study of McMullan et al. [89] shows that some regions may be more sensitive to the grid quality and numerics than others. The second aim is therefore to determine which regions in particular are sensitive to the SGS model and the numerical scheme, and the relative importance between the two. Like many of the studies summarised in Section 2.4, the CFD code to be used in this thesis is a second order accurate unstructured code. Due to the importance of controlling dissipative and dispersive errors in such codes (covered in Section 2.4.1), a key focus here will be on seeking ways to improve the suitability of the code for LES applications.
3. The study of Gourdain [91] shows that even with very large meshes, uncertainty in features such as inflow conditions can lead to inaccuracies. Due to the significant impact of endwall separations, it is important to determine the sensitivity of this region to the inflow conditions such as the free-stream T_i and the state of the inlet boundary layer.

Finally, the key causes of the poor predictions given by RANS models in the endwall flow region are still not fully understood. As discussed in Section 2.2.4.3; transition may be important, while some studies have also hinted at the possible importance of the non-equilibrium and misalignment of turbulence. Turbulent anisotropy, shown to be influential in wing-junction flows, could also be a factor. The LES results may provide a valuable insight into some of these endwall flow features.

Due to the better availability of experimental measurements and the lower computational cost, linear compressor cascades will be used for the investigations presented in this thesis. Despite their idealised nature (see Sec. 2.4.2), the review of the LES studies in Table 2.3 indicates that they can still provide important insights into transition mechanisms [9, 26], endwall separations [35, 120], and the influence of unsteady inflow conditions [9, 26] in compressors.

Chapter 3

Numerical Methods

The majority of the simulations discussed in this report were carried out on a modified version of Rolls-Royce’s in-house HYDRA CFD code [121, 122]. This code was originally designed to perform steady RANS simulations and has been used within Rolls-Royce for a large range of numerical flow studies. The key features of the code are outlined in this chapter, and the approaches used to generate unsteady boundary conditions are presented. Two different vortex identification methods are also briefly introduced.

3.1 The solver

HYDRA is a node-centred, compressible, density-based Reynolds Averaged Navier-Stokes solver. It is edge-based and unstructured, giving it powerful geometric flexibility when decomposing the highly complex domains seen in industrial turbo-machinery applications.

The temporal and spatial discretisation schemes employed by HYDRA are second order accurate on smooth grids. As discussed in section 2.4 the use of a second order scheme for LES isn’t necessarily disadvantageous compared to a higher order scheme. It will require a finer grid in order to satisfactorily resolve the filtered flow field, but this increased computational cost may perhaps be partially offset by the more efficient parallelisation.

3.1.1 Spatial discretisation

The second order accurate scheme of Moinier [121, 123] is used for spatial discretisation. This scheme involves constructing dual median control volumes (shown in grey in Figure 3.1) around the nodes. Edge e_{ij} connects nodes i and j and has an edge weight

\underline{A}_{ij} . This edge weight is the area of the control volume's face associated with the edge. There is thus a one to one connectivity between edges and faces.

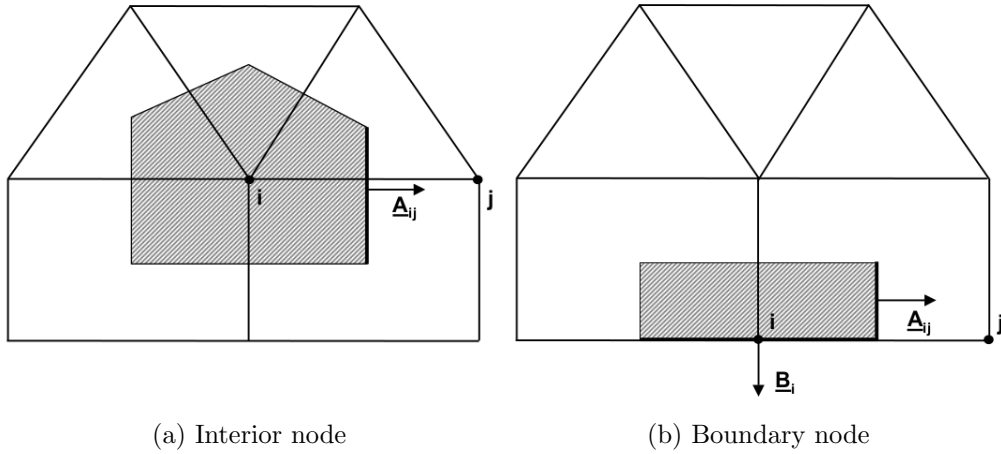


FIGURE 3.1: HYDRA dual control volumes for interior and boundary nodes (extracted from [124]).

The 3D compressible Navier-Stokes equations can be written in vector form:

$$\frac{\partial Q}{\partial t} + R(Q) = 0 \quad (3.1)$$

where:

$$Q = \begin{Bmatrix} \rho \\ \rho u_1 \\ \rho u_2 \\ \rho u_3 \\ \rho E \end{Bmatrix}, \quad R(Q) = \begin{Bmatrix} \rho u_i \\ \rho u_1 u_i + p\delta_{i1} - \tau_{1i} \\ \rho u_2 u_i + p\delta_{i2} - \tau_{2i} \\ \rho u_3 u_i + p\delta_{i3} - \tau_{3i} \\ (\rho E + p)u_i - u_j \tau_{ij} + q_i \end{Bmatrix}.$$

Following the well known finite volume approach, and using the divergence theorem, the viscous and inviscid terms in Equation 3.1 can be integrated over some control volume Ω_i to give:

$$\begin{aligned} R_i^I &= \frac{1}{V_i} \oint_{\partial\Omega_i} F^I(\mathbf{n}, Q) dS \\ R_i^V &= \frac{1}{V_i} \oint_{\partial\Omega_i} F^V(\mathbf{n}, Q, \nabla Q) dS \end{aligned} \quad (3.2)$$

where V_i is the size of the i^{th} median dual cell volume, R_i^I and R_i^V are the inviscid and viscous contributions to $R(Q)$, and $F^I(\mathbf{n}, Q)$ and $F^V(\mathbf{n}, Q)$ are the inviscid and viscous fluxes in the direction of the unit vector \mathbf{n} . For an interior node Equation 3.2 can be

discretised as:

$$\begin{aligned} R_i^I &= \frac{1}{V_i} \sum_{j \in E_i} F_{ij}^I \underline{\Lambda}_{ij} \\ R_i^V &= \frac{1}{V_i} \sum_{j \in E_i} F_{ij}^V \underline{\Lambda}_{ij} \end{aligned} \quad (3.3)$$

where F_{ij}^I and F_{ij}^V are the numerical inviscid and viscous fluxes through the face associated with the e_{ij} edge, and $\underline{\Lambda}_{ij}$ is the edge weight of the e_{ij} edge. E_i is the set of all the nodes connected to node i via an edge. Since each stored edge is associated with a control volume surface, HYDRA can perform the summations in Equation 3.3 by simply looping through all the edges in the domain and accumulating the fluxes. This operation is order independent which is beneficial for an unstructured code.

The computation of the fluxes F_{ij}^I and F_{ij}^V is one of the main computational tasks for HYDRA and is the subject of the following two sections.

3.1.1.1 Inviscid fluxes

HYDRA uses the Roe flux-differencing method [108] to solve for the inviscid flux through each control volume face. The implementation is only briefly discussed here, for a more detailed discussion see Moinier et al. [121, 123]. This is essentially a central differencing method smoothed by some upwinding based on one dimensional characteristic variables. The smoothed inviscid flux through a cell face, $F_{ij}^{I,S}$, is given by:

$$F_{ij}^{I,S} = \frac{1}{2} (F_{ij}^I(Q_i) + F_{ij}^I(Q_j)) - \frac{1}{2} \epsilon_2 |A_{ij}| (L_i^{lp} - L_j^{lp}) \quad (3.4)$$

where $|A_{ij}|$ is the flux Jacobian ($\partial F_{ij}^I / \partial Q$), ϵ_2 is a user defined smoothing constant, and L^{lp} is a Laplacian operator given by:

$$\begin{aligned} L_j^{lp} &= \hat{L}_j - \nabla Q_j \cdot \hat{L}_j \\ L_j &= \left(\sum_{i \in E_j} \frac{1}{|\mathbf{x}_i - \mathbf{x}_j|} \right)^{-1} \sum_{i \in E_j} \frac{Q_i - Q_j}{|\mathbf{x}_i - \mathbf{x}_j|} \end{aligned} \quad (3.5)$$

where ∇Q_j is approximated by:

$$\nabla Q_j = \sum_{i \in E_j} \frac{1}{2} (Q_i + Q_j) n_{ij} \underline{\Lambda}_{ij} \quad (3.6)$$

3.1.1.2 Viscous fluxes

The viscous fluxes are approximated at the midpoint of the edges i.e. where the edges cross their associated dual median control volume faces. In this way, the viscous fluxes are treated consistently with the inviscid fluxes. The gradients of the conserved variables at each midpoint are obtained with a central difference type scheme:

$$\overline{\nabla Q_{ij}} = \frac{1}{2}(\nabla Q_i + \nabla Q_j) \quad (3.7)$$

However, as this is a central difference type scheme, it will not damp high frequency modes. The numerical dissipation terms in the inviscid flux calculation damp these modes in most of the flow, but are not sufficient inside the boundary layer where viscous terms are dominant. To solve this problem the scheme is modified slightly [123]:

$$\begin{aligned} \nabla Q_{ij} &= \overline{\nabla Q_{ij}} - \left(\overline{\nabla Q_{ij}} \cdot \delta \mathbf{s}_{ij} - \frac{Q_i - Q_j}{|\mathbf{x}_i - \mathbf{x}_j|} \right) \delta \mathbf{s}_{ij} \\ \delta \mathbf{s}_{ij} &= \frac{\mathbf{x}_i - \mathbf{x}_j}{|\mathbf{x}_i - \mathbf{x}_j|} \end{aligned} \quad (3.8)$$

3.1.2 Conversion to an incompressible solver

The original HYDRA code is a compressible CFD solver. However, because all the flows simulated in this study have a low Mach number ($Ma < 0.07$), an incompressible version of HYDRA was used. This version was developed by Dr Cui (University of Cambridge), and has been used successfully for a number of LES studies [125].

The incompressible version of HYDRA uses an artificial compressibility scheme [126]. This couples the velocity and pressure fields using an artificial density term given by:

$$\tilde{\rho} = \beta^{-1} p \quad (3.9)$$

where β is the pseudo-compressibility constant. A pseudo-time (τ) derivative is added to Equation 3.1, and for an unsteady solution it becomes:

$$\frac{\partial D}{\partial \tau} + \Gamma_t \frac{\partial D}{\partial t} + R(D) = 0 \quad (3.10)$$

where:

$$D = \begin{Bmatrix} p \\ u_1 \\ u_2 \\ u_3 \end{Bmatrix}, \quad R(D) = \begin{Bmatrix} \beta u_i \\ u_1 u_i + p \delta_{i1} - \tau_{1i} \\ u_2 u_i + p \delta_{i2} - \tau_{2i} \\ u_3 u_i + p \delta_{i3} - \tau_{3i} \end{Bmatrix}, \quad \Gamma_t = diag[0, 1, 1, 1].$$

The system (3.10) consists of four equations since the energy equation no longer needs to be solved. The ability to optimise the value of β leads to significantly improved convergence for low Mach number flows. For further details, see Cui et al. [125] and Rogers et al. [126].

3.1.3 Temporal discretisation

Dual time stepping is used to advance the solution in real time. Second order backward-differencing is used to approximate the $\partial D / \partial t$ term in Equation 3.10, so that the equation discretised around the real time-step n becomes:

$$\frac{D^{n+1,m+1} - D^{n+1,m}}{\Delta\tau} + \Gamma_t \frac{3D^{n+1} - 4D^n + D^{n-1}}{2\Delta t} = -R^{n+1,m} \quad (3.11)$$

where m denotes the pseudo-time step. During pseudo-time the $\partial D / \partial \tau$ term is driven towards zero, which ensures a divergence-free velocity field is satisfied. For pseudo-time marching a 3-stage Runge-Kutta (RK) scheme [127] is used. Equation 3.11 can then be rearranged:

$$\Gamma_{t\tau i} (D^{n+1,m,i} - D^{n+1,m,0}) = -R^{n+1,m,i-1} - \frac{\Gamma_m}{\Delta t} (1.5D^{n+1,m,i-1} - 2D^n + 0.5D^{n-1}) \quad (3.12)$$

where $i = 1$ to 3 is the RK level and the matrices $\Gamma_{t\tau i}$ and Γ_m are defined as:

$$\Gamma_{t\tau i} = \text{diag} \left[\frac{1}{\alpha_i \Delta\tau}, \frac{1}{\alpha_i \Delta\tau} + \frac{1.5}{\Delta t}, \frac{1}{\alpha_i \Delta\tau} + \frac{1.5}{\Delta t}, \frac{1}{\alpha_i \Delta\tau} + \frac{1.5}{\Delta t} \right], \Gamma_m = \Gamma_t$$

with α_i being the standard RK coefficients defined by [127]. A global time-step Δt is chosen that ensures the CFL condition is met everywhere, where the condition is defined as:

$$CFL = \max \left(\frac{u}{\Delta x}, \frac{v}{\Delta y}, \frac{w}{\Delta z} \right) \Delta t < CFL_{max} \quad (3.13)$$

In the present LES cases, a value of $\beta = 20$ was used, and the pseudo time-steps $\Delta\tau$ were set locally to satisfy $CFL < 2$ in pseudo time. The number of pseudo time-steps is adjusted at each physical time-step to ensure satisfactory convergence ($\partial D / \partial \tau < 1e-5$). Usually, 5 – 15 pseudo time-steps were required.

3.1.4 High performance computing

To compute LES in reasonable time-frames requires efficient application of massively parallel computers.

HYDRA is parallelised using the OPLUS library [128], which utilises MPI for message passing. The parallel implementation has been tuned for large-scale problems and near linear speed-up is demonstrated for up to 1024 processors on an IBM Power5 system [129]. The domain decomposition is performed using k-way graph partitioning with the ParMeTis library [130]. MeTis partitioning involves minimising the edges cut by the partitions (thus minimising the message size) while load balancing the nodes.

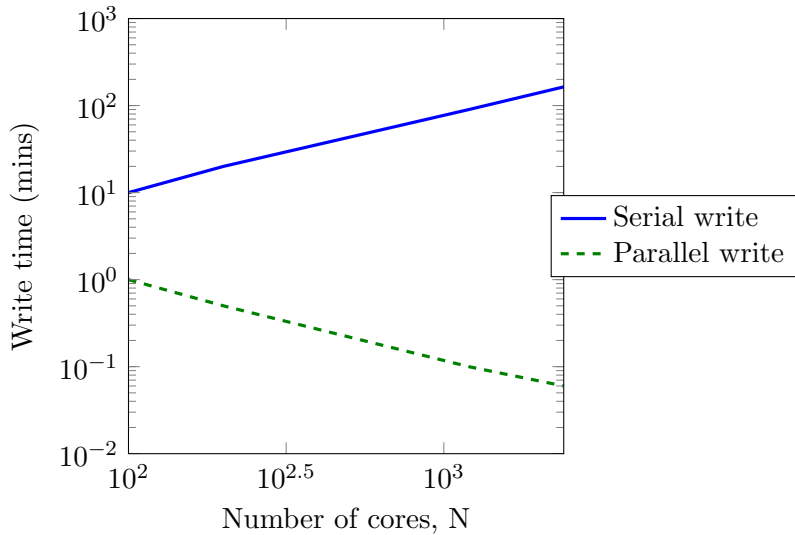


FIGURE 3.2: Time taken for HYDRA to write a 16GB file on ARCHER.

The standard version of HYDRA uses serial data output, whereby all the processors send their data to one processor which performs the write operation. This was found to be a significant bottleneck when running large simulations. Therefore, the code was enhanced to make use of parallel output, with each processor writing its own data. The time taken for HYDRA to write out a 16GB solution file using the serial and parallel data output was recorded, and is presented in Figure 3.2. The parallel output is seen to be significantly faster than the serial output. In contrast to the serial output, the parallel write time decreases when HYDRA is run on more processing cores, since each core must now write out a smaller amount of data.

3.1.5 Turbulence treatments

The HYDRA CFD code has a number of RANS models available. In this thesis, the Spalart-Allmaras (SA) model and the shear-stress transport (SST) model are used. The implementation of these in HYDRA is summarised in Section A.2. A number of RANS model extensions, such as the SA-QCR model, were also added to the HYDRA code. These are described in Section A.3.

The HYDRA code also contains the Smagorinsky-Lilly SGS model, outlined in Section 2.3.2. To explore the importance of SGS modelling, the WALE and Sigma (σ) SGS models, introduced in the following sections, have also been added. Both models use the Boussinesq approximation (Equation 2.15) and an implicit filter:

$$\mu_{sgs} = \rho(C_s \Delta_{vol})^2 D_{w/\sigma} \quad (3.14)$$

However, to obtain the SGS viscosity they replace the magnitude of strain (S) used in the Smagorinsky-Lilly model by more complex operators (D_w or D_σ). These operators are formulated so that zero SGS viscosity is returned in certain flow regions where the Smagorinsky-Lilly model incorrectly returns a non-zero SGS viscosity. One example of this is the case of pure shear, found in a laminar boundary layer. The properties of the models under these conditions, and the recommended model constants [67, 68], are presented in Table 3.1.

| SGS Model | | Smagorinsky-Lilly [62, 63] | WALE [67] | σ [68] |
|--------------------------------|----------------|----------------------------|-------------------|-------------------------|
| Operator | | $S = \sqrt{2S_{ij}S_{ij}}$ | D_w (Eqn. 3.15) | D_σ (Eqn. 3.17) |
| Value of Operator [†] | Pure Shear | 1 | 0 | 0 |
| | Solid Rotation | 0 | ≈ 0.9 | 0 |
| | Axisymmetric | ≈ 3.46 | 0.15 | 0 |
| | Isotropic | ≈ 2.45 | 0 | 0 |
| Model Constant | | $C_s \approx 0.165$ | $C_w \approx 0.5$ | $C_\sigma \approx 1.35$ |

[†] This is the value of the differential operator S , D_w or D_σ when all the velocity gradients are zero except: Solid rotation $\partial u_1 / \partial x_2 = -1$ and $\partial u_2 / \partial x_1 = 1$; Pure shear: $\partial u_1 / \partial x_2 = 1$; Axisymmetric expansion/contraction: $\partial u_1 / \partial x_1 = \pm 2$, $\partial u_2 / \partial x_2 \mp 1$, $\partial u_3 / \partial x_3 \mp 1$; Isotropic expansion/contraction: $\partial u_1 / \partial x_1 \pm 1$, $\partial u_2 / \partial x_2 \pm 1$, $\partial u_3 / \partial x_3 \pm 1$.

TABLE 3.1: Properties of the Smagorinsky-Lilly, WALE and σ SGS models.

3.1.5.1 WALE SGS model

Nicoud et al. [67] propose the Wall-Adapting-Local-Eddy-viscosity (WALE) model. The differential operator D_w for the WALE model is:

$$D_w = \frac{(S_{ij}^d S_{ij}^d)^{3/2}}{(S_{ij} S_{ij})^{5/2} + (S_{ij}^d S_{ij}^d)^{5/4}} \quad (3.15)$$

where the $S_{ij}^d S_{ij}^d$ term is:

$$\begin{aligned} S_{ij}^d S_{ij}^d &= \frac{1}{6} (S^2 S^2 + \Omega^2 \Omega^2) + \frac{2}{3} S^2 \Omega^2 + 2 I V_{S\Omega} \\ S^2 &= S_{ij} S_{ij}, \quad \Omega^2 = \Omega_{ij} \Omega_{ij}, \quad I V_{S\Omega} = S_{ik} S_{kj} \Omega_{jl} \Omega_{li} \end{aligned} \quad (3.16)$$

As seen in Table 3.1 this term is designed so that $D_w = 0$ in regions of pure shear.

3.1.5.2 Sigma SGS model

Recently, Nicoud et al. [68] also proposed the sigma (σ) model. The differential operator D_σ is based on the singular values $(\sigma_1, \sigma_2, \sigma_3)$ of the resolved velocity gradient tensor:

$$D_\sigma = \frac{\sigma_3(\sigma_1 - \sigma_2)(\sigma_2 - \sigma_3)}{\sigma_1} \quad (3.17)$$

Unlike the WALE model, this formulation also returns $D_\sigma = 0$ in solid rotation, and axisymmetric compression/expansion. In the present implementation, the singular values of the velocity gradient tensor are computed using a self-contained method [131]. This avoids the use of an external library such as LAPACK.

3.2 Unsteady boundary conditions

The compressor LES cases presented in Chapters 5 and 6 require unsteady turbulent inflow conditions. Following the approach of Cui et al. [125] and Nagabhushana Rao et al. [132], the unsteady turbulent inflow is decomposed into three key components; unsteady wakes to represent the wakes from upstream blade rows, turbulent boundary layers (TBL's) to represent the incoming boundary layer found on endwalls, and isotropic turbulence to represent free-stream turbulence (FST). The turbulence for each of these is obtained from pre-cursor simulations or synthetic methods, and the velocity fluctuations for each are then superimposed onto the mean inflow:

$$\begin{aligned} u_i(x, y, z) &= U_0 [\bar{u}_i(y, z) + \phi(y) u'_i(x, y, z)_{FST} + u'_i(x, y, z)_{TBL} + u'_i(x, y, z)_{wakes}] \\ \rho &= \rho_0 \\ p &= p_0 \end{aligned} \quad (3.18)$$

For each dataset of inflow turbulence (e.g. FST, TBL or wake data) the velocity components must be transformed from the (x', y', z') local coordinate system to the (x, y, z)

coordinate system of the compressor cascade. For example:

$$\begin{aligned} u'(x, y, z) &= u'(x', y', z') \cos(\beta_1) - v'(x', y', z') \sin(\beta_1) \\ v'(x, y, z) &= u'(x', y', z') \sin(\beta_1) + v'(x', y', z') \cos(\beta_1) \\ w'(x, y, z) &= w'(x', y', z') \end{aligned} \quad (3.19)$$

where β_1 is the inlet flow angle. This procedure gives a box of turbulence which is appended to the inflow of the cascade, as shown in Figure 3.3. The box is then stepped through in the x-direction ($x = x_{inlet} - tU_0$) as the simulation time t progresses. For spatial interpolation a k-d tree algorithm is used [133].

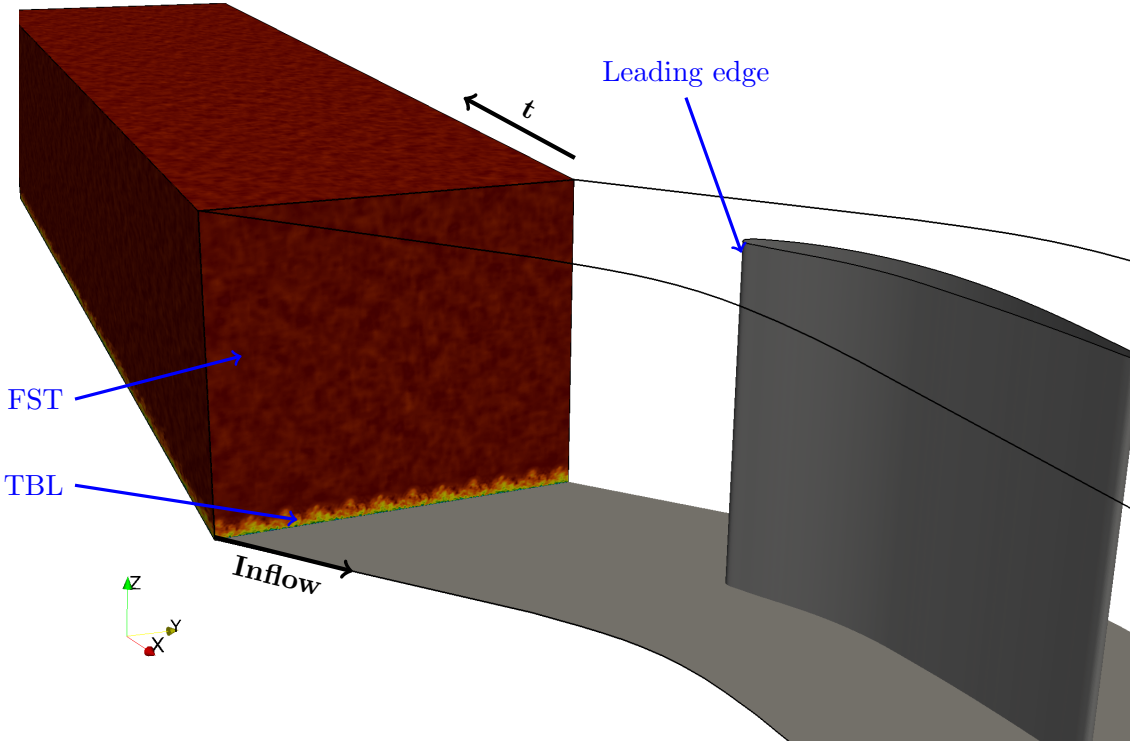


FIGURE 3.3: Inflow turbulence box (FST + TBL) appended to compressor cascade.

3.2.1 Turbulent boundary layers

To generate turbulent boundary layer data, a precursor channel flow LES was run using the Lund recycling/rescaling technique [101]. The code for this was kindly provided by Dr. Naqavi at the University of Cambridge. Time-series data is extracted from the streamwise growing TBL when $Re_\theta = 1350$.

The velocity fluctuations and Reynolds stress profiles for the generated TBL agree well with a DNS of a TBL ($Re_\theta = 1410$) performed by Spalart [134], as shown in Figure 3.4.

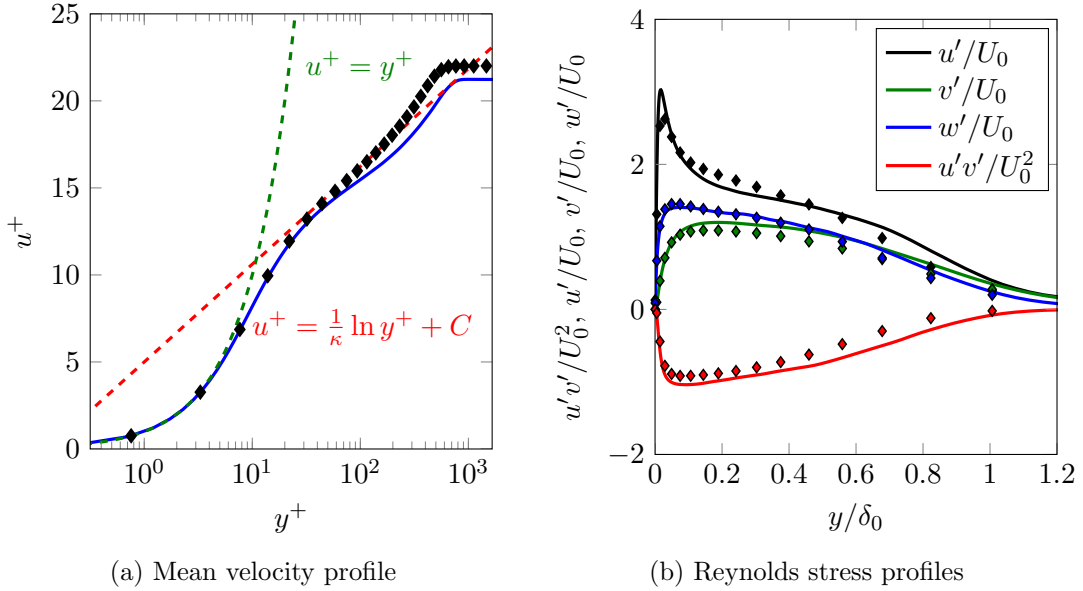


FIGURE 3.4: Velocity and stress profiles of TBL generated with Lund recycling. *Lines: Lund recycling, Symbols: DNS from Spalart [134].*

3.2.2 Unsteady wakes

The turbulent planar wake data is obtained from a separate simulation [25], which has been kindly provided by Dr. Xiaohua Wu. This data was generated by initially “fusing” two “half-channel flow” simulations ($Re_b = 3300$) and allowing the solution to develop until it reaches a statistically steady state. In Figure 3.5a, the resulting mean velocity profile can be seen to closely match the self-similar plane cylinder wake of Schlichting et al. [135].

| Wake parameter | Value |
|--|------------------------------|
| Mean velocity deficit, $\bar{u}_{wake,max}$ | $0.2U_0$ |
| Half-width, b | $0.05C_x$ |
| Vertical separation, D | $0.9P$ (P is blade pitch) |
| Cycle velocity, U_{cyl} | $0.8U_1$ |
| Wake passing period, τ_w | $1.09C_x/U_1$ |
| Reduced frequency, $f_r = \frac{1}{\tau_w} \frac{C_x}{U_{TE}}$ | 1.2 |

TABLE 3.2: Parameters of unsteady turbulent wake.

The wake data is scaled by the parameters given in Table 3.2. These values are chosen so that the incoming wakes are representative of those seen by stator stages in a gas

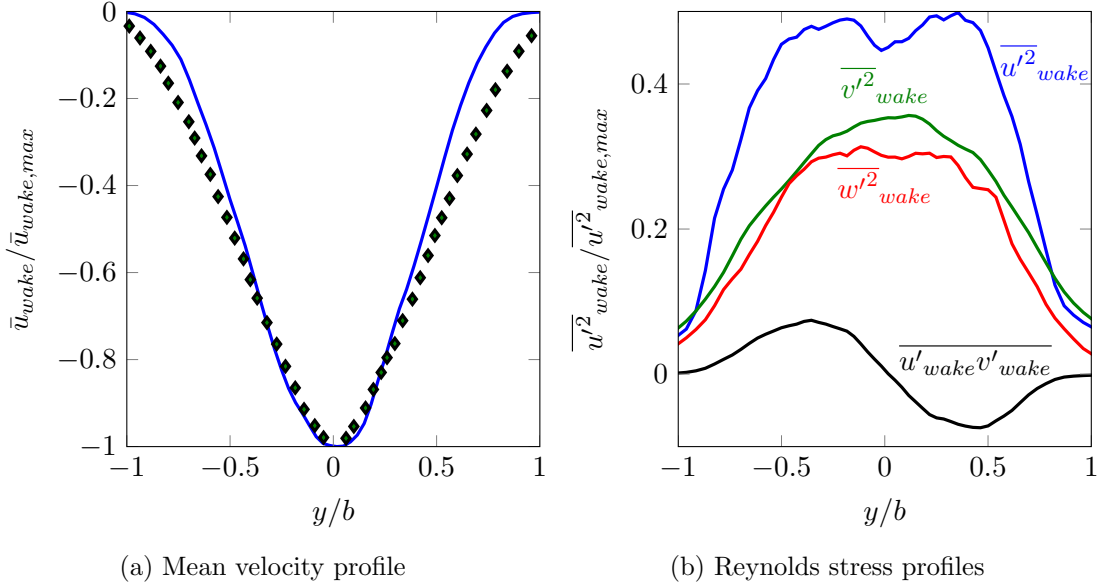


FIGURE 3.5: Velocity and stress profiles of wake data. *Lines:* wake data from Wu et al. [25], *Symbols:* self-similar plane cylinder wake of Schlichting et al. [135].

turbine engine. The wake data is applied to the inflow using the procedure given in Wu et al. [25].

3.2.3 Free-stream turbulence

A new method recently proposed by Saad et al. [136] is used to synthetically generate the isotropic turbulence seen in Figure 3.6a. This method is based upon that of Rogallo [137], which involves representing the spatio-temporal velocity field as a superposition of sine and cosine waves, essentially computing a Fourier series in real space. Each waveform is then scaled deterministically so that an input energy spectrum is matched. The input spectrum used is the von Kármán-Pao spectrum shown in Figure 3.6b. The equation for this is:

$$E(\kappa) = \alpha \frac{u'^2}{\kappa_e} \frac{(\kappa/\kappa_e)^4}{[1 + (\kappa/\kappa_e)]^{17/6}} \exp \left[-2 \left(\frac{\kappa}{\kappa_\eta} \right)^2 \right] \quad (3.20)$$

where u' is the RMS value of the velocity fluctuations, κ_e is related to the wavenumber of maximum energy ($\kappa_p = \sqrt{12/5}\kappa_e$), and $\kappa_\eta = \epsilon^{1/4}\nu^{-3/4}$ is the Kolmogorov wave number. For isotropic turbulence $\alpha = 1.453$, and $\epsilon = u'^3/L$ with L being the integral length scale $L = 0.746834/\kappa_e$. Lardeau et al. [86] showed that the transition mechanisms in a compressor flow are sensitive to the inflow turbulence spectrum. The spectrum is not typically measured in experiments, therefore there is some uncertainty here when attempting to replicate experiments.

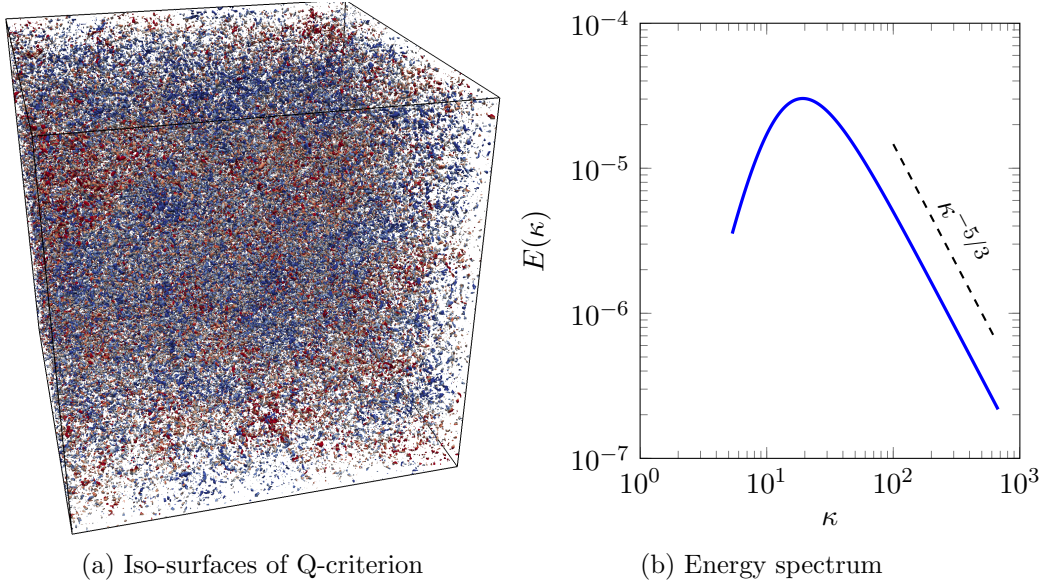


FIGURE 3.6: Isotropic turbulence from synthetic method of Saad et al. [136].

The Saad et al. [136] method extends that of Rogallo [137] by enforcing a divergence-free velocity field on discrete grids, which is important for an incompressible simulation. The approach was formulated for a staggered grid arrangement. Therefore, the method had to be re-formulated for collocated grids such as those used in the present work. The original and reformulated methods are described in Appendix B.

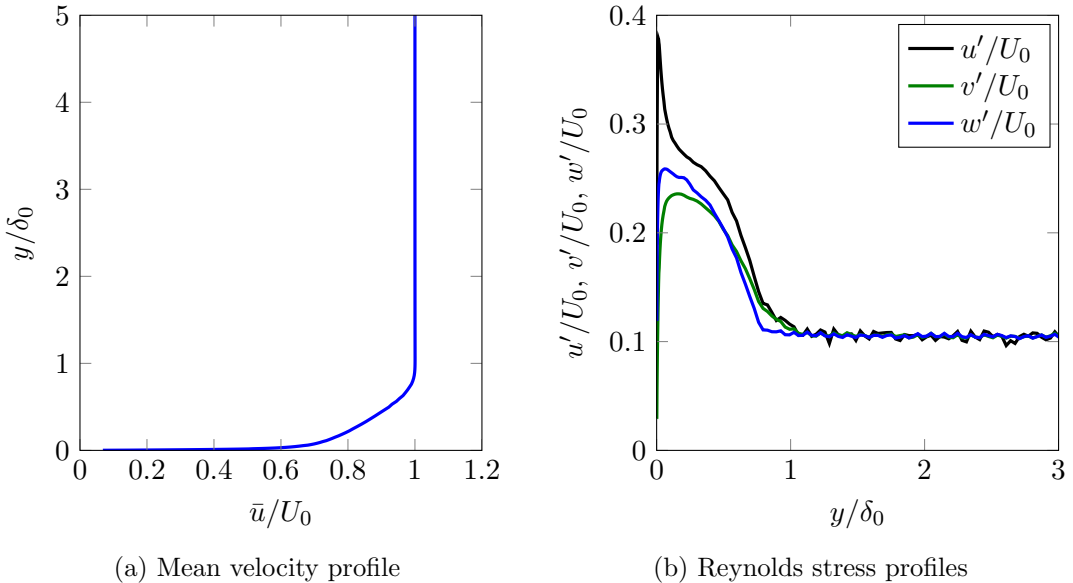


FIGURE 3.7: Velocity and stress profiles of inflow box with TBL + FST blended together.

If a TBL is present in the inflow box, the FST is blended into the box to avoid contaminating the TBL. The blending function ϕ in Equation 3.18 is given by:

$$\phi(y) = 0.5 \left[1 + \tanh \left(\frac{y - d\delta^*}{w\delta^*} \right) \right] \quad (3.21)$$

where δ^* is the displacement thickness of the TBL. The constants d and w are chosen so that the Reynolds stress profiles of the TBL smoothly approach the FST stress levels. For an FST intensity of $u'/U_1 = 0.1$ the constants are set to $d = 6.5$ and $w = 0.5$, and the resulting profiles are shown in Figure 3.7.

3.2.4 Enforcing periodicity

The turbulent inflow boxes consist of a finite number of planes. After the last plane is reached, the box will be restarted at the first plane. The FST, TBL and wake datasets are not inherently periodic in the x-direction, therefore a Gaussian-like filter similar to that used by Zaki et al. [100] is applied in this direction. For example, applying it to u velocity snapshots for a wake case (with 432 planes), gives:

$$\left(u_{y,z}^{(k)} \right)_{k=1}^{432} = \sum_{i=-5}^5 \left\{ w_i^{(k)} u_{y,k}^{[mod(k-i-1, 432)+1]} \right\}, \quad (3.22)$$

where $k = 1, \dots, 432$, and the filter weights $w_i^{(k)}$ are given by:

$$w_i^{(k)} = \lambda_k \exp \left(\frac{-i^2}{2\sigma_k^2} \right), \sigma_k = \frac{5}{\sqrt{\min(k, 433-k)}} \quad (3.23)$$

with $w_i^{(k)}$ normalised by λ_k :

$$\lambda_k = \frac{1}{\sum_{j=-5}^5 w_j^{(k)}}. \quad (3.24)$$

Figure 3.8a shows values of $w_i^{(k)}$ for various k planes, and illustrates that the filter only significantly alters the planes near the beginning and end of the box. As seen in Figure 3.8b, this ensures a smooth transition between $\hat{u}_{y,z}^{(432)}$ and $\hat{u}_{y,z}^{(1)}$.

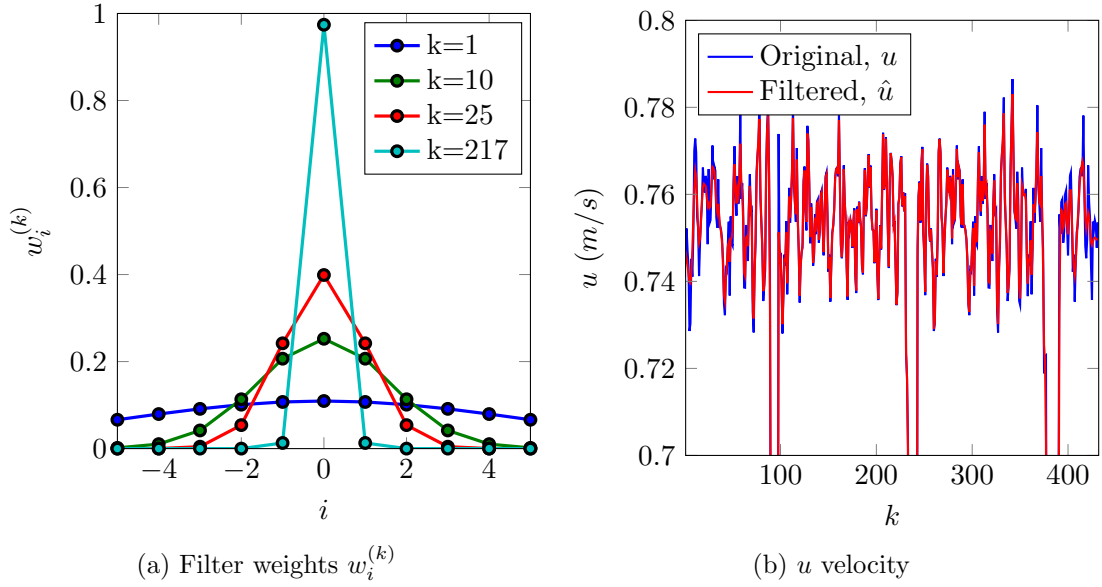


FIGURE 3.8: Gaussian-like filtering applied to inflow turbulence box with wake and FST

3.3 Vortex identification methods

In this thesis, two methods are used to identify vortices. The first is the commonly used Q-criterion, first proposed by Hunt et al. [138]. Q is defined as:

$$Q = \frac{1}{2} (\Omega^2 - S^2) \quad (3.25)$$

where S and Ω are the magnitude of the strain and vorticity tensors:

$$S = \sqrt{2S_{ij}S_{ij}}, \quad \Omega = \sqrt{2\Omega_{ij}\Omega_{ij}}. \quad (3.26)$$

Vortices can then be identified using iso-surfaces of positive Q-criterion.

The second method used is the kinematic vorticity number [139], defined as:

$$N_k = \frac{\Omega}{S} \quad (3.27)$$

Values of $N_k = 1 - 1.3$ are typically used (e.g. by Bordji et al. [57]) to identify vortices. The Q-criterion is more commonly used. However, N_k proved to be more useful when examining the vortical structures that occur in the endwall flow in Chapter 6.

Part II

Results

Chapter 4

A Robust Numerical Scheme for Eddy Resolving Simulations

In order for eddy resolving simulations to become an integral part of the compressor design process, it is crucial for the numerics to be *robust*. The word *robust* is used here to mean that the solution must not be too sensitive to the numerical scheme. If it is overly sensitive then the numerics may not be reliable across a range of flows, and the simulation would cease to be a proper predictive tool.

In this chapter the Taylor-Green vortex (TGV) test case is used to study the influence of the numerics in HYDRA. The TGV case involves transition to turbulence and anisotropic decay, and thus it replicates some of the important flow physics seen in a transitional compressor flow. Some problems with the current numerical scheme are discussed, and a new scheme is proposed.

4.1 Numerical challenges for eddy resolving simulations

It is attractive to reuse as much of the existing RANS code as possible in the development of an LES solver. The RANS solver HYDRA is in many ways a good starting point for an LES solver. However, there is one area in particular where the RANS heritage of HYDRA does not suit its use as an LES solver; this is the Roe scheme used to solve for the inviscid fluxes. As shown in Equation 3.4 (and repeated in Equation 4.1) this scheme is essentially a central differencing method, smoothed by some upwinding scaled by the smoothing constant ϵ_2 :

$$F_{ij}^{I,S} = \underbrace{\frac{1}{2} (F_{ij}^I(Q_i) + F_{ij}^I(Q_j))}_{\text{Central differencing}} - \underbrace{\frac{1}{2}\epsilon_2 |A_{ij}| (L_i^{lp} - L_j^{lp})}_{\text{Upwinding}} \quad (4.1)$$

where $F_{ij}^{I,S}$ is the smoothed inviscid flux through a cell face (see Section 3.1.1.1). The Péclet number gives the relative importance of convection and diffusion in a problem. In one dimension, for a computational cell with spacing Δx , it can be defined [140] as:

$$Pe = \frac{\rho u}{\Gamma/\Delta x} \quad (4.2)$$

where Γ is a diffusion coefficient. When pure central differencing is used with $Pe_x > 2$, dispersive errors will occur in the solution. These errors, referred to as "wiggles" due to their point-wise nature, can be damaging to the solution. In Figure 4.1 wiggles are seen to cause instabilities, leading to premature transition in a compressor LES case. In both RANS and LES cases some upwinding, controlled by ϵ_2 , is required to prevent wiggles occurring when $Pe_x > 2$. In LES however, the upwinding can lead to excessive numerical dissipation of turbulent vortices. Thus, there is a balance that must be found when selecting a value of ϵ_2 , as explored in Section 4.1.1.

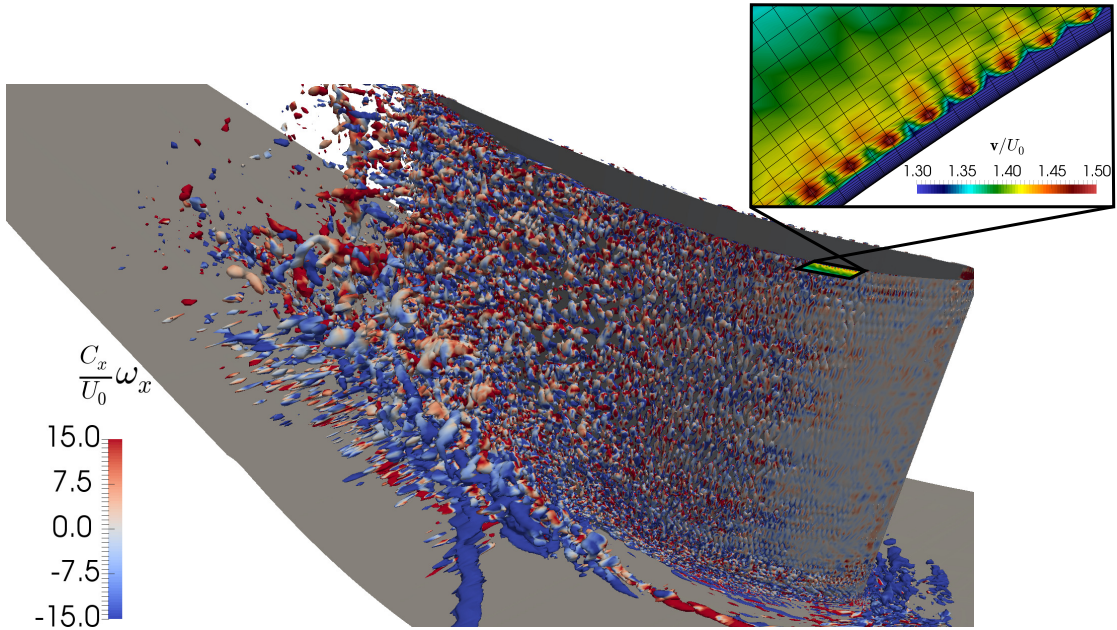


FIGURE 4.1: Iso-surfaces of Q-criterion (defined in Eqn. 3.25) for LES of compressor endwall flow showing excessive dispersive errors.

Gresho et al. [140] argue: "Don't suppress the wiggles - They're telling you something!". The key argument here is that the wiggles are occurring because the grid is not sufficiently fine to resolve the flow physics at that location. Thus, it is argued that instead of smoothing the wiggles, the grid should be refined where wiggles are occurring. However, it is not always practical (or possible) to sufficiently refine the grid so that no smoothing is required. In the compressor cases presented in this thesis, wiggles occurred even as DNS resolution was approached (with $\epsilon_2 = 0$). Refining the grid to avoid smoothing would be impractically expensive. Due to the complexity of some industrial LES grids,

it may also be too time consuming to refine some grids. Therefore, for predictive LES in an industrial context, some smoothing is usually necessary.

4.1.1 The Taylor-Green vortex

The Taylor-Green vortex (TGV) case is one of the simplest systems in which the generation of small scales and the turbulence resulting from three-dimensional vortex stretching can be studied. It has been one of the test cases studied at the “International Workshop on High-Order CFD Methods” for a number of years (2012, 2013, 2014). Results are compared to a reference incompressible DNS obtained by Rees et al. [141], using a de-aliased pseudo-spectral code on a 512^3 grid.

4.1.1.1 Case set-up

The problem domain is a tri-periodic box defined as $-\pi L \leq x, y, z \leq \pi L$. The incompressible TGV is initialised at $t = 0$ as:

$$\begin{aligned} u &= V_0 \sin\left(\frac{x}{L}\right) \cos\left(\frac{y}{L}\right) \cos\left(\frac{z}{L}\right), \\ v &= -V_0 \cos\left(\frac{x}{L}\right) \sin\left(\frac{y}{L}\right) \cos\left(\frac{z}{L}\right), \\ w &= 0, \\ p &= p_0 + \frac{\rho_0 V_0^2}{16} \left(\cos\left(\frac{2x}{L}\right) + \cos\left(\frac{2y}{L}\right) \right) \left(\cos\left(\frac{2z}{L}\right) + 2 \right). \end{aligned} \quad (4.3)$$

The initial flow is visualised in Figure 4.2a. The reference values L and V_0 are set to unity, and the viscosity is set to give $Re = \rho_0 V_0 L / \mu = 1600$ in order to match the reference DNS solution. The simulation time, t , is scaled by the characteristic convective time $t_c = L/V_0$, such that $\tau = t/t_c$. A number of different grid resolutions are investigated, and in each case the time-steps are chosen to match the CFL number used by Rees et al. [141]. At each time-step a number of quantities are integrated on the domain Ω so that the temporal evolution of the following quantities can be monitored:

- Turbulent kinetic energy:

$$E = \frac{1}{\Omega} \int_{\Omega} \frac{\mathbf{u} \cdot \mathbf{u}}{2} d\Omega. \quad (4.4)$$

- Total turbulent kinetic energy dissipation rate:

$$\epsilon_{tot} = -\frac{dE}{dt}. \quad (4.5)$$

- Enstrophy:

$$\varepsilon = \frac{1}{\Omega} \int_{\Omega} \frac{\omega \cdot \omega}{2} d\Omega. \quad (4.6)$$

In an incompressible flow this quantity is directly linked to the resolved kinetic energy dissipation rate i.e.

$$\epsilon_{res} = \frac{2\nu}{\Omega} \int_{\Omega} S_{ij} S_{ij} d\Omega = 2\nu\varepsilon. \quad (4.7)$$

- Turbulent kinetic energy dissipation rate due to SGS model:

$$\epsilon_{SGS} = \frac{2\nu_t}{\Omega} \int_{\Omega} S_{ij} S_{ij} d\Omega. \quad (4.8)$$

- Turbulent kinetic energy dissipation rate due to numerical scheme:

$$\epsilon_{num} = \epsilon_{tot} - (\epsilon_{res} + \epsilon_{SGS}) \quad (4.9)$$

4.1.1.2 Effect of smoothing constant

The evolution of the Taylor-Green vortex system is visualised in Figure 4.2. The initial flow field is laminar, but by $\tau_c = 4$ (Fig. 4.2b), vortex stretching leads to the generation of small scale turbulent structures. At $\tau_c = 8$ (Fig. 4.2c) the generation of turbulence is slowing down, and beyond this (i.e. Fig. 4.2d) the flow field undergoes an anisotropic turbulent decay.

In Figure 4.3a the volume averaged resolved kinetic energy (Eqn. 4.4) is seen to decay in the DNS of the TGV. Also plotted here are 128^3 LES results, all run with the σ SGS model but with different values of the ϵ_2 smoothing constant. At first glance, it appears the LES results are in good agreement with the baseline DNS. However, examining the rate of energy decay (Eqn. 4.5) in Figure 4.3b shows there are noticeable differences between the LES and DNS, especially at high ϵ_2 values.

Figure 4.3c shows that as the ϵ_2 constant is increased, the volume averaged enstrophy (Eqn. 4.6), which is proportional to the resolved dissipation, decreases. Recalling the concepts of resolved and numerical stress from Section 2.3.1; increasing ϵ_2 causes the resolved stress to be damped, and the numerical stress must now replace the missing resolved stress. Unsurprisingly, the inaccuracies seen in Figure 4.3b suggest that the numerical stress is not able to correctly represent the resolved turbulence it has damped out.

The effects of excessive numerical dissipation are also evident when comparing the vorticity contours from the LES with those from the DNS in Figure 4.4. Key features in

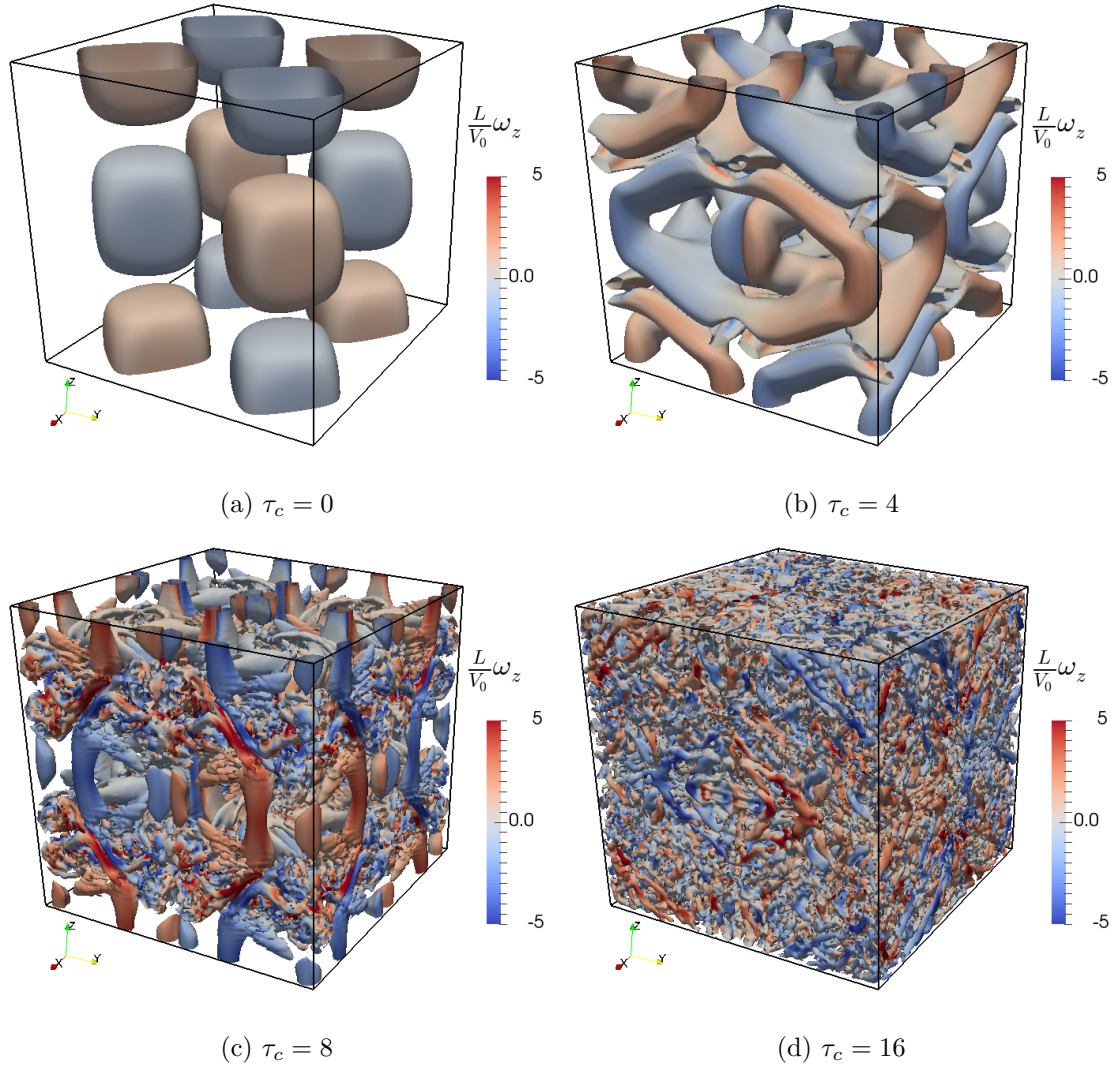


FIGURE 4.2: Iso-surfaces of Q-criterion ($Q = 0.1(V_0/L)^2$) coloured by the z-component of non-dimensional vorticity $\frac{L}{V_0} \omega_z$.

the $\epsilon_2 = 0.25$ case (Fig. 4.4d) have been smoothed out, and it is clear that the $\epsilon_2 = 0.1$ case (Fig. 4.4c) is in closer agreement with the DNS (Fig. 4.4a). However, Figure 4.4b demonstrates that reducing the smoothing too far can also be damaging. Some features, such as the very low vorticity in the vortex cores, are better captured. However, the lack of smoothing is resulting in dispersive errors, which have mixed out the $0.2 < z/\pi < 0.8$ region.

It is clear that there is a conflict between the two roles of the ϵ_2 smoothing term in Equation 4.1; a relatively high value of ϵ_2 is required for stability, while a low value is required in order to reduce the excessive numerical dissipation.

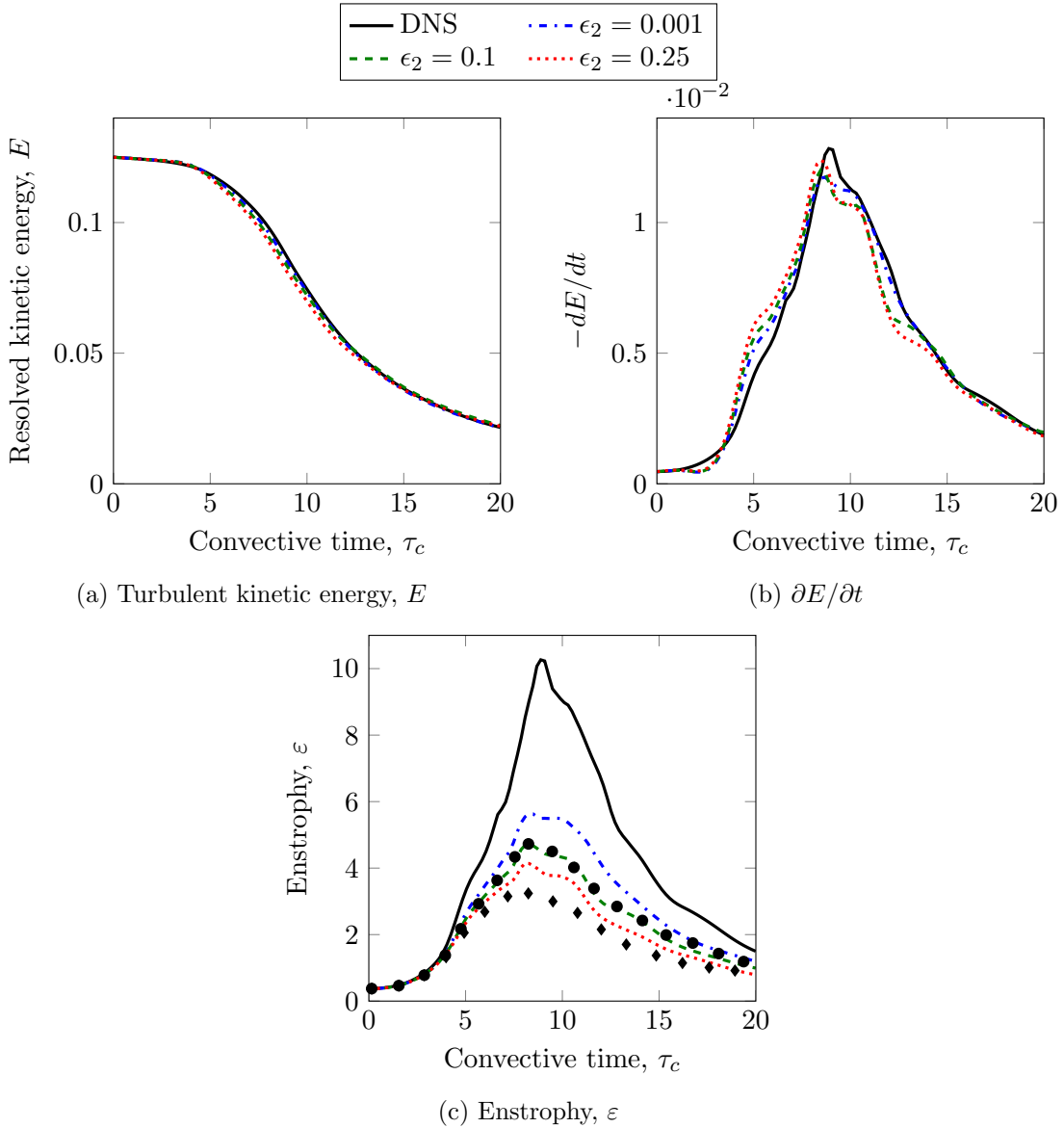


FIGURE 4.3: Effect of ϵ_2 on temporal evolution of TGV. 128^3 grid and σ SGS model. Symbols are 128^3 LES results of Boom et al. [142]: \blacklozenge 2nd-order, \bullet 4th-order.

4.1.1.3 Numerical and SGS contributions

As Ghosal [60] demonstrates, the intrinsic relationship between the resolved, SGS and numerical stress is dependent on the grid resolution. To investigate this, the TGV case is run at two further grid resolutions, 64^3 and 256^3 .

As expected, Figure 4.5a demonstrates that increasing the grid resolution increases the amount of resolved turbulent content, with the LES solution approaching the DNS as the grid is refined. Figure 4.5b is in agreement with the findings of Boom et al. [142], in that 64^3 is an insufficient resolution for the TGV case with a second order code.

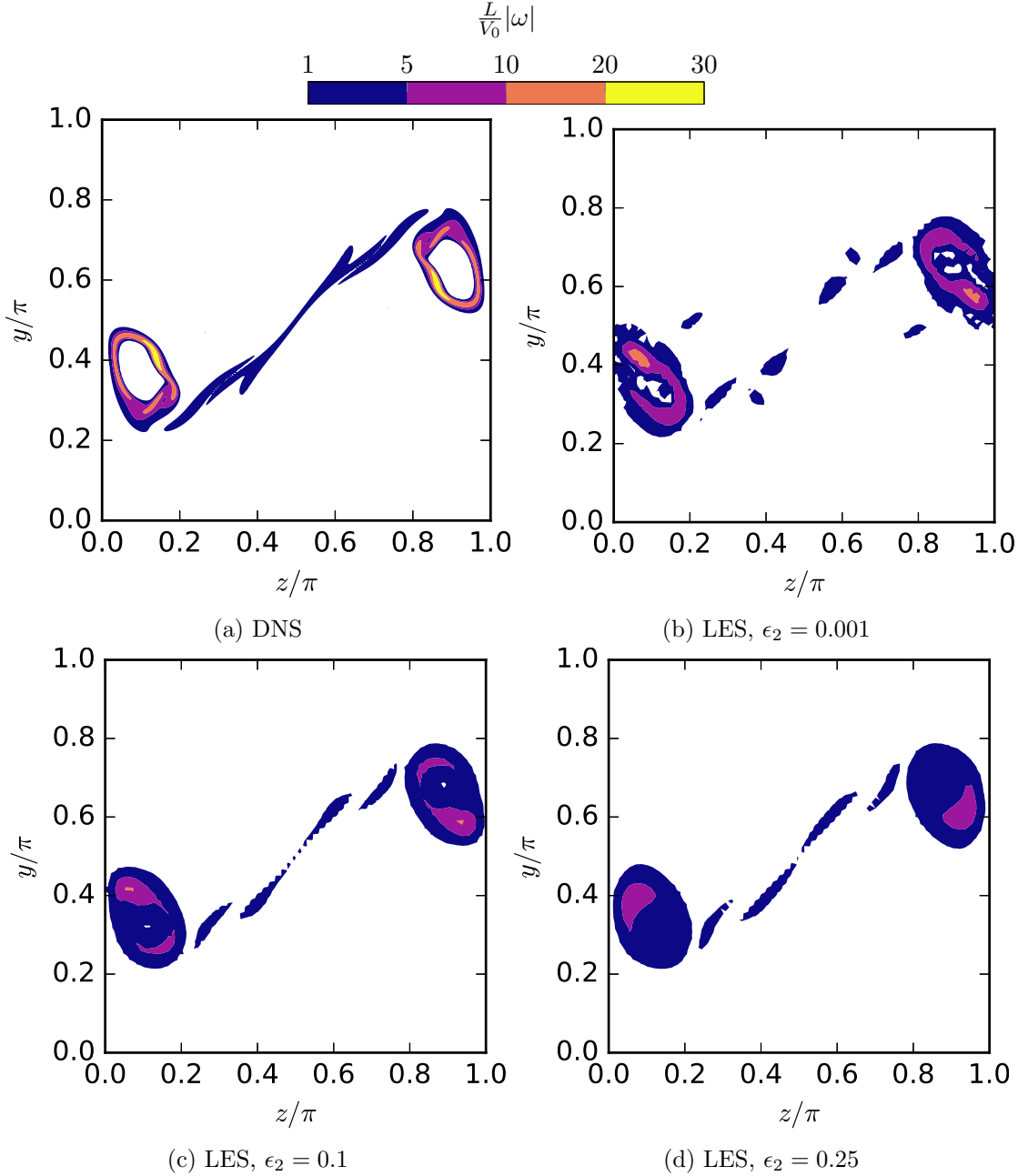


FIGURE 4.4: Iso-lines of non-dimensional vorticity $\frac{L}{V_0}|\omega| = 1, 5, 10, 20, 30$, on a subset of the periodic face $x = -\pi L$ at time $t/\tau_c = 8$.

Using Equations 4.5 to 4.9, the total energy dissipation for all the TGV LES cases is broken down into resolved dissipation and contributions from the SGS and numerical scheme. These are integrated across the time interval $0 < t/\tau_c < 20$, for example,

$$\overline{\langle \epsilon_{num} \rangle} = \int_{t=0}^{t=20\tau_c} \langle \epsilon_{num} \rangle(t) dt \quad (4.10)$$

and plotted as a percentage of the total dissipation in Figure 4.6.

There are no formal definitions as to what constitutes a properly resolved large eddy

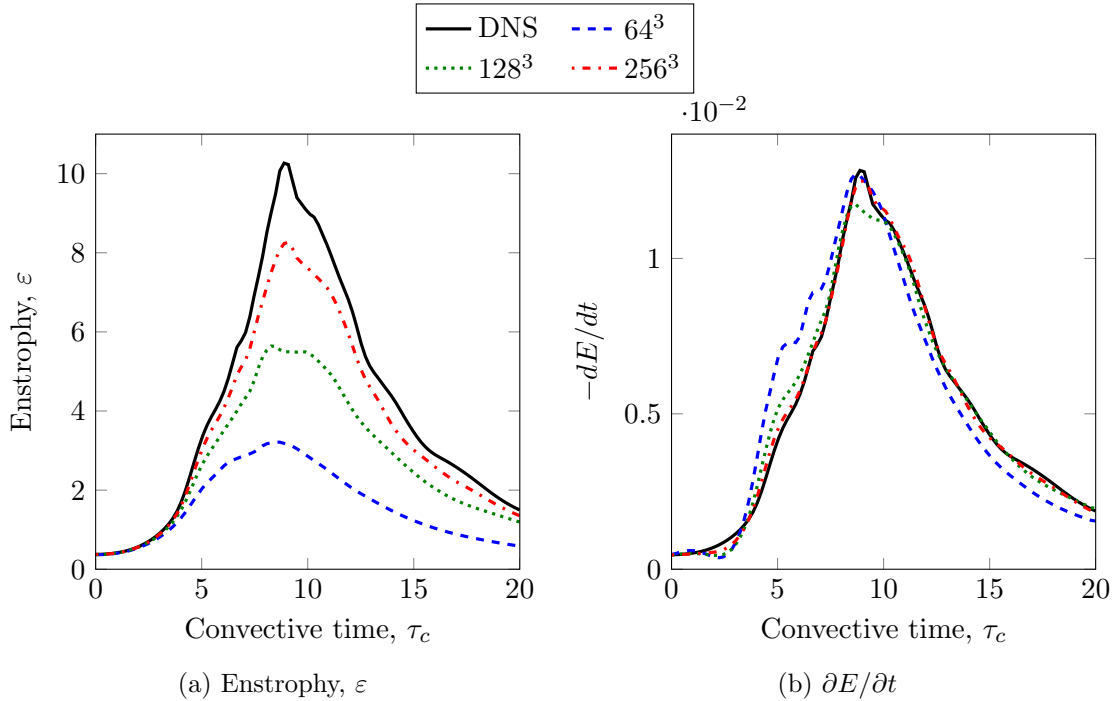


FIGURE 4.5: Effect of mesh resolution on temporal evolution of TGV. $\epsilon_2 = 0.001$ and σ SGS model.

simulation, but a commonly suggested guideline [76, 143] is that at least 80-90% of the turbulent kinetic energy should be resolved. Although this guideline isn't directly transferable to the proportion of resolved dissipation, and the energy and dissipation spectra should also be taken into account, it provides a rough guide. From Figure 4.6a it is apparent that when $\epsilon_2 = 0.25$, less than 60% of the total dissipation is due to the resolved scales, and the numerical dissipation is greater than the SGS dissipation.

It is undesirable for the numerical stress to be of similar magnitude to the SGS stress, since the numerical scheme isn't designed to represent the unresolved (sub-grid) scales like a SGS model should be. Figure 4.6b supports the arguments of Ghosal [60]. It shows that simply refining the mesh does not solve the problem, since the numerical and SGS contributions to the dissipation are seen to reduce at a similar rate as the grid is refined (while ϵ_2 is held constant). The ratio of numerical to SGS dissipation can only be reduced when ϵ_2 is decreased (Fig. 4.6a). However, this may result in excessive dispersive errors.

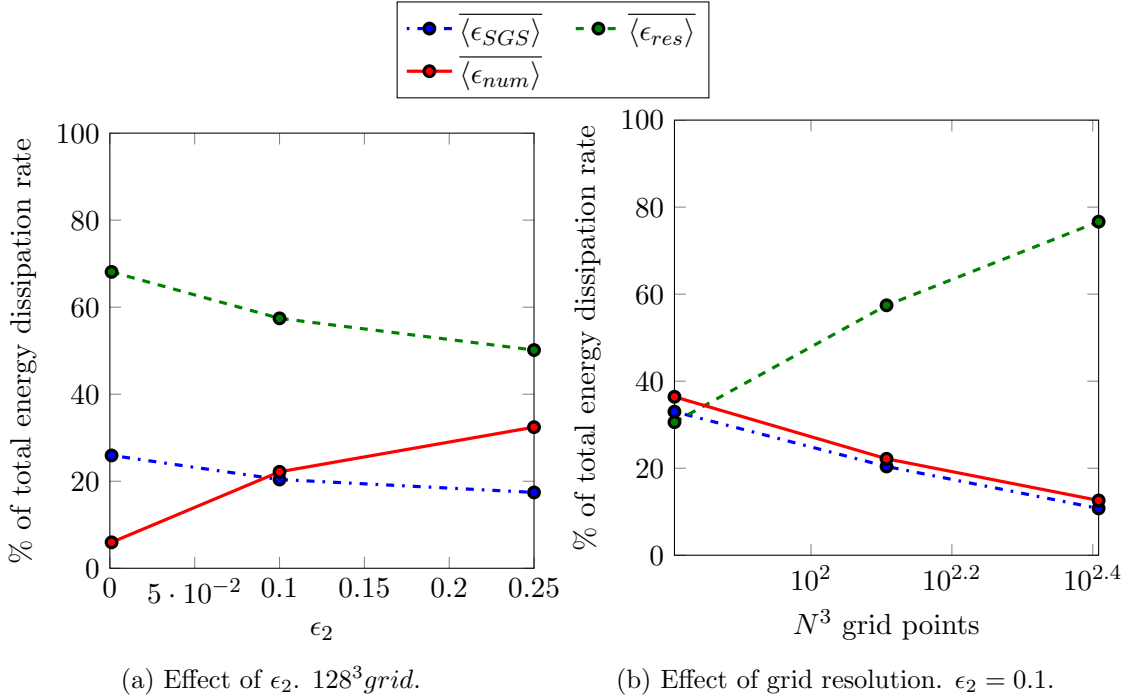


FIGURE 4.6: Resolved, numerical and SGS contribution to energy dissipation. σ SGS model.

4.2 Locally adaptive smoothing schemes

The Taylor-Green vortex case has demonstrated the sensitivity of HYDRA to the ϵ_2 smoothing when used as an LES code. When there is an a priori solution or when experimental results are available, it is possible to tune the value of ϵ_2 to match the flow physics. However, as the smoothing terms are not designed to act as a SGS model, the value of ϵ_2 isn't designed to act as a global constant and must often be tuned locally. This approach has been used successfully for specific LES applications in the past, for example in the transonic jet flows of Eastwood et al. [84]. Trial and error can also be used to find the minimum stable value of ϵ_2 for specific cases, as was done in the compressor blade studies by McMullan et al. [89, 144, 145].

With the above approaches, the reliance on a priori data or tuning can limit the usefulness of LES as a predictive tool. A higher order scheme or an ENO type scheme could potentially reduce the sensitivity to the numerical scheme. However, as discussed in Section 2.4.1, such schemes still have problems. For example, Garnier et al. [107] found that ENO schemes are still overly dissipative at the small scales. While Figure 4.3c suggests that the second order HYDRA code is resolving as much as the fourth order code used by Boom et al. [142] for the TGV case. Additionally, such schemes are hard to implement in a second order unstructured code like HYDRA, and might be impractical for complex geometries. A Kinetic Energy Conserving (KEP) scheme was also added to

HYDRA. However, despite the stability gain, preliminary tests on a hybrid RANS/LES of an endwall flow (Figure 4.1) suggested that some smoothing was still required to prevent spurious wiggles.

Another potential solution is to use locally-adaptive smoothing schemes, hereafter referred to as LAS schemes. The general concept is not to attempt to explicitly decouple the filtering/modelling from the numerical scheme. Instead, it is accepted that some numerical smoothing is necessary, and an attempt is made to minimise it. The LAS approach is in some ways similar to the TVD and ENO approaches, in that it detects when oscillatory solutions are present, and alters the discretisation scheme accordingly.

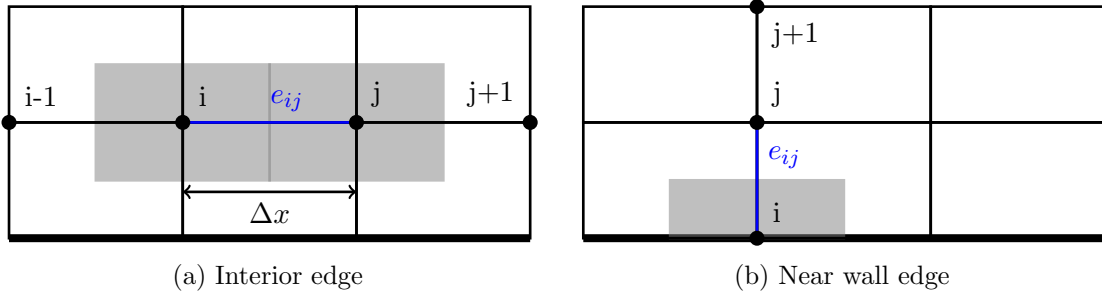


FIGURE 4.7: Four-point stencil for LAS scheme.

Ciardi [146] implemented a LAS scheme in HYDRA which simply altered the ϵ_2 constant by set increments/decrements when a wiggle was or was not detected. More recently a similar scheme was proposed by Tajallipour et al. [110], and used for a jet cross-flow LES by Kumar et al. [111]. For each e_{ij} edge in the domain, the scheme monitors the edge's four point stencil shown in Figure 4.7a. The existence of wiggles across each stencil is monitored by looking for the coexistence of a maximum and a minimum along the stencil:

$$\theta_i(t) = (\phi_i - \phi_{i-1})(\phi_j - \phi_i) < \theta_t < 0 \quad (4.11)$$

$$\theta_j(t) = (\phi_{j+1} - \phi_j)(\phi_j - \phi_i) < \theta_t < 0 \quad (4.12)$$

where θ_t is the target wiggle magnitude, a user defined constant, and ϕ can be any of the primitive variables (u, v, w, p). If inequalities (4.11) and (4.11) are satisfied, as is the case for the solid red lines in Figure 4.8, a wiggle is said to be present.

Tajallipour et al. [110] propose using a control scheme analogous to the proportional term in a PID controller, whereby the change in smoothing is proportional to the error term, defined as the difference between the actual and the target wiggle magnitude. The change in ϵ_2 at each physical timestep is defined as:

$$\Delta\epsilon_2(t) = \begin{cases} [\theta_t - \min(\theta_i(t), \theta_j(t))] \alpha & \text{if } \theta_i(t) < \theta_t \text{ and } \theta_j(t) < \theta_t \\ [\theta_t - \max(\theta_i(t), \theta_j(t))] \alpha & \text{otherwise} \end{cases} \quad (4.13)$$

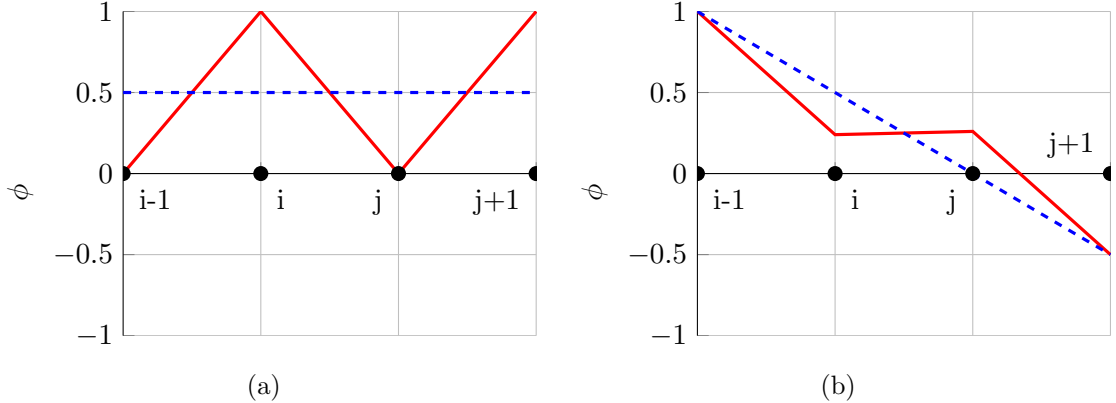


FIGURE 4.8: Two examples of signals ϕ with (red) and without (blue) wiggles.

where α is the proportional gain parameter, kept at $\alpha = 1$ by Tajallipour et al. [110] and Kumar et al. [111].

Tunable parameters such as ϵ_2 are undesirable, as they can prevent the method from being predictive across a range of flows, if the solution is sensitive to them. In implementing the LAS scheme, the tunable parameter ϵ_2 has been replaced by two tunable parameters, θ_t and α . In order for the LAS scheme to be suitable for industrial LES, it thus appears to be reasonable to expect the following criteria to be met:

- (I) *Any tunable parameters should not have a significant effect on the solution.*
- (II) *If a parameter does have a significant effect it should at least have a clear physical meaning, such that it is a simulation metric rather than a tunable parameter.*

An example of criterion II is the θ_t parameter. This parameter has a significant effect on the solution. However, unlike the rather abstract ϵ_2 parameter, the θ_t parameter has a clear physical meaning. It sets the maximum permissible magnitude of wiggles ($\theta_t = 0$ is an option). The parameter functions more like a quality metric, and can be set beforehand without any tuning. Similar to the user choosing what convergence criterion to use for a simulation, they can state that, for example, “only wiggles of $\theta_t < 0.5\%$ are allowed”. The LAS scheme should then locally adjust ϵ_2 so that this target is met.

Ciardì [146] finds that for optimum performance, different values must be used for the increment and decrement of ϵ_2 , thus implying the method is sensitive to the $\Delta\epsilon_2$ values chosen. The method therefore does not meet criterion I; we have removed one tunable parameter ϵ_2 and replaced it with other equally influential ones.

To test whether the LAS scheme of Tajallipour et al. [110] meets the criteria, a forced isotropic turbulence (FIT) test case is used. This case is less demanding on an LAS

scheme than a HDT¹ case as it is statistically stationary. In this regard, the FIT is also more representative of a compressor cascade. In the absence of incoming wakes and with sufficiently long time averaging, this flow can also be thought of as statistically stationary².

A simple test to see if the LAS scheme meets criteria I and II is to check that the LAS scheme converges to the same ϵ_2 value regardless of the chosen gain parameter α . If this is the case, the user could specify the target wiggle magnitude, and be confident that the LAS scheme will return the minimum amount of smoothing necessary to achieve this, without having to tune other parameters.

Once the ϵ_2 field is converged, the LES case is ready for statistics to be collected.

4.2.1 Forced isotropic turbulence test case

DNS of forced isotropic turbulence are most often formulated in Fourier space, where forcing is applied to low-wavenumber modes. However, this is difficult and expensive to apply in physical space. Instead, Lundgren [147] introduced the linear forcing technique. Here a linear forcing term Au_i , proportional to the local velocity, is applied to the momentum equations (Eqn. 2.13) in physical space:

$$\langle \rho \rangle \frac{\partial \langle u_i \rangle}{\partial t} + \langle \rho \rangle \frac{\partial \langle u_i \rangle \langle u_j \rangle}{\partial x_j} = \frac{\partial}{\partial x_j} [-\langle p \rangle \delta_{ij} + 2\mu \langle S_{ij} \rangle - \tau_{ij}^r] + Au_i \quad (4.14)$$

where the parameter A is determined from a balance of kinetic energy:

$$A = \frac{\epsilon_0}{2k_0} \quad (4.15)$$

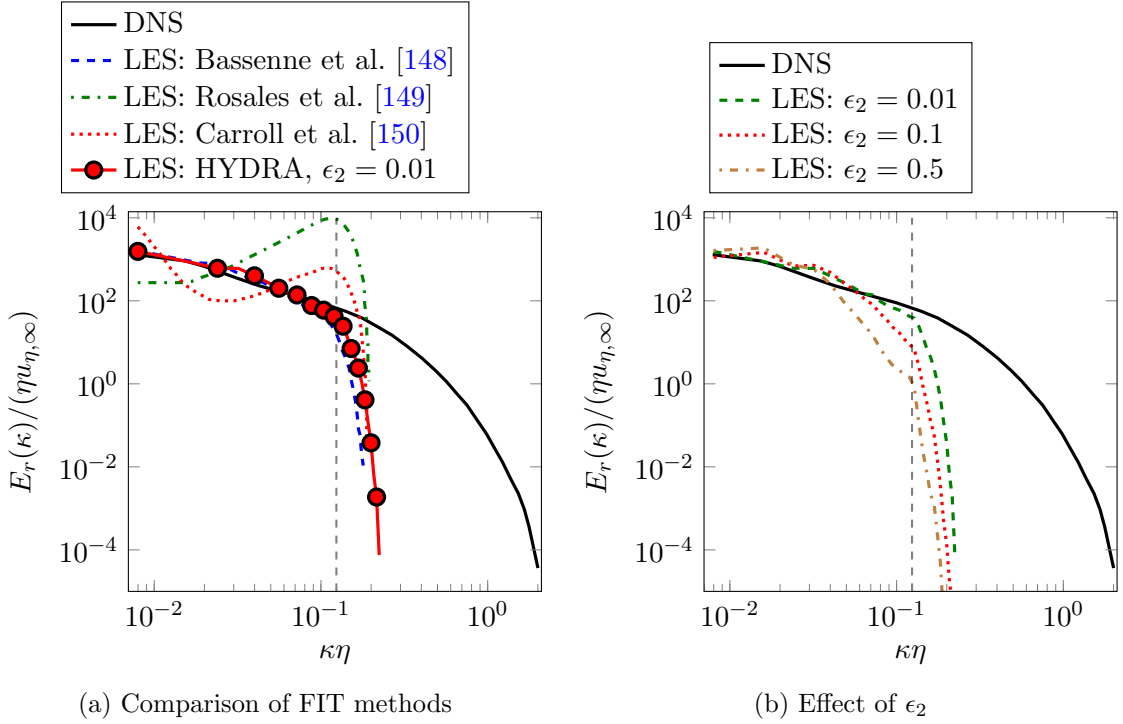
with ϵ_0 equal to the volume averaged turbulent dissipation $\langle \epsilon_{res} \rangle$ defined in Equation 4.7, and k_0 equal to the resolved turbulent kinetic energy $\langle k \rangle$ from Equation 4.4.

After a transient period a statistically stationary turbulent field is developed, which is independent from the initial velocity field. The stationary field is determined only by the domain size, the Reynolds number and the forcing constant.

Recently, Bassenne et al. [148] tested the above FIT method for LES. It was found that, unlike for DNS, the final stationary field was strongly dependent on the initial condition, and was often non-physical. Recent modifications by Rosales et al. [149] and Carroll et al. [150] did not work either, as shown in the energy spectra in Figure 4.9a. Bassenne

¹Homogeneous Decaying Turbulence

²This might not be true if very low frequency modes are present in the flow, for example if the endwall separation is particularly large or there are low frequency interactions between blades in the cascade.

FIGURE 4.9: Energy spectra of stationary state of FIT on 32^3 grid

et al. [148] suggest that interplay between the forcing and SGS model is to blame, and suggest an alternative forcing coefficient:

$$A(t) = \frac{\langle \epsilon_{res}(t) \rangle - G [\langle k(t) \rangle - k_0] \tau_l}{2 \langle k(t) \rangle} \quad (4.16)$$

which is essentially a proportional controller with $\langle k(t) \rangle - k_0$ as the error term and G being the proportional gain. Bassenne et al. [148] found that this control scheme returned the correct stationary state, independently of the initial condition. This FIT scheme was implemented in HYDRA and Figure 4.9a shows that the final steady state energy spectra is in good agreement with the DNS, up to the filter cut-off wave number (shown by the vertical dashed line).

In this and all subsequent FIT computations, the synthetic turbulence method described in Section 3.2.3 is used to generate the initial velocity field. A triply periodic box with $L = 2\pi$ is used. The other input parameters are $G = 67$, $\rho = 1.2$, $k_0 = 0.096$, $\epsilon_0 = 1.35 \times 10^{-2}$, and $\kappa_p = 6.25$. The viscosity is chosen so that $Re_\lambda = (15u_{rms}^4/\nu\epsilon_0)^{1/2} = 110$ to match Bassenne et al. [148]. The time is non-dimensionalised by the integral time $\tau_l = L_0/u_{rms}$, where L_0 is the integral length scale at $t = 0$, given by $L_0 = u_{rms}^3/\epsilon_0$.

The temporal evolution of 32^3 FIT is shown in Figure 4.10. $\langle k \rangle(t)$ and $\langle \epsilon_{res} \rangle(t)$ are seen to reach a statistically steady state after less than 10 eddy turnover times. $\langle k \rangle(t)$ settles closely to the target k_0 as expected. Similarly to the TGV case, the steady state resolved

dissipation ($\langle \epsilon_{res} \rangle(t)$) is dependent on the ϵ_2 value. The velocity skewness derivative $S_r = -\{(\partial \bar{u}_1 / \partial x_1)^3\} / [\{(\partial \bar{u}_1 / \partial x_1)^2\}]^{3/2}$ also settles around a value consistent with a turbulent flow at this Reynolds number [151].

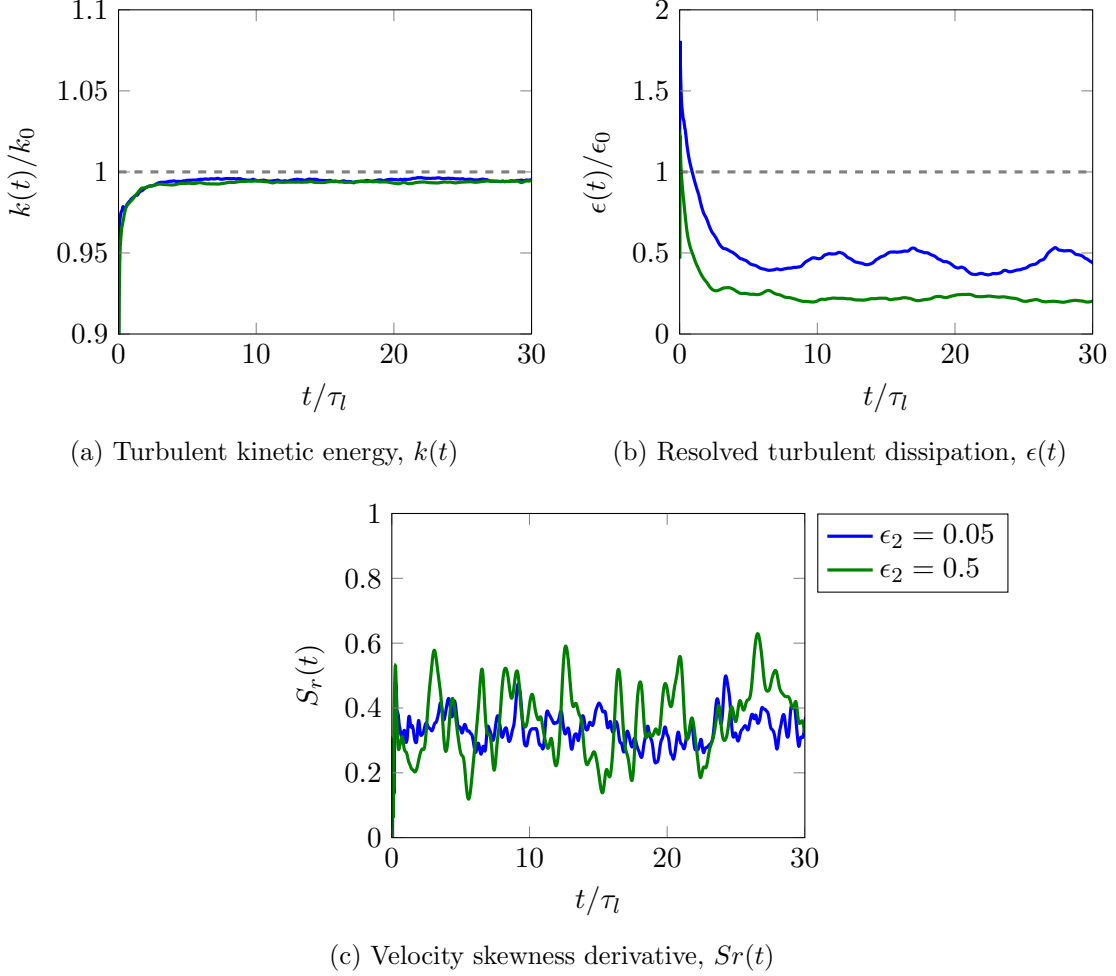


FIGURE 4.10: Temporal evolution of FIT on 32^3 grid

The resulting 32^3 FIT fields are visualised in Figure 4.11. In both cases, physical worm-like structures caused by the vortex-stretching mechanism are visible. However, the size of these structures is significantly affected by the ϵ_2 constant. This effect is also apparent in the energy spectra in Figure 4.9b; with a high ϵ_2 the energy at high wavenumbers (small scales) is significantly damped, and a pile up at low wavenumbers is observed. This is another problem with the ϵ_2 smoothing, it does not just damp the undesirable small scale wiggles, but also acts on the larger scales.

4.2.2 Appraisal of existing LAS scheme

To determine whether the LAS scheme proposed by Tajallipour et al. [110] meets the requirement posed in Section 4.2.1, it was tested on the 32^3 FIT case. The flow field

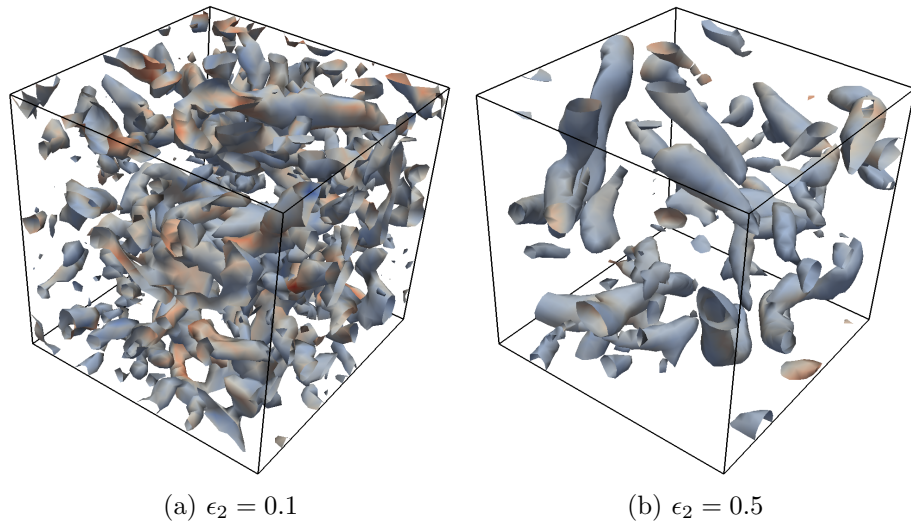


FIGURE 4.11: Iso-surfaces of Q-criterion for FIT on a 32^3 grid, coloured by vorticity magnitude.

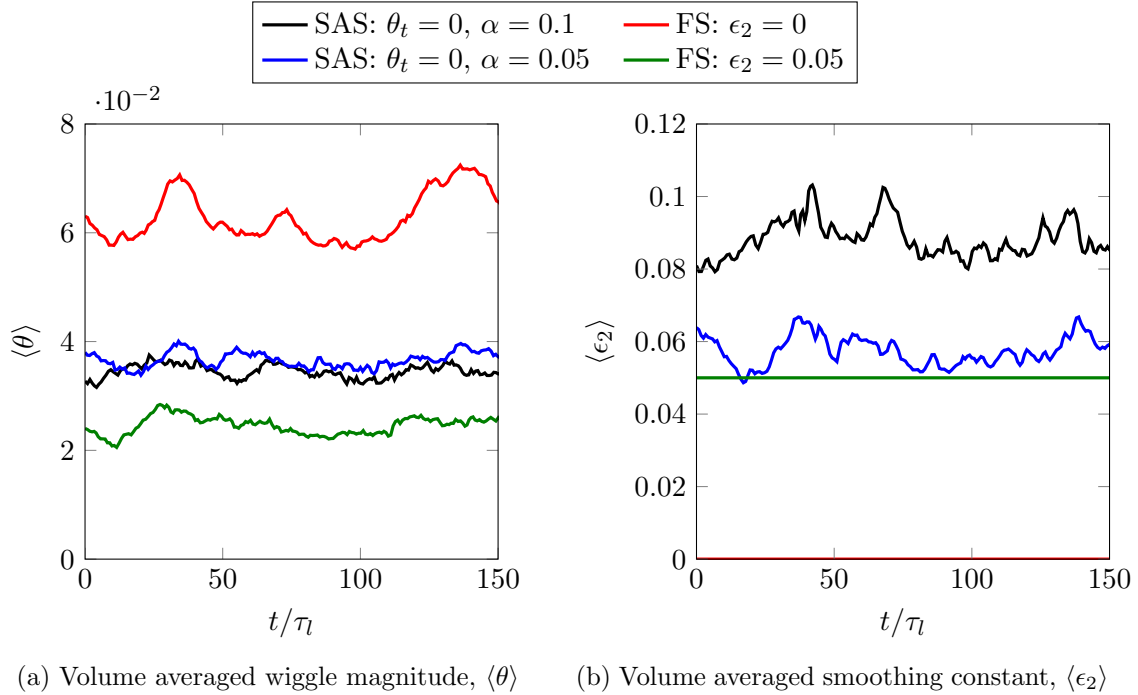
from the 32^3 FIT case ($\epsilon_2 = 0.1$) at $t/\tau_l = 30$ was used as an initial condition. The wiggle magnitude is defined as:

$$\theta(t) = \begin{cases} \sqrt{|\max(\theta_i(t), \theta_j(t))|} & \text{if } \theta_i(t) < 0 \text{ and } \theta_j(t) < 0 \\ 0 & \text{otherwise} \end{cases} \quad (4.17)$$

The maximum of θ_i or θ_j is taken as this is the least dispersive side of the wiggle, and thus the easiest difference to smooth in order to eliminate the wiggle. The time history of the volume averaged θ and ϵ_2 are plotted in Figure 4.12.

The volume averaged quantities shown in Figure 4.12 quickly settle to a fairly constant value. However, Figure 4.12a shows that for the two different gain values (α) tested, the LAS scheme was unable to drive the wiggle magnitude to the target of $\theta_t = 0$. Instead, the magnitude stalled at around $\langle \theta \rangle = 4\%$. To make matters worse, the average ϵ_2 returned is clearly sensitive to the gain parameter, and therefore criterion I set in Section 4.2 is not met.

When comparing the LAS results to the result with fixed smoothing (FS: $\epsilon_2 = 0.05$), it is apparent that the LAS scheme returns a higher average wiggle magnitude, despite the average ϵ_2 being higher for both gain values. The LAS scheme is clearly not performing well, even for this relatively simple test case. To investigate the cause of this behaviour, the LAS scheme must be examined at a local level. In Figure 4.13a the time history of the wiggle magnitude at a single edge in the 32^3 FIT case is plotted. The wiggle magnitude fluctuates substantially as turbulent vortices convect across the edge, changing the local Peclet number. This behaviour does not appear to be an artefact of the FIT forcing, as



(a) Volume averaged wiggle magnitude, $\langle \hat{\theta} \rangle$ (b) Volume averaged smoothing constant, $\langle \epsilon_2 \rangle$

FIGURE 4.12: Temporal history of volume averaged ϵ_2 and θ for 32^3 FIT case with LAS and FS schemes.

it is also observed in all the compressor flows examined, for example on an edge near peak suction shown in Figure 4.13b.

PID controllers are intended for linear systems, or for systems linearised around a fixed point. Thus, it is not surprising that the proportional type controller proposed by Tajallipour et al. [110] is struggling to respond to such an intermittent and apparently non-linear θ signal. Figure 4.14 shows the response of the LAS scheme to the θ signal. The ϵ_2 constant (solid green line) is increased when a wiggle is detected (solid blue line). However, the wiggle then disappears or is damped, and ϵ_2 quickly returns to zero. The lack of smoothing means another large wiggle is then able to appear, and the process repeats.

Figure 4.12b is a histogram of the full time history ($20 < t/\tau_l < 1000$) of ϵ_2 for the edge. It highlights the main problem with the LAS scheme; ϵ_2 is often driven to a very low value (i.e. $\epsilon_2 < 0.05$) since it is quickly reduced when there is no wiggle. However, from the θ histogram (Fig. 4.15a) for a fixed smoothing of $\epsilon = 0.05$, we know that even $\epsilon_2 = 0.05$ is not high enough to prevent wiggles occurring quite frequently. Therefore, because the LAS scheme drives the ϵ_2 smoothing to even lower values as soon as wiggles are not present, wiggles can appear again. It seems that more smoothing is required to eliminate these wiggles than what would be required to prevent them from appearing in the first place. Thus, the LAS scheme results in bigger wiggles occurring more frequently,

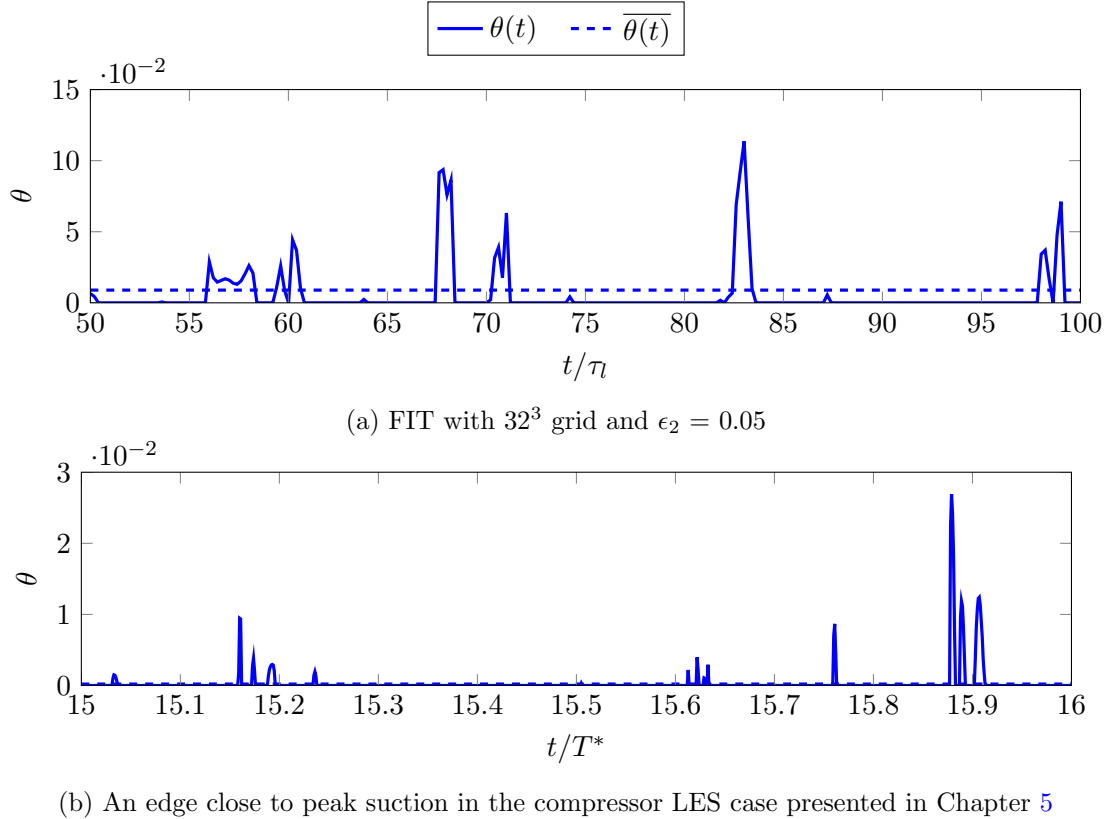


FIGURE 4.13: Temporal history of wiggle magnitude θ_1 at a single computational edge, for two different LES cases (with FS).

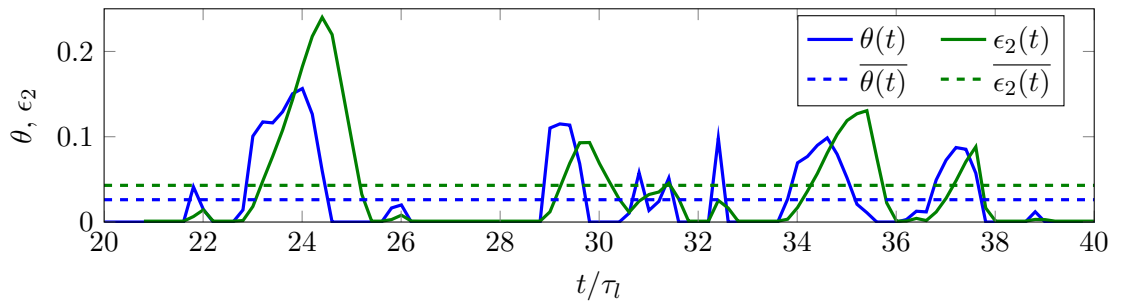


FIGURE 4.14: Time history of wiggle magnitude θ_1 and ϵ_2 at a single computational edge, for 32^3 FIT case with LAS ($\theta_t = 0$, $\alpha = 0.05$).

despite the average smoothing being higher overall than the comparable fixed smoothing case.

Setting α to a very small value could improve the above situation as it will reduce the rate at which ϵ_2 is decreased when a wiggle is not present. However, the LAS scheme would respond more slowly when wiggles appear. Additionally, the average ϵ_2 value (and the solution) will still be dependent on this α value, and tuning may be required.

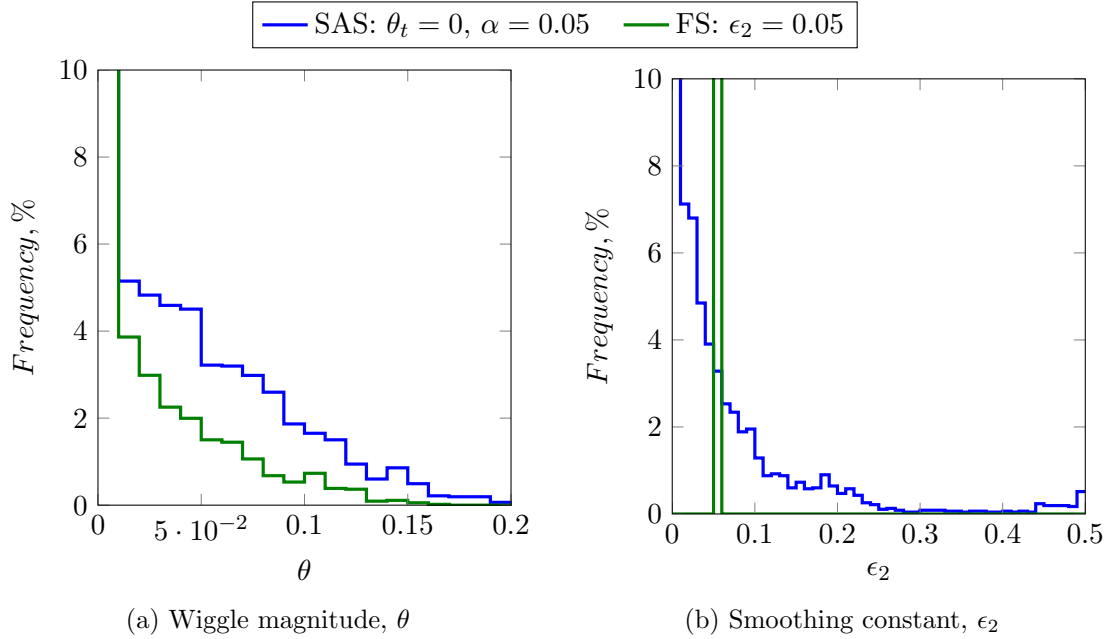


FIGURE 4.15: Histogram showing frequency of ϵ_2 and θ values occurring at a single edge for 32^3 FIT case.

4.3 A locally adaptive smoothing scheme with windowing

To fix the poor performance of the LAS scheme, a new scheme, the locally adaptive smoothing with windowing (LASW) scheme is proposed. The fundamental basis of this scheme is the use of a time averaging to reduce the variability of the error term, so that the proportional controller on ϵ_2 can behave more reliably.

The first attempt at this involved replacing the proportional control in Equation 4.13 with an integral control term similar to that seen in a PID controller:

$$\Delta\epsilon_2(t) = \frac{\alpha}{t} \int_0^t \theta(t) - \theta_t dt \quad (4.18)$$

which can be written as $\Delta\epsilon_2(t) = \alpha [\bar{\theta}(t) - \theta_t]$. Assuming a constant Δt , the average wiggle magnitude $\bar{\theta}$ at the n^{th} timestep is:

$$\bar{\theta}^n = \frac{1}{n\Delta t} \int_0^{t=n\Delta t} \theta(t) dt = \left[\left(\frac{n-1}{n} \right) \bar{\theta}^{n-1} + \frac{1}{n} \theta^n \right] \quad (4.19)$$

Although this drastically reduces the intermittency of the error term, the convergence behaviour of the ϵ_2 field is very poor. As the simulation progresses, the $(n-1)/n$ term in Equation 4.19 becomes increasing dominant, and $\Delta\epsilon_2$ becomes increasing unresponsive to the current wiggle magnitude θ^n . This is an intended consequence of the time averaging, as it removes the problems experienced with an intermittent θ signal. However,

it means that the scheme becomes overly contaminated by historical effects. If after a long time, ϵ_2 was reduced slightly too much so that wiggles appeared, the responding increase in ϵ_2 would be damped due to the dominance of the $(n - 1)/n$ term. By this time the wiggles may have already caused the solution to diverge.

4.3.1 The windowing procedure

To improve the convergence behaviour, windowing is introduced to the scheme, whereby the wiggle magnitude is integrated over a time window T_w :

$$\theta_{w1} = \frac{1}{T_w} \int_{t_w=0}^{t_w=T_w} \theta(t_w) dt_w \quad (4.20)$$

Only when $t_w = T_w$ is the ϵ_2 value adjusted using a proportional controller:

$$\Delta\epsilon_2(t) = \begin{cases} (\theta_{w1}(t) - \theta_t) \alpha & \text{if } t \geq t_w \\ 0 & \text{otherwise} \end{cases} \quad (4.21)$$

and then the time through the window t_w and θ_{w1} are reset to zero ready for the next window. This is equivalent to resetting $\bar{\theta}^n$ and n in Equation 4.19.

Any variance in the θ_{w1} signal will cause noise in the converged ϵ_2 field, therefore the window length T_w must be long enough to sufficiently filter out the high frequency fluctuations in the wiggle magnitude. Figure 4.16a shows how increasing T_w smooths the θ_{w1} signal. However, since the ϵ_2 field is only adjusted at the end of each window, a large T_w will result in slower convergence. A larger gain parameter α can be used, but this will also result in a noisier ϵ_2 field.

If the user is more concerned about preventing single large wiggles, rather than decreasing the average wiggle magnitude, then the error term could instead be based upon the maximum wiggle magnitude out of N_{wig} wiggles seen in throughout the window:

$$\theta_{max} = \max_{n \in N_{wig}} (\theta_n) \quad (4.22)$$

Alternatively, instead of performing a true time average of the θ signal (Eqn. 4.20), the average out of the set of N_{wig} wiggles could be taken:

$$\theta_{w2} = \frac{1}{N_{wig}} \sum_{n=1}^{n=N_{wig}} \theta_n \quad (4.23)$$

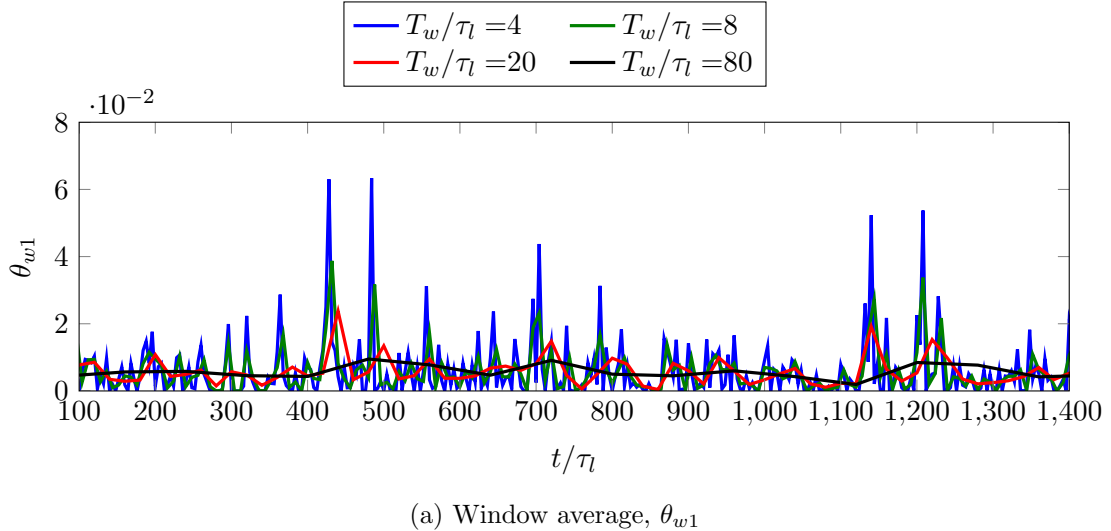


FIGURE 4.16: Window averaging applied to the θ signal measured at a single edge in the 32^3 FIT case with FS ($\epsilon_2 = 0.1$).

The normalised root-mean-square deviation (NRMSD), given by:

$$NRMSD(x) = \frac{1}{\bar{x}} \sqrt{\frac{\sum_{i=1}^n (x_i - \bar{x})^2}{n}} \quad (4.24)$$

is plotted against window length in Figure 4.17, for the three windowing techniques. Over the entire range of window lengths, the θ_{w2} offers less variance than the other two methods, while the θ_{w1} performs less well throughout. The θ_{w1} approach takes into account $\theta = 0$ samples (i.e. when there is no wiggle), while the θ_{w2} approach only averages the samples where a wiggle is present. The θ_{w1} method is therefore affected more by the intermittent nature in which wiggles appear.

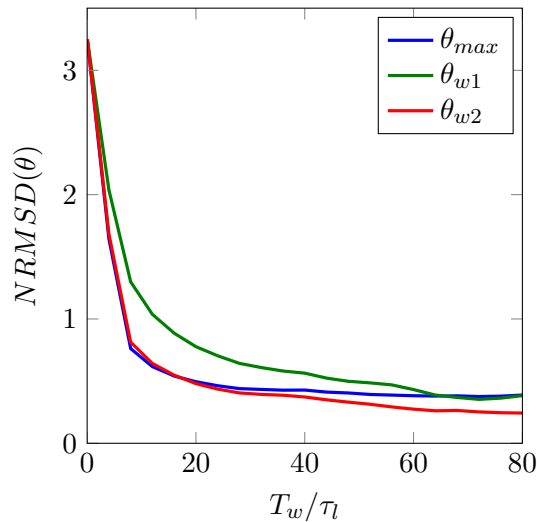


FIGURE 4.17: Normalized root-mean-square deviation of windowed signals for various windowing methods and window lengths. Raw θ signal measured at a single edge in the 32^3 FIT case with FS ($\epsilon_2 = 0.1$).

Since the focus here is on developing a robust and efficient scheme, the θ_{w2} approach is chosen, as it should allow for a shorter window length T_w and a higher gain parameter α .

4.3.2 Modification for small target values

If inequalities (4.11) and (4.12) are not satisfied, Tajallipour et al. [110] use the maximum of θ_i or θ_j in the error term to reduce Δt (Eqn 4.13). The rationale behind this may be that $\max(\theta_i, \theta_j)$ can provide a measure of how far the solution across the stencil is from being dispersive.

However, it is not clear how good a measure this is, since it would result in ϵ_2 being reduced very quickly in areas with high gradients. Also, ϵ_2 would not be reduced at all in a uniform flow region (i.e. ϕ uniform across the stencil), even though the gradients are low (meaning that wiggles are unlikely to occur). Therefore, to make the LASW scheme more robust, it was instead decided not to allow positive θ values, and instead set θ to zero when wiggles are not detected (i.e. Eqn 4.17).

The disadvantage of the above approach is that ϵ_2 is reduced slowly when θ_t is small. This is shown in Figure 4.18, where the proportional control term in Equation 4.21 is plotted (solid black line). If θ_t (the $\Delta\epsilon_2 = 0$ intercept) is small, then the maximum negative value of $\Delta\epsilon_2$ will also be small. One solution is to multiply the usual gain parameter α by an extra gain parameter A when $\theta_{w2} < \theta_t$:

$$\Delta\epsilon_2(t) = \begin{cases} (\theta_{w2}(t) - \theta_t) \alpha & \text{if } t \geq t_w \text{ and } \theta_{w2}t \geq \theta_t \\ (\theta_{w2}(t) - \theta_t) \alpha A & \text{if } t \geq t_w \text{ and } \theta_{w2}t \leq \theta_t \\ 0 & \text{otherwise} \end{cases} \quad (4.25)$$

This approach is also plotted in Figure 4.18 (the dashed black line). It can increase the speed of convergence but can cause additional noise in the ϵ_2 field due to the discontinuity between the solid and dashed black lines. A compromise is to apply some damping to the $\theta_{w2} < \theta_t$ portion of the control equation. For example:

$$\Delta\epsilon_2(t) = \begin{cases} \left\{ \max \left[1 - \left(\frac{\theta_{w2}(t)}{\theta_t} \right)^\gamma, 0 \right] A + \min \left[\left(\frac{\theta_{w2}(t)}{\theta_t} \right)^\gamma, 1 \right] \right\} (\theta_{w2}(t) - \theta_t) \alpha & \text{if } t \geq t_w \\ 0 & \text{otherwise} \end{cases} \quad (4.26)$$

The damping is controlled by γ , and is plotted in Figure 4.18 for different values of γ .

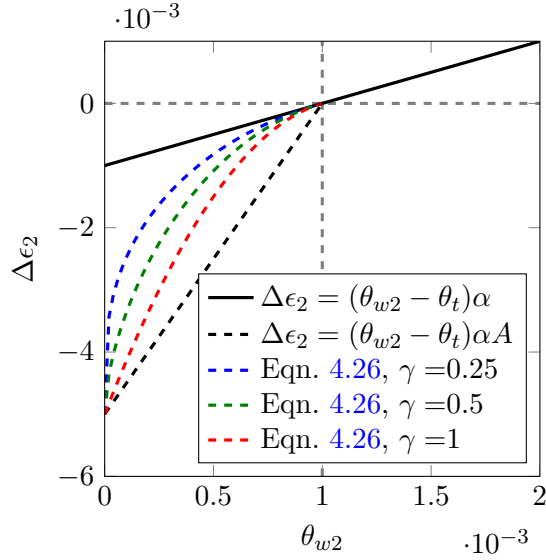


FIGURE 4.18: Modification to LASW control equation for cases with small θ_t . $\theta_t = 0.001$, $\alpha = 1$, $A = 5$.

4.3.3 Extrapolation using gradients

Since HYDRA is a second order edge based code, the e_{ij} edge can only “see” nodes i and j . To obtain ϕ_{i-1} and ϕ_{j+1} , extra connectivity information is needed. This requires a pre-processing step to select which edges to use for the four point stencils, based on minimising the angles between edges (see Ciardi [146]). More importantly, the extra communication significantly damages the parallel scaling of HYDRA.

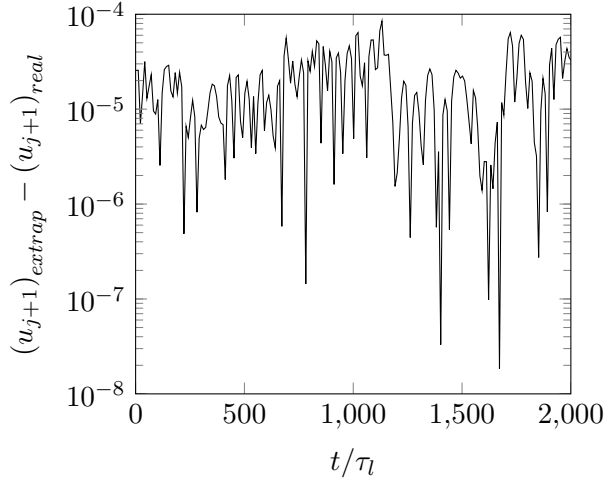
Instead, the gradients of ϕ at i and j can be used to extrapolate a solution for ϕ_{i-1} and ϕ_{j+1} :

$$\begin{aligned}\phi_{j+1} &= \phi_i + 2\Delta\mathbf{x} \cdot (\nabla\phi)_j \\ \phi_{i-1} &= \phi_j - 2\Delta\mathbf{x} \cdot (\nabla\phi)_i\end{aligned}\tag{4.27}$$

Figure 4.19 plots the error of this extrapolation method for the u velocity at a single edge in a 32^3 FIT case. Since the user is usually concerned with wiggle magnitudes with comparatively larger values, say 0.1% or 1%, these error levels are considered to be sufficiently small. Therefore, this extrapolation technique is used for the LASW method.

4.3.4 The final LASW scheme

Bringing the above sections together, it is relatively straightforward to implement the LASW scheme in HYDRA. A standalone LASW module, shown in Algorithm 4.1, is called at the first pseudo time-step of each physical time-step (see Section 3.1.3). The module must be called after the gradients have been calculated, but before the inviscid

FIGURE 4.19: Error of extrapolation using cell centred gradients, for 32^3 FIT case.

fluxes (see Section 3.1.1.1) are calculated, so that the updated ϵ_2 field can be used in this calculation.

Algorithm 4.1 LASW module

```

1: procedure LASW
2:   for  $e_{ij} \in E_{ij}$  do                                 $\triangleright$  Loop through the set of  $E_{ij}$  edges
3:     if  $t_w < T_w$  then                          $\triangleright$  If not at end of window
4:       if  $\theta_i < 0$  and  $\theta_j < 0$  then            $\triangleright$  Check if wiggle
5:          $\theta = \dots$                                  $\triangleright$  Eqn. 4.17
6:          $n = n + 1$ 
7:          $\theta_{w2} = [(n - 1)\theta_{w2} + \theta] / n$      $\triangleright$  Accumulate  $\theta_{w2}$  (Eqn. 4.23)
8:       else
9:          $\theta = 0$                                  $\triangleright$  If no wiggle
10:      end if
11:       $t_w = t_w + \Delta t$ 
12:    else                                      $\triangleright$  If at end of window
13:       $\Delta\epsilon_2 = \dots$                        $\triangleright$  Eqn. 4.26
14:       $\epsilon_2 = \epsilon_2 + \Delta\epsilon_2$            $\triangleright$  update  $\epsilon_2$  at edge
15:       $t_w = 0$                                  $\triangleright$  Reset windowing variables
16:       $n = 0$ 
17:       $\theta_{w2} = 0$ 
18:    end if
19:  end for
20:  return  $\epsilon_{2ij}$ 
21: end procedure

```

The module loops through each edge in the domain (the E_{ij} set). If a wiggle is detected the wiggle magnitude θ is added to the window average θ_{w2} for that edge. Once the end of the window is reached ($t \geq t_w$), the ϵ_2 field is updated and the windowing counters (e.g. n) are reset. Only two new edge based arrays, ϵ_2 and θ_{w2} , must be stored in memory.

4.3.5 Performance of the LASW scheme

To test the performance of the LASW scheme, a number of FIT cases are run on different resolution meshes and with different target wiggle magnitudes. Figure 4.20 plots the convergence history of the LASW scheme for a 32^3 FIT case with a number of θ_t values. Figure 4.20a shows that for all the θ_t values tested, the LASW scheme converges to a steady state ϵ_2 level. Figure 4.20b suggests that these ϵ_2 levels offer the correct amount of smoothing in order for the target wiggle magnitude to be achieved. In all cases the volume averaged wiggle magnitude $\langle \theta \rangle$ (solid lines) reaches a level close to the target magnitude (dash-dot lines).

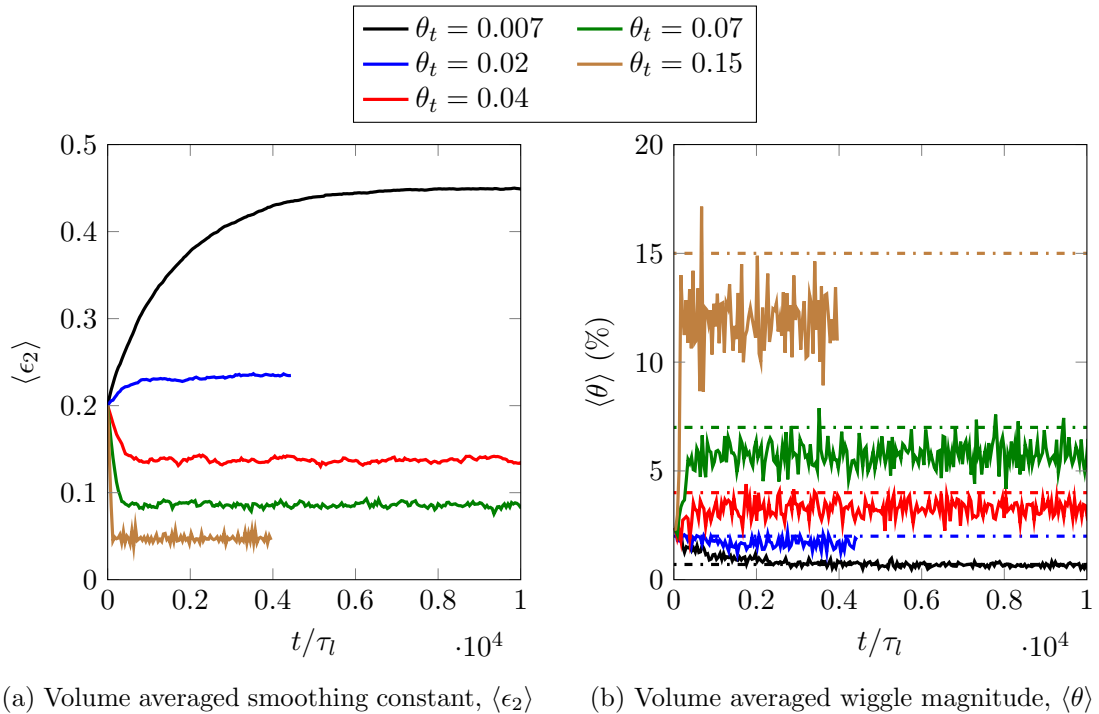


FIGURE 4.20: Temporal history of volume averaged ϵ_2 and θ for 32^3 FIT case with LASW scheme and different θ_t values. $\alpha = 0.1$.

In Figure 4.21 the same analysis is presented, but with the θ_t parameter fixed and the gain parameter α varied. Reducing α increases the time taken until the ϵ_2 field converges, but it does not alter the steady state ϵ_2 value.

Due to the natural variations of the FIT the average wiggle magnitude (and other properties) fluctuate slightly, even with a fixed level of ϵ_2 (see Fig. 4.12). Figure 4.20b shows that these fluctuations are worse at high θ_t values, perhaps because the FIT control scheme is less damped due to the lower steady state $\langle \epsilon_2 \rangle$. Figure 4.21a shows that increasing α also increases the fluctuations seen in $\langle \epsilon_2 \rangle$, as any fluctuations in θ_{w2} will return a larger $\Delta\epsilon_2$. However, despite these small fluctuations, the LASW still successfully achieves $\langle \theta \rangle \leq \theta_t$ for all the θ_t and α values tested.

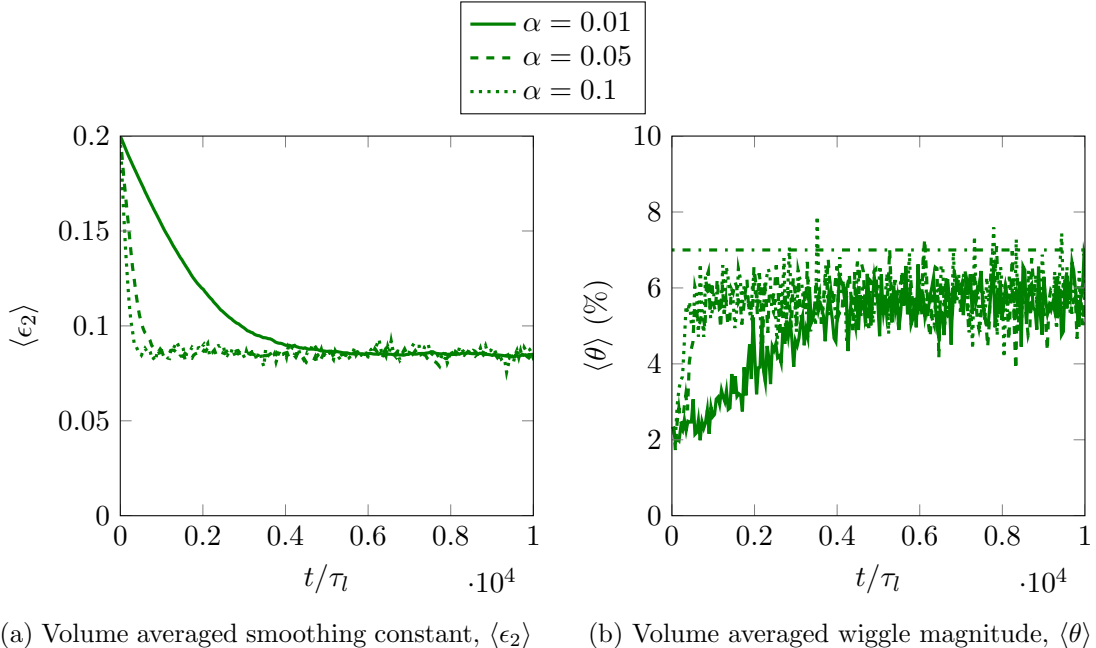


FIGURE 4.21: Temporal history of volume averaged ϵ_2 and θ for 32^3 FIT case with LASW scheme and different α values. $\theta_t = 0.07$.

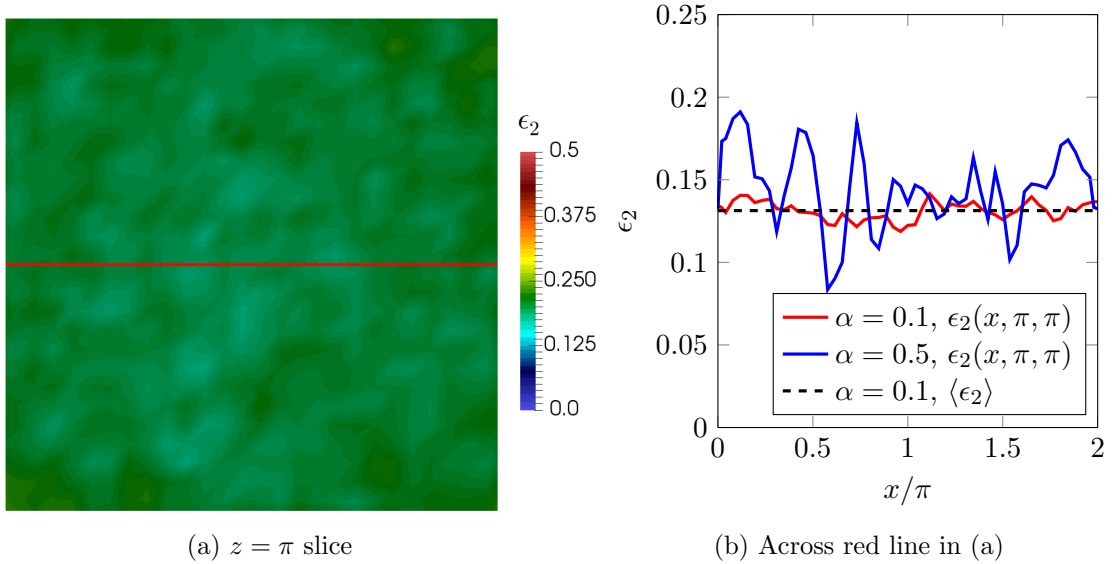


FIGURE 4.22: Contours and line plot of ϵ_2 field at a given instance in time for the 32^3 FIT with LASW ($\theta_t = 0.04$).

To check that volume averaging is not hiding the true extent of the ϵ_2 fluctuations, the spatial variation of ϵ_2 is shown in Figure 4.22. Similar conclusions are drawn here, the ϵ_2 level fluctuates slightly around the volume averaged level $\langle \epsilon_2 \rangle$ (dashed black line in Fig. 4.22b). With $\alpha = 0.1$ the maximum variation of ϵ_2 from $\langle \epsilon_2 \rangle$ is under 10%. However, with $\alpha = 0.5$, this rises to an unacceptably high value of 45%. If these variations are too large, the user could increase the window length so that the physical fluctuations

of the flow are more effectively filtered out¹. Alternatively, a smaller α means that any unfiltered fluctuations have less of an impact. There is therefore a balance between having a large T_w and small α to achieve a smooth ϵ_2 field, without pushing these parameters so far that convergence is impractically slow.

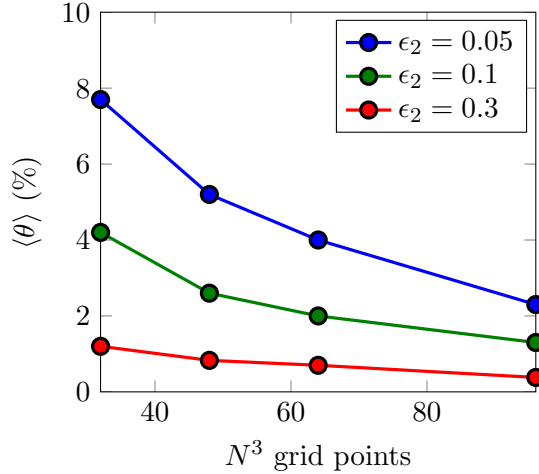


FIGURE 4.23: Effect of FIT grid resolution on volume averaged θ for different ϵ_2 values with the FS scheme.

The FIT case was run on 32^3 , 64^3 and 96^3 grids with different ϵ_2 levels. Figure 4.23 shows that the resulting wiggle magnitude is strongly dependent on both ϵ_2 and the grid resolution. In Figure 4.24 curves of the form $\langle \epsilon_2 \rangle = A \langle \theta \rangle^{-B}$ are fitted to this data for each grid resolution (the \bullet markers). The LASW scheme is then run at the different grid resolutions with different θ_t values, and the converged ϵ_2 levels are plotted (the \times markers).

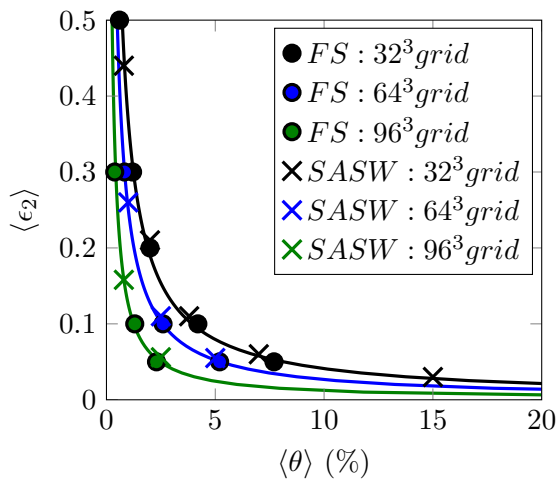


FIGURE 4.24: Comparison of volume averaged θ and ϵ_2 relationship for the FS and LASW schemes. Solid lines are $\langle \epsilon_2 \rangle = A \langle \theta \rangle^{-B}$ curves fit to the \bullet data points.

¹Currently $T_w = 40\pi$. Figure 4.12a suggests that the natural fluctuations of the FIT are not at a much higher frequency than this, hence a larger T_w would more effectively filter out these fluctuations.

The LASW data points all lie very close to the fitted curves. This indicates that, if the user simply selects their target wiggle magnitude θ_t , the LASW scheme will find the ϵ_2 level required to achieve that target on the current grid.

4.4 Concluding remarks

The LASW scheme has been shown to meet the criteria posed in Section 4.2. Criterion I is met as the α parameter only affects the convergence behaviour of ϵ_2 , not the steady state value itself. Criterion II is met as θ_t and T_w are directly relatable to the flow physics, and do not require tuning with reference to a priori data. For example, if a case was run with incoming wakes, T_w should be set to the wake passing period. In this way the periodicity is filtered out and the problem remains a statistically stationary problem, with a converged ϵ_2 field attainable.

Chapter 5

Boundary Layer Transition in Compressors

A more reliable numerical scheme, the LASW¹ scheme, was presented in Chapter 4. Although the scheme performed well on a forced isotropic turbulence test case, it is necessary to test it on a flow more representative of an industrial compressor flow.

The literature review (Chapter 2) highlighted the importance of boundary layer transition in aero-engine compressors, and the complex nature of the different transition mechanisms was discussed. It is well known that the Smagorinsky-Lilly SGS model performs poorly in transitional flows [65]. Therefore, it is important to assess whether the WALE or σ SGS models, and the LASW scheme, perform better in such flows. For this assessment, a quasi-2D transitional compressor flow is investigated.

The focus here is to determine the sensitivity of the flow to the inflow turbulence, the numerical scheme, and the SGS model, which is done in Section 5.4. To properly understand these sensitivities, it is first necessary to understand the flow physics. In Sections 5.2 and 5.3, an LES solution is compared to the DNS solution from Zaki et al. [9] to examine how much of the flow physics is being correctly captured by the LES.

5.1 The V103 compressor cascade

The compressor cascade investigated in this chapter is the V103 cascade, tested experimentally by Hilgenfeld et al. [152]. The key geometrical and inflow parameters for the cascade are presented in Table 5.1. The cascade is a linear cascade consisting of NACA-65-K48 aerofoils. Although not an up-to-date aerofoil profile, NACA-65 aerofoils have

¹Locally Adaptive Smoothing with Windowing

been used in many studies [30, 96, 99, 152] to represent the compressor stator blades found in an axial flow gas-turbine compressor.

TABLE 5.1: Geometrical and inflow parameters for the V103 compressor cascade.

| Parameter | Value |
|-------------------------------|--------------------|
| Blade profile | NACA-65-K48 |
| Chord length, c | 220mm |
| Axial chord length, C_x | 204mm |
| Reynolds number, Re_c | 1.38×10^5 |
| Blade span, h/c | 1.36 |
| Blade pitch, S/c | 0.55 |
| Blade thickness, t/c | 0.055 |
| Inflow incidence, i | -6.0° |
| Inlet flow angle, α_1 | 44.0° |
| Outlet flow angle, α_2 | 8.0° |
| Flow turning | 36.0° |
| 2D Diffusion Factor [153] | 0.42 |

Zaki et al. [9] used DNS to study the effects of free-stream turbulence intensity on the transitional processes in this cascade. The experimental Reynolds number of the cascade is $Re_c = 4.5 \times 10^5$, while the Mach number is $Ma = 0.67$. Since the computational cost of DNS (and LES) scales significantly with Reynolds number (see Section 2.3.3), the DNS computations were run at a reduced Reynolds number of $Re_c = 1.38 \times 10^5$, with an incompressible code. LES of this scaled case has been performed by Lardeau et al. [86], where the performance of the Dynamic Smagorinsky (DSM) and Mixed-Time-Scale SGS models is examined. Due to the scaled Mach number, compressibility effects (see Section 2.4.2) likely to be present in the experiment (and a real compressor) will not be present in this case.

5.1.1 Case set-up

The computational grid used for this case is shown in Figure 5.1. The mesh consists of an H-O-H topology, commonly used for blade cascades. Downstream of the blade, a sponge zone is used to prevent reflections from the static pressure outflow boundary. Pitchwise periodicity is enforced with periodic boundaries at mid-pitch. The quasi-2D condition is enforced with periodic boundaries in the spanwise (z) direction. The spanwise extent is set to 20% span, and the inflow boundary set at $x/C_x = -0.4$, to match the DNS case [9].

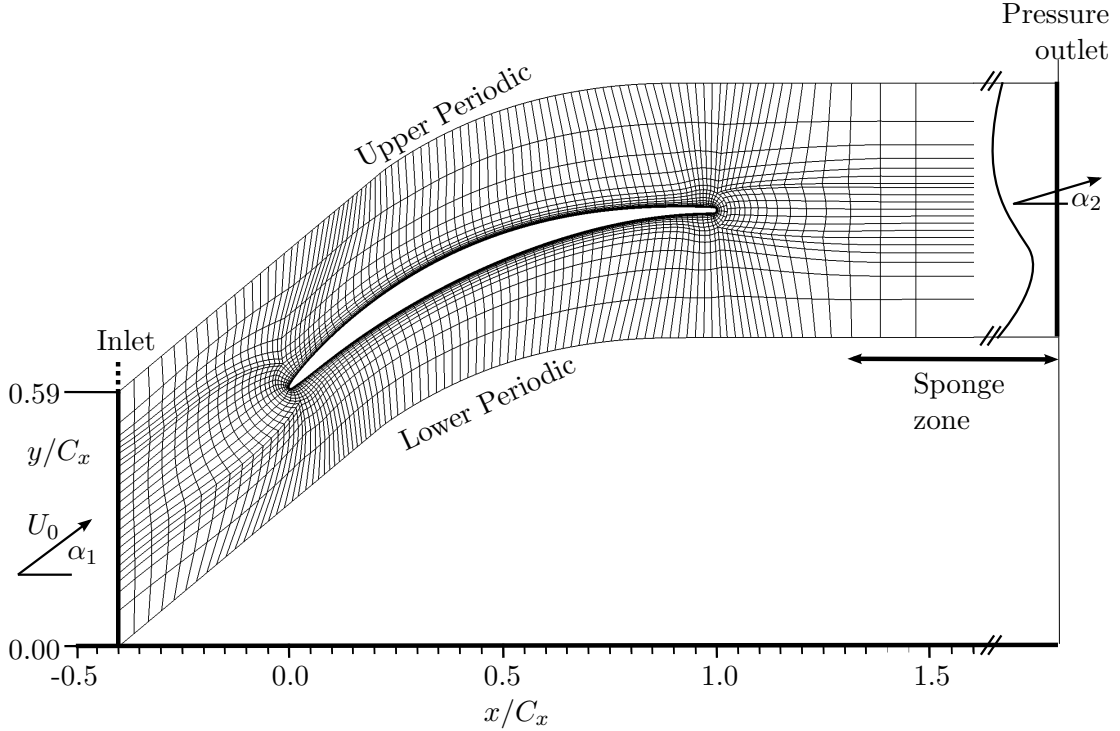


FIGURE 5.1: Two-dimensional slice of computational grid used for LES of V103 compressor cascade. Every 5th grid point shown.

The O-mesh wrapped around the blade has dimensions $844 \times 45 \times 101$ in the wall tangential, normal and spanwise directions respectively. Adding the H-mesh sections leads to 1.04×10^5 grid points per xy-plane, and 1.05×10^7 grid points in total. In comparison, the LES studies of Lardeau et al. [86] used 6.3×10^6 grid points, and Zaki et al. [9] used 8.4×10^7 grid points for their DNS computations.

The focus here is on predictive LES for industrial applications, where performing a full mesh dependency study is likely to be impractical. Therefore, such a study is not performed here¹. The mesh is instead designed to ensure that the grid resolution is well within the recommended values for wall-resolved LES given by Piomelli et al. [71]:

$$\Delta^+ = \frac{\Delta \sqrt{\tau_w / \rho}}{\nu} \leq 50 - 100/1/15 - 30 \quad (5.1)$$

where $\tau_w = \mu \left(\frac{\partial u_t}{\partial x_n} \right)$ is the wall shear stress² and Δ is the near wall grid spacing in the wall tangential/normal/spanwise directions respectively. Following Tucker [43], close to the wall the wall-normal mesh stretching is controlled to ensure there are at least 3-5 grid points within a distance of $y^+ < 10$ from the wall. In the stream-wise direction the

¹The value of mesh dependency studies for predictive LES is also questionable since, unless an explicit test filter is used (Section 2.3.1), a truly mesh independent solution will not be reached until the mesh is refined to the DNS limit.

²where u_t is the velocity tangential to the wall surface and x_n is the wall normal distance to the wall.

mesh stretching is limited to less than 2%, and in all regions the cell equiangle skewness is less than 0.6.

For all cases, the physical time-step is set to give $CFL_{max} \approx 0.8$, and a flow-through time then equates to approximately 10000 time-steps. The flow-through time, T^* , is defined as:

$$T^* = C_x/U_0 \quad (5.2)$$

The LES cases run are presented in Table 5.2. For all cases, a time dependent velocity $u_i(t, y, z)$ is enforced at the inflow boundary. The inflow velocity field is prescribed using the method discussed in Section 3.2. The free-stream turbulence (FST) is generated using the method of Saad et al. [136], explained in Section 3.2.3. To investigate how well the influence of free-stream turbulence intensity (Ti) is captured with the current LES approach, two different Ti cases are run (C2 and C5). Zaki et al. [9] run DNS cases at five different Ti 's (0%, 3.25%, 6.5%, 8.0% and 10.0%). Here, the $Ti = 3.25\%$ and $Ti = 10.0\%$ cases are chosen for investigation due to the range of different transition mechanisms seen in these two cases. To examine the performance of the SGS models and the LASW scheme, a number of cases (C2,3,4,6,7) are run with the same Ti but different SGS models and smoothing schemes.

TABLE 5.2: LES cases run for V103 compressor cascade.

| Case | Inflow turbulence | | SGS model | Numerical scheme |
|------|-------------------|---------|-------------------------------------|---------------------------|
| | Ti (%) | L/C_x | | |
| C1 | 3.25 | 0.03 | σ ($C_\sigma = 1.35$) | LASW |
| C2 | 3.25 | 0.06 | σ ($C_\sigma = 1.35$) | LASW |
| C3 | 3.25 | 0.06 | WALE ($C_w = 0.5$) | LASW |
| C4 | 3.25 | 0.06 | Smagorinsky-Lilly ($C_s = 0.165$) | LASW |
| C5 | 10.0 | 0.06 | σ ($C_\sigma = 1.35$) | LASW |
| C6 | 3.25 | 0.06 | σ ($C_\sigma = 1.35$) | FS ($\epsilon_2 = 0.0$) |
| C7 | 3.25 | 0.06 | σ ($C_\sigma = 1.35$) | FS ($\epsilon_2 = 0.5$) |

For the majority of the cases the integral length scale of the FST was chosen as $L = 0.06C_x$ in order to match the DNS [9]. The turbulence intensity is defined as

$$Ti = \sqrt{\frac{1}{3} \frac{\overline{u'u'} + \overline{v'v'} + \overline{w'w'}}{U_1^2}} \quad (5.3)$$

where U_1 is the inflow bulk velocity. Ti at mid-pitch in a number of LES cases is compared to the DNS in Figure 5.2. It was found that $L = 0.06C_x$ resulted in a slower decay rate of Ti compared to the DNS. This may be due to differences in the definition of

the integral length scale used by Zaki et al. [9] and that used in the synthetic turbulence method of Saad et al. [136], or due to differences in the energy spectra of the FST.

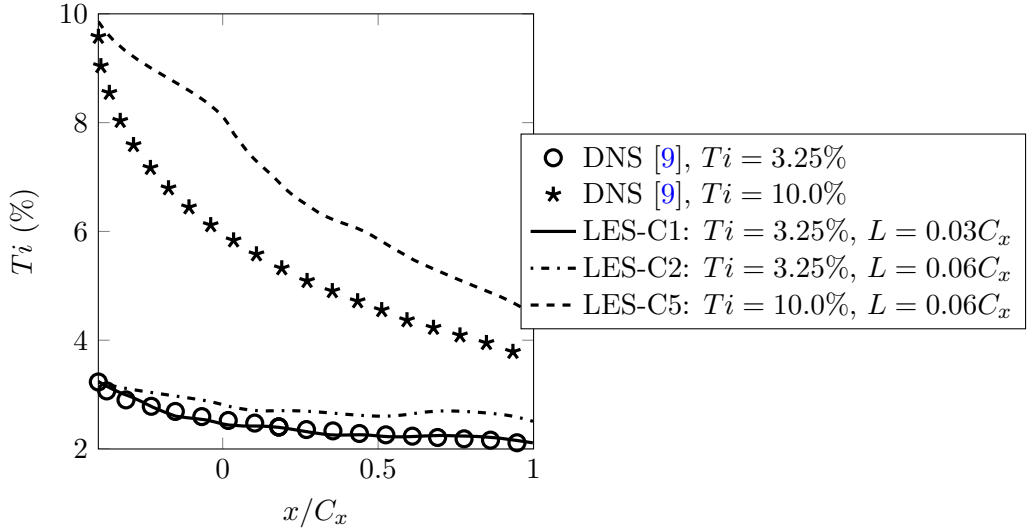


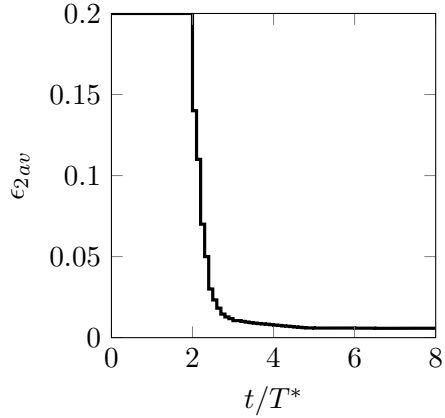
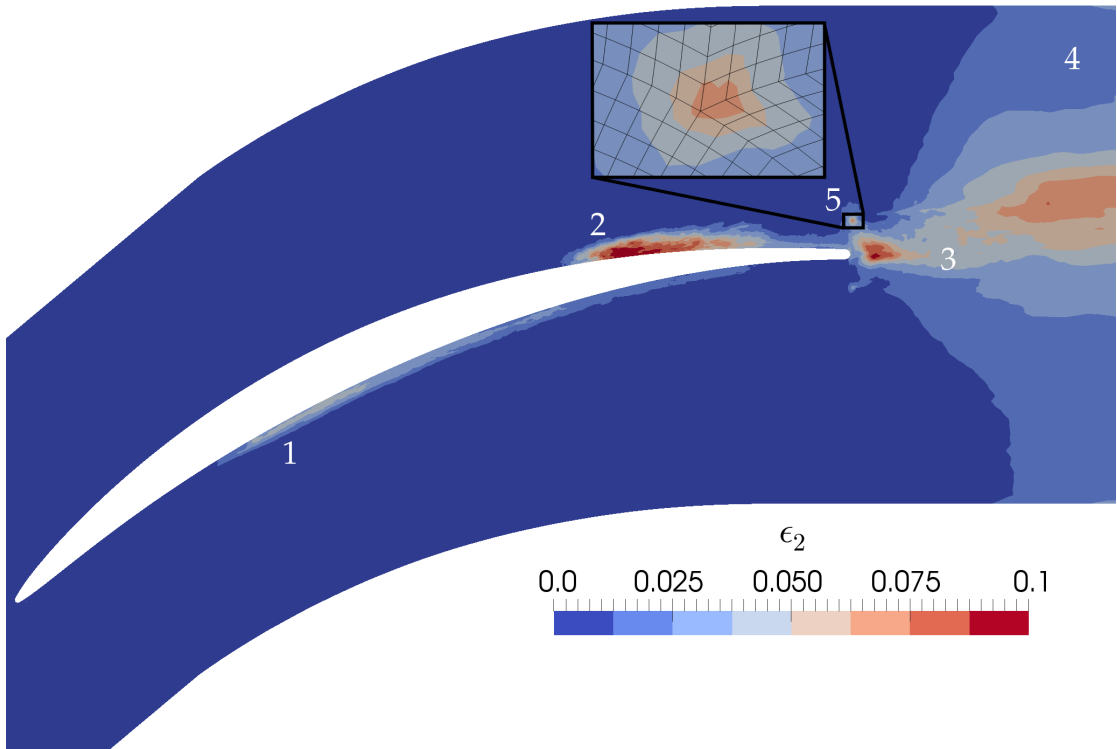
FIGURE 5.2: Turbulence intensity at mid-pitch for a selection of the V103 LES and DNS cases.

To enable a fair comparison with the DNS, one additional case (C1) was run with a smaller inflow integral length scale $L = 0.03C_x$. Figure 5.2 shows that the FST decay rate is in much closer agreement with the DNS in this case. Despite the lower FST decay rate in the other cases, they still provide a valid basis to examine the influence of free-stream T_i , SGS model and numerical scheme.

5.1.2 LASW scheme

In cases C1 to C5 the LASW scheme presented in Chapter 4 is used. Case C1 was initialised from a RANS solution, and the other LES cases from the C1 flow. Each case was run with $\epsilon_2 = 0.2$ for $2T^*$ to flush out initial transients. The LASW scheme was then switched on, with a small target wiggle magnitude of $\theta_t = 0.001$. Figure 5.3 shows that the domain averaged ϵ_2 converged within $6T^*$ for case C1, and similar convergence was seen in the other cases.

The resulting ϵ_2 field for case C1 is shown in Figure 5.4. The LASW scheme found that in most of the domain, only a very small level of smoothing is necessary to prevent wiggles. In a number of regions, labelled (1) to (5) in Figure 5.4, the LASW scheme has had to increase the smoothing to prevent wiggles. At (1) and (2) the flow is transitioning from laminar to turbulent, while (3) highlights the particularly turbulent wake region. At (4) the mesh is being coarsened before the downstream sponge zone, while at (3) a number of slightly skewed cells are located where the O and H mesh blocks are joined.

FIGURE 5.3: Case C1. Convergence history of domain averaged ϵ_2 with LASW scheme.FIGURE 5.4: Case C1. Contours showing converged ϵ_2 smoothing field with LASW scheme, at $z = 0.05C_x$.

Due to the large number of cases being run, fairly aggressive LASW parameters of $T_w = 0.2T^*$ and $\alpha = 1.0$ are chosen to give rapid convergence. This does mean that, as discussed in Section 4.3.5, the ϵ_2 field is slightly noisy. To mitigate this, the converged ϵ_2 fields are spanwise averaged. The ϵ_2 fields are then frozen, and the cases are run for $10T^*$ to collect statistics. Unless otherwise specified, all time averaged quantities presented in the following sections are also averaged in the spanwise direction. This significantly reduces the time taken to acquire converged statistics.

5.2 Pressure surface transition mechanisms

The LES cases C1 and C5 are now examined to determine how well the pressure surface transition mechanisms are captured. The pressure surface time averaged pressure coefficient,

$$C_p = \frac{\bar{p} - \bar{p}_1}{\frac{1}{2}\rho U_1^2}, \quad (5.4)$$

and the time-averaged skin friction coefficient,

$$C_f = \frac{\tau_w}{\frac{1}{2}\rho U_1^2}, \quad (5.5)$$

are plotted in Figure 5.5. τ_w is the wall shear stress and \bar{p}_1 is the time averaged static pressure at the inflow.

To demonstrate the influence of free-stream turbulence (FST), the laminar inflow DNS from Zaki et al. [9] is also included in Figure 5.5. From the C_p distribution in Figure 5.5a, it is clear that the FST has some effect, and this becomes more apparent in the C_f distribution in Figure 5.5b. In the absence of free-stream perturbations (DNS, $Ti = 0\%$ case) the flow is seen to separate (indicated by $C_f \leq 0$). On the other hand, when free-stream perturbations are present, the boundary layer is transitioned to turbulence and the flow is prevented from separating.

The momentum thickness of the boundary layer, θ , is calculated by integrating in the wall normal (x_n) direction

$$\theta = \int_0^{\delta_\omega} \frac{u(x_n)}{\bar{u}_e} \left(1 - \frac{u(x_n)}{\bar{u}_e} \right) dx_n \quad (5.6)$$

where \bar{u}_e is the mean streamwise velocity at the edge of the boundary layer¹. The pressure surface momentum thickness Reynolds number, $Re_\theta = u_e \theta / \nu$, is plotted in Figure 5.6a. The DNS Re_θ data shows that the presence of free-stream perturbations also causes the boundary layer to grow significantly faster. Both this, and the effect of the FST on the transition location, are well captured by the LES. However, as discussed in Section 2.1.1, breakdown to turbulence in turbo-machinery flows can be caused by a number of different mechanisms. In the following sections the pressure surface transition mechanisms are examined in more detail to see if the finer physics is being properly captured by the LES.

¹A vorticity magnitude threshold, the same as that used by [125] and Lardeau et al. [86], is used to detect the edge of the boundary layer $x_n = \delta_\omega$.

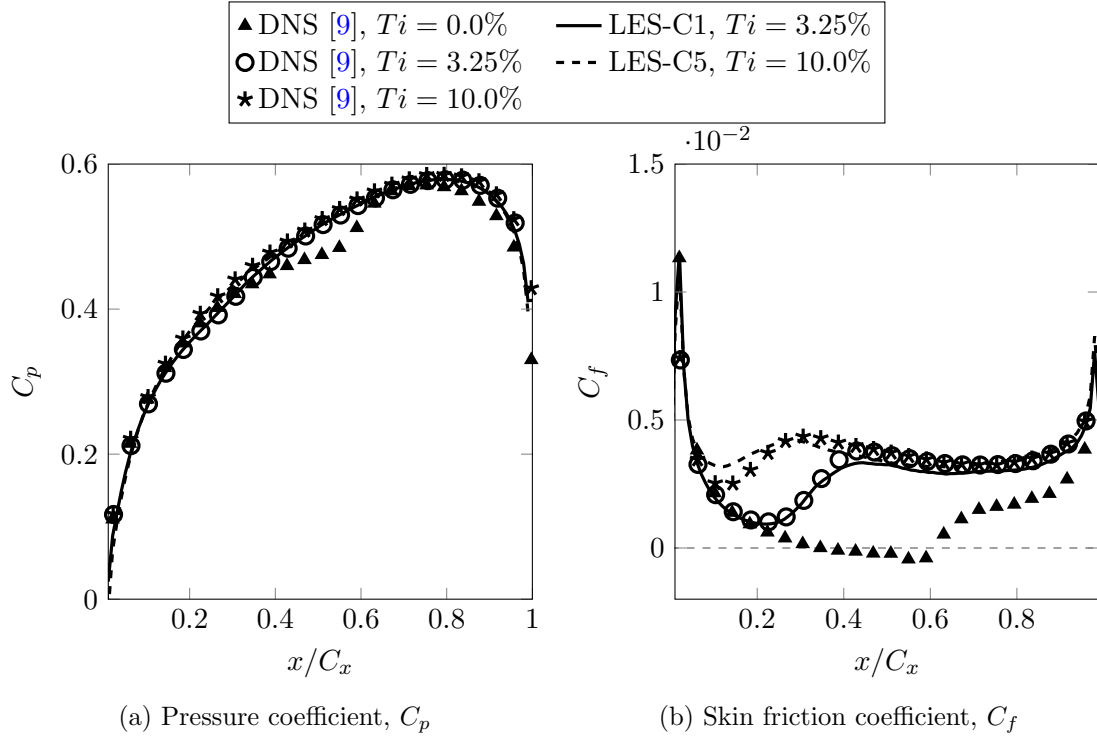


FIGURE 5.5: Cases C1 and C5. Pressure and skin friction coefficients on the pressure surface, at various free-stream turbulence intensities.

5.2.1 Moderate free-stream turbulence intensity

In Figure 5.7 the pressure surface transition process under moderate FST (Case C1, $Ti = 3.25\%$) is visualised using iso-surfaces of Q-criterion. The locations of transition onset (X_s) and completion (X_e) are shown by the white lines. Following Zaki et al. [9], X_s is defined as the minimum C_f location in Figure 5.5b, while X_e is the point where C_f plateaus. Contours of the tangential velocity perturbations,

$$u'_t = u't_x + v't_y, \quad (5.7)$$

are also shown in Figure 5.7¹. These contours show that in the laminar region ($x < X_s$), the boundary layer is dominated by streaks of strong forward and backward tangential velocity. To determine whether these streaks are related to Görtler instabilities the Görtler number

$$G \equiv \left(\frac{\bar{u}_e \theta}{\nu} \right) \left(\frac{\theta}{R} \right)^{1/2} \quad (5.8)$$

is plotted in Figure 5.6b. Here, R is the local radius of curvature of the wall. Saric [154] found that the boundary layer on a concave surface becomes unstable at $G \sim 0.3$, but Görtler vortices are not detected until $G \sim 5 - 6$. Figure 5.6b shows that $G > 5$ for only a very small streamwise distance before transition, and thus Görtler vortices are not

¹(t_x, t_y) is the two-dimensional stream-wise unit tangent

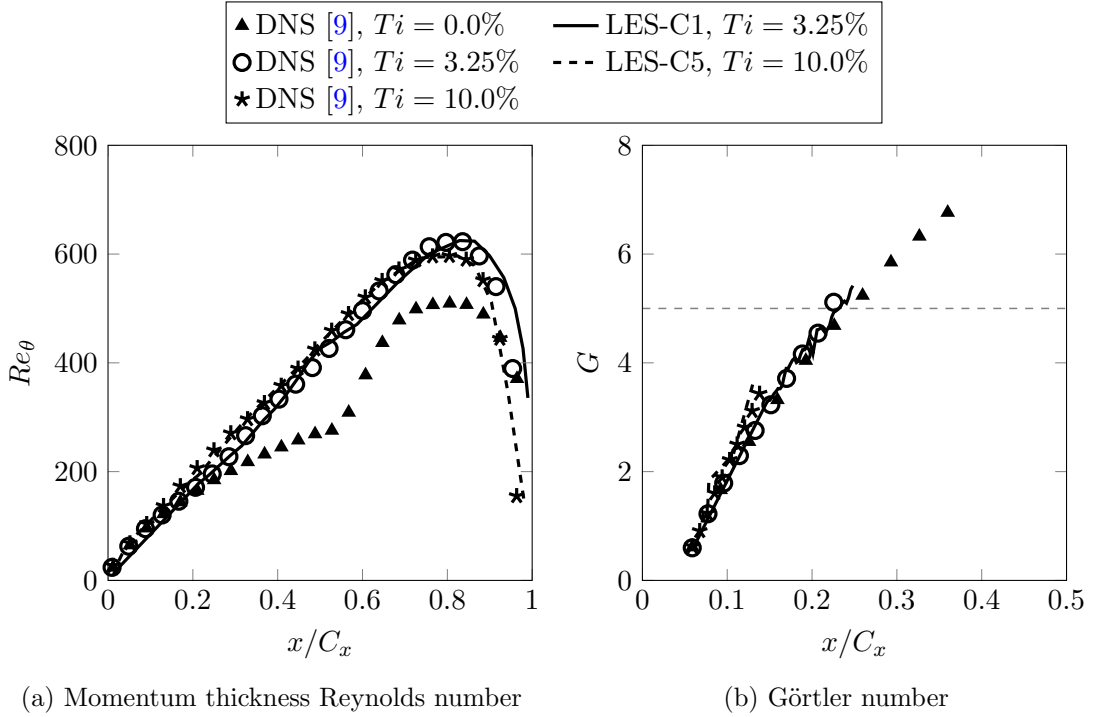


FIGURE 5.6: Cases C1 and C5. Momentum thickness Reynolds number Re_θ and Görtler number G (upstream of transition/separation) on the pressure surface, at various free-stream turbulence intensities.

likely to occur. Zaki et al. [9] also failed to detect Görtler vortices, and instead showed that these streaks are Klebanoff distortions forced by the low-frequency component of the FST.

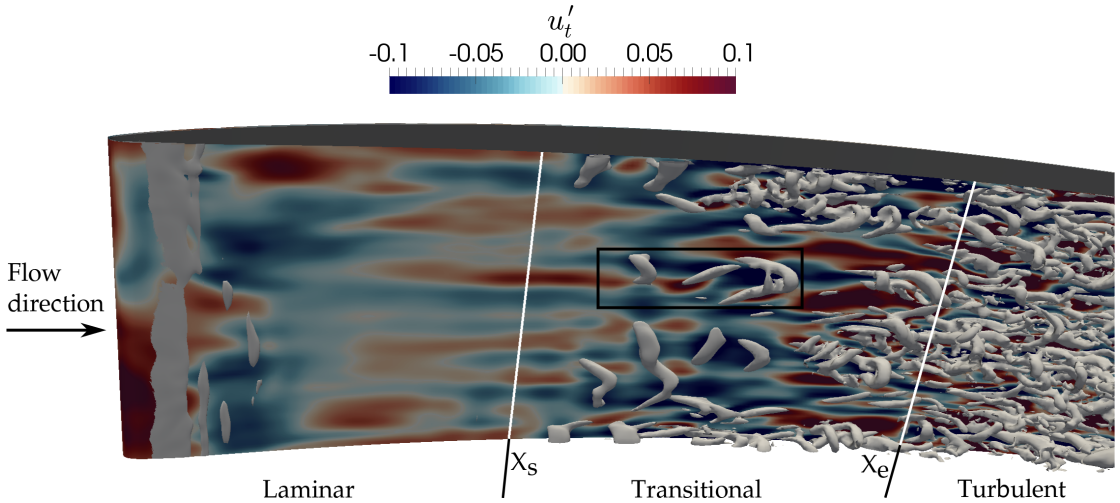


FIGURE 5.7: Case C1. Contours of the tangential velocity perturbations, u'_t , on a plane inside the pressure surface boundary layer $d = 1.64 \times 10^{-3}$ from the wall. An iso-surface of $Q = 200U_0/C_x$ is superimposed.

As discussed in Section 2.1.1.2, the natural transition of boundary layers via Tollmien-Schlichting (TS) waves is often bypassed when $Ti > 1\%$ [12]. However, Zaki et al. [9]

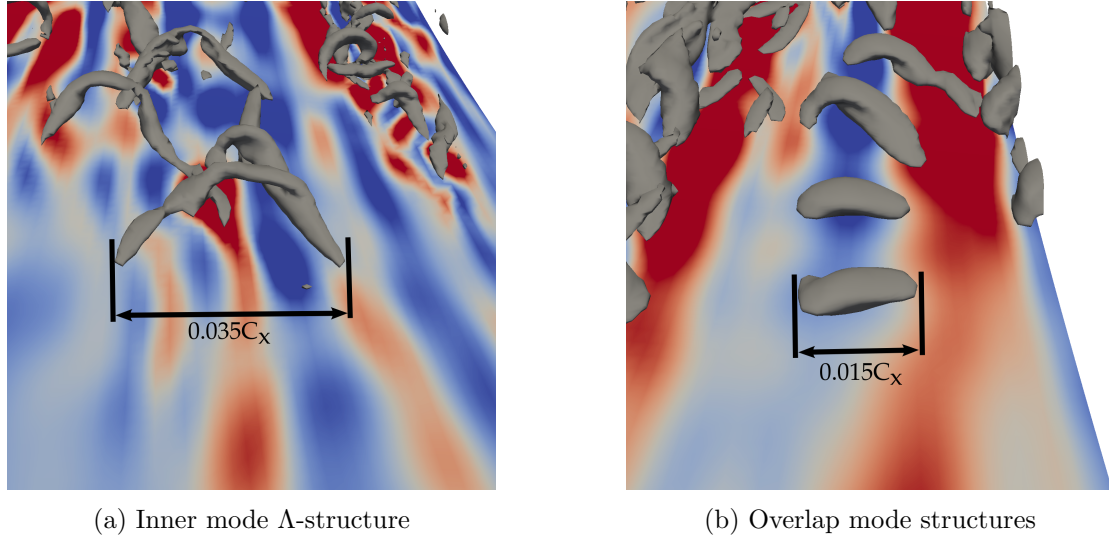


FIGURE 5.8: Case C1. Close-up of the two types of vortical structures that occur on the pressure surface, visualised using iso-surfaces of $Q = 200U_0/C_x$. Contours of $-0.1 < u'_t < 0.1$ are also shown.

found that at $Ti = 3.25\%$, the instability modes observed on the pressure surface do not resemble the traditional bypass mechanism. Instead, two distinct near-wall modes were found. These modes were also observed in the present LES case, and are visualised in Figure 5.8. Although these modes are not streak instabilities, they are influenced by the Klebanoff streaks. In both modes, vortical structures develop in (or slightly upstream of) the transitional region ($X_s < x < X_e$), and then breakdown to turbulence. The origin of these modes in the LES is investigated further in the following two sections.

5.2.1.1 Inner mode

The so-called *inner mode* structure shown in Figure 5.8a is also highlighted by the black box in Figure 5.7. These strong vortices are referred to as Λ -vortices due to their shape. Their presence hints at a natural transition mechanism. However, as noted by Zaki et al. [9], they can not be independent of the streaks as they would then be observed homogeneously across the blade span. The structures spanwise size is not directly related to the streaks; in LES case C1 the average spanwise wavelength of the streaks is approximately $0.015C_x$, but the Λ structures' width ranges from $0.02C_x$ to $0.035C_x$.

To highlight the breakdown mechanism, contours of the wall-normal velocity perturbation field,

$$u'_n = -u't_y + v't_x, \quad (5.9)$$

are shown at three time-instances spanning $\Delta t = 0.2T^*$ in Figure 5.9. An instability appears at $t = t' - 0.1T^*$, is amplified downstream as the Λ -structure is convected, and begins to breakdown at $t = t' + 0.1T^*$. It then sustains the fully turbulent boundary layer downstream.

The Λ -structure is visible above the $d = 1.64 \times 10^{-3}$ plane in Figures 5.7 and 5.9, meaning it must be “lifted” away from the wall. However, the structures originate very close to the wall. Figure 5.10 shows the u'_t field on an xy-plane bisecting the Λ -structure, at $t = t' - 0.15T^*$. The disturbance (highlighted by the black dashed box) is initiated below the forward-velocity streak, hence the name “inner” mode. Identical behaviour is observed in the DNS of Zaki et al. [9], where it is noted that this near-wall peak is consistent with the classical TS wave instability.

5.2.1.2 Overlap mode

The second transition mode observed is the overlap mode, shown in Figure 5.8b. This mode is also an inner instability, with its origin being linked to the TS waves. However, it is characterised by a significantly shorter spanwise wavelength than the inner mode. Here, the instability has the same width as the host streak. In Figure 5.11 the u'_n field is again used to track the instability. At $t = t''$ the instability is seen to originate slightly upstream of X_s . By $t = t'' + 0.1T^*$ the instability has been amplified significantly, and it is beginning to breakdown at $t = t'' + 0.2T^*$.

In Figure 5.12 the same time instance as in Figure 5.11b is shown but with u'_t contours instead. The instability appears to be located where a high speed streak meets a low speed streak. This is confirmed in the side view shown in Figure 5.13 (x_t is the tangential/streamwise distance from the leading edge). As Zaki et al. [9] found; “The instability is located near the upstream edge of the long, low-speed perturbation region, where it overlaps with the downstream edge of the high-speed region”.

5.2.2 High free-stream turbulence intensity

At a free-stream turbulence intensity of 3.25%, the pressure surface transition has been shown to be caused by two different modes. Both modes originate in the convection of TS waves by Klebanoff streaks. When Ti is increased to 10%, Zaki et al. [9] observed that the transition mode changed to the classical bypass mode characterised by Jacobs et al. [12]. This occurs early, with the onset of transition (X_s) moving from $X_s = 0.22C_x$ for $Ti = 3.25\%$ to $X_s = 0.13C_x$ for $Ti = 10\%$.

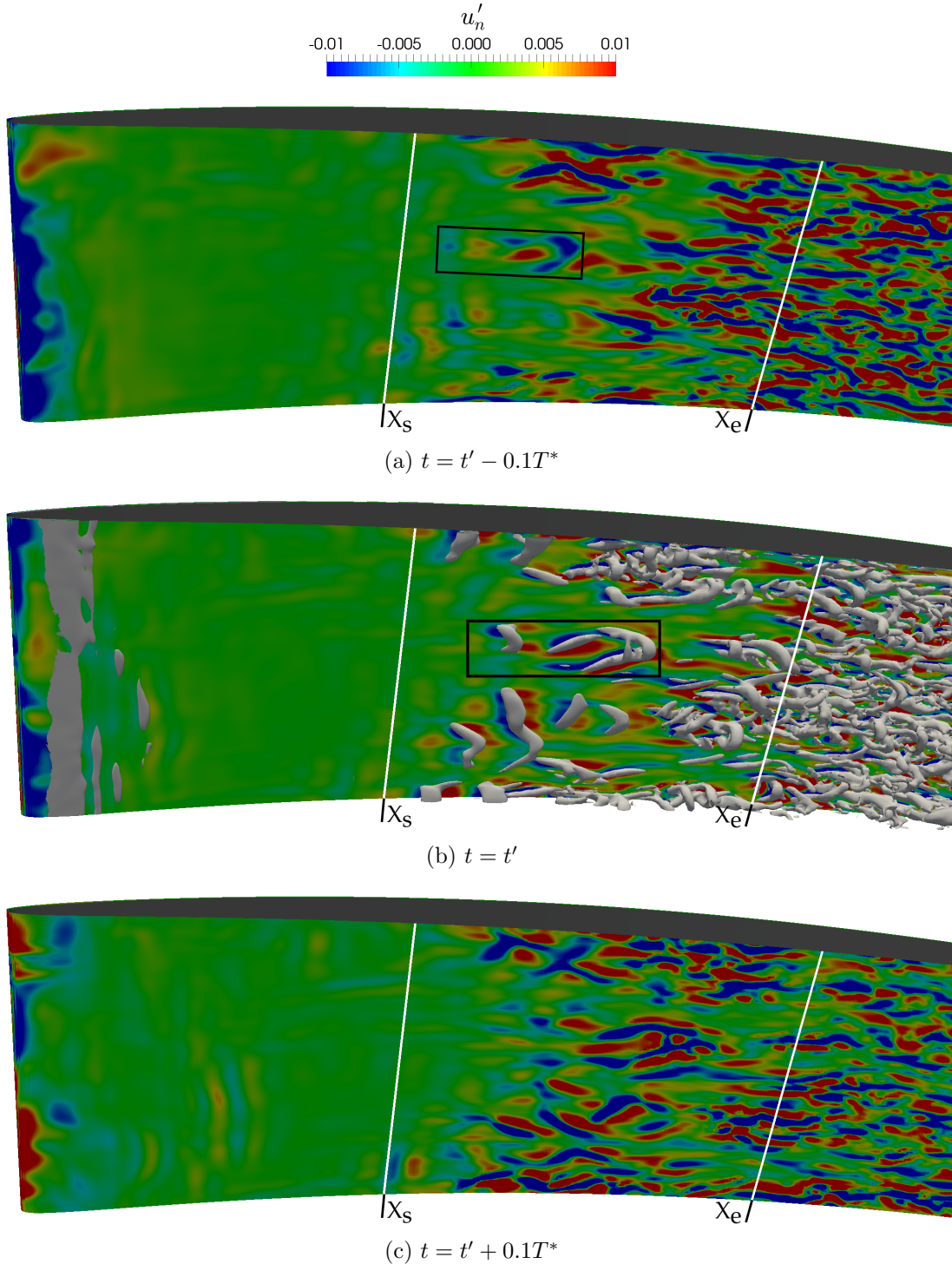


FIGURE 5.9: Case C1. Contours of the normal velocity perturbations, u'_n , on the $d = 1.64 \times 10^{-3}$ plane. Three time instances are shown, where $t = t'$ is the time in Figure 5.7. An iso-surface of $Q = 200U_0/C_x$ is superimposed in the second time instance.

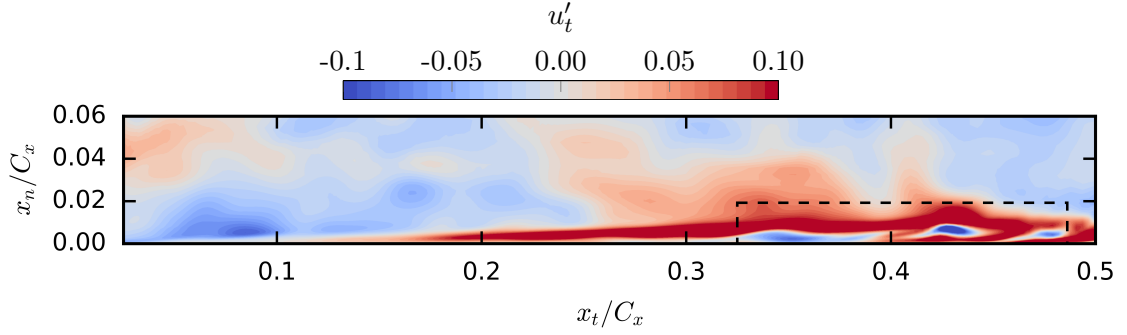


FIGURE 5.10: Contours of the tangential velocity perturbation, u'_t , on an xy -plane bisecting the Λ -structure seen in Figure 5.9. The snapshot corresponds to $t = t' - 0.15T^*$.

Figure 5.5b shows that the LES captures the earlier X_s in the $Ti = 10\%$ case (C5) quite well, but X_s is predicted to occur slightly too early ($X_s = 0.12C_x$). This is primarily due to the reduced FST decay rate in case C5, which means that the turbulence intensity at the leading edge ($x = 0$) is higher in the LES compared to the DNS (see fig. 5.2). The LES prediction could be improved by reducing the inflow turbulent length scale to $L = 0.03C_x$ (like case C1), but this isn't done as case C5 is already sufficient to examine how the LES captures the effect of increasing Ti . The bypass transition mechanisms in the LES case C5 are explored further when the suction surface is examined in Section 5.3.2.

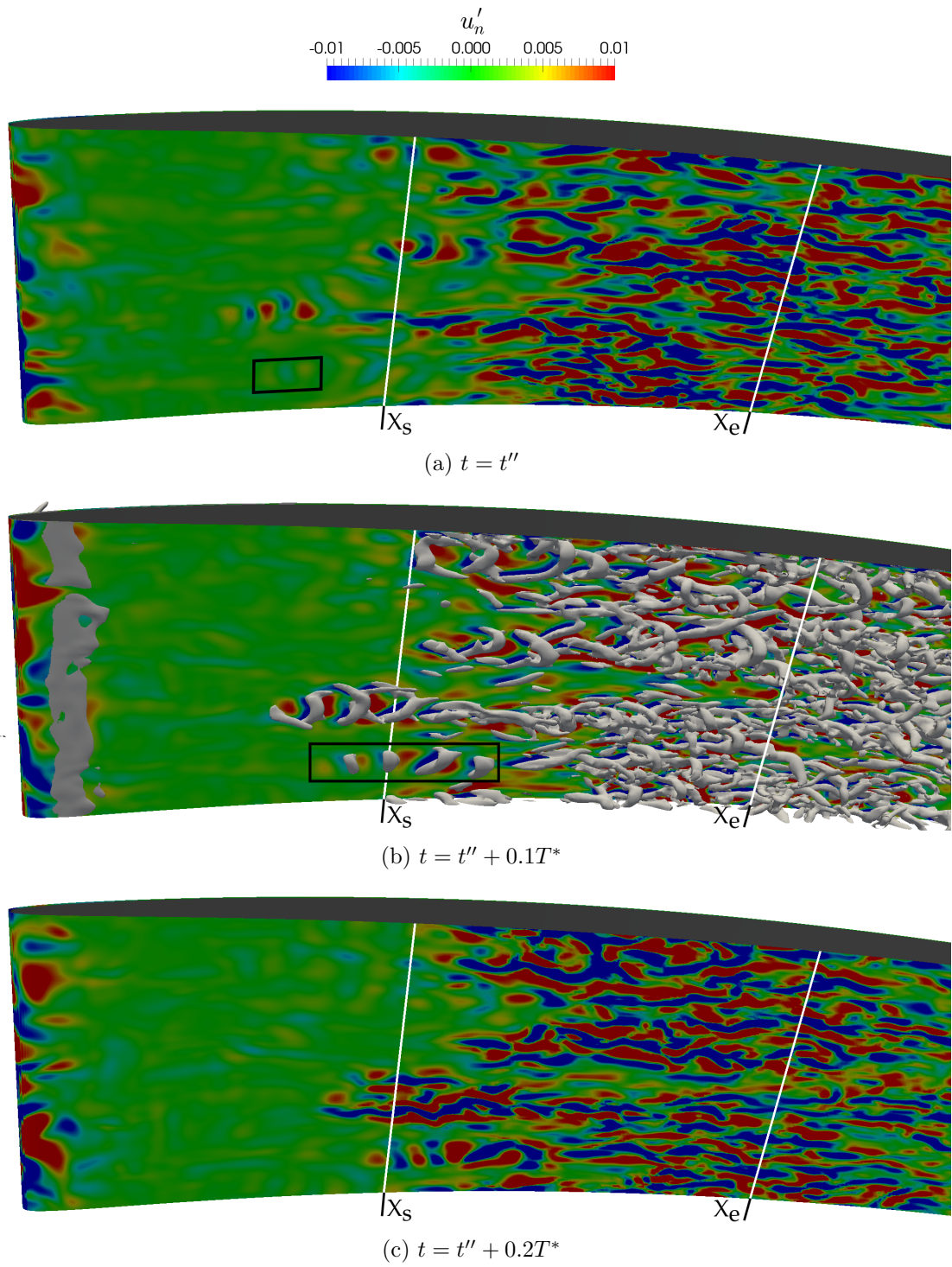


FIGURE 5.11: Case C1. Contours of the normal velocity perturbations, u'_n , on the $d = 1.64 \times 10^{-3}$ plane. Three time instances are shown, where $t = t''$ is a different time to t' . An iso-surface of $Q = 200U_0/C_x$ is superimposed in the second time instance.

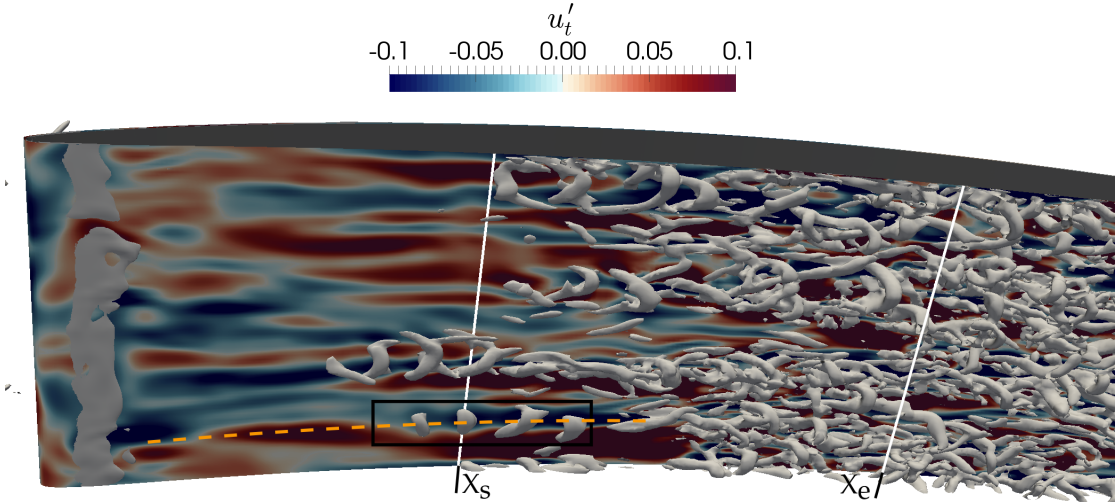


FIGURE 5.12: Case C1. Contours of the tangential velocity perturbations, u'_t , on the $d = 1.64 \times 10^{-3}$ plane at time $t = t'' + 0.1T^*$. An iso-surface of $Q = 200U_0/C_x$ is superimposed.

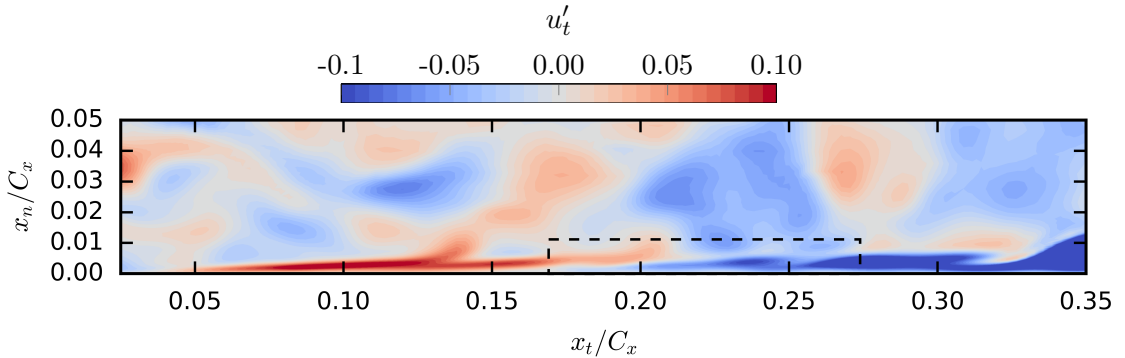


FIGURE 5.13: Case C1. Contours of the tangential velocity perturbations, u'_t , on the plane marked by the orange dashed line in Figure 5.12. The snapshot corresponds to $t = t''$.

5.3 Suction surface transition mechanisms

In this section the suction surface transition mechanisms seen in LES cases C1 and C5 are explored. The suction surface C_p and C_f distributions are plotted in Figure 5.14. Unlike on the pressure surface, the flow on the suction surface separates for both the $Ti = 0\%$ and $Ti = 3.25\%$ cases. Only at $Ti = 10\%$ does the boundary layer transition prevent flow separation.

Generally, like for the pressure surface, the overall effect of Ti on the suction surface transition is well captured by the LES. In Sections 5.3.1 and 5.3.2 the suction surface transition mechanisms are examined in more detail, and differences between the suction and pressure surface mechanisms are explained.

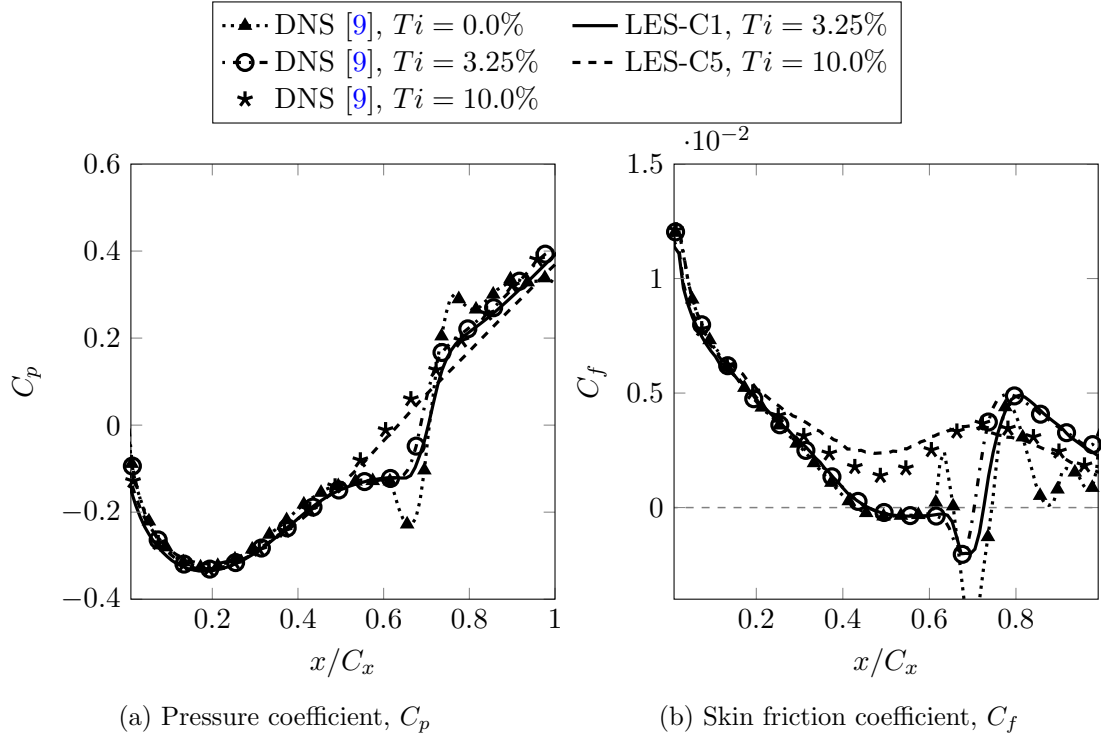


FIGURE 5.14: Cases C1 and C5. Pressure and skin friction coefficients on the suction surface, at various free-stream turbulence intensities.

5.3.1 Moderate free-stream turbulence intensity

In Figure 5.15 the suction surface in LES case C1 ($Ti = 3.25$) is displayed. Similarly to the pressure surface, a streaky laminar region is visible. The laminar boundary layer undergoes separation in the adverse pressure gradient region close to the time-averaged separation location x_s^1 , and Kelvin-Helmholtz (K-H) rolls develop. Transition has still not occurred at $x_s = 0.46$, which is significantly downstream from the pressure surface transition location ($X_s = 0.22$). This is explained by the fact that Klebanoff streaks, a precursor for transition here, are found to amplify faster in the presence of an adverse pressure gradient [155].

In the laminar DNS case of Zaki et al. [9], the K-H rolls remain laminar and convect downstream, maintaining a separation region in their shadow. However, in the $Ti = 3.25\%$ DNS case, the K-H rolls are quickly destabilized by the free-stream turbulence. The rolls break down and are followed by turbulent reattachment of the boundary layer. This process is well captured by the LES; with an attached turbulent boundary layer visible after x_r in Figure 5.15, and the LES C_f agreeing well with the DNS at $x \geq 0.72$ in Figure 5.14b.

¹The time-averaged separation (x_s) and reattachment (x_r) locations are defined as the points where the time-averaged C_f (Fig. 5.14b) crosses the $C_f = 0$ axis.

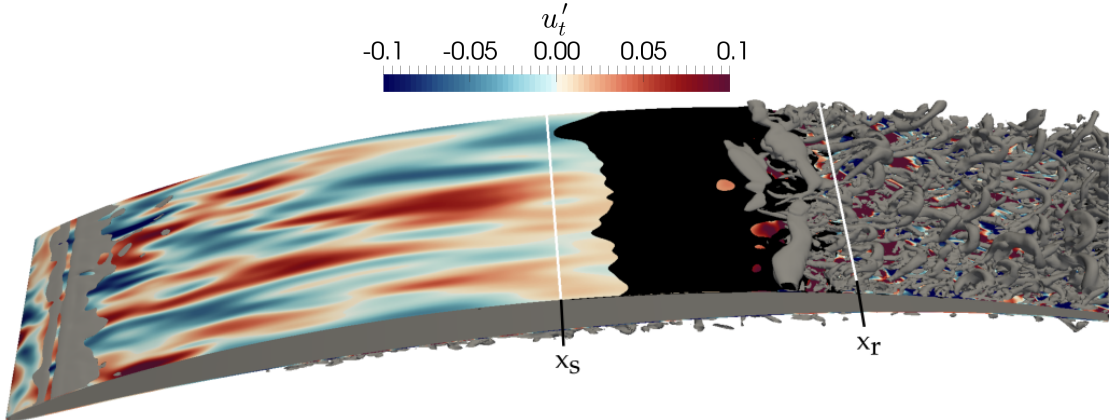


FIGURE 5.15: Case C1. Contours of the tangential velocity perturbations, u'_t , on a plane inside the suction surface boundary layer $d = 1.64 \times 10^{-3}$ from the wall. Iso-surfaces of $Q = 300U_0/C_x$ (grey) and $u_t < 0$ (black) are superimposed.

The time averaged C_f profile in Figure 5.14b suggests that a free-stream Ti of 3.25% has little influence on the separation location. However, the instantaneous separation region shown by the black iso-surface in Figure 5.15 shows that the separation location varies in time. Zaki et al. [9] found that this was due to the Klebanoff streaks; separation is shifted upstream where elongated u'_t contours are negative, and downstream where they are positive. This effect is well captured by the LES, with the resulting K-H rolls seen to be more three-dimensional than in the laminar DNS case of Zaki et al. [9].

5.3.2 High free-stream turbulence intensity

Figure 5.16 shows the suction surface in LES case C5. At this higher free stream Ti (10%), the same streaky laminar boundary layer is seen, but no laminar separation occurs. The C_f distribution in Figure 5.14b suggests the boundary layer is transitioning earlier; there is little change in C_f in the favourable pressure gradient region, but C_f increases over the $Ti = 3.25\%$ case in the adverse pressure region. This higher C_f prevents the boundary layer from separating.

The origin of this transition mechanism becomes clearer when the contours of u'_n in Figure 5.17 are studied. At time $t = t'''$ a small disturbance appears (highlighted by the black box). At $t = t''' + 0.2T^*$, this small disturbance grows into a turbulent spot, which is convected downstream. At $t = t''' + 0.4T^*$, the turbulent spot reaches the average start of the transition region X_s , where it begins to breakdown to form a fully turbulent boundary layer.

The transition mode occurring here is the classical bypass mechanism, also seen on the pressure surface at $Ti = 10\%$ (Section 5.2.2). To understand the mechanics of this mode,

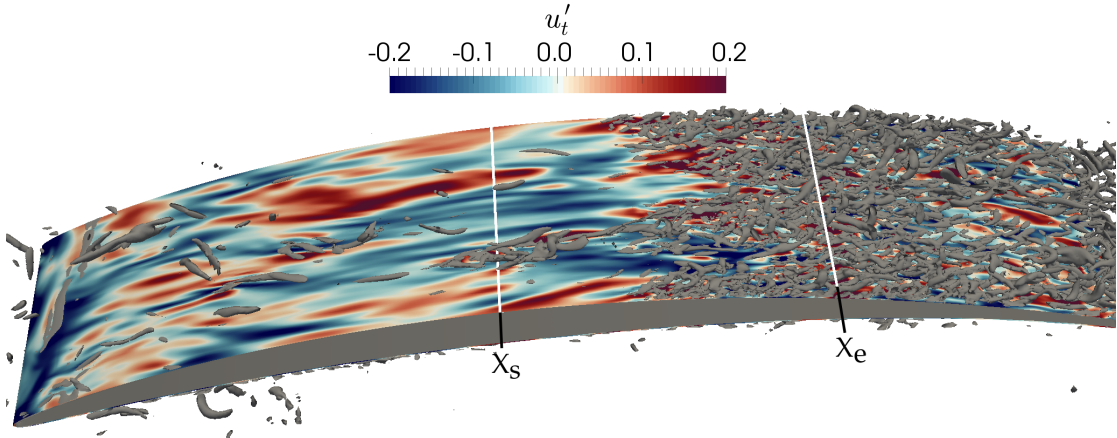


FIGURE 5.16: Case C5. Contours of the tangential velocity perturbations, u'_t , on a plane inside the suction surface boundary layer $d = 1.64 \times 10^{-3}$ from the wall. An iso-surface of $Q = 500U_0/C_x$ is superimposed.

a plane bisecting the disturbance in Figure 5.17a is shown in Figure 5.18. A perturbation with the appearance of a backward facing jet is seen near the wall. This is a Klebanoff streak, which lifts towards the top of the boundary layer, where it is exposed to the free-stream turbulence. The interaction here is unstable and initiates a breakdown to turbulence [12]. This process is in good agreement with the mechanism observed by Zaki et al. [9] at higher free-stream Ti's.

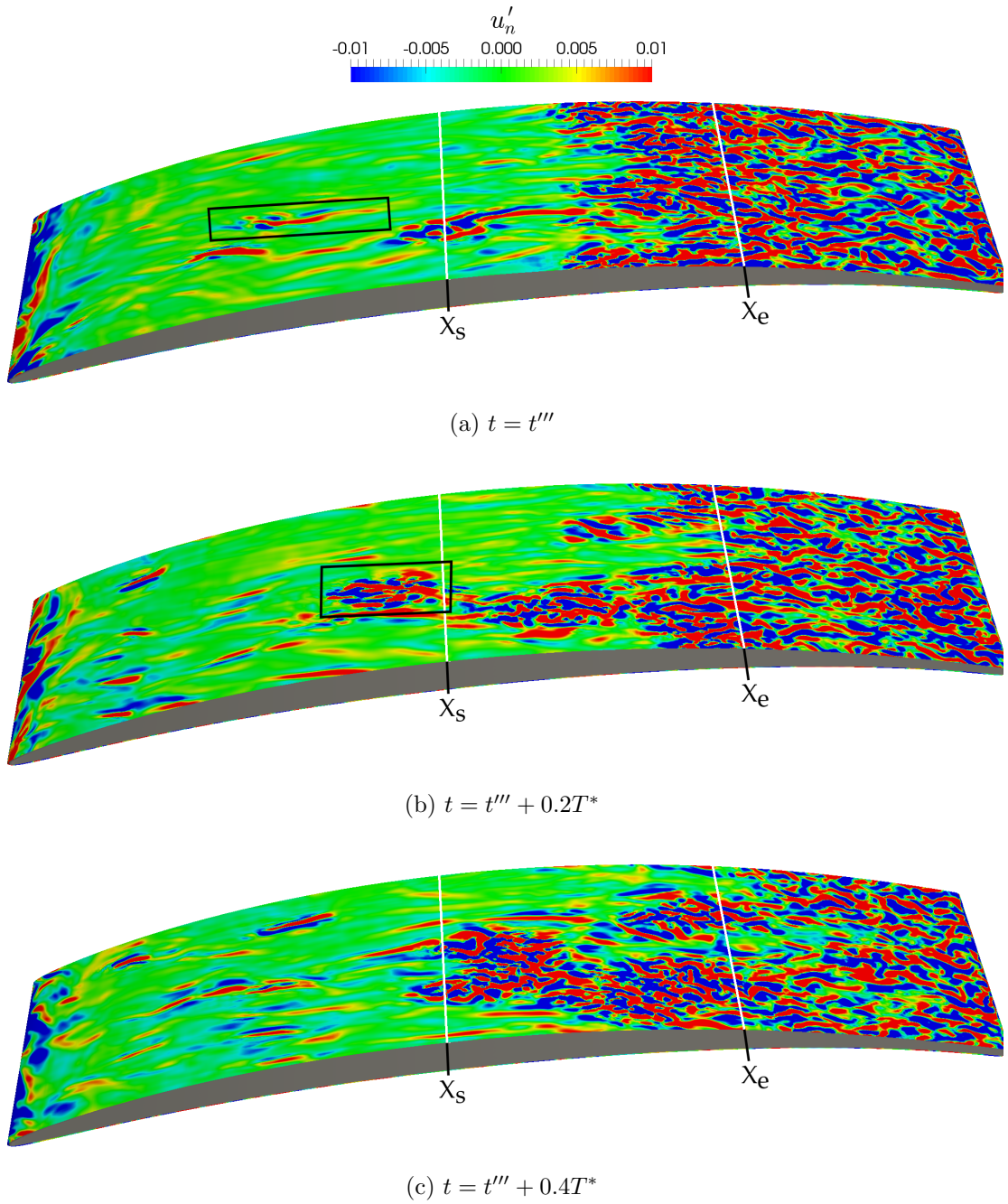


FIGURE 5.17: Case C5. Contours of the normal velocity perturbations, u'_n , on the $d = 1.64 \times 10^{-3}$ plane. Three time instances are shown, where $t = t'''$ is the time in Figure 5.16.

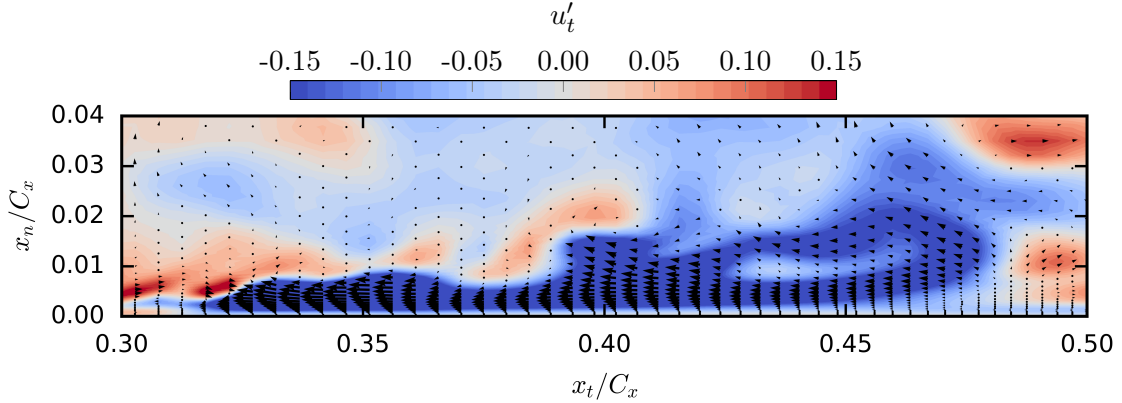


FIGURE 5.18: Case C5. Contours of the tangential velocity perturbations, u'_t , on an xy -plane bisecting the turbulent spot highlighted in Figure 5.17. Vectors of $[u'_t, u'_n]$ at every second grid point are superimposed. The snapshot corresponds to $t = t'''$.

5.4 An assessment of sensitivities

In the previous two sections, it has been shown that the σ SGS model and LASW scheme provide a LES framework that gives a good prediction of a transitional compressor flow. Now that the transition mechanisms captured by the LES are better understood, it is important to further investigate the sensitivities of these mechanisms.

5.4.1 Specification of inflow turbulence

It is common for the intensity of the incoming turbulence to be known, but not the length scales or energy spectra of the turbulence. This is the case in the compressor cascade experiments of Hilgenfeld et al. [152] and Gbadebo [35] investigated in this thesis. To demonstrate the significance of this, the C_f distributions of cases C1 and C2 are compared in Figure 5.19.

Figure 5.19a shows that the inflow turbulent integral length scale L has little effect on suction surface mean flow. However, it is seen to noticeably influence the pressure surface transition in Figure 5.19b. To investigate this further, the maximum velocity fluctuations within the boundary layer are plotted in Figure 5.20a. The maximum fluctuations are found by searching in the wall-normal direction at each x location:

$$(u'_i)_{max}(x) = \max_{\substack{x_n=\delta_\omega \\ x_n=0}} \left(\sqrt{u'_i u'_i} (x, x_n) \right) \quad (5.10)$$

It was shown that a larger L results in a slower FST decay rate (recall Fig. 5.2). So, it is not surprising that the maximum u'_t in Figure 5.20a begins at a higher value in the $L = 0.06C_x$ case. However, the downstream amplification of u'_t is slower for the larger

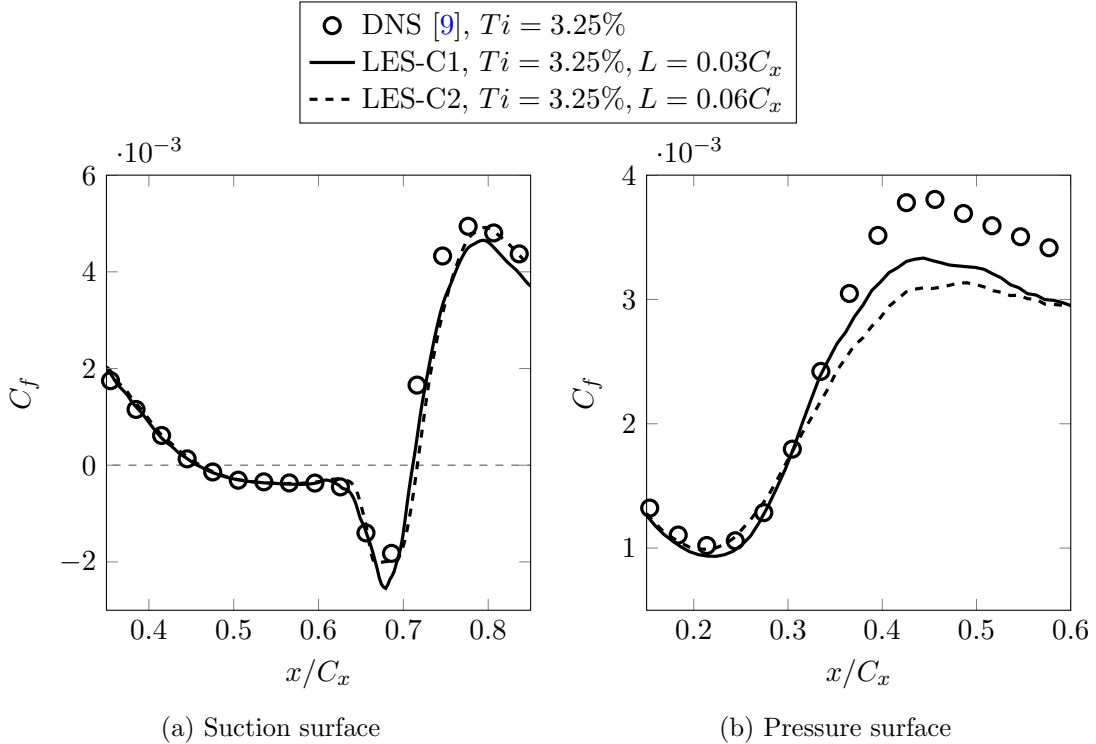


FIGURE 5.19: Cases C1 and C2. Sensitivity of the suction and pressure surface skin friction coefficient to the incoming turbulent length scale.

length scale case, which may explain the more gradual rise in the pressure surface C_f for case C2 compared to C1. A similar observation can be made on the suction surface in Figure 5.20b. Despite the higher initial maximum value of w' in the $L = 0.06C_x$ case, a higher maximum value of w' is reached in the $L = 0.03C_x$ case.

The work of Ovchinnikov et al. [156] demonstrates the importance of the FST length scales. Here, Klebanoff streaks were observed at two different FST length scales, but only at the smaller length scale did the streaks have a clear dynamical significance. The FST length scale was therefore found to have a significant influence onset of transition. The detailed physics of this is beyond the scope of the present work, but the comparison between cases C1 and C2 does highlight the need for detailed measurement of the inflow turbulence in experiments.

5.4.2 Sub-grid scale modelling

In this section, the influence of the SGS model is examined. In Figure 5.21 the C_f distributions for cases C2, C3 and C4 are plotted, along with the LES results of Lardeau et al. [86]. Lardeau et al. [86] use the Dynamic Smagorinsky (DSM) and the mixed-time-scale SGS models on the $Ti = 3.25\%$ case. The σ SGS model predictions are seen to compete well with the VMS and DSM predictions. Additionally, the WALE model

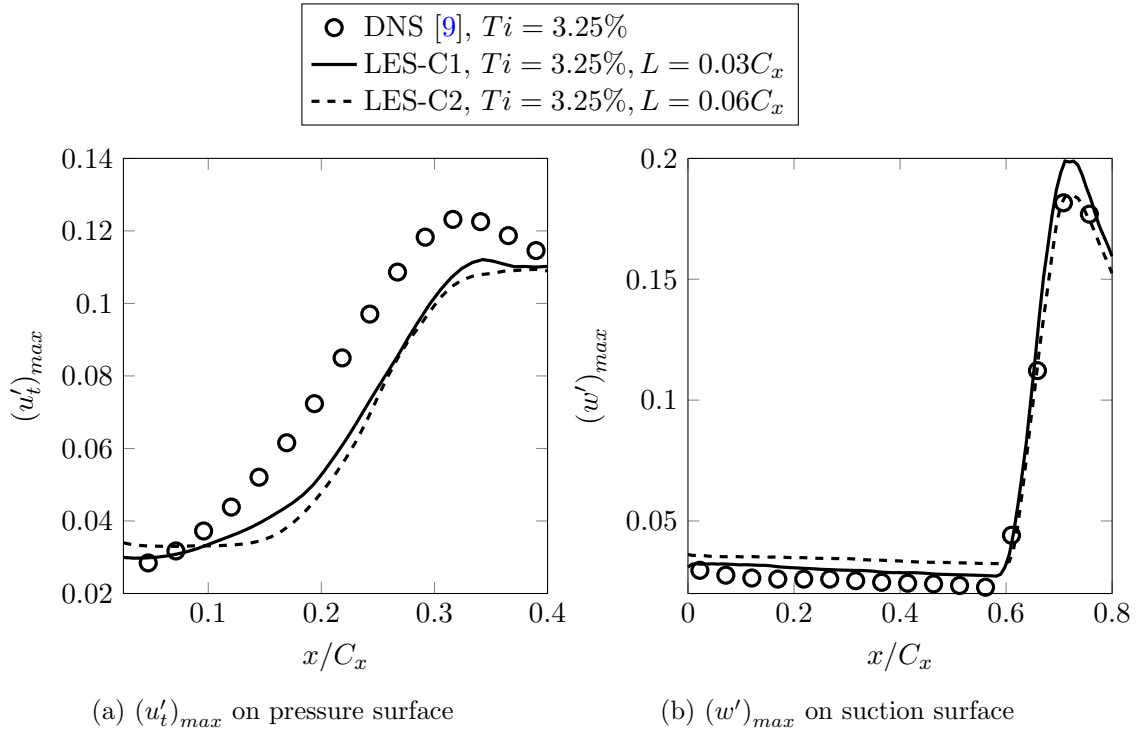


FIGURE 5.20: Cases C1 and C2. Maximum of tangential and spanwise velocity fluctuations in the pressure and suction surface boundary layers respectively.

results agree very closely with the σ model's, despite the models' significantly different formulations.

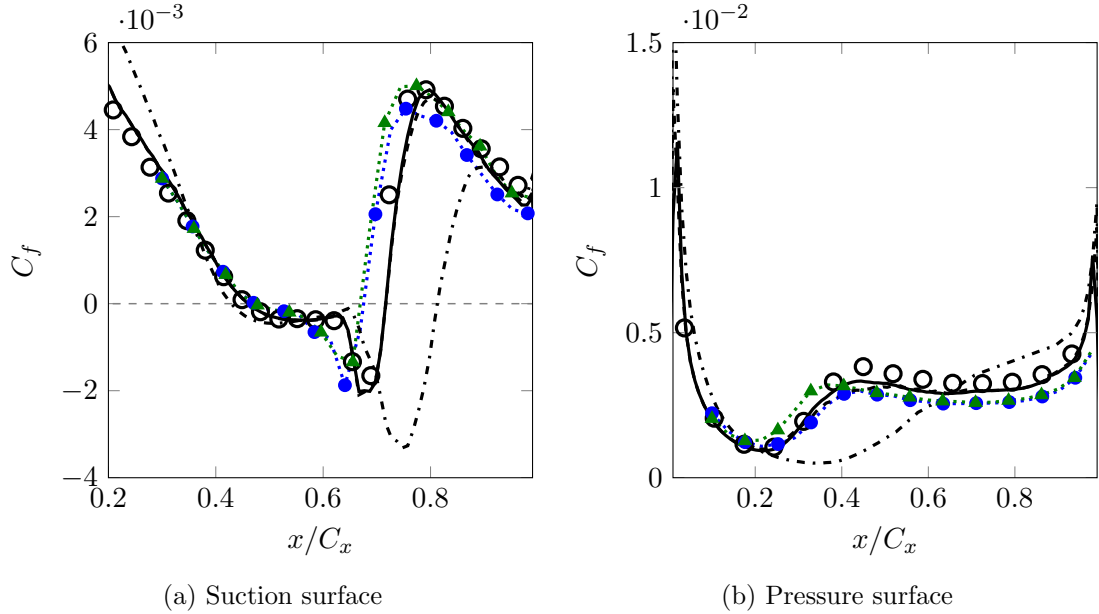


FIGURE 5.21: Cases C2 to C4. Sensitivity of the suction and pressure surface skin friction coefficient to the SGS model.

On the other hand, the Smagorinsky-Lilly (SM) model performs poorly on both surfaces. In Figure 5.22, the modelled turbulent kinetic energy $k_{SGS} = \frac{1}{2}\overline{u'_i u'_i}_{SGS}$ returned by the

σ and SM models is shown. The modelled Reynolds stresses are obtained from the Boussinesq approximation in Equation 2.15 ($\overline{u'_i u'_i}_{SGS} = -\tau_{ii}^r$). When comparing the two k_{SGS} fields, it is unsurprising to find that the mean flow-fields in cases C2 and C4 are different, as the behaviour of the two SGS models is very different.

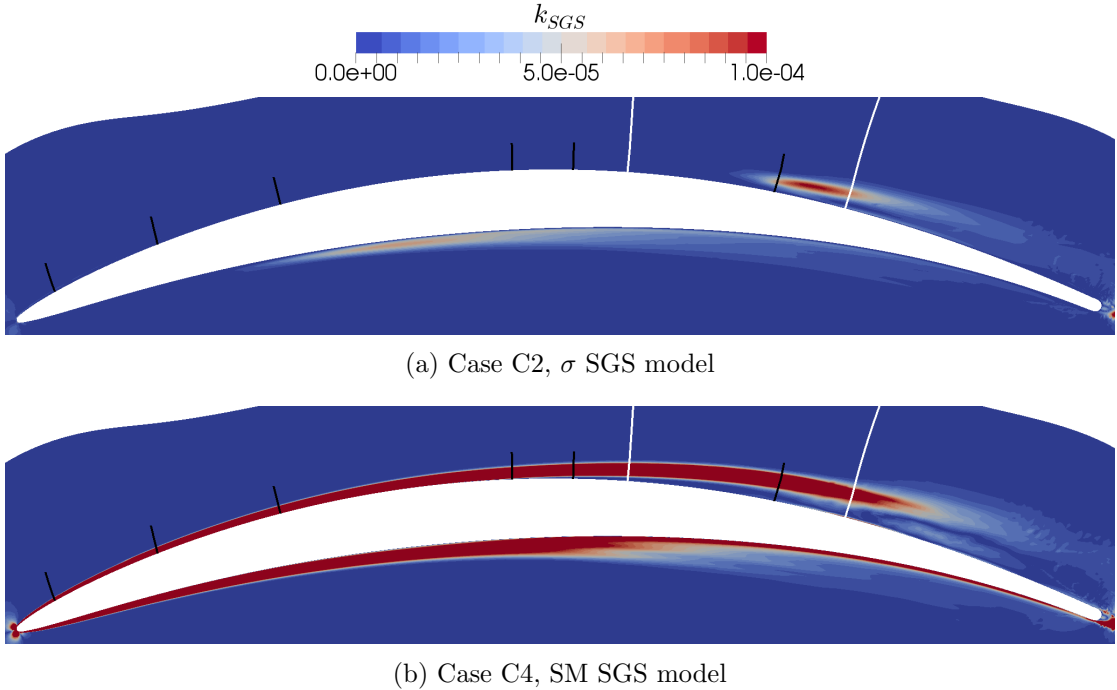


FIGURE 5.22: Cases C2 to C4. Contours of the time averaged modelled turbulent kinetic energy, k_{SGS} . The black and white lines are labelled in Figure 5.23.

The σ model returns a k_{SGS} field that appears to be similar qualitatively to the resolved turbulent stress $k_r = \frac{1}{2}\overline{u'_i u'_i}_r$ field in Figure 5.23. The energy is low in the laminar boundary layers upstream of transition, and it increases at the onset of transition on both surfaces. However, the SM model returns a high k_{SGS} in the laminar boundary layers. The effect this has on the transition mechanisms is explored in the following two sections.

5.4.2.1 Suction surface

Zaki et al. [9] discuss how the term $u'_n \partial \bar{u}_t / \partial x_n$ contributes to the production of turbulent shear stress $\overline{u'_t u'_n}$. Figure 5.24 shows that the high free-stream forcing in the $Ti = 10\%$ case (C5) leads to significantly increased $u'_n \partial \bar{u}_t / \partial x_n$ in the suction surface boundary layer. The resulting shear-stress production leads to more momentum transport inside the boundary layer. Consequently, by $x = 0.4C_x$, the mean velocity profile for the $Ti = 10\%$ case (C5) is noticeably different to the $Ti = 3.25$ case (C2), as shown in Figure 5.24c. The increased C_f means that the $Ti = 10\%$ boundary layer is more able to resist the adverse pressure gradient, and separates later.

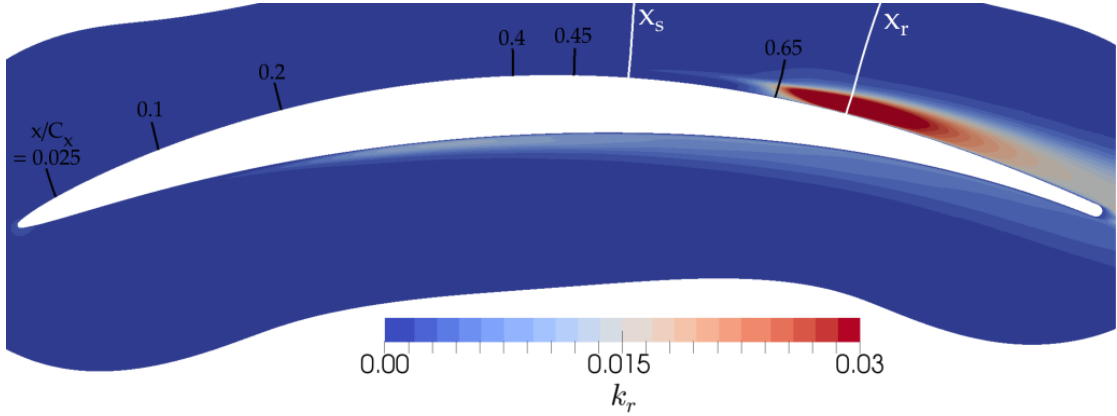


FIGURE 5.23: Case C2. Contours of the time averaged resolved turbulent kinetic energy, k_r . The average separation and reattachment locations are marked by x_s and x_r .

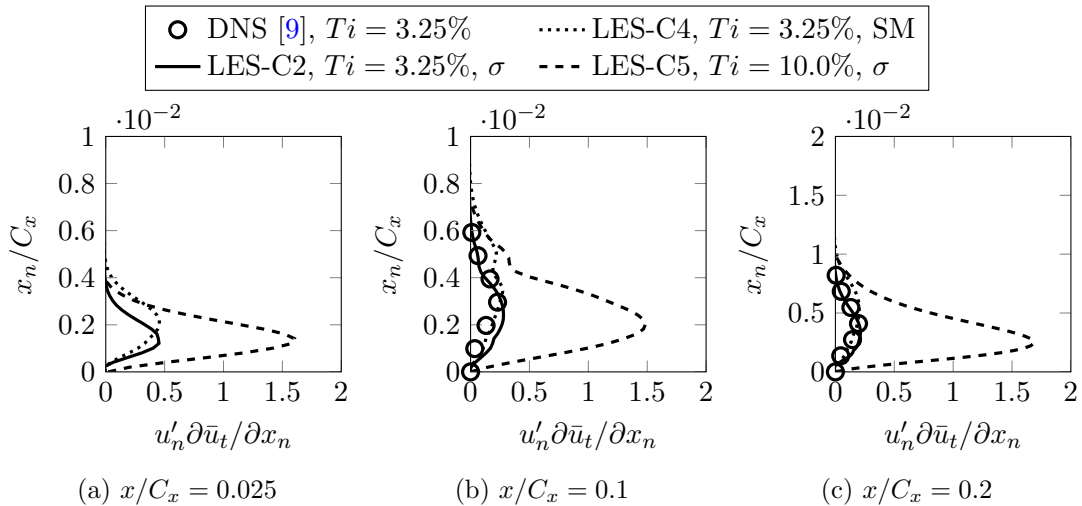


FIGURE 5.24: Profiles of $u'_n \partial \bar{u}_t / \partial x_n$ on the suction surface upstream of transition/separation.

Despite Ti being equal in cases C2 and C4, Figure 5.21a shows that the boundary layer separates earlier in case C4. At $x = 0.4C_x$, upstream of case C4's separation point at $x = 0.429$, the tangential velocity profile (Fig. 5.25c) is in significant disagreement with case C2 and the DNS. The C_f is lower here, and premature separation soon follows. The boundary layer in case C4 was already thicker prior to separation, and it separated earlier in an adverse pressure gradient region. Therefore, the separation bubble in case C4 is much thicker, as shown in Figure 5.26a. The shear layer δ_s is also thicker, which leads to a smaller $u'_n \partial \bar{u}_t / \partial x_n$ term, as shown in Figure 5.26b. The reduced production of turbulent shear in the bubble contributes to slower reattachment, leading to the significant disagreement in C_f predictions between case C4 and C2.

One possibility for the significantly different suction surface boundary layer in case C4 is that the high μ_{sgs} returned by the SM model is damping turbulent fluctuations.

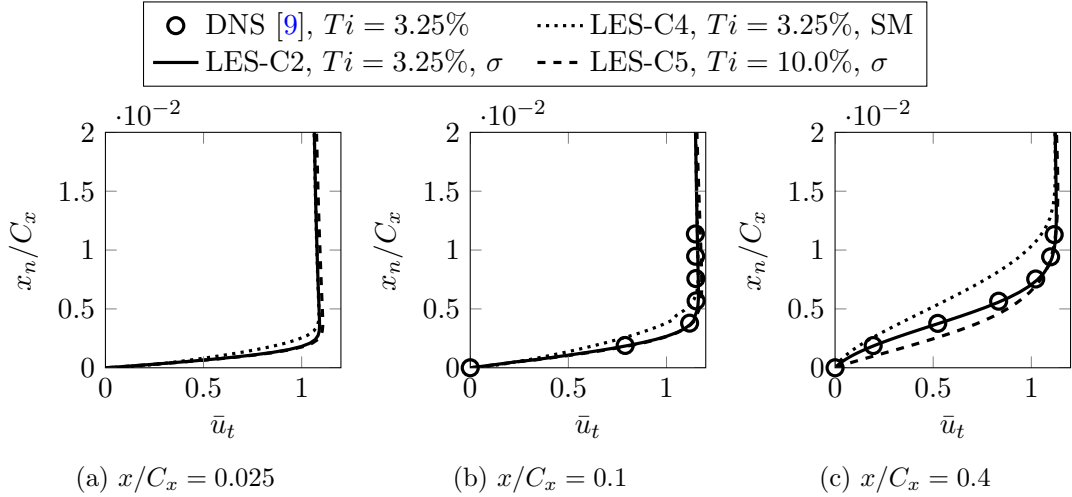


FIGURE 5.25: Profiles of the mean tangential velocity \bar{u}_t on the suction surface upstream of transition/separation.

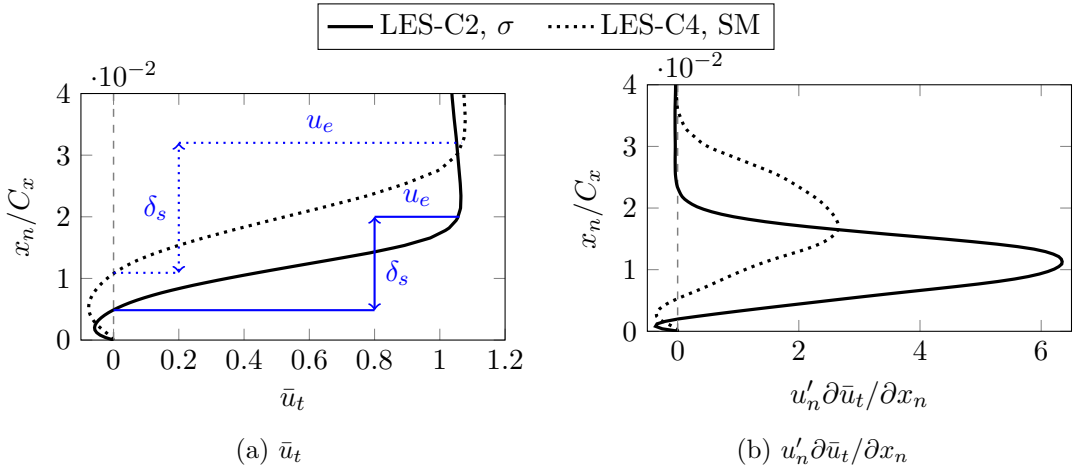
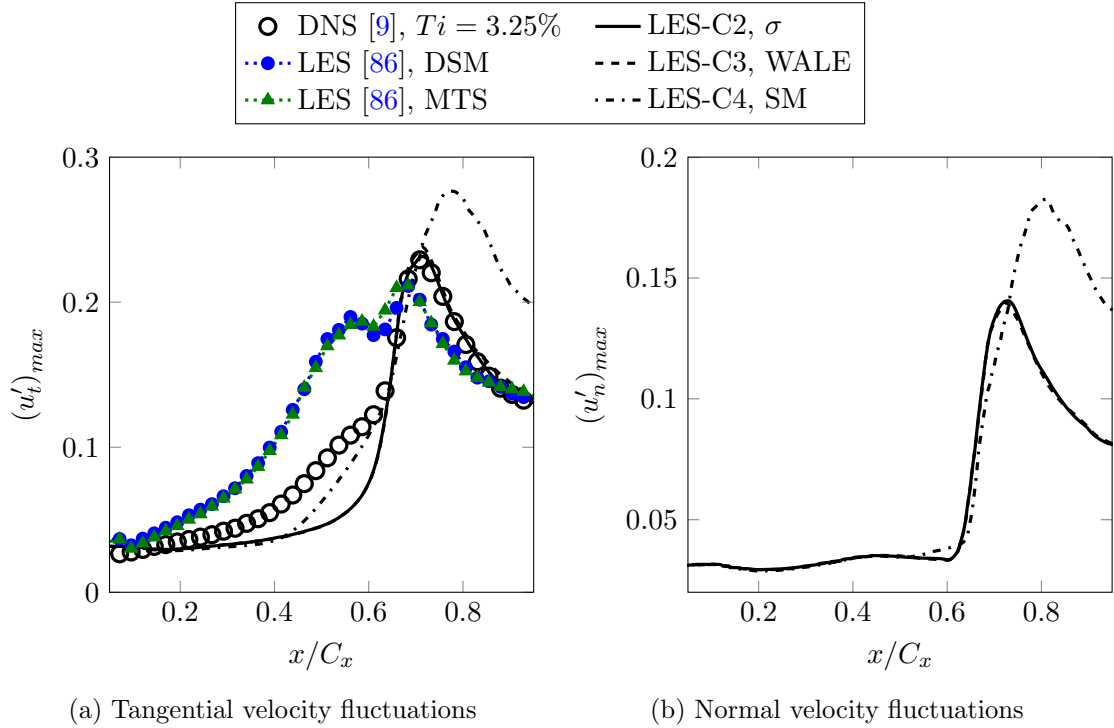


FIGURE 5.26: Profiles of \bar{u}_t and $u'_n \partial \bar{u}_t / \partial x_n$ within the separation bubble at $x/C_x = 0.65$.

However, Figures 5.24 and 5.27 show this isn't the case, with the velocity fluctuations upstream of transition quite similar in cases C4 and C2¹. A more significant difference is seen when the tangential ($\overline{u'_t u'_t}$) and shear ($\overline{u'_t u'_n}$) stress profiles are separated into resolved and modelled contributions, in Figure 5.28. In the separation bubble at $x = 0.65C_x$ most of the turbulent stress comes from the resolved stress (filled area in Figs. 5.28c and 5.28f). However, in the laminar boundary at $x = 0.025C_x$ (Figs. 5.28a and 5.28d) the large value of μ_{sgs} returned by the SM model leads to a very large $\overline{u'_t u'_n}_{SGS}$. This additional shear stress would be expected to cause additional momentum transfer in the boundary layer. A large $\overline{u'_t u'_n}_{SGS}$ is not seen in the σ model case

¹The increasing dominance of u'_t over u'_n is an indicator of the Klebanoff disturbances [9]. These disturbances are amplified at noticeably different rates in the present results, those of Lardeau et al. [86] and those of Zaki et al. [9]. Zaki et al. [9] note how this process is very sensitive to the exact make-up of the FST as well as the history of the pressure gradient.

(C2), and it seems plausible that it is this term causing the large discrepancy in the suction surface predictions of cases C2 and C4.



(a) Tangential velocity fluctuations

(b) Normal velocity fluctuations

FIGURE 5.27: Cases C2 to C4. Maximum value of the tangential and normal velocity fluctuations in the suction surface boundary layer.

The time averaged SGS model viscosity $\bar{\mu}_{sgs}$ in the laminar boundary layer is plotted for cases C2 and C4 in Figure 5.29a. The SM model's $\bar{\mu}_{sgs}$ (black dotted line) is also broken down into the standard part based on the cell volume (red dashed line),

$$\mu_\Delta = \rho(C_s \Delta_{vol})^2 \sqrt{2S_{ij}S_{ij}} \quad (5.11)$$

and the near-wall wall limiting part (blue dash-dot line),

$$\mu_{ml} = \rho(\kappa x_n)^2 \sqrt{2S_{ij}S_{ij}}. \quad (5.12)$$

The near-wall limiting term used by the SM model (see Section 2.3.2) is intended for use in turbulent boundary layers [64], and from Figure 5.29a it is obvious that it doesn't adequately limit $\bar{\mu}_{sgs}$ in the laminar boundary layer. Figure 5.29b shows that the laminar boundary layer is a pure shear region, where one velocity gradient ($\partial u_t / \partial x_n$) dominates. This suggests the σ model is operating as Nicoud et al. [68] intended; returning a low value of $\bar{\mu}_{sgs}$ in pure shear regions.

In Equations 5.11 and 5.12 $\bar{\mu}_{sgs}$ is calculated based on the time averaged product of

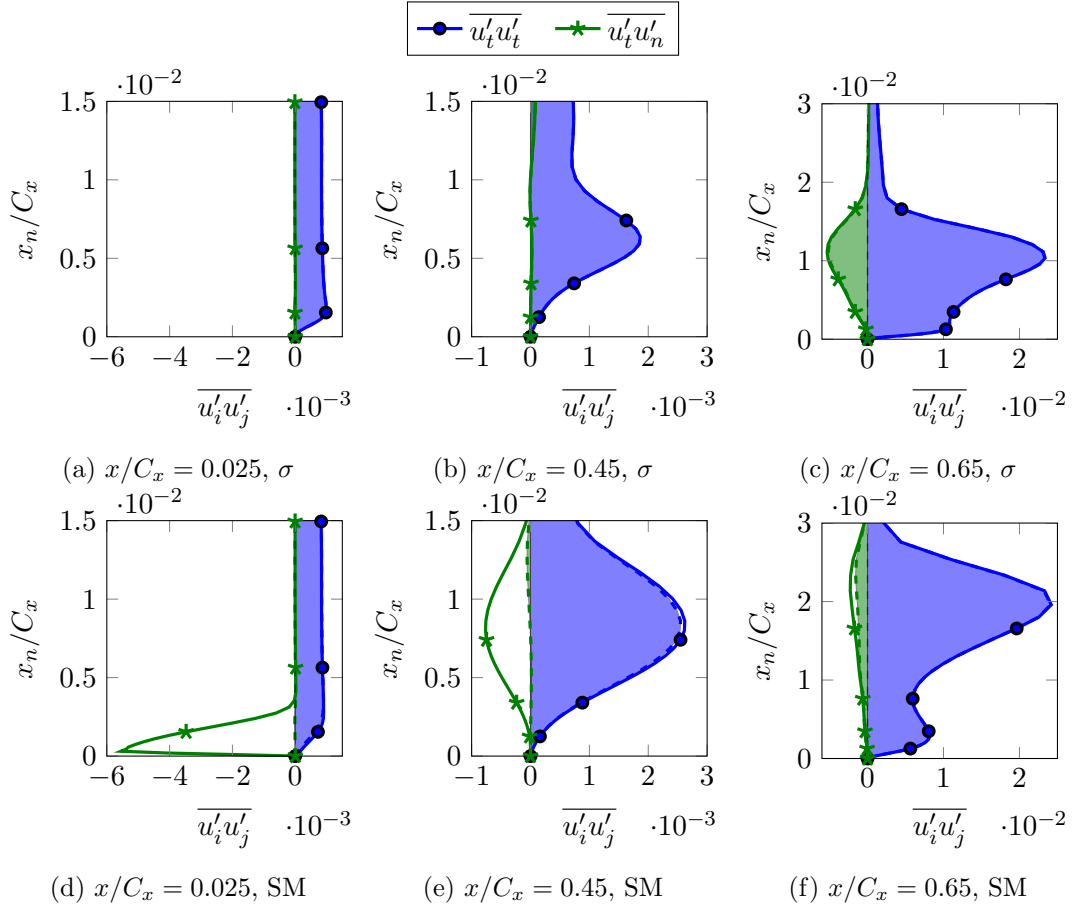


FIGURE 5.28: Cases C2 (a-c) and C4 (d-f). Profiles of the tangential ($\overline{u'_t u'_t}$) and shear ($\overline{u'_t u'_n}$) components of the Reynolds stresses on the suction surface. Solid lines show the total ($\overline{u'_i u'_j} = \overline{u'_i u'_{j,SGS}} + \overline{u'_i u'_{j,r}}$) stresses, filled areas show the resolved stresses ($\overline{u'_i u'_{j,r}}$) only.

the strain rate tensor $\overline{S_{ij} S_{ij}}$. Following the Reynolds decomposition approach in Equation 2.7, this term can be broken down into two parts:

$$\overline{S_{ij} S_{ij}} = \bar{S}_{ij} \bar{S}_{ij} + S'_{ij} S'_{ij} \quad (5.13)$$

where $\bar{S}_{ij} \bar{S}_{ij}$ is calculated from the time averaged flow field. Figure 5.30a shows that in the laminar boundary layer the $\overline{S_{ij} S_{ij}}$ term primarily results from strain in the mean flow field (dark grey area). On the other hand, in the turbulent boundary layer in Figure 5.30b, there is also a large contribution from the fluctuating velocity field (light grey area). This suggests the SM model is incorrectly reacting to a highly strained mean flow field, although there is little turbulence in this region.

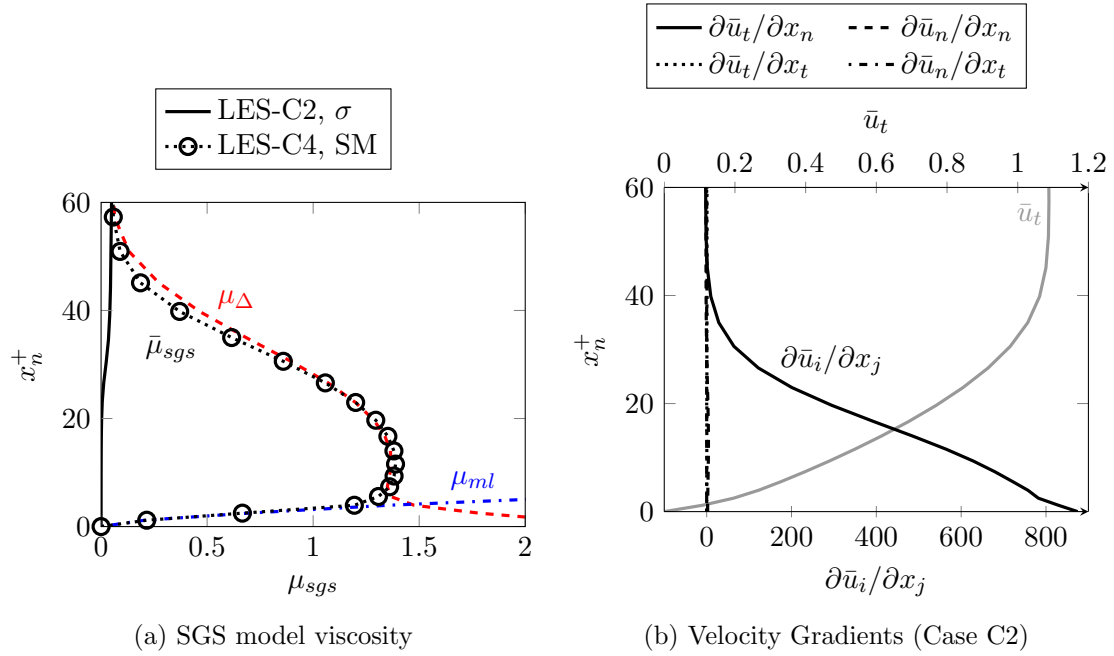


FIGURE 5.29: Profiles of SGS model viscosity and velocity gradients in the suction surface laminar boundary layer, at $x/C_x = 0.025$.

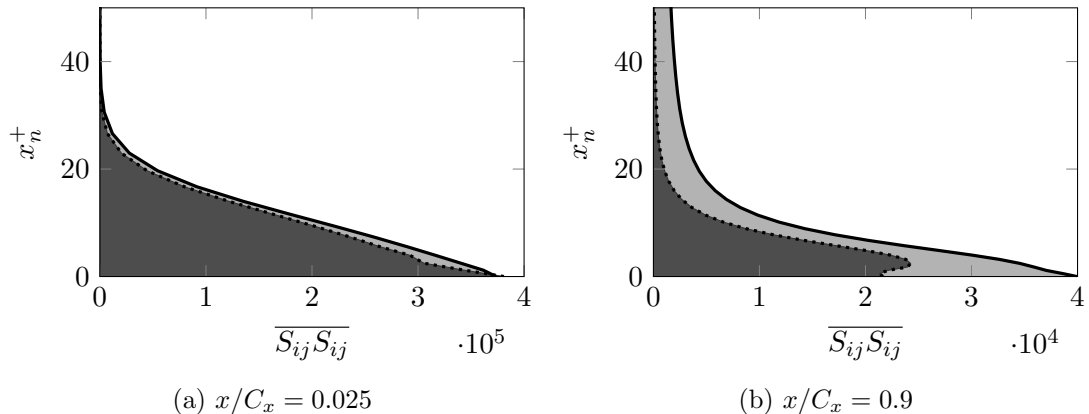


FIGURE 5.30: Profiles of the $S_{ij}S_{ij}$ term on the suction surface, in a laminar ($x/C_x = 0.025$) and turbulent ($x/C_x = 0.9$) region. The dark grey area represents the mean flow field contribution ($\bar{S}_{ij}\bar{S}_{ij}$) and the light grey the fluctuating field contribution ($S'_{ij}S'_{ij}$).

5.4.2.2 Pressure surface

The C_f distribution in Figure 5.21b shows that the onset of transition on the pressure surface is significantly delayed by the SM model. Figure 5.22b shows that the SM model also returns a higher μ_{sgs} compared to the σ model above the pressure surface. Like on the suction surface, this higher μ_{sgs} is found to significantly affect the boundary layer. However, since there is no flow separation on this surface, this is not explored further here. More relevant is the fact that the high μ_{sgs} appears to damp the transition to turbulence on the pressure surface, and this is explored in the following section.

5.4.3 Numerical scheme

In this section the influence of the numerical smoothing is examined. Figure 5.31 shows the C_f distributions on both surfaces for cases C2, C6, and C7. Case C2 is run with the LASW scheme, while C6 and C7 are run with the smoothing constant fixed to $\epsilon_2 = 0$ and $\epsilon_2 = 0.5$. The location of flow separation on the suction surface is not found to be sensitive to the numerical smoothing, but the reattachment point is. This is likely to be due to the numerical smoothing damping the amplification of instabilities within the separation region.

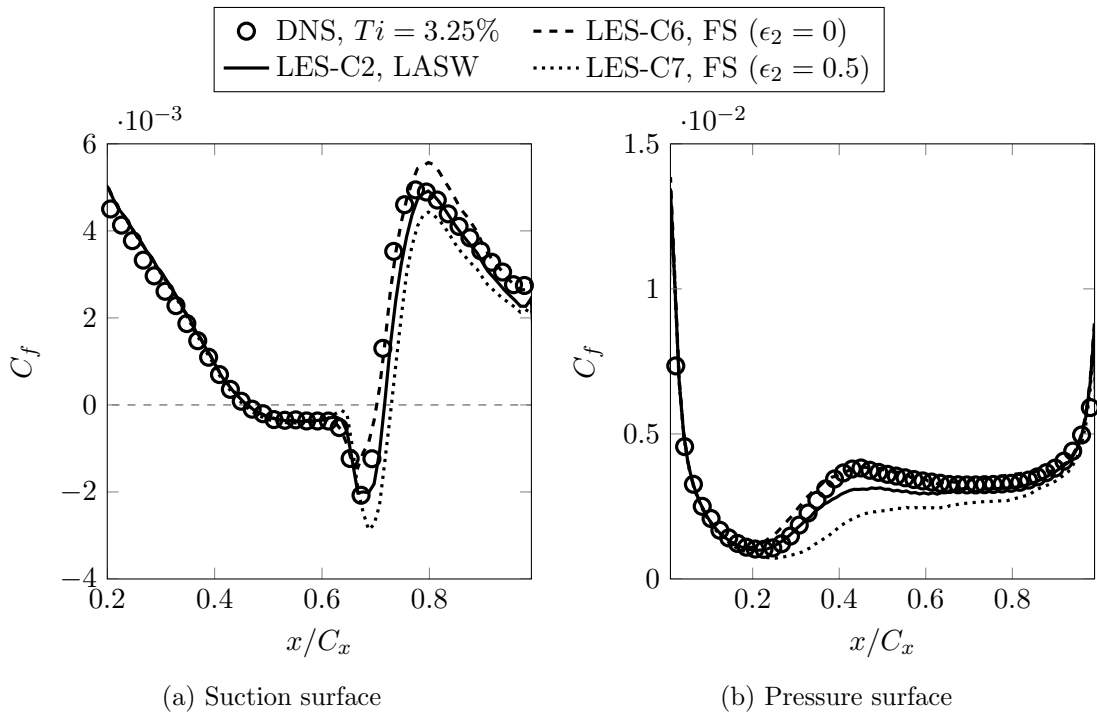


FIGURE 5.31: Sensitivity of the suction and pressure surface skin friction coefficient to the numerical smoothing.

Conversely, on the pressure surface, the numerical smoothing is seen to significantly influence the boundary layer transition. This is thought to be due to the numerical smoothing affecting the behaviour of the complex transition mechanisms uncovered in Sections 5.2.1.1 and 5.2.1.2. Figure 5.32 shows that the u'_n fluctuations in the laminar region, which precipitate the instabilities, are less strong and occur further downstream in the $\epsilon_2 = 0.5$ case. As a result, the average onset and finish of transition, shown by the white (case C2) and yellow (case C7) lines, are further downstream. The vortical structures, visualised by the Q-criterion iso-surface, are also seen to be significantly larger. The same process is observed when the Smagorinsky-Lilly SGS model is used in case C4. Thus, it is clear that the pressure surface is very sensitive to any excess numerical dissipation.

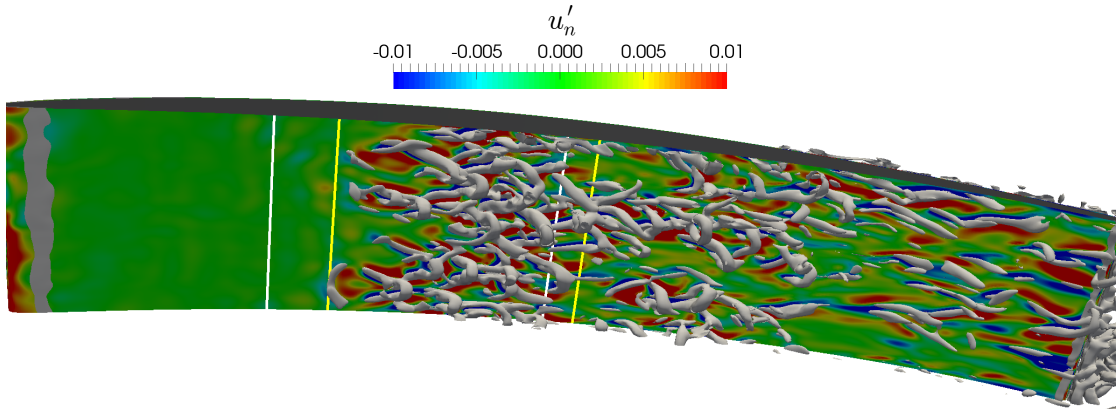


FIGURE 5.32: Case C7. Contours of the normal velocity perturbations, u'_n , on a plane inside the pressure surface boundary layer $d = 1.64 \times 10^{-3}$ from the wall. Iso-surfaces of $Q = 200U_0/C_x$ are superimposed. The white lines show the average start and finish of the transition region for case C2, while the yellow shows the same for case C7.

In the present case, the C_f distributions suggest that running with no numerical smoothing ($\epsilon_2 = 0$) is a viable option. The pressure surface C_f for case C6 is in closer agreement with the DNS than case C2, since the slightly increased ϵ_2 returned by the LASW scheme here is damping the transition mechanisms slightly. However, Figure 5.33 shows that the absence of numerical smoothing on the suction surface has resulted in noticeable dispersive errors. Since the mesh is very fine in this region these wiggles are not sufficiently large to cause premature transition. However, they still lead to an overly short separation bubble on the suction surface, and premature transition on the pressure surface.

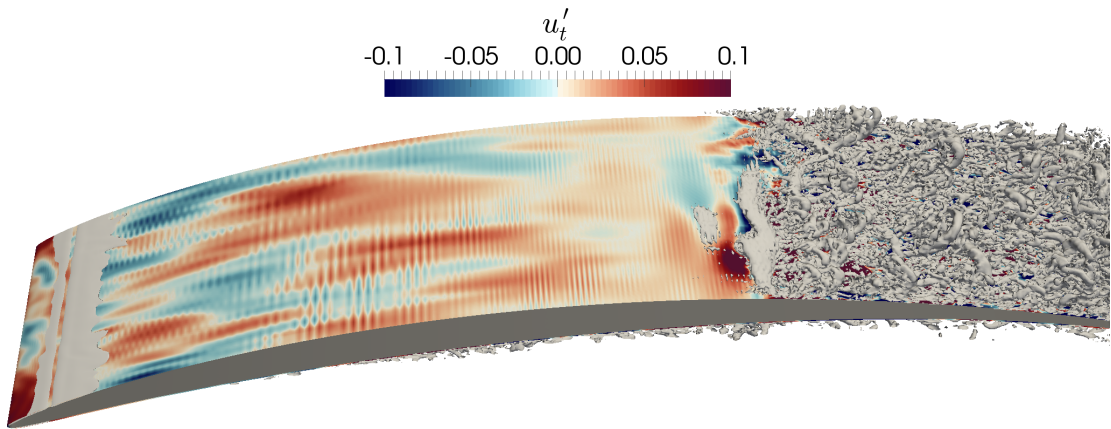


FIGURE 5.33: Case C6. Contours of the tangential velocity perturbations, u'_t , on a plane inside the suction surface boundary layer $d = 1.64 \times 10^{-3}$ from the wall. Iso-surfaces of $Q = 300U_0/C_x$ are superimposed.

5.5 Concluding Remarks

To conclude, this chapter has demonstrated the potential for performing predictive LES of transitional compressor flows. Results are generally in good agreement with the DNS of Zaki et al. [9], despite an LES to DNS mesh size ratio of only 12.5%. Furthermore:

- In addition to giving good mean flow predictions, the LES has been found to accurately capture the complex transitional mechanisms. The inner and overlap modes, observed by Zaki et al. [9], were well replicated by the LES. Although still influenced by the Klebanoff streaks, these modes don't resemble the traditional mechanism observed in DNS of bypass transition [12]. This highlights the complexity of boundary layer transition, but also shows how LES may be used to further investigate transition models and correlations for application in complex compressor flows.
- The effects of inflow turbulence are well predicted by the LES, with the traditional bypass mechanism taking over as the free-stream intensity is increased from 3.25% to 10%. The more subtle sensitivity to the length scales of the incoming turbulence is also seen, which highlights the need for detailed measurements when attempting to replicate experiments.
- The σ /WALE SGS models are found to give predictions that are (at least) as accurate as the LES results obtained by Lardeau et al. [86]. Despite not being a completely fair test due to the difference in grid size, this is encouraging as it suggests that the σ or WALE models offer a good alternative to more complex SGS models such as those used by Lardeau et al. [86]. As discussed in Section 2.3.2, models such as the DSM require additional averaging or test filters, making them less practical for complex industrial LES applications.
- Numerous studies, for example Sayadi et al. [157], have demonstrated the poor performance of the Smagorinsky-Lilly SGS model in transitional flows. However, Table 2.3 shows that it is still a commonly used model for compressor SGS studies. Therefore, to quantify the various sensitivities of the present flow, it was still important to investigate the performance of this model. This study provided useful knowledge for any further development of SGS models for compressor flows. The high sensitivity of the suction surface flow to the SGS model highlighted the need for the model to not be overly sensitive to mean strain. This validates the use of the Shear-Improved Smagorinsky model (see Section A.4.3) for compressor flows, but also suggests the σ (and WALE) model offer a promising alternative.

- It was found that the inner and overlap transition modes that occur on the pressure surface were significantly more sensitive to the numerical smoothing than the separation induced mode on the suction surface. This served as a good demonstration of the motivation for using the LASW scheme. Better results may be achievable in certain regions through careful use of the ϵ_2 constant. However, this would not fit in with the concept of predictive LES, and the LASW scheme was found to offer a more robust alternative.

Chapter 6

Towards Engine Representative Compressor Flows

In Chapter 5 it was shown that, as long as care is taken with the numerics and SGS model, LES is able to reliably capture the complex transitional mechanisms that occur in a compressor flow. Importantly, the sensitivity to the inflow turbulence intensity was well predicted. In the present chapter, this analysis is extended by considering other flow features that occur in a real gas turbine compressor.

Firstly, in Section 6.2 the effect of incoming turbulent wakes on the boundary transition is examined. These wakes are representative of the wakes a stator blade row will see coming from the upstream rotors. Then in Section 6.3.1, the sensitivity of the endwall flow region to the incoming turbulence is explored. The literature review (Chapter 2) discussed how a three-dimensional separation occurs in the endwall/hub region, and this is important to consider due to its deleterious influence on performance. In Section 6.3.2 the LES results are used to highlight a number of challenges that exist when attempting to model this complex three-dimensional separation.

Through the above studies an attempt is made to move towards more engine representative flows. However, it should be noted that there are still flow features of gas-turbine compressor flows that will not be represented in this study (see Sec. 2.4.2), such as compressibility, clearance and rotational effects.

6.1 The PVD compressor cascade

The compressor cascade investigated in this chapter was tested experimentally by Gbadebo [35], who examined the endwall flow topologies in detail. The case provides a useful

benchmark for studying an endwall flow separation with LES. In Table 6.1, the key geometrical and inflow parameters for the cascade are compared to those from the V103 cascade studied in Chapter 5. The cascade consists of PVD¹ aerofoils, and is subsequently referred to as the PVD cascade. The PVD cascade is similar to the V103 cascade, but has a larger blade pitch to chord ratio and flow turning angle, making its 2D diffusion factor larger.

| Parameter | Cascade | |
|-------------------------------------|--------------------|-------------------|
| | V103 | PVD |
| Blade profile | NACA-65-K48 | PVD |
| Chord length, c | 220mm | 151.5mm |
| Axial chord length, C_x | 204mm | 146.5mm |
| Reynolds number, Re_c | 1.38×10^5 | 2.3×10^5 |
| Blade span, h/c | 1.36 | 1.32 |
| Blade pitch, S/c | 0.55 | 0.926 |
| Blade thickness, t/c | 0.055 | 0.1 |
| Inflow incidence, i | -6.0° | 0.0° |
| Inlet flow angle, α_1 | 44.0° | 41.0° |
| Outlet flow angle, α_2 | 8.0° | 8.0° |
| Flow turning, $\alpha_1 - \alpha_2$ | 36.0° | 33.0° |
| 2D Diffusion Factor [153] | 0.42 | 0.49 |

TABLE 6.1: Comparision of geometrical and inflow parameters for the V103 and PVD compressor cascades.

6.1.1 Case set-up

Figure 6.1 shows the computational domain used for LES of the PVD cascade. A viscous (no-slip) wall is added at $z = 0$ to represent the endwall. The blade is fully resolved up to the mid-span ($z = 0.5h$). Above this the mesh is gently coarsened, and an inviscid (slip) wall is placed at 65% span².

The same H-O-H mesh topology used for the V103 cascade, shown in Figure 5.1, is used for the PVD cascade. The O-mesh wrapped around the blade has dimensions $886 \times 60 \times 349$ in the wall tangential, normal and spanwise directions respectively. Adding the H-mesh sections leads to 2.16×10^5 grid points per xy-plane, and 7.54×10^7 grid points in total. The maximum near-wall grid spacings are shown in Table 6.2. As for

¹Prescribed velocity distribution

²The blade is symmetrical about the mid-span plane, so it is desirable to only simulate half the span to reduce computational cost. However, the instantaneous flow-field is not symmetric about the mid-span. An inviscid wall placed at $z = 0.5h$ might contaminate the flow close to it, so the inviscid wall is placed at $z = 0.65$ with a sponge zone between $0.5 \leq z \leq 0.65$ instead.

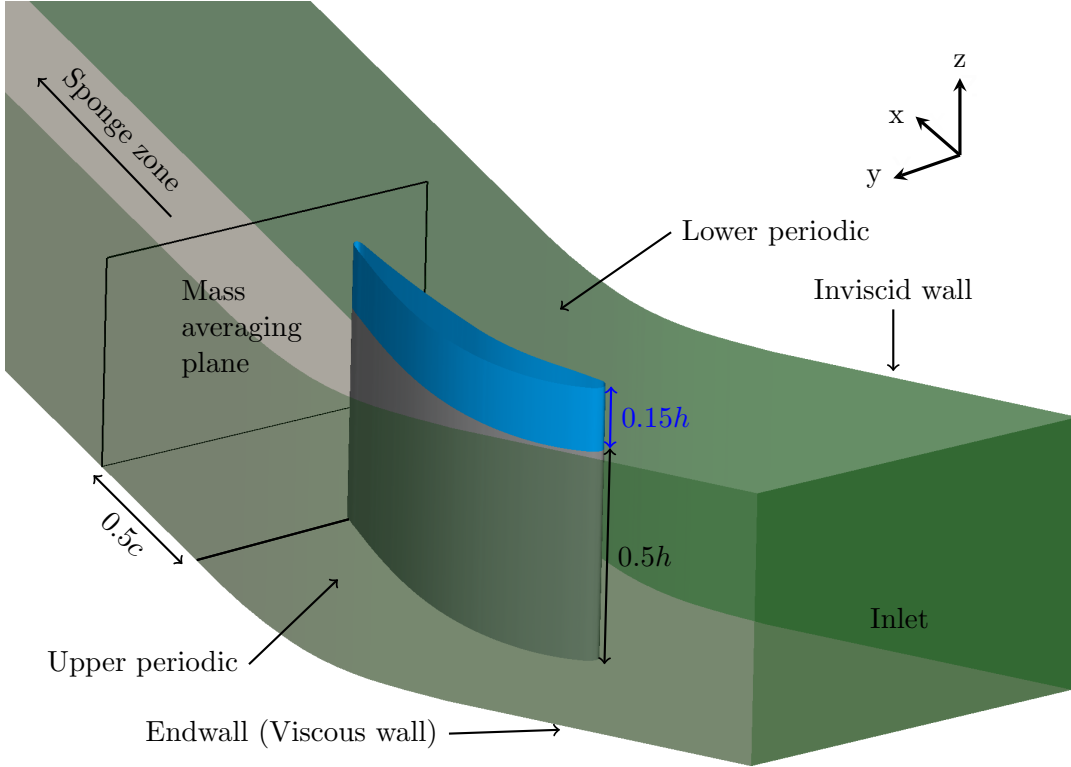


FIGURE 6.1: The computational domain for the PVD compressor cascade case with endwall included.

the V103 mesh, the PVD mesh is designed to ensure that the grid resolution is within the recommended values for wall-resolved LES, as given by Piomelli et al. [71]. This requires a significantly greater number of grid points due to the slightly higher Reynolds number and the need to resolve the endwall boundary layer.

| | Maximum near-wall grid spacing* | | |
|-----------------------------------|---------------------------------|------------------|--------------|
| | Δx^+ | $y_{1st-node}^+$ | Δz^+ |
| Blade | 60 | ≤ 1 | 25 |
| Endwall | 55 | ≤ 1 | 20 |
| Recommended range [158] | 50-100 | ≤ 1 | 15-30 |

* The x, y, z here correspond to the stream-wise, wall normal and spanw-wise directions.

TABLE 6.2: Maximum non-dimensional wall spacings for the LES PVD cascade mesh, and the suggest ranges for wall resolved LES from Piomelli [158].

Except in the span-wise direction, the remaining boundary conditions are the same as those used for the V103 cascade. Cases were originally run with the inflow at $x = -0.45C_x$ (published in Scillitoe et al. [159]), but this was moved upstream to $x = -0.7C_x$ to prevent any interactions between the inflow boundary and the nearby horse-shoe vortex system. No noticeable differences were observed between the two cases, however

as a precaution, the $x = -0.7C_x$ set-up was retained for all the cases presented in this chapter.

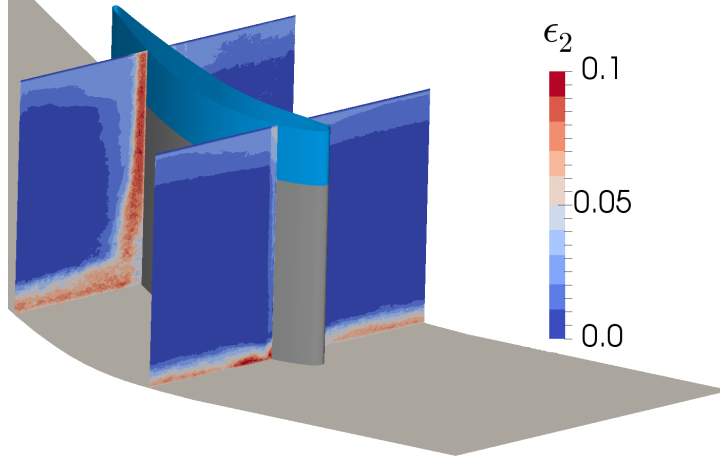


FIGURE 6.2: Contours showing ϵ_2 smoothing field at $x = 0.1C_x$ and $x = 0.7C_x$, after running the L-TBL case with the LASW scheme.

The LES cases in this chapter were run before the LASW scheme had been fully validated, so a fixed smoothing level of $\epsilon_2 = 0.1$ was used. This level was found by carefully tuning ϵ_2 so that it is as low as possible, but high enough to prevent wiggles in the solution. The LASW scheme has now been used on one of the cases, and the resulting ϵ_2 field is shown in Figure 6.2. A maximum of $\epsilon_2 = 0.1$ is returned, which is in agreement with the level found through manual tuning.

6.1.2 Mid-span cases

Table 6.3 lists the LES cases that were run for the PVD cascade. In all the cases a time dependent velocity $u_i(t, y, z)$ is enforced at the inflow boundary using the method described in Section 3.2. Two “mid-span” cases, L and L-W, were run to investigate the effect of wakes on the boundary layer transition. These cases were run on a smaller bi-periodic domain¹ to allow for the long run times required for phase-averaging.

Case L was run for $4T^*$ to flush out transients and then $10T^*$ to collect statistics. Case L-W was run for 6 wake passing periods ($\tau = 1.09T^*$) to establish a periodic flow, followed by a much longer period of 28τ to provide well converged phase averages. These cases were run on 128 processing cores, with each case requiring 1.5k CPU hours per T^* .

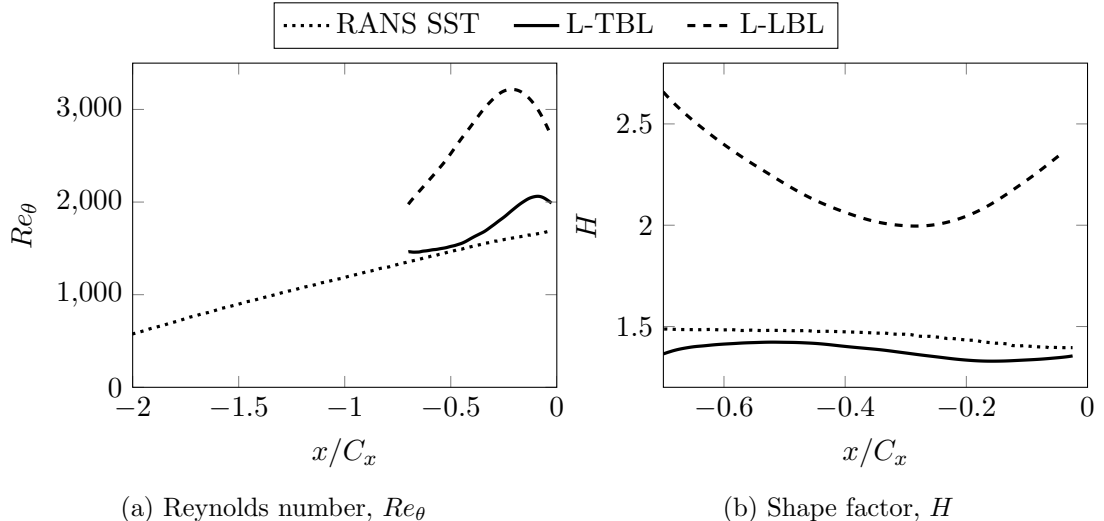
¹This domain has the same 2D mesh in the xy-plane, but a span-wise extent of only 20% span ($0 \leq z \leq 0.2h$). Periodic boundaries are placed at $z = 0$ and $z = 0.2h$. The total number of grid points is 1.6×10^7 .

| Case | Endwall present? | FST T_i | Endwall BL | Wakes present? |
|--------------|------------------|--------------|------------|----------------|
| L | No | Low (1.0%) | N/A | No |
| L-W | No | Low (1.0%) | N/A | Yes |
| L-LBL | Yes | Low (1.0%) | LBL | No |
| L-TBL | Yes | Low (1.0%) | TBL | No |
| H-TBL | Yes | High (10.0%) | TBL | No |

TABLE 6.3: LES cases for the PVD compressor cascade.

6.1.3 Endwall cases

The remaining cases are run on the full 3D domain described above. Like case L, they are run for $4T^*$ to flush out transients and then at least $10T^*$ to collect statistics. These cases were run on 960 cores, with each case requiring 161k CPU hours in total. LES case L-LBL is intended to represent the experiment of Gbadebo [35]. In the experiment the free-stream T_i is measured at $x = -2c$ to be 1.5%. For the LES, it is prohibitively expensive to run with such a long inflow. Instead, the inflow is kept at $x = -0.7C_x$ with a lower T_i of 1% applied to account for the decay of the turbulence between the two locations¹.

FIGURE 6.3: Cases L-TBL and L-LBL. Time-averaged momentum thickness Reynolds number Re_θ and shape factor H of the incoming endwall boundary layer, measured at mid-pitch.

A similar procedure was required for the incoming endwall boundary layer. A RANS SST² simulation was run with the endwall boundary layer velocity profile measured by Gbadebo [35] enforced at $x = -2c$. The resulting endwall boundary layer velocity profile was then extracted at $x = -0.7C_x$, and a turbulent boundary layer (TBL) of the same

¹A decay rate equation from Spalart et al. [160] is used for this approximation.

²Shear-Stress Transport model, described in Section A.2.2.

thickness ($Re_\theta = 1350$) was generated using the technique described in Section 3.2.1. The TBL is fed into the LES inflow, and Figure 6.3 shows the boundary layer growth downstream of this is in fairly close agreement to the RANS.

It should be noted that there is some uncertainty here. Gbadebo [35] comments that the inlet boundary layer appears to be very thin, and the relatively high shape factor ($H = 1.75$) suggests some sort of re-laminarisation, presumably due to flow acceleration in the contraction upstream of the cascade. The above approach assumes the boundary layer is fully turbulent at $x = -2c$. If this is not the case then there may be some disagreement between the incoming endwall boundary layer in the LES and the experiment.

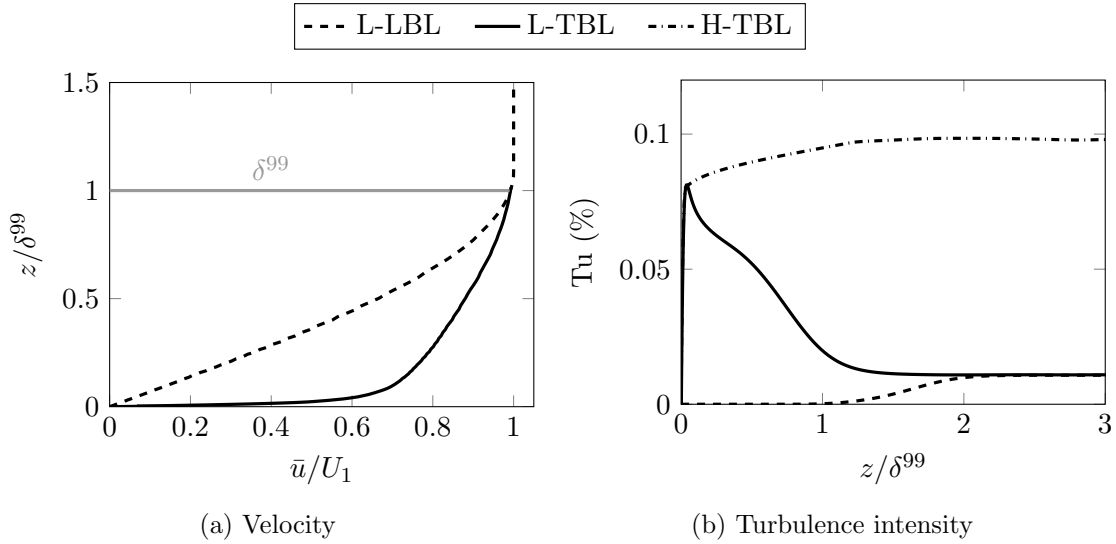


FIGURE 6.4: Cases L-TBL, L-LBL and H-TBL. Endwall boundary layer profiles of time-averaged velocity and turbulence intensity at the inflow ($x = -0.7C_x$).

In order to investigate the effect of the endwall boundary state, a laminar boundary layer is set at the inflow for case L-LBL. For this case, an approximate sinusoidal Blasius velocity profile is prescribed with $\delta^{99} = 0.06C_x$ (to match the TBL in case-L-TBL), as shown in Figure 6.4a. For all the cases, the free-stream velocity fluctuations are blended with the boundary layer fluctuations using the method described in Section 3.2.3, and the resulting Ti profiles are shown in Figure 6.4b.

6.2 Periodically varying inflow conditions

In the literature review (Chapter 2) the importance of periodically varying inflow conditions, such as incoming wakes, was discussed. The importance of wakes in the compressor cascade is examined in this section. The method used to apply the wakes at the inflow is explained in Section 3.2.2. The wake set-up used by Hilgenfeld et al. [152] is mostly

followed, but the parameters are adjusted to make the wakes more representative of those seen by a stator stage in a real gas turbine engine¹.

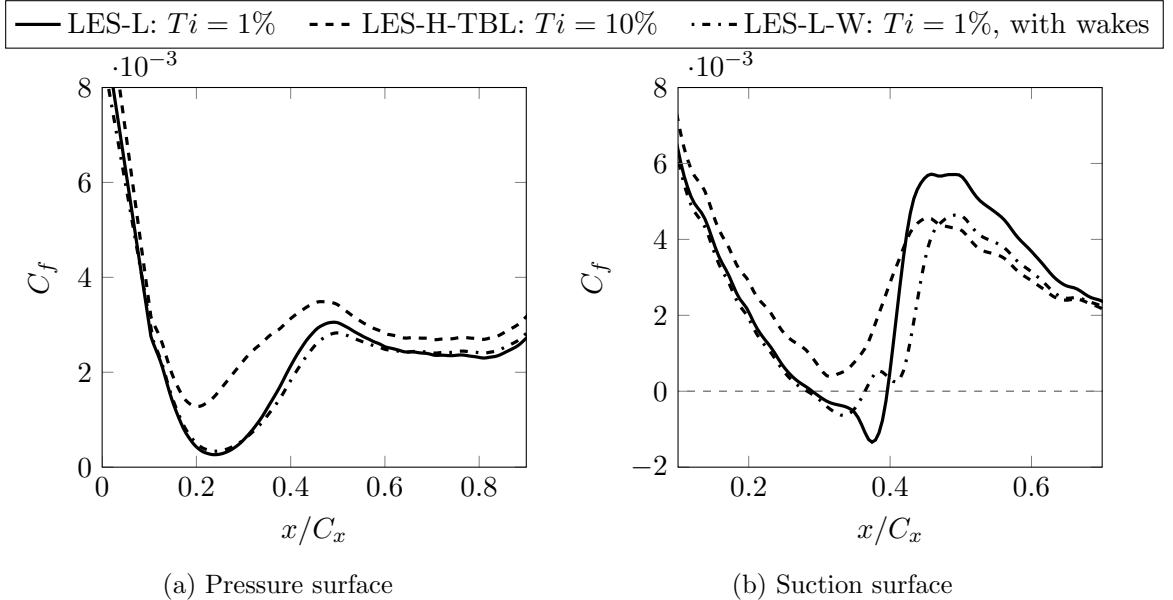


FIGURE 6.5: Cases L, L-W and H-TBL. Time-averaged skin friction coefficient \bar{C}_f on suction and pressure surfaces. *Cases L and L-W are span averaged, case H-TBL is the distribution near the mid-span ($z = 0.46h$).*

In Figure 6.5 the suction and pressure surface skin friction distributions for cases L, L-W and H-TBL are presented. It is clear that the addition of turbulent wakes (case L to L-W) has a significant influence on the time-averaged flow, and this is investigated further in Section 6.2.2. But first, to check that this flow is qualitatively similar to those seen in Chapter 5, the cases without wakes are examined in Section 6.2.1.

6.2.1 Transition mechanisms without wakes present

The suction surface flow for case L is visualised in Figure 6.6. Despite the different Reynolds number and Ti , the flow appears to be very similar to that seen in the V103 cascade at $Ti = 3.25\%$; a streaky laminar boundary layer is present, which separates in the adverse pressure gradient region, resulting in K-H rolls and turbulent reattachment. The K-H rolls are less three dimensional in this case. This is likely to be due to the lower free-stream Ti leading to weaker Klebanoff distortions, which were found to locally disrupt the K-H rolls in the V103 cascade.

¹In experiments the speed of the moving bar, U_{cyc} , which produces the wakes is often limited, For example see Hilgenfeld et al. [152]. This leads to unrealistic wake angles, $\alpha_{wake} = \tan^{-1}[(\bar{v}_{in} - U_{cyl})/\bar{u}_{in}]$. The use of LES allows for U_{cyl} to be increased to give a more realistic wake angle.

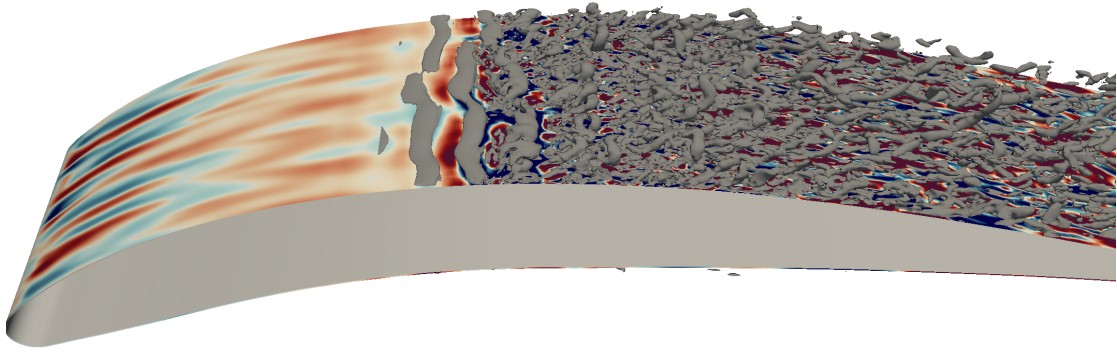


FIGURE 6.6: Case L-W. Contours of the tangential velocity perturbations, u'_t , on a plane inside the suction surface boundary layer $d = 1.02 \times 10^{-3}$ from the wall. An iso-surface of $Q = 400U_0/C_x$ (clipped at $x > 0.3C_x$) is superimposed.

Figure 6.7 shows that the pressure surface transition mechanisms are also similar to those seen in the V103 $Ti = 3.25\%$ case; with an overlap mode disturbance seen at (1), and a larger inner mode Λ structure seen at (2).

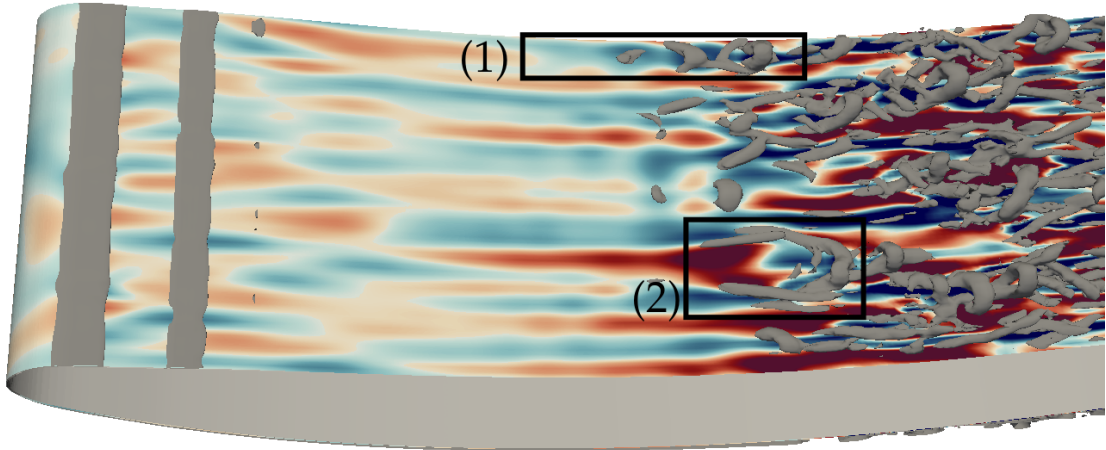


FIGURE 6.7: Case L-W. Contours of the tangential velocity perturbations, u'_t , on the suction surface $d = 1.02 \times 10^{-3}$ plane. An iso-surface of $Q = 250U_0/C_x$ is superimposed.

As seen in Figure 6.5b, suction surface flow separation is avoided in the higher $Ti = 10\%$ case. Like in the V103 $Ti = 10\%$ case, the transition mechanism changed to the standard bypass mode on both surfaces at this FST intensity¹. It is therefore reasonable to conclude that the transition mechanisms seen in the PVD cascade are similar to those seen in Chapter 5, at both Ti's.

¹Not shown for brevity.

6.2.2 Transition mechanisms with wakes present

So far, the inflow conditions considered have been unsteady yet statistically stationary, so the flow-field can be decomposed into a mean \bar{f} and a fluctuating component f' :

$$f = \bar{f} + f' \quad (6.1)$$

In this section the influence of upstream wakes, which vary periodically, is studied. An additional component of the flow-field, $\hat{f}(\phi)$, the periodic perturbation to the time-average, must now be considered:

$$f = \bar{f} + \hat{f}(\phi) + f'(\phi) = \langle f \rangle(\phi) + f'(\phi) \quad (6.2)$$

The influence of the wakes can be elucidated by obtaining averaged quantities at a particular phase, $0 \leq \phi \leq 1$, of the wake passing period,

$$\langle f \rangle(\phi) = \frac{1}{N} \sum_{n=1}^N f(t = \phi\tau + n\tau) \quad (6.3)$$

where $\langle \cdot \rangle$ denotes a phase-averaged quantity, τ is the wake passing period, and N is the total number of wake passing periods. Rearranging Equation 6.2 shows that fluctuating quantities can then be obtained from $f' = f - \langle f \rangle(\phi)$. The phase-averaged turbulence kinetic energy, $\langle k \rangle(\phi)$, can then be obtained, and is shown for four phases of the wake passing period in Figure 6.8. At $\phi = 0.2$, (Fig. 6.8a) the wake that entered the bottom of the inflow at $\phi = 0$ is visible. At $\phi = 0.4$, (Fig. 6.8b) the wake is still being convected into the domain, but the previous wake has now reached the leading edge of the blade.

In Figure 6.5, wakes are seen to influence the time-averaged skin friction distribution $\overline{C_f}$, with the time-averaged reattachment location on the suction surface being moved upstream. However, time-averaging obscures the full effects. In Figure 6.9 the phase-averaged skin friction $\langle C_f \rangle(\phi)$ is plotted for a number of phases. The skin friction is not significantly altered on the pressure surface, but on the suction surface, the large filled grey area in Figure 6.9a demonstrates the significant impact of the wakes.

The phase dependent variation of $\langle C_f \rangle(\phi)$ on the suction surface can be seen more clearly in a phase-averaged space-time (ST) plot, presented in Figure 6.10¹. The separation bubble region is identified by the region of negative $\langle C_f \rangle(\phi)$ (blue region), and it is bounded by the separation and reattachment lines (dashed blue lines), identified by $\langle C_f \rangle(\phi) = 0$. Throughout the wake passing period, the separation and reattachment points of the laminar separation bubble (dashed blue lines) are seen to move away from

¹For clarity the range $0 \leq \phi \leq 1$ is repeated to $1 \leq \phi \leq 2$.

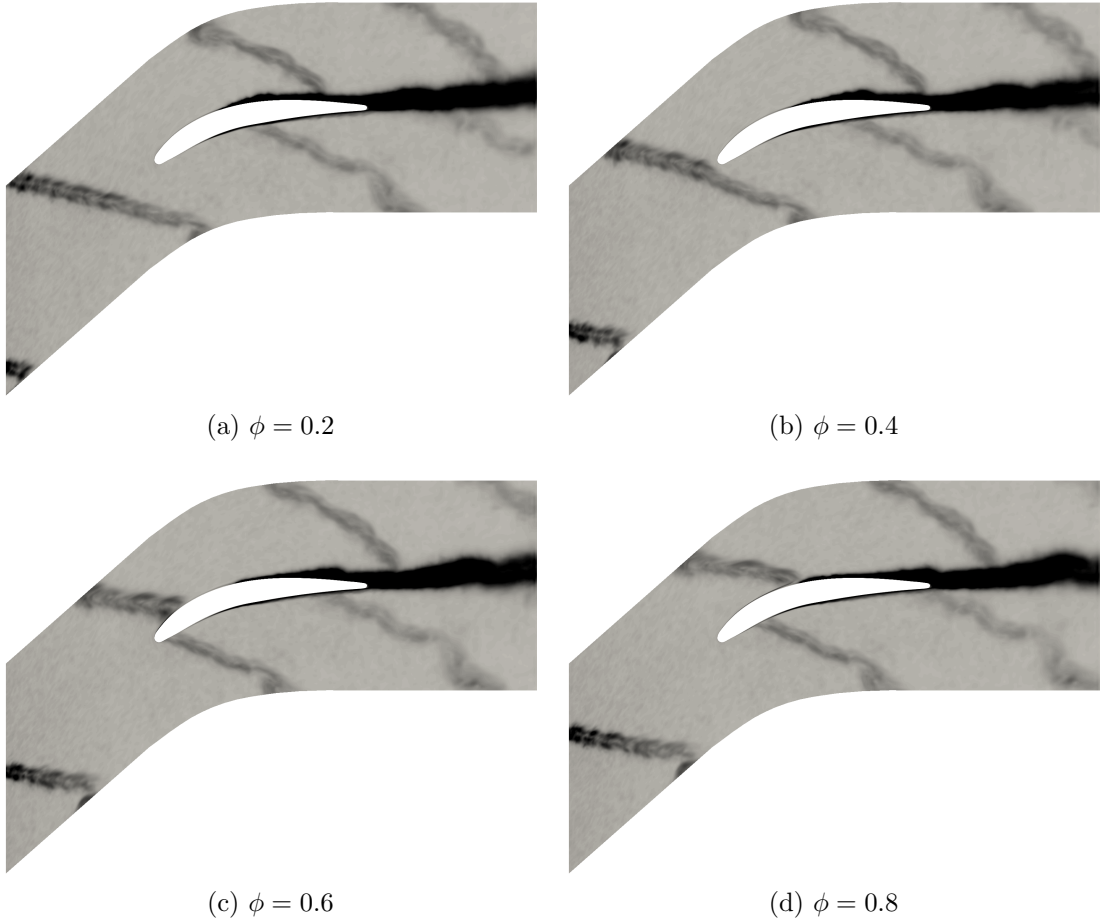


FIGURE 6.8: Case L-W. Contours of phase-averaged turbulent kinetic energy $\langle k \rangle (\phi)$.

the time-averaged locations in the case without wakes (dashed grey lines). As a result, the bubble length fluctuates from a maximum of $0.177C_x$ to a minimum of $0.043C_x$, compared to a length of $0.105C_x$ in the case without wakes.

As the wake convects over the suction surface boundary layer, the leading edge of the wake accelerates the flow while the trailing edge decelerates it. Following the approach of Coull et al. [20], the loci of the points of maximum acceleration and deceleration are used to represent an approximate path (or celerity line) of the leading (W_{LE}) and trailing (W_{TE}) edges of the wake. These are overlaid on Figure 6.10 (dashed lines), along with their mean (dash-dot line), which represents the mean wake path.

Figure 6.10 shows that the centre of the wake passes $x = 0.44C_x$ at $\phi = 0.88$, but the reattachment point isn't brought forward until $\phi = 1.01$. To explain this lag, celerity lines of $0.5U_{fs}$, $0.7U_{fs}$, $0.88U_{fs}$ are overlaid (as done by Coull et al. [20], Wheeler et al. [27], and Walker et al. [161]). U_{fs} is taken as the free-stream (edge of time-averaged boundary layer) velocity magnitude¹, and the lines are positioned to originate from

¹As in Chapter 5, the edge of the boundary layer is detected using a vorticity magnitude threshold [86, 125].

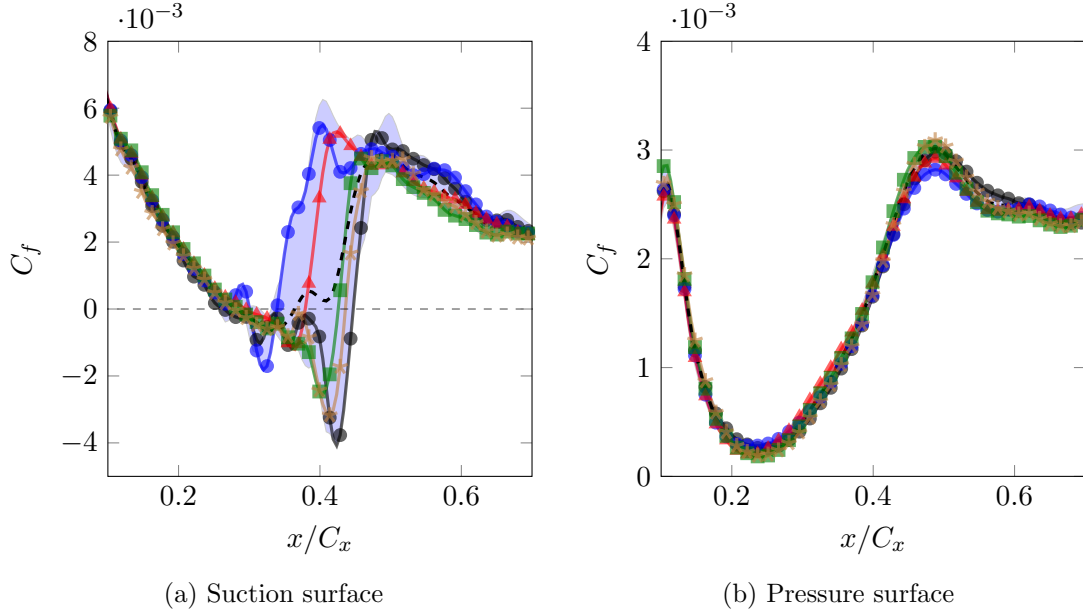


FIGURE 6.9: Case L-W. Phase-averaged and time-averaged friction coefficient on suction and pressure surfaces. The filled grey area shows the full range of $\langle C_f \rangle (\phi)$ variation throughout the wake passing period.

where the phase-averaged C_f indicates the first appearance of turbulent disturbances ($x = 0.06C_x$). The $0.88U_{fs}$ and $0.5U_{fs}$ celerity lines are important because these are the approximate convection rates of a turbulent spot leading and trailing edge [20]. Numerous studies have shown that the $0.7U_{fs}$ celerity line is important in both compressors and turbines; Wheeler et al. [26] found regions of thickened boundary layer θ , caused by the wake at a compressor leading edge, convect at this speed. Coull et al. [20] showed that the strongest wake induced disturbances on a turbine blade, which they demonstrated are amplified Klebanoff streaks, also convect at this speed.

The ST plot (Fig. 6.10) shows that early reattachment induced by the wake is bounded by the $0.5U_{fs}$ and $0.7U_{fs}$ celerity lines. This suggests that wake induced disturbances, originating from near the leading edge, convect at approximately $0.7U_{fs}$. Once they reach the separation region, they initiate earlier transition in the K-H rolls, leading to earlier reattachment. This process is visualised in Figure 6.11. At $\phi = 0.6$, amplified Klebanoff streaks have been induced by the passing wake, but they are lagging some distance behind due to their slower convection speed. In Figure 6.12a, these amplified Klebanoff streaks are seen to initiate a turbulent spot¹. In Figure 6.12b, the spot is continuing to grow. By Figure 6.12c, it has caused the K-H rolls to transition earlier, resulting in the reattachment point being brought upstream.

¹The mechanism here is the same as that observed in the bypass transition mode in Section 5.3.2, with the negative-jet of a Klebanoff streak lifting fluid away from the surface, where it then interacts with the FST.

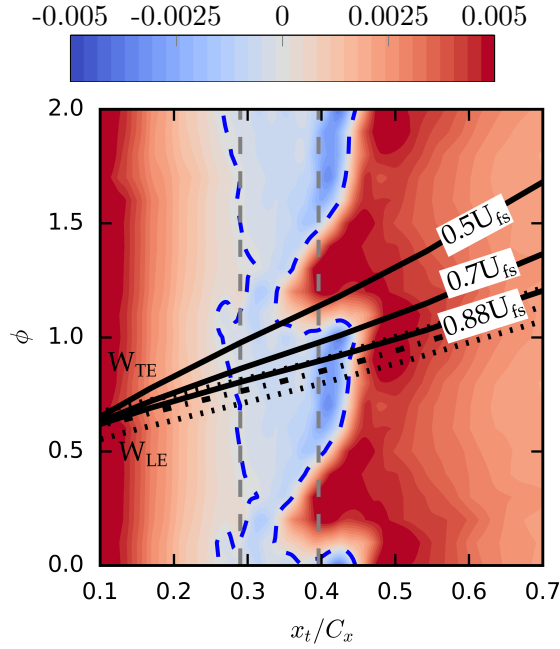


FIGURE 6.10: Case L-W. Phase-averaged space-time plot of the suction surface skin friction C_f . The dashed blue lines indicate the phase dependent separation/reattachment locations (indicated by $\langle C_f \rangle(\phi) = 0$), while the dashed grey lines indicate the time-averaged locations of the no wake simulation (case L).

Figure 6.10 shows that, after the trailing edge of the wake-amplified Klebanoff streaks (travelling at $0.5U_{fs}$) have convected past, a relatively slow drop in shear stress occurs. Eventually, the reattachment line moves downstream of its wake-free location. This is characteristic of the calmed region that has been found to follow turbulent spots [162]. To further examine this effect, the boundary layer shape factor, $H = \delta^*/\theta$, is calculated¹. The phase-averaged displacement thickness is given by

$$\langle \delta^* \rangle(\phi) = \int_0^{\langle \delta_\omega \rangle(\phi)} \left(1 - \frac{\langle u \rangle(\phi, x_n)}{\langle u_e \rangle(\phi)} \right) dx_n, \quad (6.4)$$

and the phase-averaged momentum thickness $\langle \theta \rangle(\phi)$ is calculated using Equation 5.6². Space-time plots of $\langle \theta \rangle(\phi)$ and $\langle H \rangle(\phi)$ are presented in Figure 6.13, with the same celerity lines overlaid. The passing of the wake-induced turbulent spots (bounded by the $0.5U_{fs}$ and $0.7U_{fs}$ celerity lines) is associated with an increase in momentum thickness, as highlighted by the dashed red lines in Figure 6.13a. This is in agreement with the study of turbulent spots by Walker et al. [163]. Behind these spots, a calmed region follows, with an elevated shape factor more typical of those in laminar boundary layers (despite the adverse pressure gradient). This region persists until the next wake-induced turbulent spots reaches it.

¹ $H = 2.59$ is typical of laminar (Blasius) boundary layers, while $1.3 \leq H \leq 1.4$ is typical of turbulent boundary layers [135].

² but with the phase-averaged velocity field.

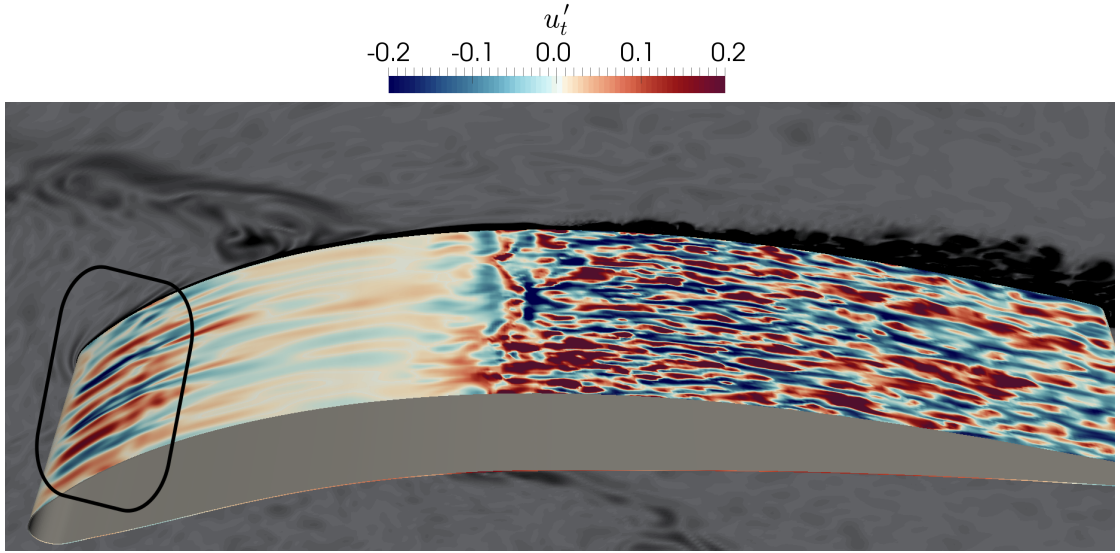


FIGURE 6.11: Case L-W. Contours of the tangential velocity perturbations, u'_t , on the suction surface $d = 1.02 \times 10^{-3}$ plane. Contours of vorticity magnitude, $|\omega|$, at $z = 0$ are shown (greyscale) to identify the passing wake. The snapshot corresponds to $\phi = 0.6$.

The key features of a transitional compressor flow in the presence of wakes have been captured here. For example, the phase-dependent bubble length, the elevated boundary layer thickness due to the wake-induced turbulent spots, and the calmed region behind these spots. Figure 6.11 shows that wake-amplified Klebanoff streaks convecting at $0.7U_{fs}$ cause turbulent spots to form. This mechanism resembles that observed by Coull et al. [20] in turbine flows, and by Zaki et al. [100] in their DNS of the present NACA65 compressor flow. In the compressor studies of Wheeler et al. [26], regions of elevated momentum thickness (θ) were found to convect at $0.7U_{fs}$ and form turbulent spots. Figure 6.13a suggests that in the present flow, a region of noticeably elevated θ doesn't follow the $0.7U_{fs}$ line. This may be due to the elliptical leading edge of the NACA65 blade profile. Wheeler et al. [27] finds that the wake induced θ fluctuations are significantly smaller for an elliptical leading edge blade compared to one with a circular trailing edge, like that used by Wheeler et al. [26].

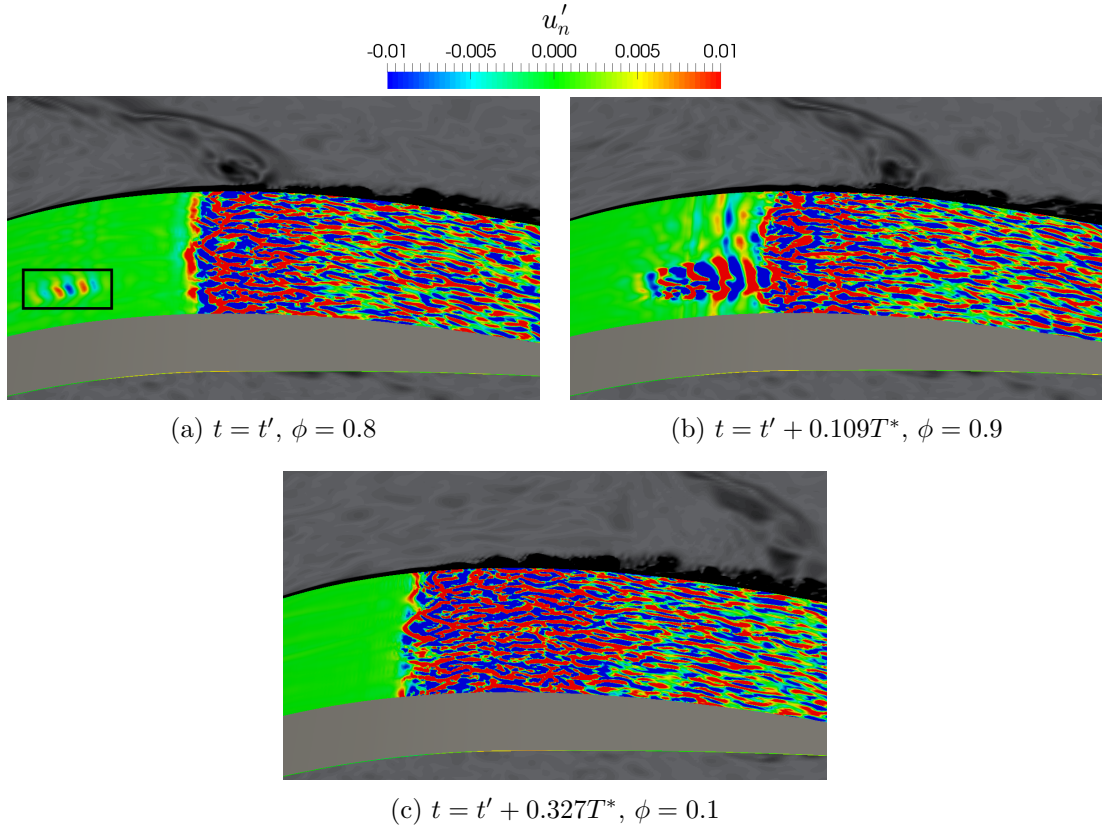


FIGURE 6.12: Case L-W. Contours of the normal velocity perturbations, u'_n , on the suction surface $d = 1.02 \times 10^{-3}$ plane. Three time instances are shown, where $t = t'$ is the time in Figure 6.11. To show the passing wake contours of vorticity magnitude, $|\omega|$, are shown at $z = 0$ (greyscale).

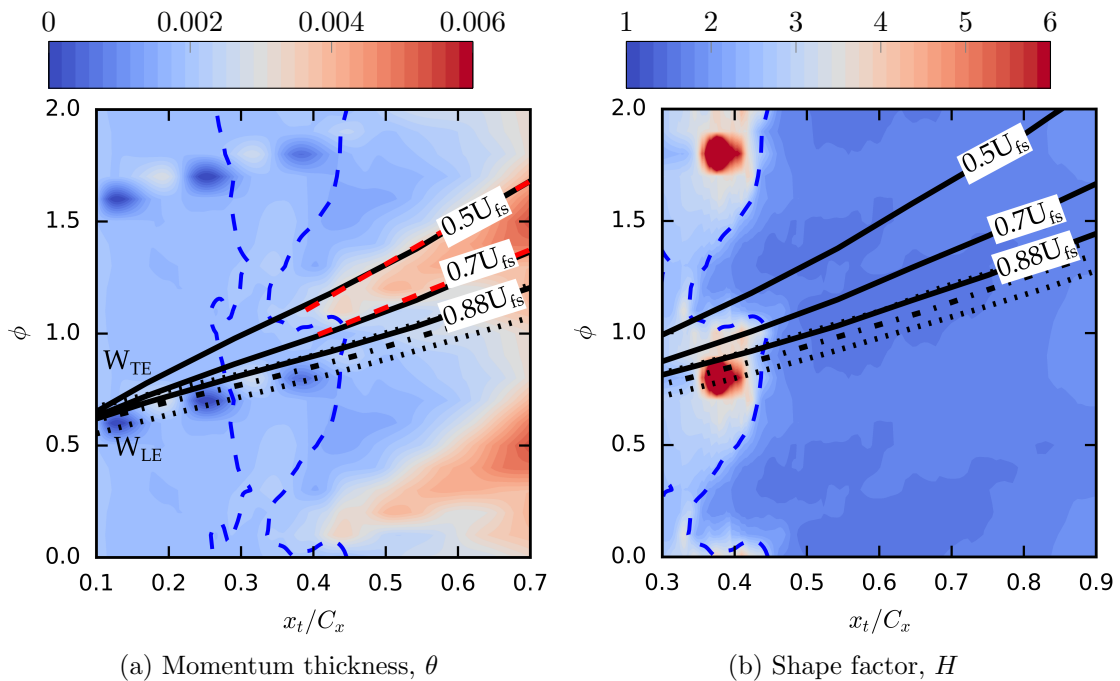


FIGURE 6.13: Case L-W. Phase-averaged space-time plots of the suction surface boundary layer momentum thickness θ and shape factor H . The dashed blue lines indicate the phase dependent separation/reattachment locations (indicated by $\langle C_f \rangle(\phi) = 0$).

6.3 The endwall flow

The detrimental effect of the three-dimensional separation occurring in suction surface-endwall corner of axial flow compressors was highlighted in the literature review. In this section, the three-dimensional separation that occurs in the PVD cascade is explored. An instantaneous snapshot of case L-TBL is shown in Figure 6.14. The suction surface flow near the mid-span is qualitatively similar to the mid-span case L; with a streaky laminar boundary layer, laminar separation and turbulent reattachment. The obvious difference is that there is now a turbulent endwall boundary layer at $z = 0$, and a larger three-dimensional "corner separation" is seen in the suction surface-endwall corner.

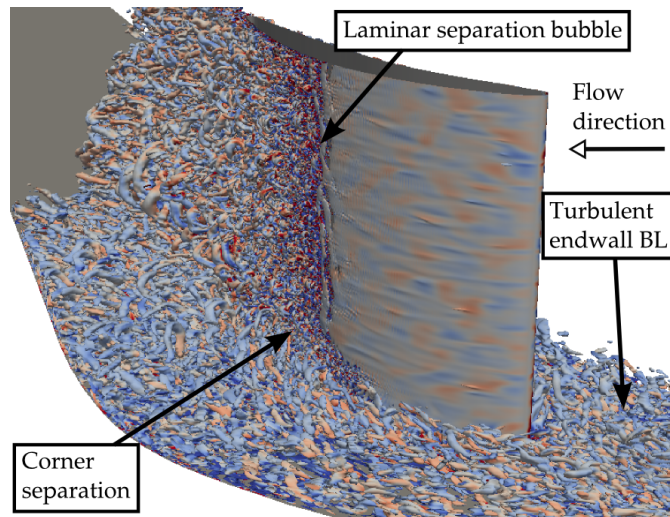


FIGURE 6.14: Case L-TBL. Instantaneous iso-surfaces of $Q = 400$ coloured by axial vorticity ω_x , showing the suction surface endwall flow.

The flow topology becomes clearer when the time-averaged skin friction lines¹ are examined in Figure 6.15. The laminar separation bubble is visible, as is the large three-dimensional corner separation. Comparing these streamlines to the oilflow from Gbadebo [35] indicates that, qualitatively, the time-averaged LES agrees well with the experiment. A laminar separation bubble is seen on the suction surface in both. The origin of suction surface corner separation is closely predicted, and the corner separation line extends away from the endwall at a similar angle in both. Below the separation line, the flow topology also appears to be closely matched.

A hub-corner stall is not observed in the experimental oilflow or the time-averaged LES endwall streamlines. In Figure 6.16, Lei's [33] stall indicator map (discussed in Section 2.1.3.4) is presented again, but with the PVD operating point added. It is clear that the present case is well within the range in which a full hub-corner stall would not be expected.

¹Obtained by computing the streamlines of the skin friction vector field.

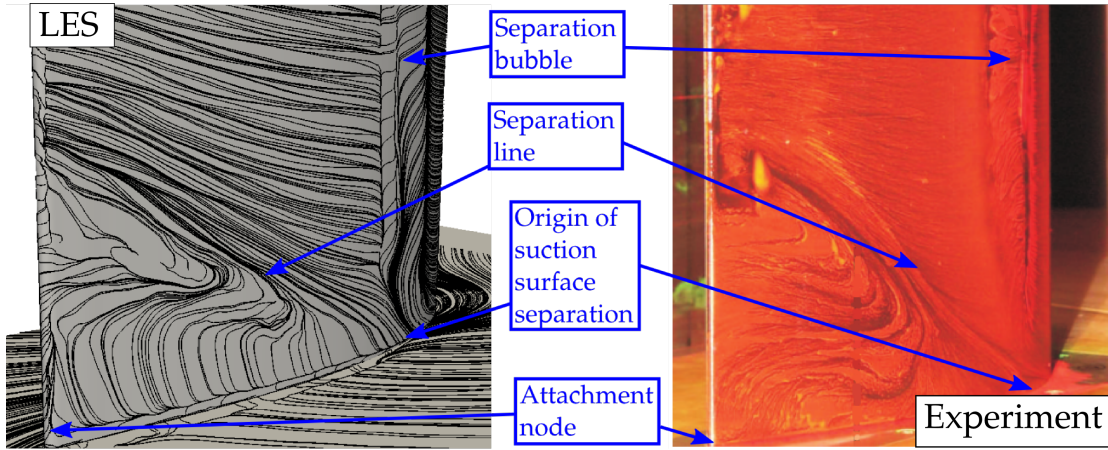


FIGURE 6.15: Case L-TBL. Time-averaged skin friction lines from LES flow compared to the experimental oilflow [35] in the suction surface-endwall corner region.

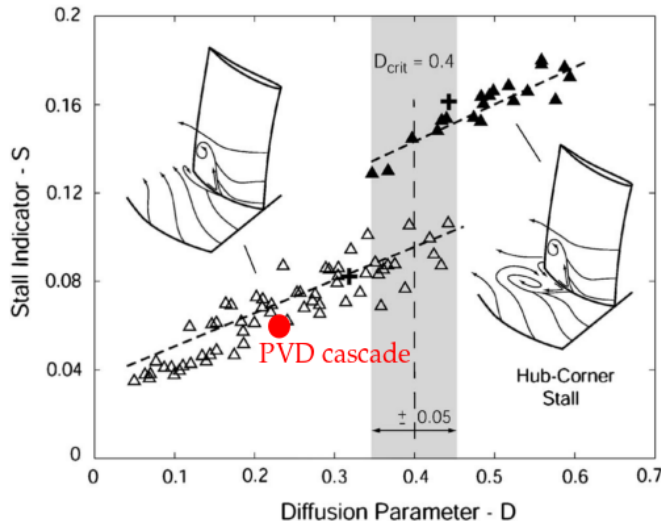


FIGURE 6.16: The operating condition of the PVD cascade (calculated from the experimental C_p distributions [35]) added to Lei's stall indicator map (extracted from Lei et al. [33])

The time-averaged pressure coefficient C_p distributions for a number of the LES cases are plotted in Figure 6.17. Generally, the LES-TBL case is seen to agree well with the experiment¹. The C_p distributions from a RANS SST computation are also plotted in Figure 6.17. Significant disagreement is seen close to the endwall in Figure 6.17b. This is due to the endwall separation occurring prematurely in the RANS solution. The RANS also over-predicts the span-wise extent of the endwall separation, leading to the

¹There is some deviation from the experimental C_p distribution close to the trailing edge near the mid-span (Fig. 6.17a). The higher aspect ratio of the blade (caused by the sponge zone at $0.5 \leq z/h \leq 0.65$) results in the endwall separation's influence on the mid-span C_p being reduced slightly. However, the C_p prediction near the endwall (Fig. 6.17b) is still closely matched, and the above is thought to be more favourable than having non-physical contamination of the mid-span flow caused by an inviscid wall at $z/h = 0.5$.

mid-span C_p prediction being contaminated as seen in Figure 6.17a. The deficiencies in RANS predictions are explored further in Section 6.3.2.

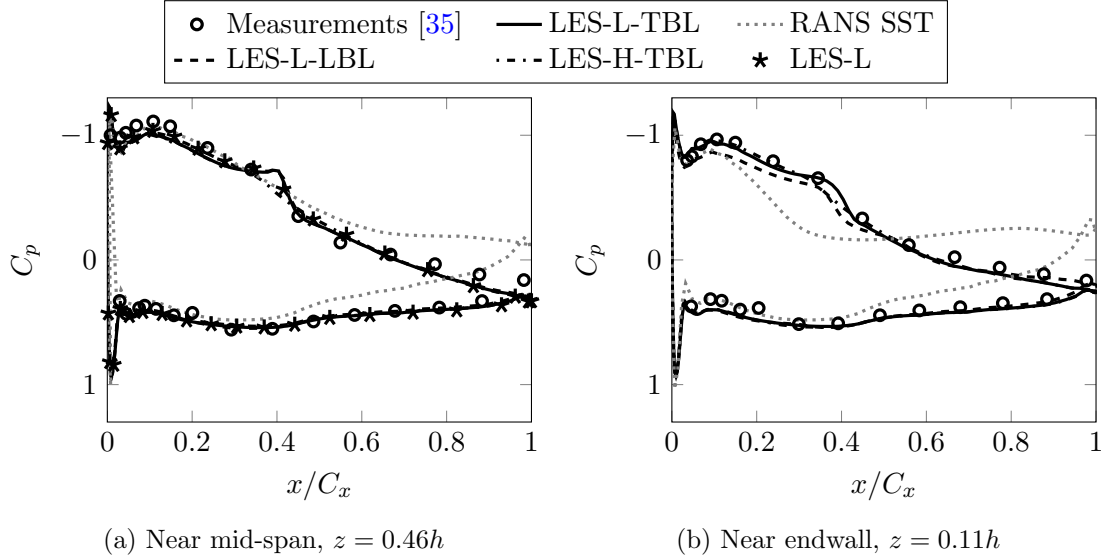


FIGURE 6.17: Cases L, L-TBL, L-LBL and H-TBL. Time-averaged pressure coefficient C_p at $z = 0.11h$ and $z = 0.46h$. The case L distribution is spanwise averaged.

To compare with Gbadebo [35], the time-averaged loss coefficient $Y_p = (\bar{p}_{01} - \bar{p}_0)/(\frac{1}{2}\rho U_1^2)$ and exit angle α_2 are mass-averaged in the pitch-wise direction at the plane shown in Figure 6.1. They are then plotted against span in Figure 6.18. The downstream exit angle prediction from case L-TBL (Fig. 6.18b) is in good agreement with the experiment. The downstream loss prediction (Fig. 6.18a) also agrees well, with only a slight deficit in the predicted loss between 5% and 25% span. Again, the RANS SST prediction is poor here, with the downstream loss and under-turning of the flow being significantly over-predicted.

6.3.1 Effect of inflow turbulence

When comparing case L-LBL to case L-TBL in Figure 6.18, it is apparent that changing the endwall boundary layer state has a significant influence on the loss. However, perhaps surprisingly, increasing the free-stream Ti by an order of magnitude (1% to 10%) has had only a small effect on the endwall flow. In Sections 6.3.1.1 and 6.3.1.2 reasons for the above observations are explored. The sources of loss are then examined in Section 6.3.1.3.

6.3.1.1 Endwall boundary layer state

Gbadebo [35] varies the thickness of the incoming endwall boundary layer, and finds that a thicker endwall boundary layer leads to a significantly larger endwall separation.

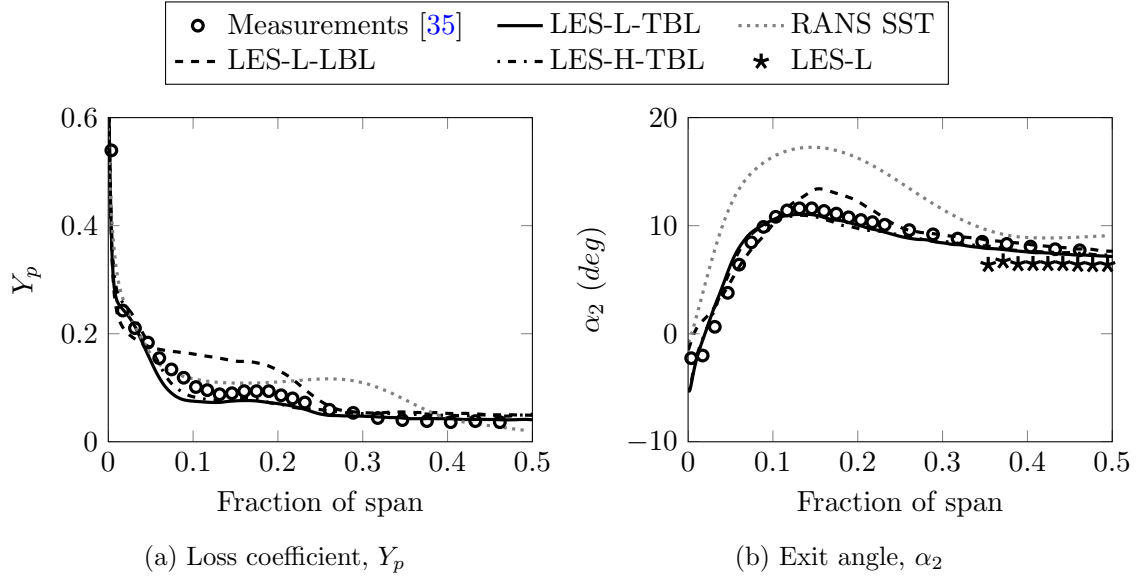


FIGURE 6.18: Cases L, L-TBL, L-LBL and H-TBL. Time-averaged loss coefficient Y_p and exit angle α_2 versus span. Both are mass-averaged in the pitch-wise direction across the downstream plane shown in Figure 6.1.

It is also of interest to determine whether the state of the endwall boundary layer is important, as there is often uncertainty here in experiments.

Figure 6.3 (in Section 6.1.3) shows that, as expected, the shape factor H for the laminar boundary layer (LBL) in case L-LBL is higher than for the TBL in case L-TBL. The laminar boundary layer cannot withstand the adverse pressure gradient as it approaches the leading edge, and the shape factor rises. Consequently, the laminar endwall boundary layer lifts off the endwall much further upstream compared to the TBL in case L-TBL. This is seen in Figure 6.19, where the horse-shoe vortex saddle point¹ is much further upstream in Figure 6.19a compared to Figure 6.19b. This significantly alters the topology of the surface streamlines on the endwall. The footprint of the pressure leg of the horse-shoe vortex suggests this vortex is much larger in case L-LBL. This large vortex migrates down from the blade above, interacts with the corner separation and results in a larger passage vortex. The endwall separation region is larger, and the endwall separation line is less clear.

The larger pressure leg of the horse-shoe vortex, and the resulting large passage vortex, are also visible in Figure 6.20a. Comparing the surface streamlines on the blade in Figures 6.19a and 6.19b suggests that the endwall boundary layer state has not significantly influenced the flow topology on the forward part of the suction surface. It follows that the larger passage vortex is responsible for much of the differences in the outflow angle and loss seen in cases L-LBL and L-TBL. The effect on loss is explored in Section 6.3.1.3.

¹For a description of the endwall flow topology, see Section 2.1.3.

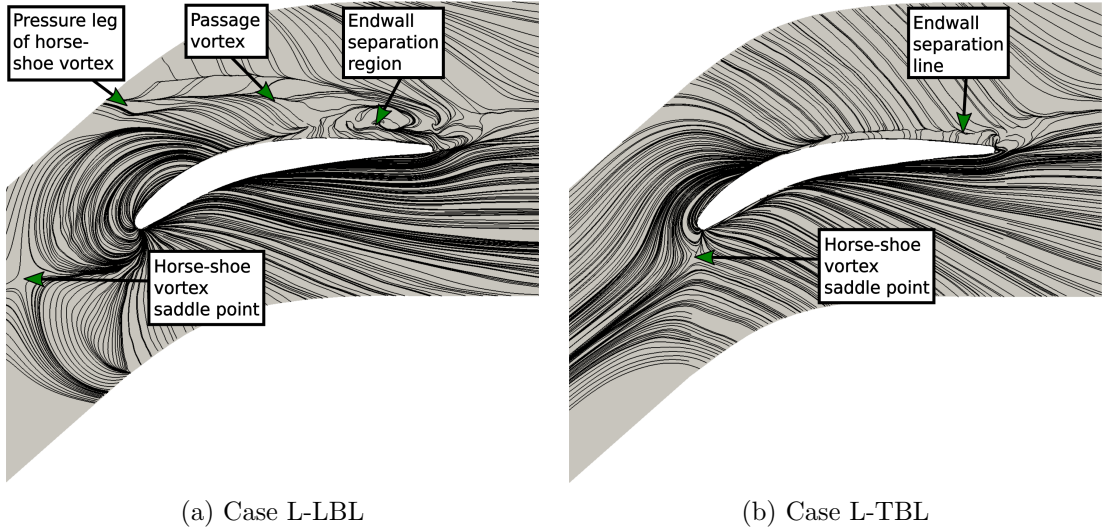
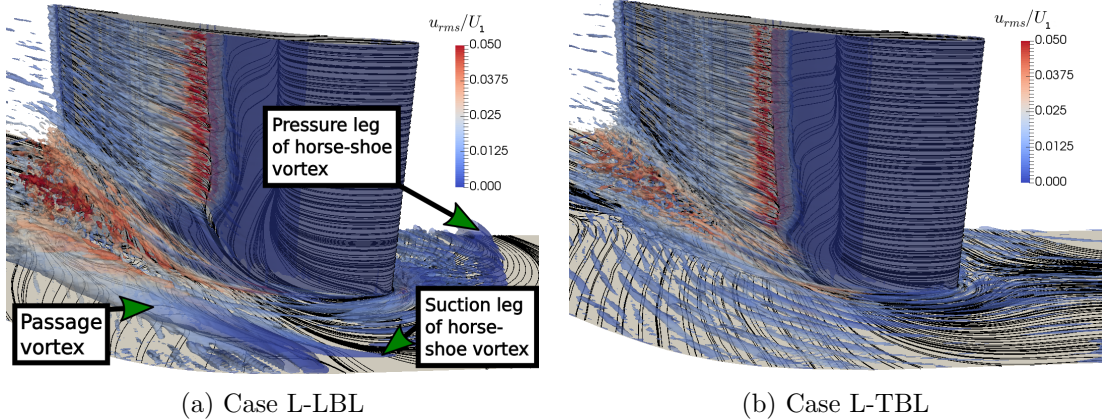


FIGURE 6.19: Cases L-TBL and L-LBL. Time-averaged skin friction lines on endwall.

FIGURE 6.20: Cases L-TBL and L-LBL. Time-averaged (for 4*) iso-surfaces of vorticity magnitude $|\bar{\omega}|$ coloured by u_{rms} .

6.3.1.2 Free-stream turbulence intensity

Increasing the free-stream Ti has little influence on the time-averaged endwall flow. This is surprising, since Goodhand et al. [37] show that if the transition point moves upstream, the thickened suction surface boundary layer will lead to a larger endwall separation. To test if the endwall separation in the PVD cascade is sensitive to the suction surface boundary layer thickness, a boundary layer trip is added to the LES case L-TBL. The method of Boudet et al. [164] is used, where a virtual roughness element of dimensions $L_t \times L_n \times L_z$ is imposed. The element is indented to cause a small separation bubble, with transition occurring above it. The drag force per unit volume of this element is given by

$$F_{trip} = \frac{-1}{2L_t} \rho C_D u_t |u_t|, \quad (6.5)$$

where $C_D = 1$ is used. The drag force is transformed from the wall tangential/normal coordinate system (x_t, x_n) to the x, y coordinate system, and then added as a force term to the x, y momentum equations (Eqn. 2.13) where a trip is desired. The trip was added at $x = 0.07C_x$, and as in the study of Goodhand et al. [37], the trip height L_n is set to 4.6 times the local time-averaged momentum thickness. The aim is to trip the suction surface boundary layer without directly influencing the endwall separation, therefore C_D is set to zero at $z < 0.1h$. A tanh blending function is used to blend C_D to prevent any discontinuities around $z = 0.1h$.

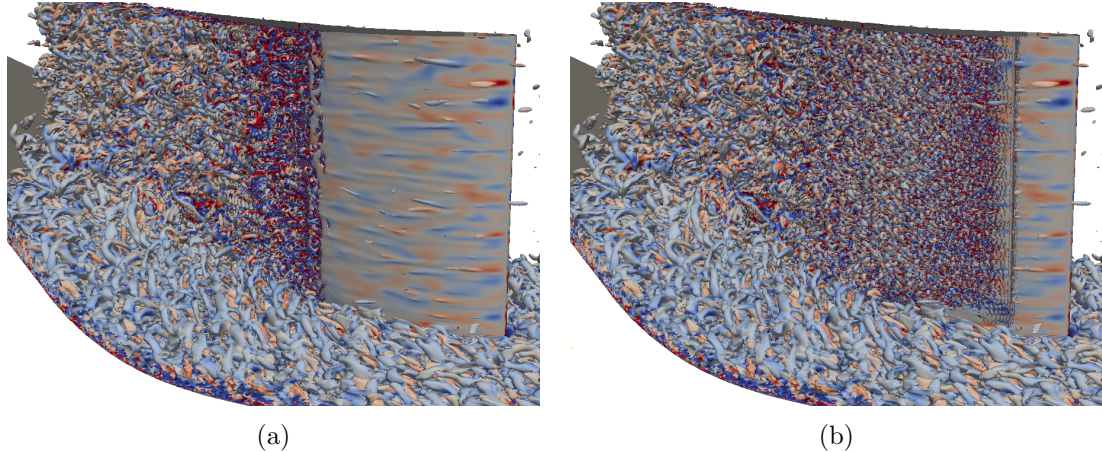


FIGURE 6.21: Case L-TBL. Iso-contours of Q-criterion on suction surface (a) before and (b) after boundary layer trip added.

A snapshot of the flow field, a short time after the numerical trip was switched on, is shown in Figure 6.21b. The trip appears to have moved the transition point upstream as intended. This is confirmed in the C_f plot in Figure 6.22a. Figure 6.22b shows the effect of the trip on the suction surface displacement thickness. The boundary layer δ^* is 53% larger than in the no-trip case at $x = 0.6C_x$. The effect this has on the endwall separation is shown in Figure 6.23.

In the clean blade flow (Fig. 6.23a), the laminar boundary layer is seen to separate at $x = 0.29C_x$. The endwall separation line originates at $x = 0.48C_x$, and the endwall separation grows to a maximum span-wise extent of $0.28h$. In comparison, in the tripped case (Fig. 6.23b) the small separation bubble at $x = 0.07C_x$ is seen, and the endwall separation line once again originates at $x = 0.48C_x$. However, in this case, the angle formed between the endwall separation line and the endwall is 10° larger¹, and the maximum span-wise extent of the endwall separation is thus $0.1h$ greater.

¹The accelerated growth rate of the endwall separation is not thought to be due to the lower C_f in the tripped boundary layer case, since the endwall separation grows at the same rate in case H-TBL as case L-TBL despite the difference in C_f (see Fig. 6.22a). It is instead thought to be due to the endwall separation entraining more of the thicker suction surface boundary layer in the tripped case.

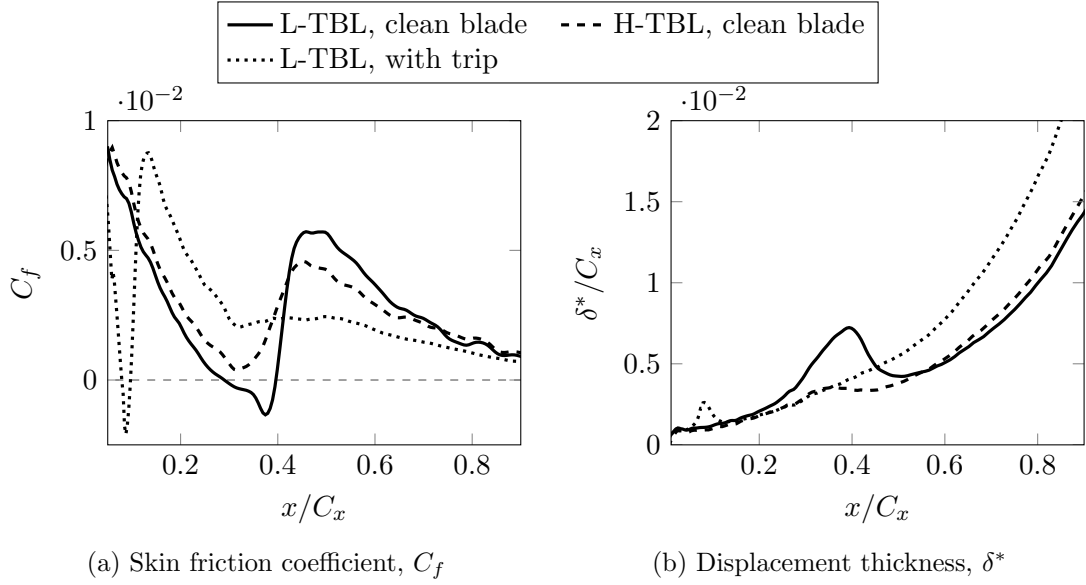


FIGURE 6.22: Case L-TBL. Time-averaged skin friction coefficient C_f and boundary layer displacement thickness δ^* with and without a boundary layer trip applied at $x = 0.07C_x$.

The sensitivity of the endwall separation to the premature transition induced by the numerical trip is clear. Conversely, the free-stream Ti is not observed to have a similar effect. Despite the higher Ti level changing the transition mode from separation induced to bypass, Figure 6.5 shows that the transition region ends at a similar stream-wise location in both cases. The boundary layer thickness, shown in Figure 6.22b, is also similar in both cases. Little direct interaction between the FST and endwall separation is observed, and since the suction surface boundary layer is not noticeably thickened, the endwall separation is relatively insensitive to FST in this flow.

6.3.1.3 Sources of loss

To determine the sources of loss and examine their sensitivity to the inflow conditions, the mean flow energy equation is used:

$$\frac{\partial E}{\partial t} + \bar{u}_j \frac{\partial E}{\partial x_j} = \underbrace{\frac{\partial}{\partial x_j} \left(-\bar{u}_j \frac{\bar{p}}{\rho} + 2\nu \bar{u}_j \bar{s}_{ij} - \bar{u}'_i \bar{u}'_j \bar{u}_i \right)}_{\text{Transport}} - \underbrace{2\nu \bar{s}_{ij} \bar{s}_{ij}}_{\substack{\text{Viscous} \\ -\psi_v}} + \underbrace{\bar{u}'_i \bar{u}'_j \bar{s}_{ij}}_{\substack{\text{Turbulent} \\ -\psi_t}} \quad (6.6)$$

In Equation 6.6 the viscous and turbulent dissipation terms are the only sink (or source) terms. The viscous dissipation represents the dissipation of mean-flow energy by the velocity gradients, and is always negative (i.e. $\psi_v > 0$). The turbulent dissipation represents the energy transfer from the mean flow into turbulent fluctuations. It is usually negative (i.e. $\psi_t > 0$), meaning energy is being transferred from the mean flow.

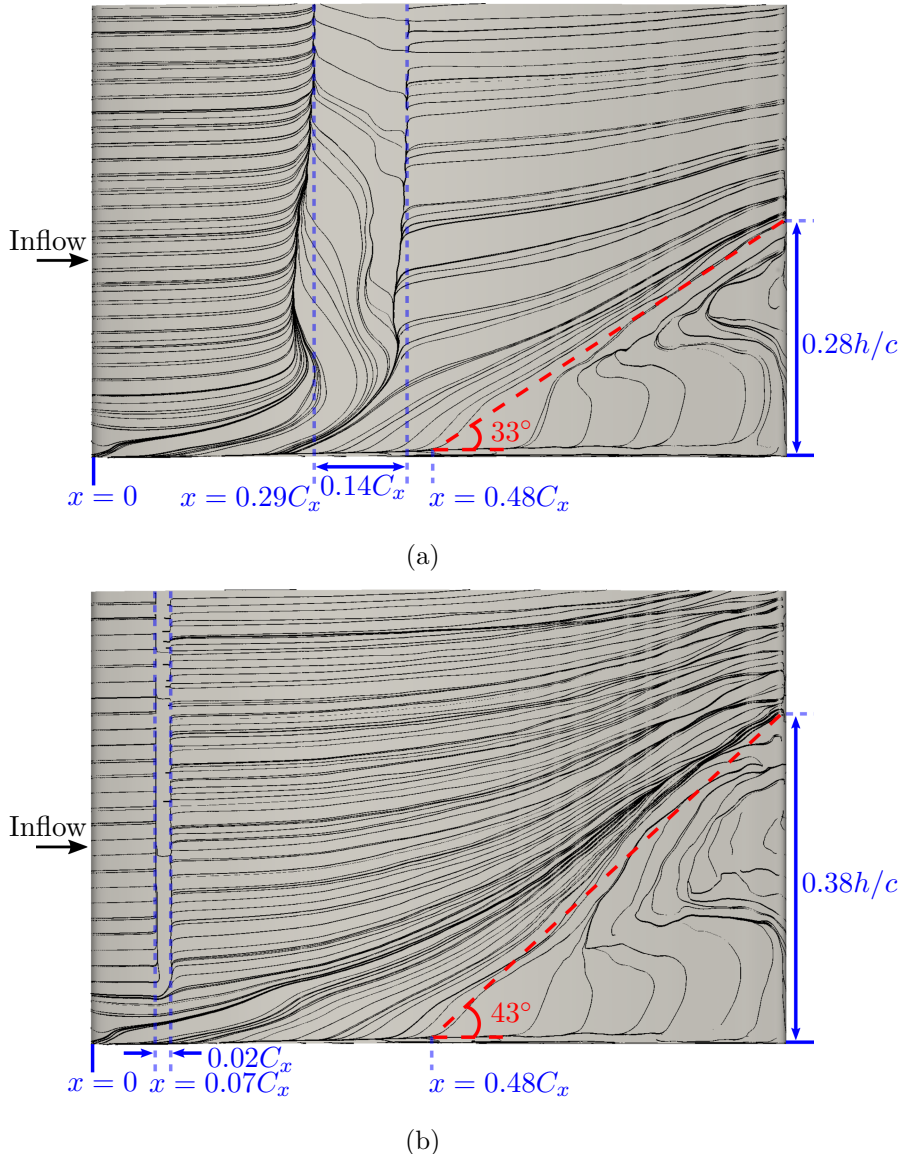


FIGURE 6.23: Case L-TBL. Time-averaged skin friction lines on the suction surface, (a) with and (b) without a boundary layer trip applied at $x = 0.07C_x$.

On some occasions it can be positive (i.e. $\psi_t < 0$), implying the presence of turbulent energy backscatter. In cases L-LBL and L-TBL, a negative value of ψ_t is observed in the separation bubble region. This is in agreement with the work of Germano et al. [65]. They found that during the early non-linear stages of transition, energy is transferred from smaller to larger scales, even in the mean.

Denton et al. [28] and Zlatinov et al. [165] use the entropy generation rate to examine the loss sources in a turbine cascade. In a similar way, the ψ_t and ψ_v terms will be used to examine the loss sources and their sensitivity to the inflow conditions. The flow here is isothermal and thus the thermal dissipation does not need to be considered. To differentiate the loss sources caused by the endwall flow, the domain is split into two

sections; a lower section ($0 \leq z \leq 0.35h$) where endwall effects mean the flow is highly three-dimensional, and an upper section ($0.35h \leq z \leq 0.5h$) where the flow is largely two dimensional. The ψ_v and ψ_t terms are then area averaged (in the pitch-wise and span-wise directions), and plotted against axial distance in Figure 6.24.

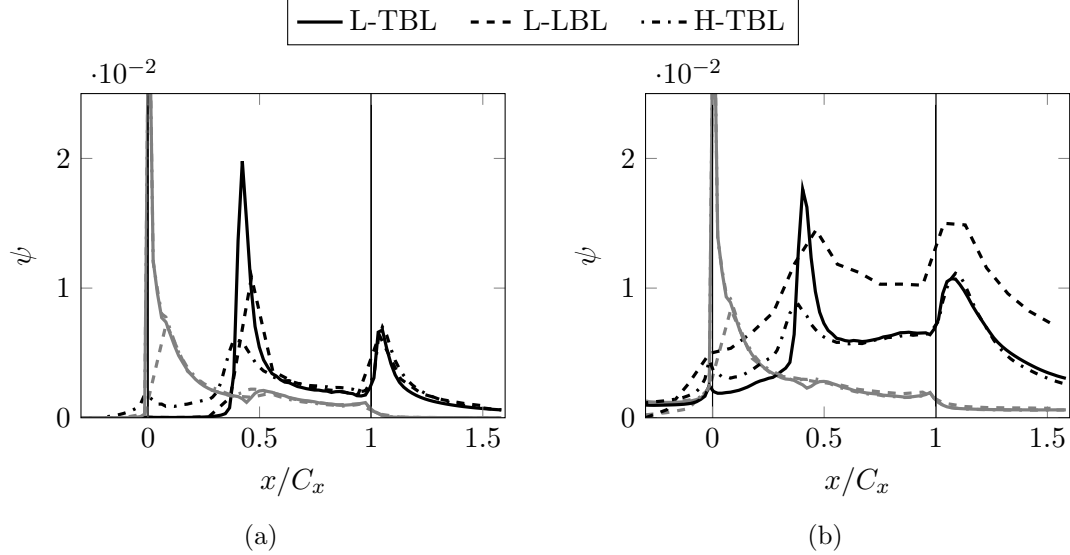


FIGURE 6.24: Cases L-TBL, L-LBL and H-TBL. Area-averaged (in y-z plane) viscous dissipation ψ_v (grey lines) and turbulent dissipation ψ_t (black lines) through the blade passage from (a) 35-50% span and (b) 0-35% span.

In the upper section (Fig. 6.24a) there are three distinct peaks of high loss generation:

Leading edge ($x/C_x \approx 0.0$)

ψ_v (grey line) is high due to the very high strain rates near the leading edge. This sink is insensitive to the inflow conditions.

Laminar separation bubble ($x/C_x \approx 0.4$)

ψ_t (black line) is high due to the high level of turbulence generated in the free shear layer at the edge of the laminar separation bubble (observed in Chapter 5). Since in case H-TBL the separation bubble is bypassed, the peak in ψ_t is lower than for case L-TBL. However, the higher FST intensity in the passage and the earlier pressure surface transition mean that the ψ_t increases earlier in case H-TBL. The state of the endwall BL has little effect here.

Trailing edge shear layers ($x/C_x \approx 1.1$)

ψ_t is high due to the turbulence generated in the shear layers at the edges of the trailing edge wake. The inflow conditions appear to have little effect here.

In the lower section close to the endwall (Fig. 6.24b), the three distinct peaks are still present. However, there is also an area of high turbulent dissipation in the aft region

of the passage ($x/C_x > 0.5$), caused by the three dimensional flow near the endwall. The FST intensity has little influence on the loss in this region, further supporting the conclusion that the endwall flow is insensitive to the FST intensity.

The laminar endwall boundary layer case (L-LBL) shows significantly higher turbulent dissipation in the endwall separation region ($x/C_x > 0.5$ in Fig. 6.24b). Figure 6.25 presents contours of turbulent dissipation at three locations ($x/C_x = 0.41, 0.7, 1.1$), for the turbulent and laminar endwall BL cases:

Figure 6.25a: Case L-TBL The ψ_t is high in the three dimensional separation region where there is reverse flow on the suction surface (seen at $x/C_x = 0.7$), and this separated region persists downstream at $x/C_x = 1.1$.

Figure 6.25b: Case L-LBL There is also high ψ_t in the shear layer between the passage vortex and the free-stream, and the ψ_t is especially high where the passage vortex interacts with the corner separation close to the suction surface.

The overall effect of the local ψ_v and ψ_t on the loss can be seen by plotting the cumulative integral of their sum with respect to the axial direction:

$$\Psi_{tot}(X) = \int_{x=-0.7C_x}^{x=X} (\psi_t(x) + \psi_v(x)) dx \quad (6.7)$$

where $\Psi_{tot}(X)$ is the total area averaged energy dissipation so far (i.e. between $-0.7C_x < x < X$). This is plotted against x in Figure 6.26.

Near the mid-span (Fig. 6.26a), the high FST intensity in case H-TBL causes a higher Ψ_{tot} early on. However, Ψ_{tot} in the other two cases rapidly increases to rejoin case H-TBL due to the high ψ_t in the separation bubble at $x/C_x \approx 0.4$. By the outflow plane at $x/C_x = 1.52$, the total dissipation in the upper section is very similar for all three cases, with case L-TBL having a slightly lower total. These findings correlate well with the loss coefficient plot in Fig. 6.18a, where the loss at mid-span is slightly lower for case L-TBL.

Near the endwall (Fig. 6.26b), where 3D flow effects are significant, the FST has little effect. The Ψ_{tot} lines for both FST cases follow closely. Conversely, Ψ_{tot} increases more rapidly in the L-LBL case downstream of the separation bubble ($x/C_x > 0.5$), due to the effects of the passage vortex discussed previously. Again, these findings correlate well with the loss coefficient distribution in Fig. 6.18a. Near the endwall, the loss in the high and low FST intensity cases are very similar, whereas the loss in the L-LBL case is much higher here.

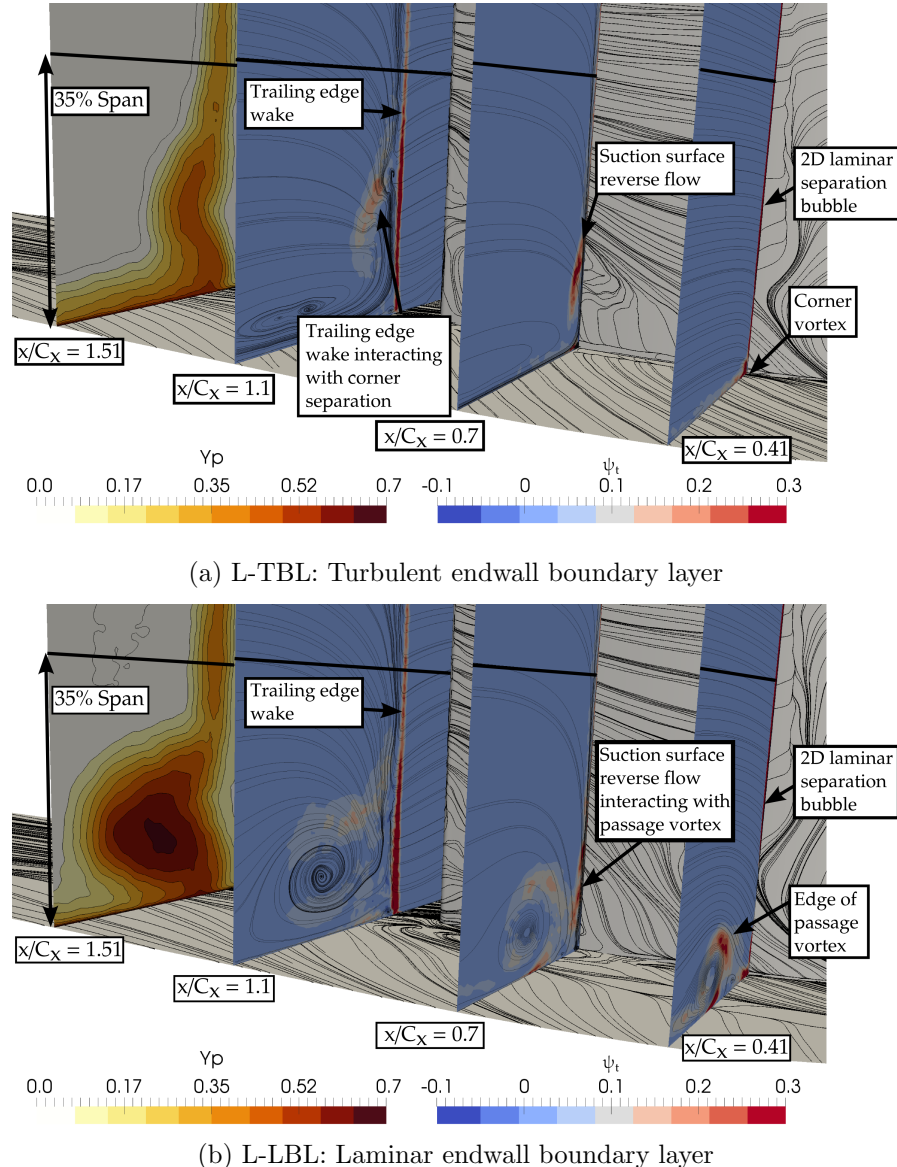


FIGURE 6.25: Cases L-TBL and L-LBL. Contours of turbulent dissipation ψ_t and loss coefficient Y_p in endwall region, showing effect of endwall boundary layer state.

6.3.2 Challenges for lower fidelity modelling approaches

As discussed in Section 2.3.3, LES requires significant computational resources. For this reason, lower fidelity modelling approaches such as RANS are likely to remain the primary CFD compressor design tool for the foreseeable future, especially for higher Reynolds number flows.

The use of RANS for such flows can lead to a high degree of uncertainty, as shown by the grey regions in Figure 6.27. As with the RANS SST result presented in Figure 6.17, the commonly used Spalart-Allmaras (SA) RANS mode also leads to a premature endwall separation and over prediction of the endwall separation extent. Section 6.3.1.2 suggests

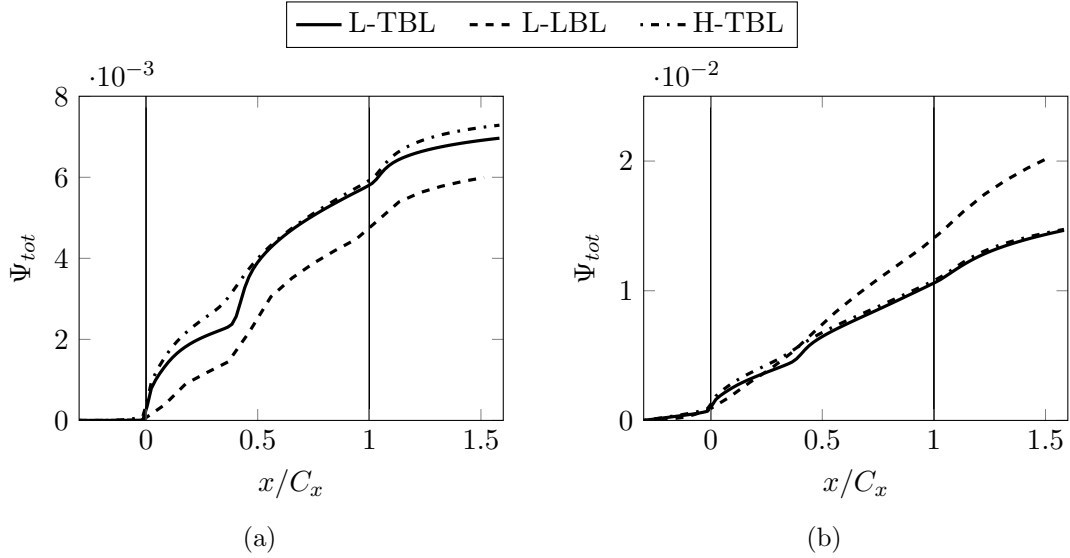


FIGURE 6.26: Cases L-TBL, L-LBL and H-TBL. Cumulative integral of area-averaged total dissipation Ψ_{tot} through the blade passage from (a) 35-50% span and (b) 0-35% span.

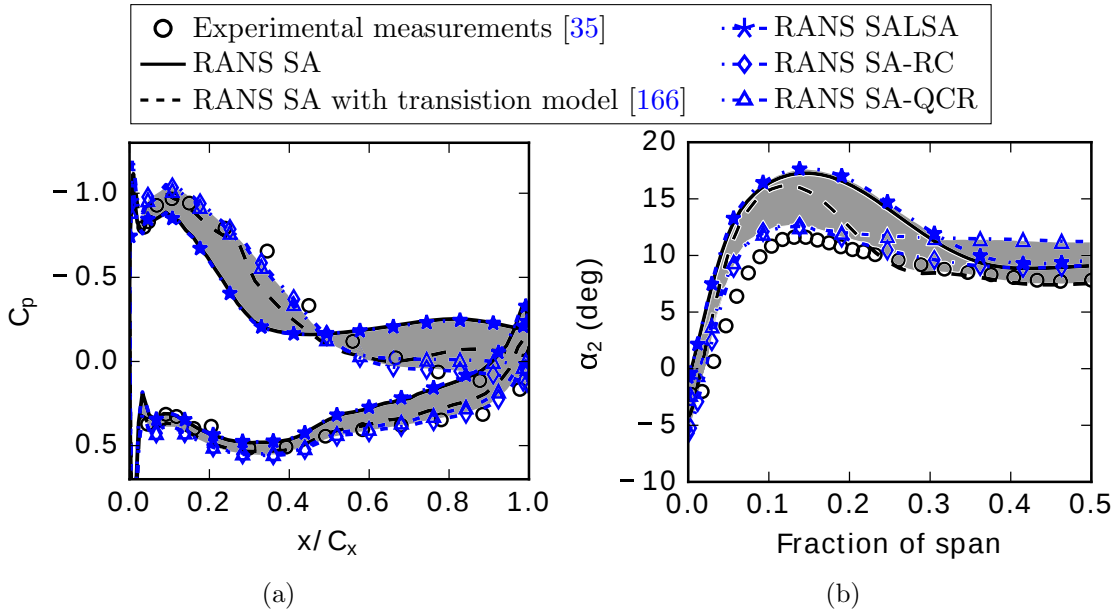


FIGURE 6.27: Time-averaged (a) pressure coefficient C_p and (b) mass averaged exit angle α_2 (on the plane shown in Figure 6.1), for a number of RANS models.

that the fully turbulent suction surface boundary layers in the RANS solutions could be one reason the span-wise extent of the endwall separation is over-predicted. Figure 6.27b shows that the addition of a transition model [166] does indeed lead to a reduced span-wise extent, with the mid-span flow no longer being under-turned. However, there is still significant disagreement close to the endwall, suggesting the RANS SA model is still not sufficient for such a flow.

To investigate if the RANS SA predictions could be improved, a number of RANS model

extensions¹ were tested. Figure 6.27 suggests that no one extension universally improves the predictions. For example; SA-RC reduces the size of the endwall separation, leading to improved C_p and exit angle predictions. However, it leads to poor loss predictions². SA-QCR improves results close to the endwall, but leads to flow separation at the mid-span (see fig. 6.27b). The key message here is that a single add-hoc correction does not appear to be able to give good predictions of the flow in the PVD cascade. In the following sections, the LES results are used to indicate some of the challenges faced by RANS approaches in the PVD flow.

6.3.2.1 Large-scale unsteady effects

To investigate the unsteady behaviour of the endwall separation, a number of probes are placed at $x = 0.9C_x$. A traverse of probes is placed in the span-wise direction at $\Delta y = 0.058C_x$ from the suction surface, and a single probe (P2) is placed in the free-stream at $\Delta y = 0.306C_x$ from the suction surface. Probe P1 is placed so that it lies on the time-averaged endwall separation line, as shown in Figure 6.28.

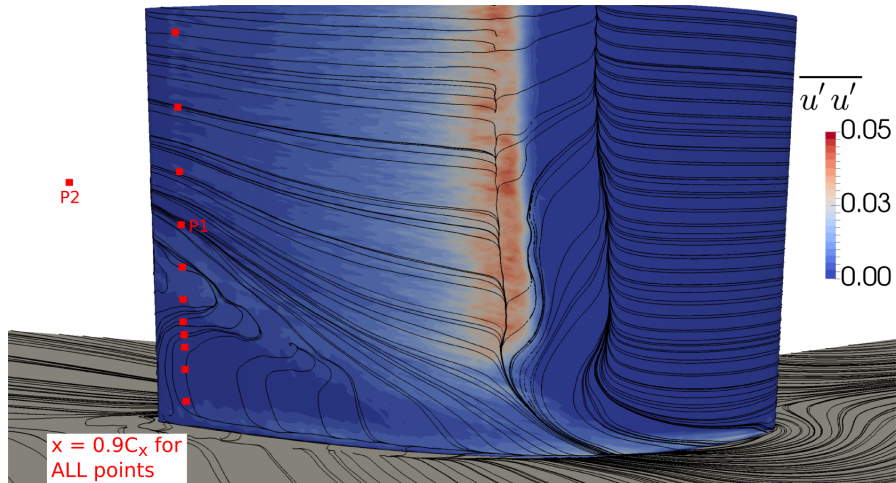


FIGURE 6.28: Case L-TBL. Time-averaged streamlines on planes $d = 1.27 \times 10^{-3}C_x$ from the endwall and the suction surface. The probes used in Section 6.3.2.1 are shown by the red squares. The suction surface plane is coloured by time-averaged resolved Reynolds stress $\overline{u'u'}$.

The power spectral density Φ_{ii} (PSD) of the fluctuating velocity signal u'_i at probes P1 and P2 is plotted in Figure 6.29. In the free-stream (P2), a significant $-5/3$ slope is seen. However, on the edge of the separation region (P1) more energy is contained in the larger scales ($f < 5.5\text{Hz}$), and the $-5/3$ region tails off at a lower frequency.

¹The implementation of the corrections in HYDRA is covered in Section A.3.

²For brevity, the loss predictions are not shown here. See Scillitoe et al. [167] for a more detailed analysis of the RANS correction results.

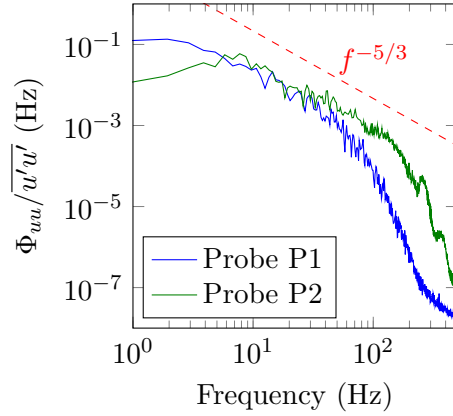


FIGURE 6.29: Case L-TBL. Power spectral density (PSD) of axial velocity fluctuations u' at probe locations P1 and P2 shown in Figure 6.28.

Following the approach of Gao et al. [96], the PSD's are used to approximate the turbulent integral length-scales in the endwall separation region. The integral length-scale in the i direction can be approximated by [38]:

$$L_{ii} = \frac{\int \frac{\Phi_{ii}(\omega)}{\omega} d\omega}{\int \Phi_{ii}(\omega) d\omega} \quad (6.8)$$

where $\omega = 2\pi f$. The resulting integral length-scales in the x,y,z directions across the span-wise traverse are plotted in Figure 6.29. The length-scales of the turbulence in the endwall separation region are over four times larger than at the mid-span. This finding is similar to that of Gao et al. [96], who observed energetic large-scale eddies in the endwall separation region. Unlike Gao et al. [96], in the present case the axial length-scales are noticeably larger than the other length-scales, possibly indicating that vortex stretching is occurring here. The significant difference in length-scales between the endwall separation region and the free-stream may help to explain why the FST does not noticeably interact with the endwall separation.

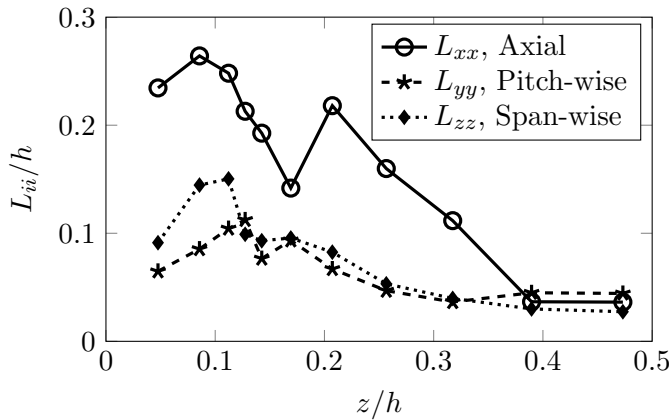


FIGURE 6.30: Case L-TBL. Integral length-scales of turbulence calculated from PSD's of velocity signals at the span-wise probe locations shown in Figure 6.28.

In Figure 6.31, probability density functions (PDF's) of the axial velocity signals at probes P1 and P2 are shown. Following the technique of Ma Wei [168], one-dimensional Gaussians are fitted to these distributions. In the free-stream (P1), the distribution is seen to be largely Gaussian. However, at the span-wise limit of the endwall separation (P2), the sum of two separate Gaussians ($G1 + G2$) provides a better fit to the PDF.

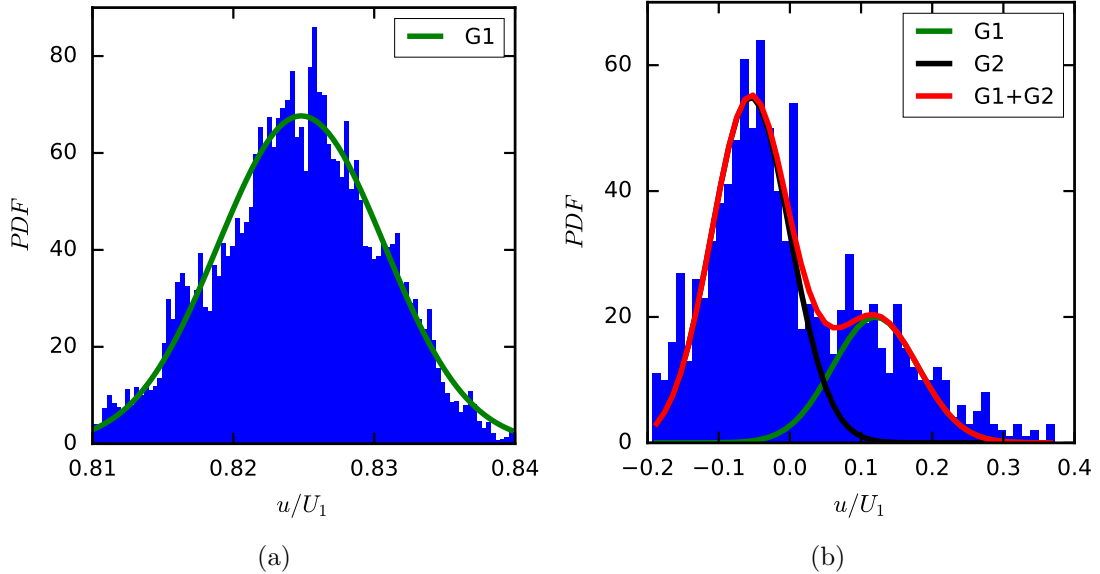


FIGURE 6.31: Case L-TBL. Probability density function of the axial velocity (a) in the free-stream (probe P2) (b) on the edge of the endwall separation region (probe P1). The solid lines are Gaussian's fitted to the PDF's.

Ma Wei [168] and Gao et al. [96] show that a compressor endwall flow can exhibit bi-modal behaviour, whereby the endwall separation switches between two distinct modes. The endwall separation could even switch between a largely open (or stalled) mode and a closed mode. In the present flow the separation remains closed¹. However, the non-Gaussian velocity distribution on the span-wise edge of the endwall separation (Fig. 6.31b) suggests that there is some aperiodic unsteadiness. While not exhibiting clearly bi-modal behaviour, the behaviour observed may still have implications for RANS approaches. The lack of a single Gaussian distribution means that a steady approach may miss some of the effects of the endwall separation. An unsteady RANS approach may therefore be more suitable.

6.3.2.2 Boundary layer transition

The importance of the suction surface transition to an endwall flow was demonstrated in Section 6.3.1.2. A similar effect is seen in the RANS predictions in Figure 6.27. Adding

¹The pitch-wise or stream-wise extents of the endwall separation were not observed to fluctuate significantly, with non-Gaussian behaviour only observed at the edge of the span-wise extent of the endwall separation (i.e. probe P1) in this case. This may be because, as Figure 6.16 shows, the PVD cascade is far from the predicted corner-stall operating region.

a transition model results in a thinner suction surface boundary layer. Therefore, the extent of the endwall separation is not over-predicted as badly.

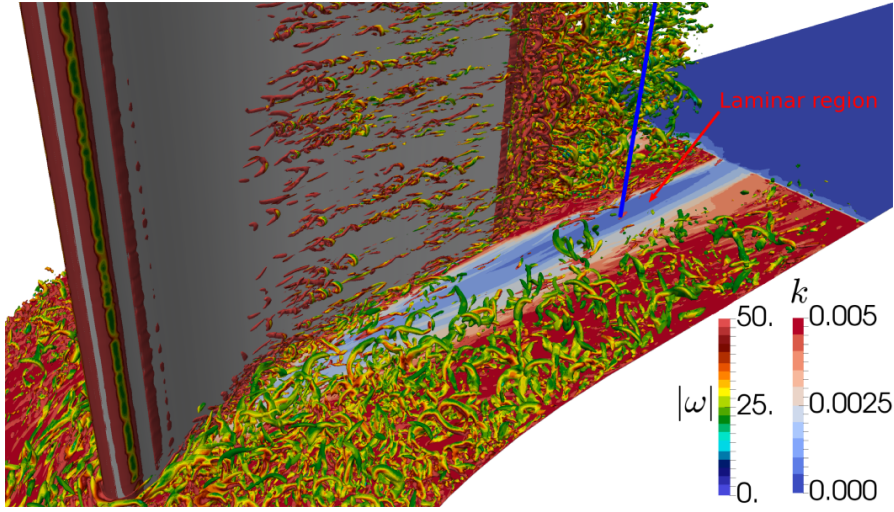


FIGURE 6.32: Case L-TBL. Contours of time-averaged resolved turbulent kinetic energy k on the $z = 1.27 \times 10^{-3} C_x$ plane, focused on the pressure surface - endwall corner. An iso-surface of $Q = 100U_0/C_x$, coloured by vorticity magnitude $|\omega|$, is superimposed.

Additionally, Figure 6.32 shows that a “laminar” region of low turbulent kinetic energy is present in the pressure surface - endwall corner. In Figure 6.33a, the shape factor at mid-pitch is shown. The shape factor is close to the range expected for a typical turbulent boundary layer ($1.3 \leq H \leq 1.4$). However, the velocity profile at the blue line in Figure 6.32, plotted in Figure 6.33b, shows that the boundary layer is closer to a laminar Blasius boundary layer profile. The shape factor here is $H = 2.6$, which indicates that the boundary layer has relaminarised.

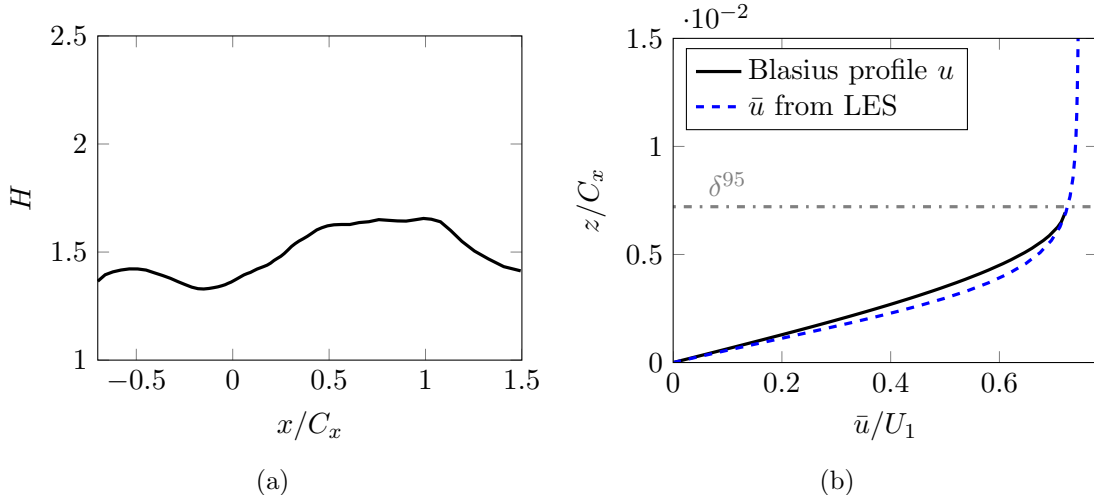


FIGURE 6.33: Case L-TBL. Time-averaged endwall boundary layer measurements. (a) Shape-factor H at mid-pitch. (b) \bar{u} velocity boundary layer profile in laminar region at $x = 1.3$ (along line in Figure 6.32). Blasius profile is given by $u = \sin[(\pi/2)(z/\delta^{95})]u_e$.

Horlock et al. [55] note that this region of relaminarisation is common in turbine endwall flows. The present study shows that, despite the globally adverse pressure gradient, it is also present in compressor endwall flows. This region is another feature that is challenging for RANS approaches to predict [55].

6.3.2.3 Turbulent anisotropy

The main defect in the RANS predictions of the PVD flow is an over-prediction of the endwall separation extent. As Figure 6.27b shows, adding a Quadratic Constitutive relation (QCR) to the SA model noticeably reduces this problem¹. The QCR term is a simple non-linear term which Spalart [8] proposes adding to the Boussinesq closure (Eqn. 2.10):

$$\tau_{ij} = \underbrace{\check{\tau}_{ij}}_{\text{Linear}} - \underbrace{c_{nl1} [O_{ik}\hat{\tau}_{jk} + O_{jk}\check{\tau}_{ik}]}_{\text{Non-linear}} \quad (6.9)$$

This term is intended to give a better prediction of the anisotropy of the Reynolds stress tensor τ_{ij} , and Bordji et al. [57] find that it improves predictions in a wing junction flow. The fact that it influences the size of the corner separation in the PVD cascade suggests turbulent anisotropy might be important. To investigate this, the QCR correction is added to the SST model². The aim is to study the importance of the turbulent anisotropy in the endwall corner, and the QCR term is thus only applied within the endwall boundary layer³. The resulting flow-fields, with and without the QCR term, are shown in Figure 6.34.

In the standard SST model solution (Fig. 6.34a), the endwall separation lifts off prematurely ($x = 0.2C_x$, compared to $x = 0.48C_x$ in LES case L-TBL), and the endwall separation then grows too large. The QCR correction (Fig. 6.34b) delays the endwall separation to $x = 0.33C_x$ and the separation size is therefore less over-predicted at $x = 1.0C_x$. The footprint of the endwall separation on the endwall surface also moves towards the LES solution.

One explanation for the delayed separation of the corner boundary layer in the SST-QCR case could be that the QCR term alters the shear stresses $\overline{u'_t u'_n}$ and/or $\overline{u'_t w'}^4$. These terms would be expected to cause momentum transfer to or from the 3D boundary layer

¹The over-prediction in the exit angle near the endwall is indicative of an over-prediction in the size of the endwall separation.

²The implementation of the QCR correction with the SA model is presented in Section A.3.1, but the QCR term can be added to any linear eddy-viscosity model.

³ c_{nl1} is set to zero at $z < 0.1h$, with a tanh blending function applied to c_{nl1} to prevent any discontinuities in τ_{ij} . Similarly, an attempt to match the transition location of the tripped LES case is made by setting the production of k term to zero at $z > 0.1h$ and $x < 0.07$, with the same tanh blending used at the interface.

⁴The subscripts t and n refer to the directions tangential and normal to the suction surface of the blade.

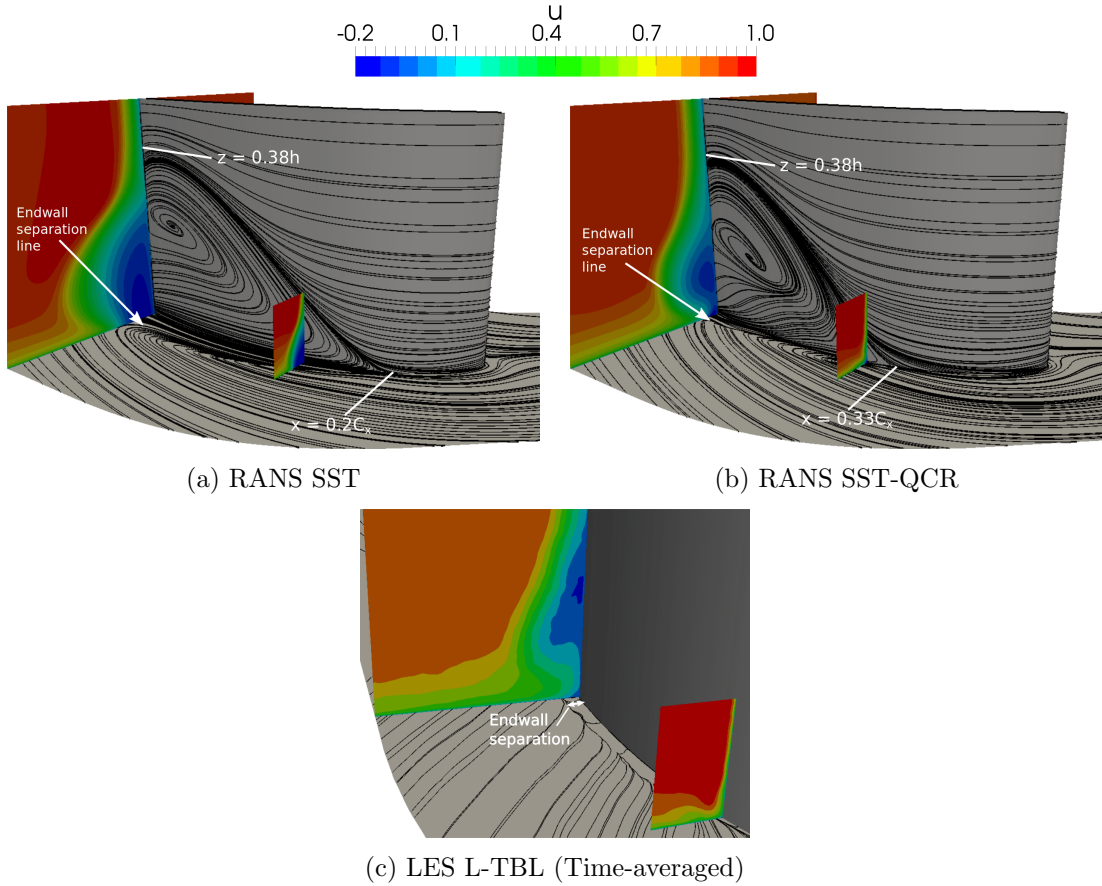


FIGURE 6.34: Skin friction lines and slices of axial velocity u (at $x = 0.4C_x$ and $x = 1.0C_x$). RANS SST, with and without QCR term, and LES case L-TBL shown.

in the corner. However, comparing Figures 6.35a and 6.35b shows that the QCR term does not significantly affect the $\overline{u'_t u'_n}$ term (the $\overline{u'_t w'}$ term is not shown but is also not significantly affected).

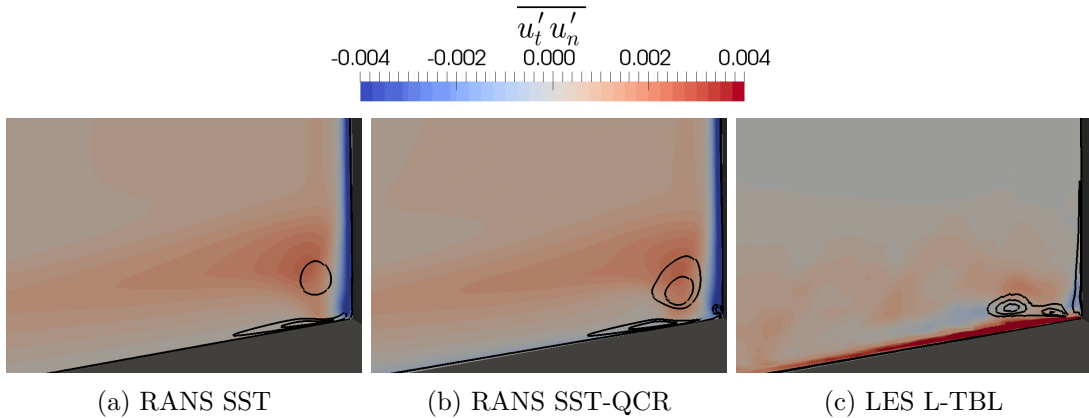


FIGURE 6.35: The Reynolds stress $\overline{u'_t u'_n}$ in the endwall-suction surface corner at $x = 0.15C_x$. The black lines are iso-lines of non-dimensional stream-wise vorticity $\omega_t U_1 / C_x = 1, 2, 3$.

An alternative scenario could be similar to that observed by Bordji et al. [57], where the

QCR correction is seen to reduce the over-prediction of the corner separation in a wing junction flow. Bordji et al. [57] notes how numerous studies disagree on the relative importance between the horse-shoe vortex (HV) system and the corner vortices (CV's) the HV induces. These vortices are shown for the SST-QCR and LES L-TBL cases in Figure 6.36. Bordji et al. [57] hypothesise that the improved prediction of the turbulent anisotropy in the corner results in a stronger corner vortex, which helps energise the corner boundary layer, thus delaying the corner separation. The CV is also seen to be stronger in the SST-QCR case compared to the SST case, as will be shown later.

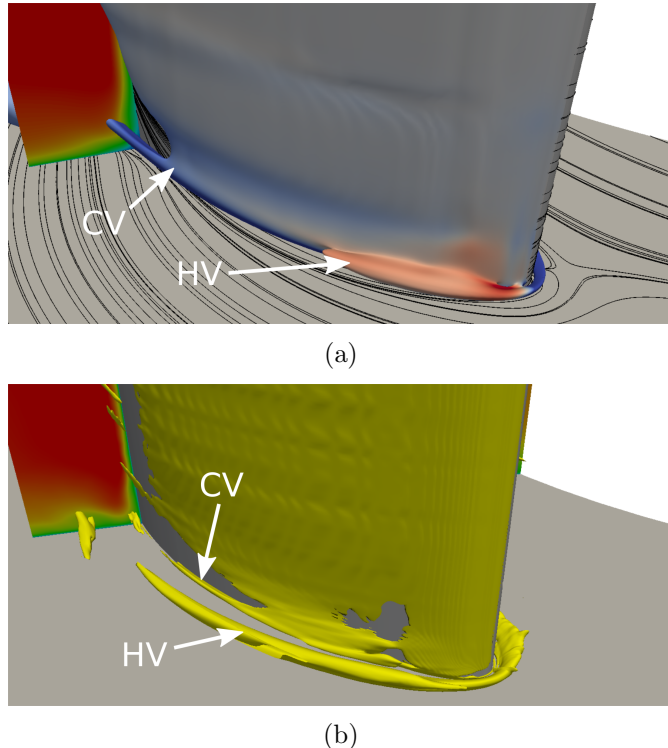


FIGURE 6.36: Iso-surfaces of kinematic vorticity number N_k (defined in Eqn. 3.27) for (a) RANS SST-QCR case ($N_k = 1.05$, coloured by axial vorticity ω_x) and (b) time-averaged LES L-TBL case ($N_k = 1.2$).

Figure 6.37c shows that there is significant turbulent anisotropy in the suction surface - endwall corner in the LES solution, which isn't captured by the SST solution (Fig 6.37a). There are still disagreements between the SST-QCR (Fig. 6.37b) and the LES solutions. However, the QCR term has pushed the prediction in the correct direction, with the dominance of $\overline{u'_n u'_n}$ over $\overline{w' w'}$ close to the endwall being correctly captured. The QCR closure has a similar effect on the $\overline{u'_n w'}$ stress (not shown for brevity), with the prediction moved towards the LES solution¹.

¹Figure 6.37c shows a wall-normal slice close to the leading edge, where the HV and CV are first created, but the strong anisotropy and closer agreement of the SST-QCR solution continue further downstream.

Following Bordji et al. [57], the generation of vortices in the corner can be described by the transport equation for stream-wise vorticity (ξ), given by

$$\underbrace{\overline{u_t} \frac{\partial \xi}{\partial x_t} + \overline{u_n} \frac{\partial \xi}{\partial x_n} + \overline{w} \frac{\partial \xi}{\partial z}}_{\text{Convection of } \xi} = \underbrace{\nu \nabla^2 \xi}_{\text{Viscous diffusion}} + \underbrace{\xi \frac{\partial \overline{u_t}}{\partial x_t} + \eta \frac{\partial \overline{u_t}}{\partial x_n} + \zeta \frac{\partial \overline{u_t}}{\partial z}}_{p_1} + \underbrace{\frac{\partial}{\partial x_t} \left(\frac{\partial \overline{u'_t w'}}{\partial x_n} - \frac{\partial \overline{u'_t u'_n}}{\partial z} \right)}_{p_2} + \underbrace{\frac{\partial^2}{\partial x_n \partial z} (\overline{w' w'} - \overline{u'_n u'_n})}_{p_3} + \underbrace{\left(\frac{\partial^2}{\partial x_n^2} - \frac{\partial^2}{\partial z^2} \right) \overline{u'_n w'}}_{p_4} \quad (6.10)$$

where (ξ, η, ζ) is the vorticity of the mean flow in the (x_t, x_n, z) co-ordinate system. The p_1 term represents the production of stream-wise vorticity ξ by deflection of mean shear, p_2 the production by primary shear stresses, p_3 the production by normal stresses, and p_4 the production by secondary shear stress. Ludwig Prandtl [169] refers to p_1 as “secondary flows of the first kind” and $p_2 + p_3 + p_4$ as “secondary flows of the second kind”. In the present flow the QCR closure does not significantly affect $\overline{u'_t w'}$ or $\overline{u'_t u'_n}$, therefore the p_2 term is not significantly altered. However, $\overline{w' w'} - \overline{u'_n u'_n}$ and $\overline{u'_n w'}$ are altered, and consequently so are p_3 and p_4 .

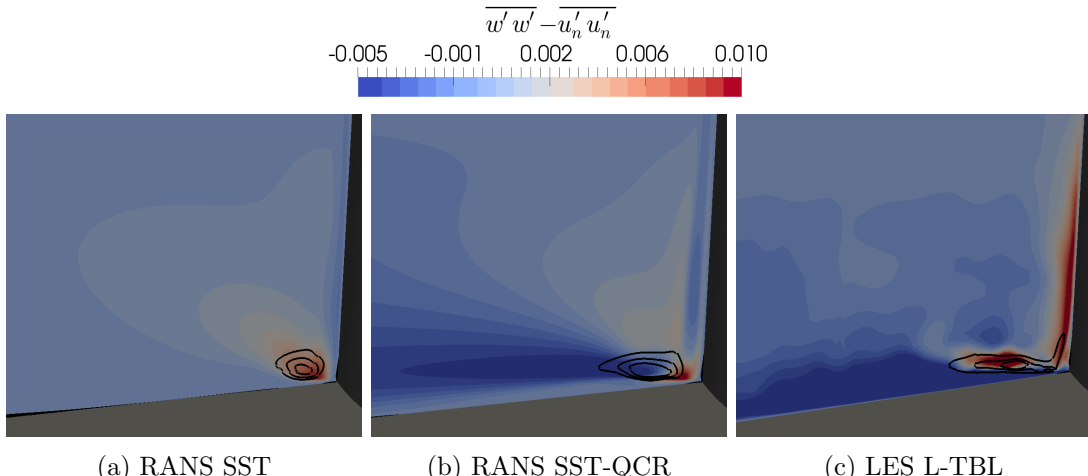


FIGURE 6.37: Difference between span-wise $\overline{w' w'}$ and wall-normal $\overline{u'_n u'_n}$ (suction surface) Reynolds stresses in the endwall corner, very close to the leading edge ($x = 0.0025C_x$). The black lines are iso-lines of non-dimensional stream-wise vorticity $\xi U_1/C_x = 1, 2, 3$.

Figure 6.38 shows contours of $p_3 + p_4$ in the suction surface - endwall corner at $x = 0.15C_x$. Iso-lines of constant streamwise vorticity are superimposed to highlight the HV ($\xi > 0$) and CV ($\xi < 0$). The change in $\overline{w' w'}$ - $\overline{u'_n u'_n}$ and $\overline{u'_n w'}$ caused by the QCR closure has resulted in a more negative $p_3 + p_4$ term in the vicinity of the CV. This additional negative production of stream-wise vorticity may be helping to sustain the CV in the SST-QCR case. Gand [170] states that a corner vortex may delay the onset of the corner separation by preventing the stagnation of low momentum fluid in the corner.

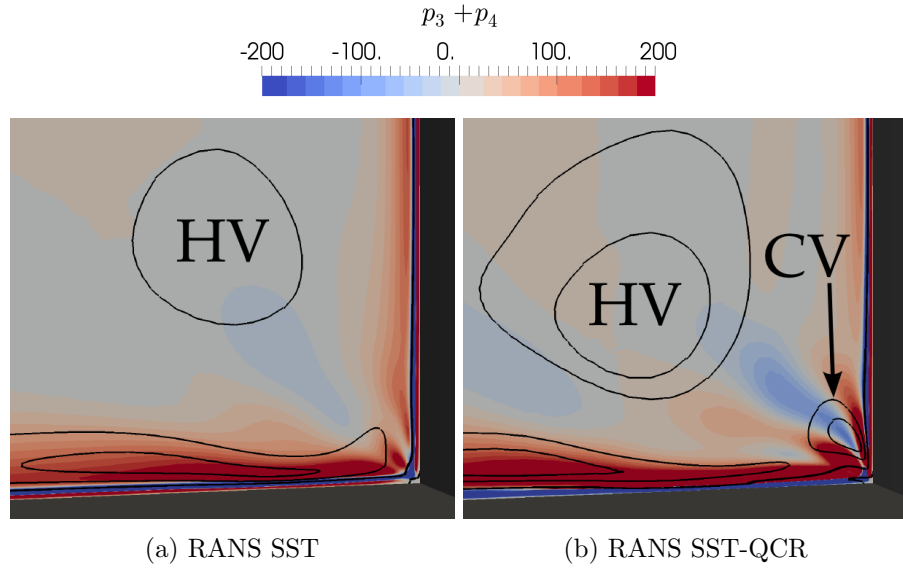


FIGURE 6.38: The production of stream-wise vorticity ξ due to the sum of normal stresses (p_3) and shear stresses (p_4) in the endwall-suction surface corner, at $x = 0.15C_x$. The black lines are iso-lines of stream-wise vorticity $\xi U_1/C_x = -15, -10, 2, 3$.

6.3.3 Addition of an endwall fillet

In many modern compressors the blade - endwall corners are filleted. There are many studies examining the effect of fillets on compressor flows. This isn't a focus here. Instead, a fillet is added to the PVD cascade to determine whether a non-linear term such as the QCR is still important. A circular fillet with a radius of $0.05c$ is added¹, as shown in Figure 6.39. A 90° “butterfly” mesh is used in the corner, with the mesh spacing held as similar to the no-fillet LES and RANS cases as possible.

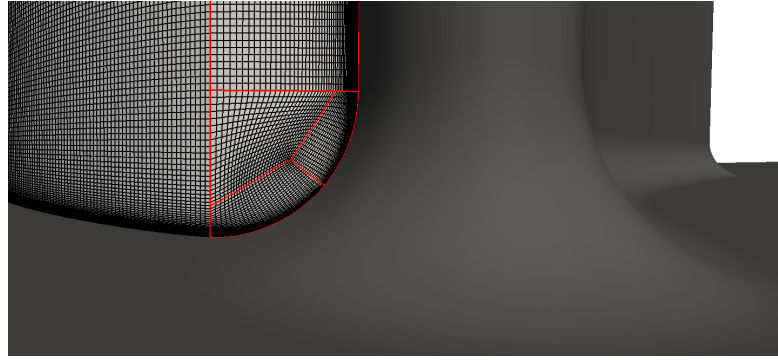


FIGURE 6.39: Close-up of the blade leading edge with a fillet added to the endwall - blade corner. The red lines show the 90° butterfly mesh topology in the endwall corner.

Figure 6.40 suggests that the addition of the corner fillet has a negligible influence on the time-averaged endwall flow. The only noticeable difference is a small increase in the over-turning of the endwall boundary layer, seen in Figure 6.40b. This finding is in

¹This fillet radius is similar to the radii used by Meyer et al. [171].

agreement with Reutter et al. [172], who find their optimised fillet design has little effect at the “on-design” operating point.

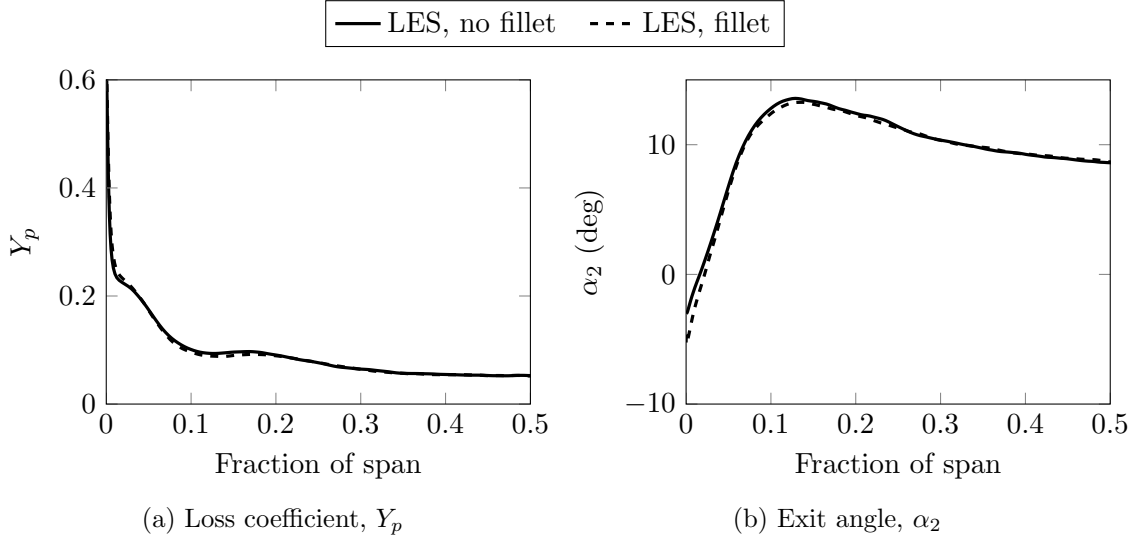


FIGURE 6.40: Case L-TBL, with and without endwall corner filleted. Time-averaged loss coefficient Y_p and exit angle α_2 versus span. Both are mass-averaged in the pitchwise direction across the downstream plane shown in Figure 6.1.

Despite not significantly influencing the mean flow in the LES, the fillet is important for the RANS predictions, as seen in Figure 6.41. A distinct separation line is no longer visible on the endwall, with the overturning endwall boundary layer instead being swept onto the suction surface. The 3D corner boundary layer, and therefore the turbulent anisotropy, is now less crucial. Consequently, the SST prediction is in closer agreement with the LES.

Comparing Figures 6.41b and 6.41a shows that the QCR term now has little influence on the overall flow. This may be because the corner vortex is no longer important. Also, Figures 6.37c shows that the turbulence in the corner region is less anisotropic. The $\overline{w'w'} - \overline{u'_n u'_n}$ term in the SST solution is now in closer agreement with the LES, even without the QCR closure.

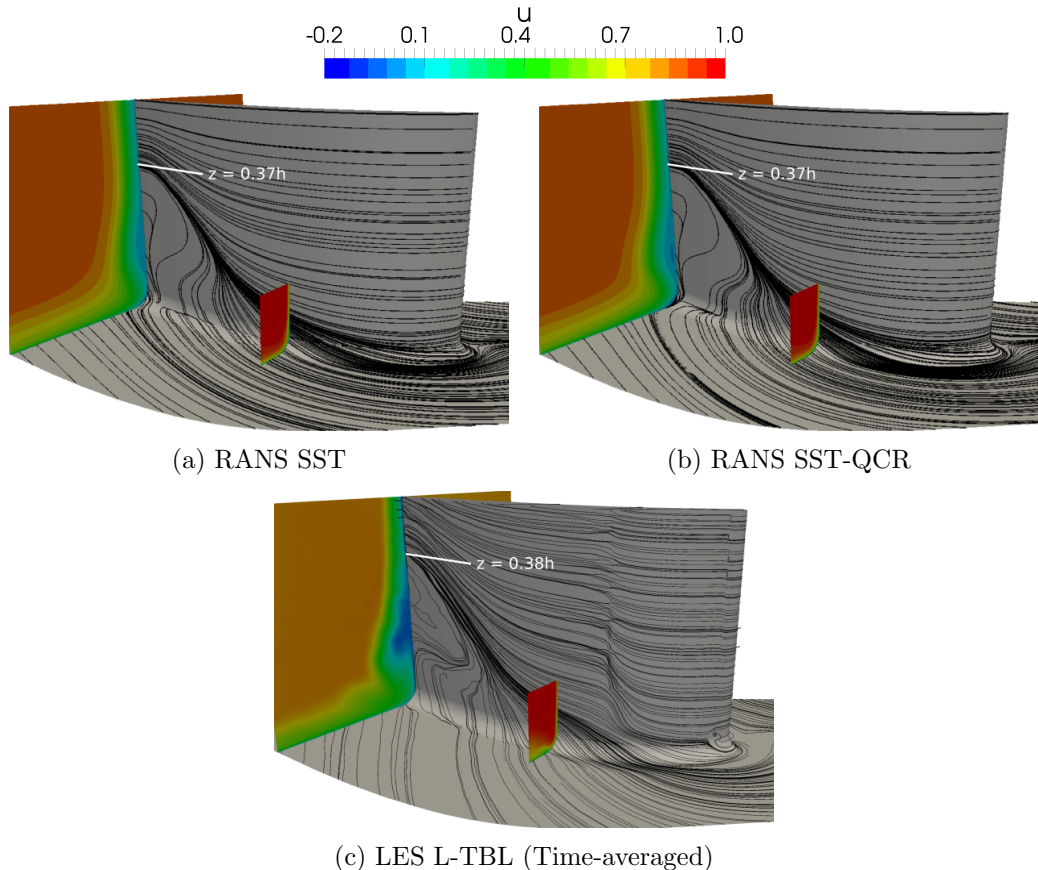


FIGURE 6.41: Endwall corner filleted. Skin friction lines and slices of axial velocity u (at $x = 0.4C_x$ and $x = 1.0C_x$). RANS SST, with and without QCR term, and LES case L-TBL shown.

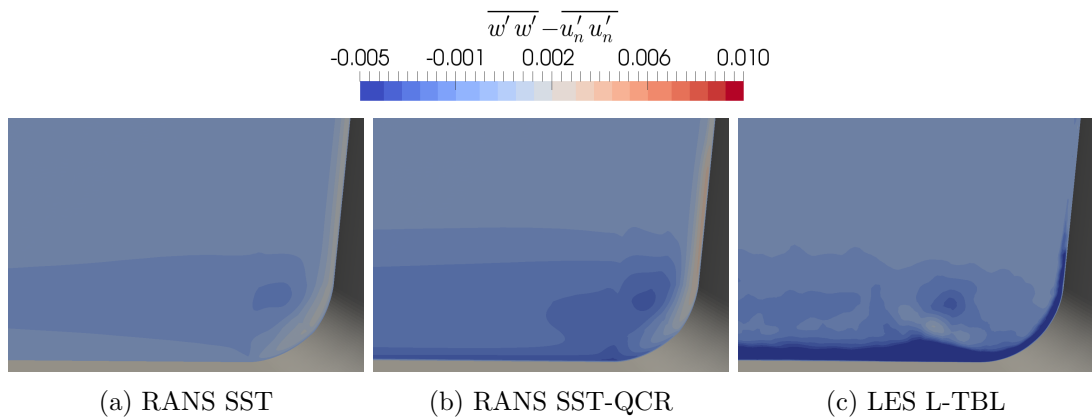


FIGURE 6.42: Endwall corner filleted. $\overline{w'w'} - \overline{u'_n u'_n}$ term in the endwall corner, very close to the leading edge ($x = 0.0025C_x$). RANS SST, SST-QCR, and LES case L-TBL.

6.4 Concluding Remarks

This chapter has demonstrated the potential of LES for exploring the complex flow features found in real gas turbine flows. The study of incoming wakes in Section 6.2.2 highlighted the importance of considering the periodically varying component of the

flow, when moving towards predictive LES of engine representative compressor flows. The key findings here were:

- Incoming wakes were found to cause a phase dependent thickening of the suction surface boundary layer. Coull et al. [173] finds that this causes an increase in the profile loss.
- The calmed region behind the wake-induced turbulent spots, seen in other wake studies, was also observed. Walker et al. [163] discuss the importance of the calmed region, and note that the majority of transition models are intermittency based and therefore do not account for the calmed region.
- Wake-amplified Klebanoff streaks were found to instigate turbulent spots which periodically shorten the suction surface separation bubble. This has more in common with the turbine flows of Coull et al. [20] than the compressor flow of Wheeler et al. [27], who found regions of large θ convecting from the leading edge causes turbulent spots.

In Section 6.3 the sensitivity of the endwall flow region to the inflow conditions was examined, and loss sources were explored. The findings and conclusions may change if inlet boundary layer skew or a different free-stream turbulence spectrum were imposed. Nevertheless, with the current inflow conditions, the key findings are as follows:

- The state of the endwall boundary layer is crucial. A laminar endwall boundary layer can not withstand the adverse pressure gradient near the leading edge and separates earlier. The larger passage vortex leads to under-turning of the flow and increased loss.
- The endwall separation was shown to be sensitive to the suction surface boundary layer thickness. A numerical trip placed at $0.07C_x$ resulted in a 50% increase in boundary layer thickness, and this lead to the span-wise extent of the endwall separation increasing by 10% span. However, increasing the free-stream turbulence intensity by an order of magnitude changed the suction surface transition mode but not the boundary layer thickness. Thus, the endwall separation was unaffected.
- Near the mid-span the viscous dissipation near the leading edge and turbulent dissipation at the laminar separation bubble are the main loss sources. A high FST intensity suppresses the separation bubble, but causes higher loss overall. This is due to the earlier pressure surface transition and higher turbulent dissipation in the free-stream. In the three-dimensional flow region near the endwall, the turbulent dissipation dominates. The FST intensity has little effect here.

Finally, in Section 6.3.2.3 some challenges for RANS models were highlighted; a region of relaminarisation was observed, large-scale unsteadiness was observed in the endwall region, and turbulent anisotropy is found to be important. Encouragingly, in Section 6.3.3 an endwall fillet is found to reduce the importance of turbulent anisotropy.

Part III

Conclusions and Future Outlook

Chapter 7

Conclusions and Recommendations for Future Work

The aim of this thesis was to explore the potential of large eddy simulation for use as a predictive tool in the design of gas turbine compressors. To begin, in Chapter 4, the performance of the existing LES framework was explored with the Taylor Green vortex case. The solution was found to be very sensitive to the numerical smoothing, which is undesirable if the LES framework is to be used in a predictive way. A commonly proposed solution is to use a locally adaptive smoothing (LAS) scheme. However, the behaviour of such a scheme in forced isotropic turbulence (FIT) was seen to be poor, because of the intermittency of the dispersive errors. A novel LAS scheme with windowing (LASW) was proposed to improve the performance.

For statistically stationary cases, such as the FIT case or a compressor flow without wakes, the LASW scheme was found to perform well; with the gain parameter only affecting the convergence of the smoothing field, not the converged field itself. Hence, the user can be confident that an appropriate amount of smoothing will be returned for different cases, without the need for tuning.

To further examine the suitability of the LASW scheme, it was tested on a transitional compressor flow in Chapter 5. The transition mechanisms were found to be sensitive to the numerical smoothing. The LASW scheme thus offers substantial benefits here. The scheme shows considerable promise, but is currently slow to converge. Improvement might be obtained if a locally varying window length was used. The length could be related to the local time-scales of turbulence or a local CFL number, and this is a possible area of future work.

Crucially, the Smagorinsky-Lilly sub-grid scale model, which is still popular, was found to behave poorly in the compressor flow. On the other hand, the sigma and WALE SGS models performed well. This is encouraging for the prospect of applying LES to complex industrial flows, as the models do not require additional filtering or averaging. One area of future work could be to add a non-linear term to the sigma or WALE models, to see if this helps account for the turbulent backscatter observed in the separation bubble.

With a suitable SGS model and the LASW scheme, the LES was shown to agree well with direct numerical simulations (DNS) of the compressor flow. With this in mind, further investigations of more engine representative flow features were performed, with a focus on the sensitivity to inflow conditions and the endwall flow region. In the following sections, the key findings of this study are summarised, from a flow physics and engineering perspective.

7.1 Flow physics perspective

7.1.1 The effect of free-stream turbulence on transition

In Chapter 5, LES was seen to capture the complex transition mechanisms that occur on the suction and pressure surfaces. At a moderate free-stream turbulence intensity the inner and overlap modes, shown to be present by Zaki et al. [9], are observed. Although still influenced by the Klebanoff streaks, these modes don't resemble the traditional mechanism observed in DNS of bypass transition [12]. The effects of incoming turbulence intensity were well predicted by the LES, with the traditional bypass mechanism taking over as the free-stream intensity is increased from 3.25% to 10%. The complexity of boundary layer transition is highlighted here, but it also shows how LES may be used to further investigate transition models and correlations in complex compressor flows.

7.1.2 Wake induced transition

In Chapter 6, LES was used to investigate the effect of periodically incoming turbulent wakes on the boundary layer transition in a compressor. Wake-amplified Klebanoff streaks were found to instigate turbulent spots, which periodically shorten the suction surface separation bubble. This has more in common with the turbine flows of Coull et al. [20] than with the compressor flow of Wheeler et al. [27], who found that regions of high momentum thickness θ convecting from the leading edge cause turbulent spots. Wheeler et al. [27] show that the wake-dependent fluctuations of θ near the leading edge are strongly dependent on the leading edge geometry, while Halstead et al. [174]

demonstrate the sensitivity of the wake-induced mechanisms to blade loading. The relative importance these mechanisms have on the wake-induced transition, and the endwall separation, are a possible area of future investigation.

The calmed region behind the wake-induced turbulent spots, seen in other wake studies, was also observed. Walker et al. [163] discusses the importance of the calmed region, and notes that the majority of transition models are intermittency based and therefore don't account for the calmed region. Incoming wakes were found to cause a phase dependent thickening of the suction surface boundary layer.

7.1.3 The endwall flow region

In Chapter 6, the three-dimensional separation that occurs in the suction surface - endwall corner was also examined. The flow in this region was found to be complex, and the main finding here was that the endwall flow is sensitive to the turbulent inflow. In particular:

- The state of the endwall boundary layer was seen to be crucial. A laminar endwall boundary layer can not withstand the adverse pressure gradient near the leading edge and thus separates earlier, leading to a larger endwall separation. This results in under-turning of the flow and increased loss.
- Early transition on the suction surface was shown to increase the span-wise extent of the endwall separation. A numerical trip placed near leading edge resulted in a 50% increase in boundary layer thickness, which caused the endwall separation to extend 10% further across the blade span.
- It is of interest to determine whether the wake-induced thickening of the suction surface boundary layer influences the endwall separation. This study isn't performed in this thesis due to the high computational cost required for phase-averaging of the endwall flow. When a numerical trip was applied in Section 6.3.1.2, it took approximately 8 wake-passing periods for the endwall separation to stop growing¹. This spectral gap may mean that phase-dependent variation of the endwall separation does not occur. However, there may be more direct interactions between the wake and endwall separation, and this is still an interesting area for future study. Additionally, Ottavy et al. [44] and Gourdain [91] find that rotor-stator interactions influence the endwall separation, and this could also be an important area for further research.

¹Similarly, Goodhand et al. [37] found that 10 wake passing periods were required.

- Increasing the free-stream turbulence intensity by an order of magnitude changed the suction surface transition mode but not the boundary layer thickness. Thus, the endwall separation was unaffected. Despite this, the sensitivity of the endwall separation to the suction surface boundary layer is still important. Figure 5.6a in Chapter 5 showed that FST can alter the boundary layer in some conditions, while leading edge geometry and surface roughness may also have an effect.
- The viscous dissipation near the leading edge, and the turbulent dissipation in the suction surface separation bubble, are found to be the primary loss sources at mid-span. A high FST intensity suppresses the separation bubble, but causes higher loss overall due to the earlier pressure surface transition and higher turbulent dissipation in the free-stream.

Various interesting, and potentially important, flow features were also observed:

- Large-scale unsteadiness was observed in the endwall separation region. While not exhibiting truly bi-modal behaviour like in the work of Gao et al. [96], the velocity distributions were still non-Gaussian, which may have implications for steady RANS modelling. The large length-scales may also help to explain why the small-scale free-stream turbulence was not seen to directly influence the endwall separation.
- A region of relaminarisation was observed in the pressure surface - endwall corner. This is something that is known to occur in turbine flows, and is likely to cause issues for RANS modelling approaches.
- The turbulence in the endwall corner is seen to be strongly anisotropic. Evidence suggested this anisotropy may be one of the reasons linear RANS models over-predict the size of compressor endwall separations. The anisotropy is incorrectly predicted by the RANS SST model, and this seems to lead to the corner vortex decaying more quickly. Without the corner vortex, low momentum fluid builds up in the corner boundary layer and separates prematurely.

The above findings and conclusions may change if inlet boundary layer skew or a different free-stream turbulence spectrum were imposed, and this would be a useful direction for future investigations.

7.2 Engineering perspective

7.2.1 Specification of turbulent inflow conditions

Chapter 5 showed that boundary layer transition processes are sensitive to the exact free-stream turbulence spectra, as well as the intensity. Therefore, it is important to specify the incoming turbulence as accurately as possible when attempting to use LES to predict compressor flows.

Additionally, the state of the endwall boundary layer was found to be crucial in Chapter 6. In many blade cascade experiments the endwall boundary layers are partly relaminarised by an upstream contraction. This highlights the need for the endwall boundary layer velocity and stress profiles to be accurately recorded in cascade experiments.

7.2.2 Compressor performance

The time-averaged loss data from a number of the LES cases presented in Chapter 6 is summarised¹ in Figure 7.1. It is clear that the endwall flow effects make up a significant proportion of the total loss in the blade passage. At this “on-design” operating point the addition of a corner fillet is relatively insignificant, with the baseline (L-TBL) loss being reduced by only around 1%.

In this case, the turbulent inflow conditions are more important. Increasing the free-stream turbulence intensity increases the total loss by around 10%. If this increase in T_i had caused the transition point to move forward, then this could have caused a significantly bigger increase in loss, as the L-TBL trip case shows. The largest increase in loss (almost 40%) was seen in the laminar endwall boundary layer case. However, a laminar incoming endwall boundary layer is unlikely to occur in a real gas turbine engine.

7.2.3 RANS modelling

The RANS SST result in Figure 7.1 is particularly important. The loss here is overpredicted by around 35%. This is a similar magnitude to the maximum change in loss caused by any of the different inflow conditions, and is much larger than the change in loss due to the fillet. Such a RANS approach, commonly used in industry, might

¹The mass-averaged loss coefficient profiles (e.g. Figure 6.18a) are integrated in the span-wise direction between 0-40% span to give $(Y_p)_{0-40}$ and between 40-50% to give $(Y_p)_{40-50}$. The 2D mid-span loss is then approximated to be equal to $5(Y_p)_{40-50}$, while the endwall loss is approximated as $(Y_p)_{0-40} - 4(Y_p)_{40-50}$.

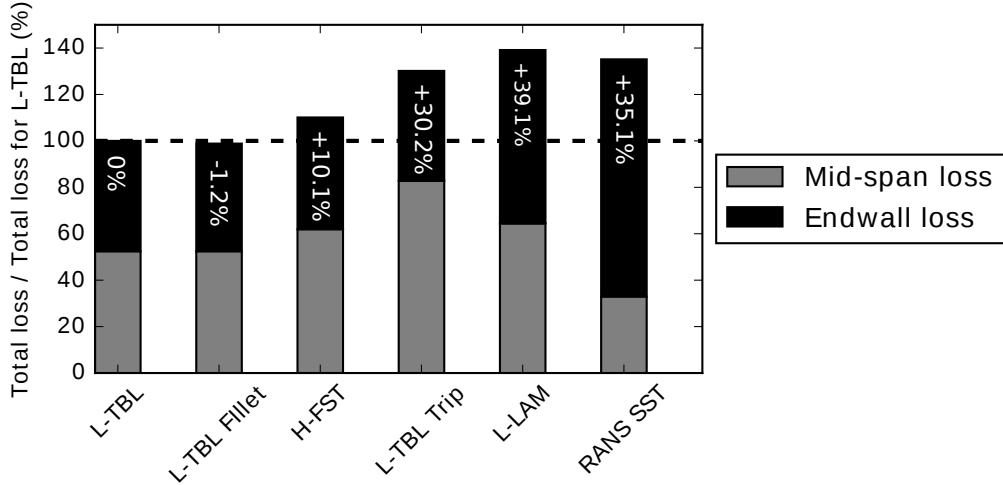


FIGURE 7.1: Total time-averaged loss 50% chord downstream of the trailing edge, for a number of LES cases from Chapter 6.

therefore not be suitable for use as a tool to predict the influence of a fillet or inflow conditions on such a flow. This finding highlights the need to improve RANS modelling capabilities in such flows.

One of the challenges for RANS models was shown to be the endwall separation's sensitivity to the suction surface transition location. Attempts to manually enforce the transition locations of the un-tripped LES in the RANS were unsuccessful, due to the highly 3D nature of the flow. Transition models are therefore necessary for such flows, but Lefas et al. [175] demonstrate the challenges a common transition model encounters in a turbine endwall flow. An area of future work could be to use the LES data to examine the performance of transition models in a compressor endwall flow.

Section 6.3.2 presented evidence suggesting that unsteady flow effects and turbulent anisotropy are important in compressor endwall flows. This makes RANS modelling of such flows more challenging. On a positive note, Section 6.3.3 showed that anisotropy is less crucial when the endwall corner is filleted. Nevertheless, the development of more advanced RANS models that can better predict the turbulent anisotropy would make RANS more predictive for such flows. Again, the LES data could be useful here.

Finally, it must be noted that LES is still very computationally expensive, and hybrid RANS-LES approaches might offer a better accuracy versus cost compromise for industrial compressor flows. Various studies [83, 84, 167] have demonstrated the potential of hybrid RANS-LES methods for use in the PVD cascade. However, Klostermeier [83] found the results to be sensitive to the thickness of the RANS layer. Additionally, the RANS layer might not correctly predict the suction surface transition and the turbulent anisotropy in the corner correctly. Once again, LES could be used to further investigate these methods.

Appendices

Appendix A

Additional Information on Turbulence Treatments

In Section A.1 this appendix reviews some additional challenges faced by RANS models, that were not covered in the literature review in Chapter 2.

The two RANS models used in this thesis, the Spalart-Allmaras (SA) model and the shear-stress transport (SST) model, are then summarised in Section A.2, and a number of RANS modelling extensions that were added to HYDRA are described in Section A.3.

Section A.4 discusses three SGS models that make use of additional filtering to alleviate some of the problems experienced by models such as the Smagorinsky-Lilly SGS model.

A.1 Additional challenges faced by RANS models

A.1.1 Compressive/Extensive strain

As discussed by Tucker [5], most eddy viscosity based RANS models are calibrated for flows dominated by simple shear strains. If compressive or extensive strains dominate, they can induce serious inaccuracies in basic RANS models. For example, the high compressive strain in stagnation regions leads to RANS models seriously over-predicting the turbulence production. This over-prediction causes suppression of leading edge separation on blades, and as Medic et al. [176] show, can also have significant downstream impacts. Hence, turbulence production corrections, such as the Kato-Launder correction [177] for the SST model, are needed. However these corrections have unintended consequences elsewhere in the flow, and some CFD practitioners use them in a localised manner [178]. This adds further empiricism and uncertainty to the RANS method.

A.1.2 Curvature and rotation

Bradshaw [179] notes that “*Streamline curvature in the plane of the mean shear produces surprisingly large changes in the turbulence structure of shear layers*”. This can be shown by considering the exact production term for a 2D shear flow [5]:

$$P_{12} = -\overline{v'v'} \frac{\partial U}{\partial y} - \overline{u'u'} \frac{\partial V}{\partial x} \quad (\text{A.1})$$

In the case of no streamline curvature the first term is dominant. However for concave streamline curvature, $\partial V / \partial x > 0$ and the turbulence production is amplified. For convex curvature, $\partial V / \partial x < 0$ and the turbulence production is damped. In fact, turbulence can be virtually eliminated around convex surfaces [179].

In addition to curvature, system rotation/swirl also cause body forces that interact with the turbulence. One example is a homogeneous rotating shear flow, where Speziale [180] reports that the strong rotation extinguishes the turbulent shear stress. Another example is in the core of a free vortex, where Bradshaw [179] reports a damping of turbulence due to the rotation.

Some argue that the significantly more complex RSM¹ approach [181] may offer an alternative to eddy resolving techniques for the prediction of complex turbo-machinery flows, for example see Morsbach et al. [182]. However, strong evidence of superior accuracy from these for complex industrial flows isn't yet available [183]. This is partly due to the difficulty RSM's have with convergence, and also because they still require a high degree of empiricism in order to close them.

Another approach is to modify existing linear EVM's to sensitise them to rotation and curvature. For example, Spalart et al. [40] proposes the SA-RC correction to sensitise the SA model to rotation and curvature, and Spalart [8] proposes the addition a simple non-linear term (a QCR²) into the Boussinesq approximation (Equation 2.10). The QCR term is intended to improve the anisotropy of turbulence caused by non-linear effects such as rotation and curvature.

¹Reynolds Stress Transport Model

²Quadratic Constitutive Relation

A.2 Baseline RANS models

A.2.1 Spalart-Allmaras model

The Spalart-Allmaras (SA) model [41] solves a transport equation for the spalart variable, $\tilde{\nu}$, which is identical to the turbulent kinematic viscosity (ν_t) except in the near-wall region. Here a damping function $f_{\nu 1}$ is used in order to properly attenuate the turbulent viscosity in the viscous sublayer:

$$\mu_t = \rho\nu_t = \rho\tilde{\nu}f_{\nu 1} \quad (\text{A.2})$$

The transport equation for $\tilde{\nu}$ that must be solved is:

$$\frac{\partial \tilde{\nu}}{\partial t} + u_j \frac{\partial \tilde{\nu}}{\partial x_j} = G_{\tilde{\nu}} + \frac{1}{\sigma} \left[\frac{\partial}{\partial x_j} \left((\nu + \tilde{\nu}) \frac{\partial \tilde{\nu}}{\partial x_j} \right) + c_{b2} \left(\frac{\partial \tilde{\nu}}{\partial x_i} \right)^2 \right] - Y_{\tilde{\nu}} + S_{\tilde{\nu}} \quad (\text{A.3})$$

where $G_{\tilde{\nu}}$, $Y_{\tilde{\nu}}$, $S_{\tilde{\nu}}$ are the production, destruction and source terms for $\tilde{\nu}$.

The $\tilde{\nu}$ production term for the standard SA model is given by:

$$G_{\tilde{\nu}} = c_{b1}(1 - f_{t2})\tilde{S}\tilde{\nu} \quad (\text{A.4})$$

where \tilde{S} is a scalar measure of the deformation tensor, given by:

$$\tilde{S} = \frac{\tilde{v}}{\kappa^2 d^2} f_{v2} + \Omega \quad (\text{A.5})$$

and Ω is the magnitude of vorticity, $\Omega = \sqrt{2\Omega_{ij}\Omega_{ij}}$, with Ω_{ij} being the vorticity tensor.

The choice of basing \tilde{S} on Ω is motivated by the observation that turbulence occurs where vorticity is generated (near solid boundaries). However, this leads to an over-prediction of eddy viscosity where vorticity exceeds strain rate, such as in vortex core regions, where pure rotation should not produce turbulence. In attempt to correct this, Dacles-Mariani et al. [184] propose the SA-R correction (otherwise known as Bradshaw correction), where \tilde{S} is rewritten as:

$$\tilde{S} = \frac{\tilde{v}}{\kappa^2 d^2} f_{v2} + \Omega + C_{rot} \min(0, S - \Omega) \quad (\text{A.6})$$

This correction results in the eddy viscosity being reduced in regions such as the vortex core, where the pure rotation should suppress turbulence. The modification is passive in thin shear layers where S and Ω are very similar.

The constant C_{rot} represents an attempt to empirically adjust the production term for vortex dominated flows. Dacles-Mariani et al. [184] found that a value of 3.5-4.0

produced the best agreement with experiments, but a more conservative value of 2.0 was recommended for the default.

A.2.2 Shear-Stress Transport model

The Menter Shear-Stress Transport (SST) model [185] blends the robust and accurate formulation of the $k - \omega$ model in the near-wall region with the free-stream independence of the $k - \epsilon$ model in the far field. The SST model solves a transport equation for the turbulent kinetic energy k and a transport equation for the specific dissipation rate ω . These equations are given by:

$$\frac{\partial \rho k}{\partial t} + \frac{\partial \rho k u_i}{\partial x_i} = \frac{\partial}{\partial x_j} \left(\Gamma_k \frac{\partial k}{\partial x_j} \right) + \tilde{G}_k - Y_k + S_k \quad (\text{A.7})$$

and

$$\frac{\partial \rho \omega}{\partial t} + \frac{\partial \rho \omega u_i}{\partial x_i} = \frac{\partial}{\partial x_j} \left(\Gamma_\omega \frac{\partial \omega}{\partial x_j} \right) + G_\omega - Y_\omega + D_\omega + S_\omega \quad (\text{A.8})$$

where G_k , Y_k , S_k and G_ω , Y_ω , S_ω are the production, destruction and source terms for k and ω . Γ_k and Γ_ω are the effective diffusivity of k and ω . D_ω represents the cross-diffusion term. The turbulent viscosity is then given by:

$$\mu_t = \frac{\rho a_1 k}{\max(a_1 \omega, SF_2)} \quad (\text{A.9})$$

where S is the magnitude of strain, $S = \sqrt{2S_{ij}S_{ij}}$, with S_{ij} being the strain rate tensor.

A.2.2.1 Production limiter

The production of k in the original $k - \omega$ model is given by:

$$G_k = \mu_t S S \quad (\text{A.10})$$

However, as recommended in Menter et al. [185], for the SST model in HYDRA, the production of k is limited:

$$\tilde{G}_k = \min(G_k, 10\rho\beta^* k\omega) \quad (\text{A.11})$$

This helps to prevent a build-up of turbulence in stagnation regions.

A.2.2.2 Kato-Launder production term

As with all the 2-equation models that use Equation A.10 for the production of k , there is a tendency for the model to over-predict the turbulent production in regions with large normal strain, e.g. in stagnation regions. The Kato-Launder modification [177] aims to reduce this problem by rewriting the k production term as:

$$G_k = \mu_t S \Omega \quad (\text{A.12})$$

This modification is passive in pure shear-flows like boundary-layers and wakes. In stagnation regions, it reduces the turbulent production, but it has little control and so can actually lead to an under-prediction of turbulence here.

In HYDRA, the production corrections given in Equations A.10 and A.12 are used in tandem.

A.3 RANS model extensions added to HYDRA

This section describes the RANS modelling extensions that were added to HYDRA. These were only applied where it is explicitly specified.

A.3.1 SA with Quadratic Constitutive Relation (SA-QCR)

Spalart [8] proposes the addition of a simple non-linear term into the Boussinesq approximation (Equation 2.10) in order to sensitise the turbulence model to non-linear turbulence effects. The Reynolds stress $\check{\tau}_{ij} = -\overline{\rho u_i u_j}$ is obtained from the Boussinesq approximation in the standard way, and the non-linear stress is then:

$$\tau_{ij} = \check{\tau}_{ij} - c_{nl1} [O_{ik} \hat{\tau}_{jk} + O_{jk} \check{\tau}_{ik}] \quad (\text{A.13})$$

where:

$$O_{ik} \equiv \frac{2\Omega_{ik}}{\sqrt{\frac{\partial u_m}{\partial x_n} \frac{\partial u_m}{\partial x_n}}} \quad (\text{A.14})$$

The denominator in Equation A.14 must be limited to prevent possible division by zero in regions of zero gradient.

Spalart [8] notes that the use of this modification with the SA model can lead to improved predictions of the flow in a square duct, with flow induced towards the corners, and more accurate skin friction predictions. However in other flows such as 3D wall jets, it has

led to negative results. It is probably necessary to tune the empirical constant c_{nl1} from its original value of 0.3 in order to get improved results with different flows, as this constant determines the degree of turbulent anisotropy predicted.

A.3.2 Strain Adaptive formulation of SA model (SALSA)

This form of the SA model was developed by Rung et al. [186] primarily to extend the predictive capability of the model to conditions with non-equilibrium of turbulence. The constant c_{b1} which scales the production¹ and destruction² of $\tilde{\nu}$ terms in the standard SA model is changed to a variable:

$$c'_{b1} = 0.1355\sqrt{\Gamma} \quad (\text{A.15})$$

where:

$$\begin{aligned} \Gamma &= \min[1.25, \max(\gamma, 0.75)] \\ \gamma &= \max(\alpha_1, \alpha_2) \\ \alpha_1 &= \left[1.01 \left(\frac{\tilde{\nu}}{S\kappa^2 d^2} \right) \right]^{0.65} \\ \alpha_2 &= \max \left[0, 1 - \tanh \left(\frac{\tilde{\nu}/\nu}{68} \right) \right]^{0.65} \end{aligned} \quad (\text{A.16})$$

The modification $\sqrt{\Gamma}$ primarily causes a reduction of production for excessive strains via α_1 , while undesirable wall damping is suppressed by the inclusion of α_2 .

A.3.3 SA with Rotation/Curvature correction (SA-RC)

The SA-RC correction [40] sensitises the SA model to streamline curvature and rotation. Shur et al. [187] tested this correction on a number of different 2D and 3D flows, with positive results. It works by multiplying the production of $\tilde{\nu}$ term ($G_{\tilde{\nu}}$) in the original SA model by a rotation/curvature function f_{r1} :

$$f_{r1} = (1 + c_{r1}) \frac{2r^*}{1 + r^*} [1 - c_{r3} \arctan(c_{r2} \check{r})] - c_{r1} \quad (\text{A.17})$$

where:

$$\begin{aligned} r^* &= S/\Omega \\ \check{r} &= \frac{2\Omega_{ik}S_{jk}}{D^4} \left(\frac{DS_{ij}}{Dt} + (\epsilon_{imn}S_{jn} + \epsilon_{jmn}S_{in}) \Omega'_m \right) \end{aligned} \quad (\text{A.18})$$

¹ $G_{\tilde{\nu}}$ in Equation A.3

² $Y_{\tilde{\nu}}$ in Equation A.3

The rotation rate Ω'_m is used when the reference frame itself is rotating. The term DS_{ij}/Dt contains the components of the Lagrangian derivative of the strain rate tensor. For a steady-state flow, the time derivative in this term can be ignored, and it can be discretised in a similar way to the fluxes in Equation 3.3 to give:

$$\frac{DS_{ij}}{Dt} = \frac{\left[\sum_{k \in E_i} S_{ij}^{(k)} U_n^{(k)} A_{ij} \right]}{V_i} \quad (\text{A.19})$$

The computation of this term adds approximately 20% to the computational cost of the model. The f_{r1} term is greater than unity in regions of strong convex curvature (stabilized flow, no turbulence production) and less than unity in regions of strong concave curvature (enhanced turbulence production). Smirnov et al. [188] applied a $f_{r1} \geq 0$ limit for “numerical stability reasons”, but Spalart et al. [40] and Shur et al. [187] did not, as they reasoned that the term should be allowed to go negative in order to represent turbulence damping effects. In the present implementation, the decision was taken not to use a limiter, but this did cause convergence issues in some cases.

A.4 SGS models with additional filtering

Various SGS models have been proposed that use an additional coarser filtering level (the test filter) in order to alleviate some of the shortcomings of models such as the Smagorinsky-Lilly model. Two of the most common are shown graphically in Figure A.1.

A.4.1 Dynamic Smagorinsky model

One shortcoming of the Smagorinsky-Lilly model is that the C_s constant is non-universal. The dynamic Smagorinsky model (Germano et al. [65]) instead allows:

$$C_s = C_s(\mathbf{x}, t) \quad (\text{A.20})$$

A test filter is used to give the SFS¹ stress T_{ij} . Germano’s identity (also see Figure A.1b) is then applied:

$$L_{ij} = T_{ij} - \tau_{ij}^r \quad (\text{A.21})$$

to obtain L_{ij} from the SFS stress T_{ij} and the SGS stress τ_{ij}^r . L_{ij} represents the resolved stress “band-pass filtered” between the grid and test filters. It is assumed that a consistent SGS model should contribute the same amount as the resolved field in this band.

¹Sub-Filter Scale

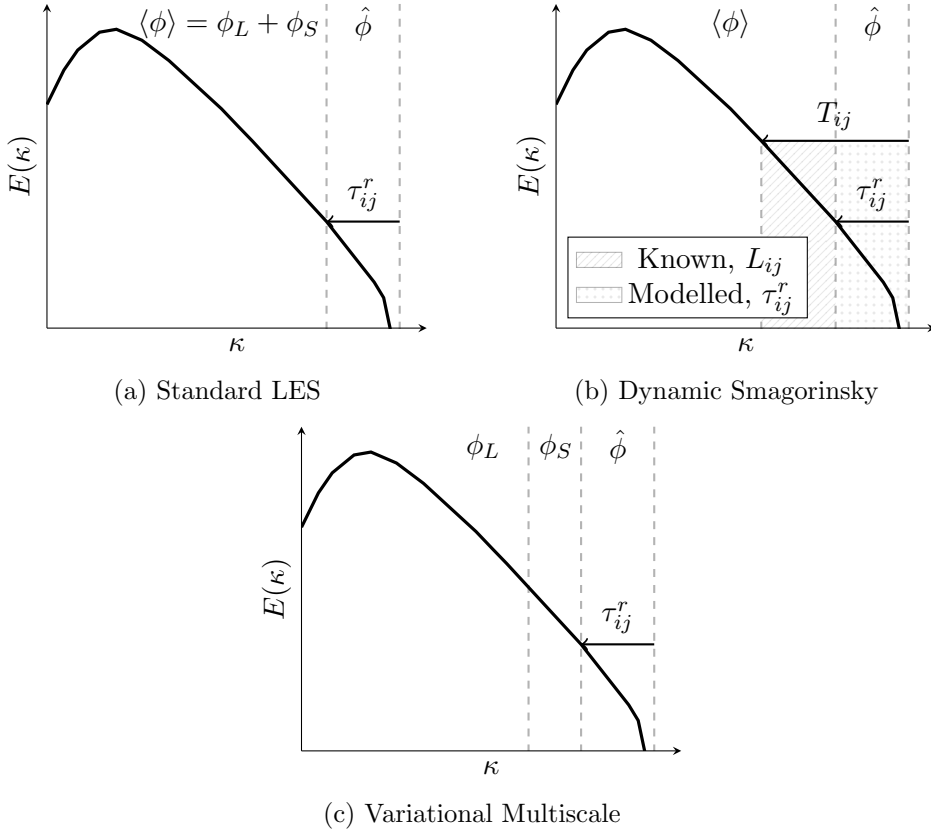


FIGURE A.1: Schematic showing the concept of dynamic Smagorinsky and VMS

Lilly [189] proposes a least squares solution for C_s :

$$C_s^2 = -\frac{1}{2} \frac{\{L_{kl}M_{kl}\}}{\{M_{mn}M_{mn}\}} \quad (\text{A.22})$$

where M_{ij} is directly related to the differential operator of the underlying SGS model (i.e. S) and the strain tensor S_{ij} . The dynamic Smagorinsky model has found considerable success in transitional flows [157], where $C_s = 0$ is required in laminar regions. However the $\{\cdot\}$ in Equation A.22 denotes additional averaging, required to deal with extreme C_s values. This adds computational expense and complexity, and can be a significant complication in flows where there isn't an obvious homogeneous flow direction.

A.4.2 Variational Multiscale method

Unless the Reynolds number is low so that the $-5/3$ range is short, the dissipative scales should only interact with the smaller scales. However, SGS models such as the Smagorinsky-Lilly model the modelled stress τ_{ij}^r acts on all scales. To solve this Hughes et al. [66] proposed the Variational Multiscale (VMS) approach. A test filter is used to

split the resolved field $\langle \phi \rangle$ into large and small scales so that Equation 2.12 becomes:

$$\phi(\mathbf{x}, t) = \phi_L(\mathbf{x}, t) + \phi_S(\mathbf{x}, t) + \hat{\phi}(\mathbf{x}, t) \quad (\text{A.23})$$

As illustrated in Figure A.1c the modelled stress τ_{ij}^r can now be made to act only on the small scales. For wall bounded flows, this approach has been found to give considerable improvements over the Smagorinsky-Lilly model [190]. However, the need for a test filter adds complexity.

A.4.3 Shear-Improved Smagorinsky model

The Shear-Improved Smagorinsky model (SISM) is proposed by Lévéque et al. [191]. To limit the effects of mean strain in the flow-field, this model uses a modified form of the Smagorinsky eddy-viscosity

$$\mu_{sgs} = \rho(C_s \Delta_{vol})^2 (S - \bar{S}), \quad (\text{A.24})$$

with the time-averaged magnitude of strain \bar{S} subtracted from the instantaneous strain magnitude S . This modification gives an improvement over the original Smagorinsky-Lilly model, but the need to first obtain \bar{S} adds complexity. Cahuzac et al. [192] use additional smoothing to approximate this term. This may add additional uncertainty, however Gao et al. [96] used this approach successfully for LES of compressors.

Appendix B

Reformulation of the Synthetic Turbulence Method

The original synthetic isotropic turbulence method of Saad et al. [136] gives a divergence-free velocity field on a staggered grid. The method is briefly described in Section B.1. For a full description of the method, see Saad et al. [136].

Since HYDRA uses a collocated grid arrangement, the original formulation had to modified to give a divergence free solution on a collocated grid. This reformulation is described here.

B.1 The synthetic turbulence method

The Fourier series representation of an arbitrary spatially varying velocity field \mathbf{u} at a point \mathbf{x} is:

$$\mathbf{u}(\mathbf{x}) = 2 \sum_{m=1}^M q_m \cos(\kappa_m \hat{\mathbf{k}}_m \cdot \mathbf{x} + \psi_m) \hat{\sigma}_m \quad (\text{B.1})$$

where M is the number of modes, q_m is the amplitude, κ_m is the m^{th} wave number, $\hat{\mathbf{k}}_m$ is the (unit) direction vector associated with the m^{th} wave number, ψ_m is the phase angle, and $\hat{\sigma}_m$ is the modal direction vector.

The procedure of Saad et al. [136] generates a Fourier series of M modes by choosing random $\hat{\mathbf{k}}_m$ and ψ_m with q_m obtained from the input energy spectrum, such that $q_m = \sqrt{E(\kappa_m)\Delta\kappa}$. The only remaining unknown is $\hat{\sigma}_m$, which can be evaluated using the

divergence-free condition:

$$\nabla \cdot \mathbf{u} = -2 \sum_{m=1}^M q_m \kappa_m \hat{\mathbf{k}}_m \cdot \hat{\sigma}_m \sin(\kappa_m \hat{\mathbf{k}}_m \cdot \mathbf{x} + \psi_m) = 0 \quad (\text{B.2})$$

This constraint can be enforced by setting $\hat{\mathbf{k}}_m$ perpendicular to $\hat{\sigma}_m$:

$$\hat{\mathbf{k}}_m \cdot \hat{\sigma}_m = 0, \forall m \in \{0, 1, \dots, M\} \quad (\text{B.3})$$

Equation B.3 is valid in the infinitesimal limit, but it becomes invalid on a discrete grid, leading to a diverging velocity field. Saad et al. [136] establish the correct divergence-free constraint for the discrete formulation.

B.2 Enforcing mass conservation on a staggered grid

For a staggered grid, the discrete continuity equation is:

$$\nabla_d \cdot \mathbf{u} = \frac{u_{i+\frac{1}{2},j,k} - u_{i-\frac{1}{2},j,k}}{\Delta x} + \frac{v_{i,j+\frac{1}{2},k} - v_{i,j-\frac{1}{2},k}}{\Delta y} + \frac{w_{i,j,k+\frac{1}{2}} - w_{i,j,k-\frac{1}{2}}}{\Delta z} \quad (\text{B.4})$$

where ∇_d is the discrete gradient operator, and for example,

$$u_{i+\frac{1}{2},j,k} = u\left(x + \frac{\Delta x}{2}, y, z\right) = 2 \sum_{m=1}^M q_m \cos\left[\kappa_m k_{x,m}\left(x + \frac{\Delta x}{2}\right) + \kappa_m k_{y,m}y + \kappa_m k_{z,m}z + \psi_m\right] \sigma_{x,m} \quad (\text{B.5})$$

Substituting into Equation B.4 and applying trigonometric identities recovers:

$$\nabla_d \cdot \mathbf{u} = -2 \sum_{m=1}^M q_m \hat{\sigma}_m \cdot \tilde{\mathbf{k}}_m \sin(\mathbf{k}_m \cdot \mathbf{x} + \psi_m) \quad (\text{B.6})$$

where

$$\tilde{\mathbf{k}}_m = \left[\frac{2}{\Delta x} \sin\left(\frac{1}{2} \kappa_m k_{x,m} \Delta x\right), \frac{2}{\Delta y} \sin\left(\frac{1}{2} \kappa_m k_{y,m} \Delta y\right), \frac{2}{\Delta z} \sin\left(\frac{1}{2} \kappa_m k_{z,m} \Delta z\right) \right] \quad (\text{B.7})$$

The discrete continuity equation (Equation B.4) can then be enforced:

$$\tilde{\mathbf{k}}_m \cdot \hat{\sigma}_m = 0, \forall m \in \{0, 1, \dots, M\} \quad (\text{B.8})$$

Note that $\hat{\mathbf{k}}_m$ has been replaced by $\tilde{\mathbf{k}}_m$. Saad et al. [136] enforces Equation B.8 by setting:

$$\hat{\sigma}_m = \frac{\zeta \times \tilde{\mathbf{k}}}{|\zeta \times \tilde{\mathbf{k}}|} \quad (\text{B.9})$$

with ζ being a unit vector randomly chosen from a uniform distribution. The discrete divergence free condition is now satisfied (on a staggered grid).

B.3 Enforcing mass conservation on a collocated grid

Assuming a collocated grid, Equation B.4 becomes:

$$\nabla_d \cdot \mathbf{u} = \frac{u_{i+1,j,k} - u_{i-1,j,k}}{2\Delta x} + \frac{v_{i,j+1,k} - v_{i,j-1,k}}{2\Delta y} + \frac{w_{i,j,k+1} - w_{i,j,k-1}}{2\Delta z} \quad (\text{B.10})$$

where, for example,

$$u_{i+1,j,k} = u(x + \Delta x, y, z) = 2 \sum_{m=1}^M q_m \cos [\kappa_m k_{x,m} (x + \Delta x) + \kappa_m k_{y,m} y + \kappa_m k_{z,m} z + \psi_m] \sigma_{x,m} \quad (\text{B.11})$$

Through substitution, and the use of trigonometric identities, we again obtain:

$$\nabla_d \cdot \mathbf{u} = -2 \sum_{m=1}^M q_m \hat{\sigma}_m \cdot \tilde{\mathbf{k}}_m \sin(\mathbf{k}_m \cdot \mathbf{x} + \psi_m) \quad (\text{B.12})$$

However, it can be proven that the vector $\tilde{\mathbf{k}}_m$ now becomes:

$$\tilde{\mathbf{k}}_m = \left[\frac{1}{\Delta x} \sin(\kappa_m k_{x,m} \Delta x), \frac{1}{\Delta y} \sin(\kappa_m k_{y,m} \Delta y), \frac{1}{\Delta z} \sin(\kappa_m k_{z,m} \Delta z) \right] \quad (\text{B.13})$$

Replacing Equations B.6 and B.7 with Equations B.12 and B.13 yeilds a divergence-free velocity field on a collocated grid arrangement.

Bibliography

- [1] Cumpsty, N. A. *Jet Propulsion: A Simple Guide to the Aerodynamic and Thermodynamic Design and Performance of Jet Engines*. Cambridge University Press, 2003.
- [2] Place, J. M. M. “Three-dimensional separation in core compressors”. PhD thesis. University of Cambridge, 1997.
- [3] Tyacke, J. et al. “Large Eddy Simulation for Turbines: Methodologies, Cost and Future Outlooks”. In: *Journal of Turbomachinery* 136.6 (2013).
- [4] Gourdain, N et al. “Large eddy simulation of flows in industrial compressors : a path from 2015 to 2035”. In: *Philosophical transactions. Series A, Mathematical, physical, and engineering sciences* 372.2022 (2014).
- [5] Tucker, P. G. “Trends in turbomachinery turbulence treatments”. In: *Progress in Aerospace Sciences* 63 (2013), pp. 1–32.
- [6] Denton, J. D. “Some Limitations of Turbomachinery CFD”. In: *ASME Turbo Expo 2010: Power for Land, Sea and Air*. 2010, pp. 1–11.
- [7] Sagaut, P., Deck, S., and Terracol, M. *Multiscale And Multiresolution Approaches in Turbulence*. Imperial College Press, 2006, p. 340.
- [8] Spalart, P. R. “Strategies for turbulence modelling and simulations”. In: *Int. J. Heat and Fluid Flow* 21 (2000), pp. 252–263.
- [9] Zaki, T. A. et al. “Direct numerical simulations of transition in a compressor cascade: the influence of free-stream turbulence”. In: *Journal of Fluid Mechanics* 665 (2010), pp. 57–98.
- [10] Klebanoff, P. S., Tidstromand, K. D., and Sargent, L. M. “The three-dimensional nature of boundary-layer instability”. In: *Journal of Fluid Mechanics* (1961), pp. 1–34.
- [11] White, F. M. *Viscous fluid flow*. McGraw-Hill, 2006.
- [12] Jacobs, R. G. and Durbin, P. A. “Simulations of bypass transition”. In: *Journal of Fluid Mechanics* 428 (2001), pp. 185–212.

- [13] Horton, H. P. "Laminar separation bubbles in two and three dimensional incompressible flow". PhD thesis. Queen Mary College, 1968.
- [14] Spalart, P. R. and Strelets, M. K. "Mechanisms of transition and heat transfer in a separation bubble". In: *Journal of Fluid Mechanics* 403 (2000), S0022112099007077.
- [15] Alam, M and Sandham, N. D. "Direct numerical simulation of 'short' laminar separation bubbles with turbulent reattachment". In: *Journal of Fluid Mechanics* 410.2000 (2000), pp. 1–28.
- [16] Nagabhushana Rao, V. "Numerical Investigation of Separated Flows in Low Pressure Turbines : Current status and Future outlook". PhD thesis. University of Cambridge, 2014.
- [17] Steinert, W. and Starken, H. "Off-Design Transition and Separation Behavior of a CDA Cascade". In: *Journal of Turbomachinery* 118.2 (1996), pp. 204–210.
- [18] Schreiber, H.-A. et al. "Advanced High-Turning Compressor Airfoils for Low Reynolds Number Condition— Part II: Experimental and Numerical Analysis". In: *Journal of Turbomachinery* 126 (2004), pp. 482–492.
- [19] Mayle, R. E. "The Role of Laminar-Turbulent Transition in Gas Turbine Engines". In: *IGTI Scholar Lecture* 113 (1991).
- [20] Coull, J. D. and Hodson, H. P. "Unsteady boundary-layer transition in low-pressure turbines". In: *Journal of Fluid Mechanics* 681 (2011), pp. 370–410.
- [21] Nagarajan, S., Lele, S. K, and Ferziger, J. H. "Leading-edge effects in bypass transition". In: *Journal of Fluid Mechanics* 572 (), pp. 471–504.
- [22] Goodhand, M. N. and Miller, R. J. "Compressor Leading Edge Spikes: A New Performance Criterion". In: *Volume 7: Turbomachinery, Parts A and B* (2009), pp. 1553–1562.
- [23] Ernst, M., Michel, A., and Jeschke, P. "Analysis of Rotor-Stator-Interaction and Blade-to-Blade Measurements in a Two Stage Axial Flow Compressor". In: *Journal of Turbomachinery* 133.1 (2011), pp. 011027 1–12.
- [24] Rolls-Royce Ltd. *The jet engine*. Rolls-Royce, 2005, p. 288.
- [25] Wu, X. et al. "Simulation of boundary layer transition induced by periodically passing wakes". In: *Journal of Fluid Mechanics* 398 (1999), pp. 109–153.
- [26] Wheeler, A. P. S., Miller, R. J., and Hodson, H. P. "The Effect of Wake Induced Structures on Compressor Boundary-Layers". In: *Journal of Turbomachinery* 129.4 (2007), pp. 705–712.
- [27] Wheeler, A. P. S., Sofia, A., and Miller, R. J. "The Effect of Leading-Edge Geometry on Wake Interactions in Compressors". In: *Journal of Turbomachinery* 131.4 (2009), pp. 041013 1–8.

- [28] Denton, J. and Pullan, G. “A numerical investigation into the sources of endwall loss in axial flow turbines”. In: *Proc. of ASME Turbo Expo.* 2012, pp. 69173 1–14.
- [29] Park, J. S. et al. “Effects of Unsteady Wake on Heat Transfer of Endwall Surface in Linear Cascade”. In: *Journal of Heat Transfer* 136.6 (2014), pp. 061701 1–8.
- [30] Schulz, H. D., Gallus, H. E., and Lakshminarayana, B. “Three-Dimensional Separated Flow Field in the Endwall Region of an Annular Compressor Cascade in the Presence of Rotor-Stator Interaction: Part 1—Quasi-Steady Flow Field and Comparison With Steady-State Data”. In: *Journal of Turbomachinery* 112.4 (1990), pp. 669–678.
- [31] Hah, C. and Loellbach, J. “Development of Hub Corner Stall and Its Influence on the Performance of Axial Compressor Blade Rows”. In: *Journal of Turbomachinery* 121.1 (1999), pp. 67–77.
- [32] Beselt, C., Eck, M., and Peitsch, D. “Three-Dimensional Flow Field in Highly Loaded Compressor Cascade”. In: *Journal of Turbomachinery* 136.10 (2014), pp. 101007 1–10.
- [33] Lei, V. M., Spakovszky, Z. S., and Greitzer, E. M. “A Criterion for Axial Compressor Hub-Corner Stall”. In: *Journal of Turbomachinery* 130.3 (2008), pp. 031006 1–10.
- [34] Yu, X. and Liu, B. “A prediction model for corner separation/stall in axial compressors”. In: *Proc. of ASME Turbo Expo.* 2010, pp. 1–12.
- [35] Gbadebo, S. A. “Three-Dimensional Separations in Compressors”. PhD thesis. University of Cambridge, 2003.
- [36] Gbadebo, S. A., Hynes, T. P., and Cumpsty, N. A. “Influence of Surface Roughness on Three-Dimensional Separation in Axial Compressors”. In: *Journal of Turbomachinery* 126.4 (2004), pp. 455–463.
- [37] Goodhand, M. N. and Miller, R. J. “The Impact of Real Geometries on Three-Dimensional Separations in Compressors”. In: *Journal of Turbomachinery* 134.2 (2012), pp. 021007 1–8.
- [38] Pope, S. B. *Turbulent Flows*. Vol. 1. 2000, p. 771.
- [39] Wheeler, A. P. S. et al. “Direct Numerical Simulations of a High-Pressure Turbine Vane”. In: *Journal of Turbomachinery* 138.7 (2016), pp. 071003 1–9.
- [40] Spalart, P. and Shur, M. “On the sensitization of turbulence models to rotation and curvature”. In: *Aerospace Science and Technology* 1 (1997), pp. 297–302.
- [41] Spalart, P. R. and Allmaras, S. R. “A one-equation turbulence model for aerodynamic flows”. en. In: *Recherche Aerospatiale* 1 (1994), pp. 5–21.

- [42] Hodson, H. P. "Blade row interaction in low pressure turbines". In: *Blade row interference in axial turbomachinery stages, VKI Lecture Series*. 1998.
- [43] Tucker, P. G. *Unsteady Computational Fluid Dynamics in Aeronautics*. Vol. 104. Fluid Mechanics and Its Applications. Dordrecht: Springer Netherlands, 2014.
- [44] Ottavy, X., Courtiade, N., and Gourdain, N. "Experimental and Computational Methods for Flow Investigation in High-Speed Multistage Compressor". In: *Journal of Propulsion and Power* 28.6 (2012), pp. 1141–1155.
- [45] Hah, C., Mueller, M., and Schiffer, H.-P. "Study of Convective Flow Effects in Endwall Casing Treatments in Transonic Compressor Rotors". In: *Volume 8: Turbomachinery, Parts A, B, and C*. ASME, 2012, pp. 68411 1–12.
- [46] Gao, F. et al. "Numerical analysis of three-dimensional corner separation in a linear compressor cascade". In: *Proc. of ASME Turbo Expo*. 2013, pp. 95581 1–11.
- [47] Abu-Ghannam, B. J. and Shaw, R. "Natural transition of boundary layers - The effects of turbulence, pressure gradient, and flow history". en. In: *Journal of Mechanical and Engineering Science* 22 (1980), pp. 213–228.
- [48] Mayle, R. E. and Schulz, A. "The Path to Predicting Bypass Transition". In: *Journal of Turbomachinery* 119 (1997), pp. 405–411.
- [49] Menter, F. R. et al. "Transition Modelling for General Purpose CFD Codes". In: *Flow Turbulence Combust* 77.77 (2006), pp. 277–303.
- [50] Dunham, J. "CFD Validation for Propulsion System Components". In: *AGARD Advisory Report 355* (1998).
- [51] Langston, L. S. "Secondary Flows in Axial Turbines-A Review". In: *Annals of the New York Academy of Sciences* 934.1 (2001), pp. 11–26.
- [52] Holley, B. M. and Langston, L. S. "Surface Shear Stress and Pressure Measurements in a Turbine Cascade". In: *Volume 6: Turbomachinery, Parts A and B*. Vol. 2006. ASME, 2006, pp. 691–700.
- [53] Marty, J. et al. "Effet de la mod{é}lisation de la tur{e}bulence en proche pompage dans un compresseur multi-{é}tages". In: *AAAF, 43{è}me Colloque d'Aérodynamique Appliqu{ée}*. Poitiers, France, 2008, vol. 204.
- [54] Wang, D., Lu, L., and Li, Q. "Improvement on S-A Model For predicting corner separation Based On Turbulence Transport Nature". In: *45th AIAA/ASME/SAE/ASEE Joint Propulsion Conference & Exhibit* August (2009), pp. 1–9.

- [55] Horlock, J. H. and Denton, J. D. “A Review of Some Early Design Practice Using Computational Fluid Dynamics and a Current Perspective”. In: *Journal of Turbomachinery* 127.1 (2005), pp. 1–13.
- [56] Rumsey, C. L., Neuhart, D., and Kegerise, M. A. “The NASA Juncture Flow Experiment: Goals, Progress, and Preliminary Testing (Invited)”. In: *54th AIAA Aerospace Sciences Meeting*. Reston, Virginia: American Institute of Aeronautics and Astronautics, 2016, pp. 1557 1–16.
- [57] Bordji, M. et al. “Investigation of a Nonlinear Reynolds-Averaged Navier–Stokes Closure for Corner Flows”. In: *2AIAA Journal* 54.2 (2016), pp. 386–398.
- [58] Yamamoto, K., Tanaka, K., and Murayama, M. “Effect of a Nonlinear Constitutive Relation for Turbulence Modeling on Predicting Flow Separation at Wing-Body Juncture of Transonic Commercial Aircraft”. In: *30th AIAA Applied Aerodynamics Conference*. Reston, Virignia: American Institute of Aeronautics and Astronautics, 2012, pp. 2895 1–9.
- [59] Clark, R. A., Ferziger, J. H., and Reynolds, W. C. “Evaluation of subgrid-scale models using an accurately simulated turbulent flow”. In: *Journal of Fluid Mechanics* 91.01 (1979), pp. 1–16.
- [60] Ghosal, S. “An Analysis of Numerical Errors in Large-Eddy Simulations of Turbulence”. In: *Journal of Computational Physics* 125.1 (1996), pp. 187–206.
- [61] Boris, J. P. et al. “New insights into large eddy simulation”. In: *Fluid Dynamics Research* 10.4-6 (1992), pp. 199–228.
- [62] Smagorinsky, J. “General circulation experiments with the primitive equations”. EN. In: *Monthly Weather Review* 91.3 (1963), pp. 99–164.
- [63] Lilly, D. *On the application of the eddy viscosity concept in the inertial sub-range of turbulence*. Boulder Colo.: National Center for Atmospheric Research, 1966.
- [64] Schumann, U. “Subgrid scale model for finite difference simulations of turbulent flows in plane channels and annuli”. In: *Journal of Computational Physics* 18.4 (1975), pp. 376–404.
- [65] Germano, M. et al. “A dynamic subgrid-scale eddy viscosity model”. In: *Physics of Fluids A: Fluid Dynamics* 3.7 (1991), pp. 1760–1765.
- [66] Hughes, T. J., Mazzei, L., and Jansen, K. E. “Large Eddy Simulation and the variational multiscale method”. In: *Computing and Visualization in Science* 3.1-2 (2000), pp. 47–59.
- [67] Nicoud, F. and Ducros, F. “Subgrid-Scale Stress Modelling Based on the Square of the Velocity Gradient Tensor”. en. In: *Flow, Turbulence and Combustion* 62.3 (1999), pp. 183–200.

- [68] Nicoud, F. et al. "Using singular values to build a subgrid-scale model for large eddy simulations". In: *Physics of Fluids* 23.8 (2011), pp. 085106 1–35.
- [69] Breuer, M. "Direkte Numerische Simulation und Large-Eddy Simulation turbulenter Strömungen auf Hochleistungsrechnern". In: *Shaker Verlag, Aachen. Habilitationsschrift, Universität Erlangen-Nürnberg* (2002).
- [70] Diurno, G. V., Balaras, E, and Piomelli, U. "Wall-layer models for LES of separated flow". In: *Modern simulation strategies for turbulent flow*. Ed. by Geurts, B. J. Philadelphia: Edwards publisher, 2001, pp. 157–174.
- [71] Piomelli, U. and Chasnov, R. "Large-Eddy Simulations: Theory and Applications". In: *Turbulence and Transition Modelling* 2 (1996), pp. 2269–336.
- [72] Piomelli, U. "Large-eddy and direct simulation of turbulent flows". In: *Short course delivered at CFD2001 - 9e conférence annuelle de la Société canadienne de CFD. Kitchener, Ontario.* (2001).
- [73] Ferziger, J. H. "Subgrid-scale modelling". In: *Large eddy simulation of complex engineering and geophysical flows*. Ed. by Galerpin, B and Orszag, S. A. Cambridge University Press, 1993, pp. 37–54.
- [74] Temmerman, L et al. "Investigation of wall-function approximations and subgrid-scale models in large eddy simulation of separated flow in a channel with streamwise periodic constrictions". In: *Int. J. Heat and Fluid Flow* 24 (2003), pp. 157–180.
- [75] Sagaut, P. "LES and DNS simulation of turbomachinery flows". In: *VKI Lecture Series - Recent Developments in Numerical Methods for Turbomachinery Flows*. Ed. by Arts, T. Von Karman Institute for Fluid Dynamics, 2001.
- [76] Chapman, D. R. "Computational aerodynamics development and outlook". In: *AIAA Journal* 17 (1979), pp. 1293–1313.
- [77] Moin, P. "Grid-point requirements for large eddy simulation: Chapman's estimates revisited". In: *Center for Turbulence Research, Annual Research Briefs* (2011), pp. 1–6.
- [78] Piomelli, U and Balaras, E. "Wall-layer models for large-eddy simulations". In: *Annu. Rev. Fluid Mech.* 34 (2002), pp. 349–374.
- [79] Teramoto, S. "Large-Eddy Simulation of a Transonic Compressor Cascade with Boundary Layer Transition". en. In: *AIAA/ASME/SAE/ASEE Joint Propulsion Conference & Exhibit.* 2005, pp. 3639 1–8.
- [80] Reese, H., Kato, C., and Carolus, T. "Large Eddy Simulation of Gust Noise Sources in a Low Pressure Axial Compressor". en. In: *12th AIAA/CEAS Aeroacoustics Conference* (2006), pp. 2576 1–10.

- [81] You, D. et al. “Effects of tip-gap size on the tip-leakage flow in a turbomachinery cascade”. In: *Physics of Fluids* 18.10 (2006), pp. 105102 1–14.
- [82] Boudet, J. et al. “Numerical studies towards practical large-eddy simulation”. In: *Journal of Thermal Science* 16.4 (2007), pp. 328–336.
- [83] Klostermeier, C. “Investigation into the capability of large eddy simulation for turbomachinery design”. PhD Thesis. University of Cambridge, 2008.
- [84] Eastwood, S. J. et al. “Developing large eddy simulation for turbomachinery applications.” In: *Philosophical transactions. Series A, Mathematical, physical, and engineering sciences* 367.1899 (2009), pp. 2999–3013.
- [85] Hah, C. *Large Eddy Simulation of transonic flow field in NASA rotor 37*. Tech. rep. NASA Glenn Research Center, 2009.
- [86] Lardeau, S., Leschziner, M., and Zaki, T. “Large Eddy Simulation of Transitional Separated Flow over a Flat Plate and a Compressor Blade”. In: *Flow, Turbulence and Combustion* 88.1-2 (2011), pp. 19–44.
- [87] Gomar, A, Gourdain, N., and Dufour, G. “High fidelity simulation of the turbulent flow in a transonic axial compressor”. In: *European Turbomachinery Conference*. Vol. 37. 1998. Istanbul, Turkey, 2011, pp. 1–11.
- [88] Hellstrom, F., Gutmark, E., and Fuchs, L. “Large Eddy Simulation of the Unsteady Flow in a Radial Compressor Operating Near Surge”. In: *Journal of Turbomachinery* 134.5 (2012), pp. 051006 1–10.
- [89] McMullan, W. A. and Page, G. J. “Towards Large Eddy Simulation of gas turbine compressors”. In: *Progress in Aerospace Sciences* 52 (2012), pp. 30–47.
- [90] Laborderie, J., Moreau, S, and Berry, A. “Compressor Stage Broadband Noise Prediction using a Large-Eddy Simulation and Comparisons with a Cascade Response Model”. en. In: *19th AIAA/CEAS Aeroacoustics Conference*. Berlin, Germany, 2013, pp. 2042 1–22.
- [91] Gourdain, N. “Validation of large-eddy simulation for the prediction of compressible flow in an axial compressor stage”. In: *Proc. of ASME Turbo Expo*. San Antonio, Texas, USA, 2013, pp. 94550 1–15.
- [92] Riéra, W. et al. “Inlet Condition Effects on the Tip Clearance Flow With Zonal Detached Eddy Simulation”. In: *Journal of Turbomachinery* 136.4 (2013).
- [93] Wang, Z. and Yuan, X. “Unsteady mechanisms of compressor corner separation over a range of incidences based on hybrid LES/RANS”. In: *Proc. of ASME Turbo Expo* (2013), pp. 95300 1–11.

- [94] Vreman, A. W. “An eddy-viscosity subgrid-scale model for turbulent shear flow: Algebraic theory and applications”. In: *Physics of Fluids* 16.10 (2004), pp. 3670–3681.
- [95] Joo, J et al. “Large-eddy simulation of a compressor rotor”. In: *Center for Turbulence Research, Proceedings of the Summer Program* (2014).
- [96] Gao, F. et al. “Unsteady behavior of corner separation in a compressor cascade: Large eddy simulation and experimental study”. In: *Proceedings of the Institution of Mechanical Engineers, Part A: Journal of Power and Energy* 229.5 (2015), pp. 508–519.
- [97] Liu, Y. et al. “Investigation of Vortical Structures and Turbulence Characteristics in Corner Separation in a Linear Compressor Cascade Using DDES”. In: *Journal of Fluids Engineering* (2016), pp. 1075 1–46.
- [98] Leggett, J. et al. “Detailed Investigation of RANS and LES Predictions of Loss Generation in an Axial Compressor Cascade at Off Design Incidences”. In: *ASME Turbo Expo 2016*. ASME, 2016, pp. 57972 1–.
- [99] Medic, G. et al. “Prediction of Transition and Losses in Compressor Cascades Using Large-Eddy Simulation”. In: *Journal of Turbomachinery* 138.12 (2016), pp. 121001 1–9.
- [100] Zaki, T. A. et al. “Direct Computations of Boundary Layers Distorted by Migrating Wakes in a Linear Compressor Cascade”. In: *Flow, Turbulence and Combustion* 83.3 (2009), pp. 307–322.
- [101] Lund, T. S., Wu, X., and Squires, K. D. “Generation of Turbulent Inflow Data for Spatially-Developing Boundary Layer Simulations”. In: *Journal of Computational Physics* 140.2 (1998), pp. 233–258.
- [102] Kuzmin, D. and Turek, S. “Flux Correction Tools for Finite Elements”. In: *Journal of Computational Physics* 175.2 (2002), pp. 525–558.
- [103] Wang, Z. et al. “High-Order CFD Methods: Current Status and Perspective”. In: *Int. J. Numer. Meth. Fluids* 00 (2012), pp. 1–42.
- [104] Vreman, B., Geurts, B., and Kuerten, H. “Comparision of numerical schemes in Large-Eddy Simulation of the temporal mixing layer”. In: *International Journal for Numerical Methods in Fluids* 22 (1996), pp. 297–311.
- [105] Meinke, M. et al. “A comparison of second- and sixth-order methods for large-eddy simulations”. In: *Computers & Fluids* 31.4-7 (2002), pp. 695–718.
- [106] Harten, A. et al. “Uniformly High Order Accurate Essentially Non-oscillatory Schemes, III”. In: *Journal of Computational Physics* 131.1 (1997), pp. 3–47.

- [107] Garnier, E. et al. “On the Use of Shock-Capturing Schemes for Large-Eddy Simulation”. In: *Journal of Computational Physics* 153.2 (1999), pp. 273–311.
- [108] Roe, P. “Characteristic-Based Schemes for the Euler Equations”. In: *Annual Review of Fluid Mechanics* 18.1 (1986), pp. 337–365.
- [109] Watson, R. “Large Eddy Simulation of Cutback Trailing Edges for Film Cooling Turbine Blades”. PhD thesis. University of Cambridge, 2013.
- [110] Tajallipour, N., Babaee Owlam, B., and Paraschivoiu, M. “Self-Adaptive Upwinding for Large Eddy Simulation of Turbulent Flows on Unstructured Elements”. In: *Journal of Aircraft* 46.3 (2009), pp. 915–926.
- [111] Kumar, V. and Paraschivoiu, M. “Self-Adaptive Upwinding for Large Eddy Simulation of Cross-Flow Jets”. In: *ASME 2010 3rd Joint US-European Fluids Engineering Summer Meeting*. ASME, 2010, pp. 2537–2547.
- [112] Jameson, A. “Formulation of Kinetic Energy Preserving Conservative Schemes for Gas Dynamics and Direct Numerical Simulation of One-Dimensional Viscous Compressible Flow in a Shock Tube Using Entropy and Kinetic Energy Preserving Schemes”. In: *Journal of Scientific Computing* 34.2 (2007), pp. 188–208.
- [113] Hobson, G. V. et al. “Effect of Reynolds Number on Separation Bubbles on Compressor Blades in Cascade”. In: *Journal of Propulsion and Power* 17.1 (2001), pp. 154–162.
- [114] Matsuura, K. and Kato, C. “Large Eddy Simulation of Compressible Transitional Cascade Flows”. In: *Journal of Fluid Science and Technology* 2.3 (2007), pp. 558–569.
- [115] Bode, C., Hoffmann, J., and Stark, U. “Effects of a skewed inlet boundary layer on the aerodynamic performance of a stator-hub equivalent high-turning compressor cascade”. In: *Proc. of ASME Turbo Expo 2016*. Seoul, 2017, pp. 1–11.
- [116] Dring, R. P., Joslyn, H. D., and Hardin, L. W. “An Investigation of Axial Compressor Rotor Aerodynamics”. In: *Journal of Engineering for Power* 104.1 (1982), pp. 84–96.
- [117] Borello, D., Hanjalic, K., and Rispoli, F. “Computation of tip-leakage flow in a linear compressor cascade with a second-moment turbulence closure”. In: *International Journal of Heat and Fluid Flow* 28.4 (2007), pp. 587–601.
- [118] Wellborn, S. R. and Okiishi, T. H. “The Influence of Shrouded Stator Cavity Flows on Multistage Compressor Performance”. In: *Journal of Turbomachinery* 121.3 (1999), pp. 486–497.

- [119] Gbadebo, S. A., Cumpsty, N. A., and Hynes, T. P. “Interaction of Tip Clearance Flow and Three-Dimensional Separations in Axial Compressors”. In: *Journal of Turbomachinery* 129 (2007), pp. 679–685.
- [120] Ma, W. et al. “Experimental Study of Corner Stall in a Linear Compressor Cascade”. In: *Chinese Journal of Aeronautics* 24.3 (2011), pp. 235–242.
- [121] Crumpton, P., Moinier, P., and Giles, M. “An unstructured algorithm for high Reynolds number flows on highly stretched grids”. In: *Tenth international conference on numerical methods for laminar and turbulent flow* (1997), pp. 1–13.
- [122] Lapworth, L. “HYDRA CFD: a framework for collaborative CFD development”. In: *Int. conf. on scientific and engineering computation*. Singapore, 2004.
- [123] Moinier, P. “Algorithm Developments for an Unstructured Viscous Flow Solver”. PhD thesis. University of Oxford, 1999.
- [124] Plc., R.-R. *The HYDRA Programmer’s Guide*. Tech. rep.
- [125] Cui, J., Nagabhushana Rao, V., and Tucker, P. “Numerical Investigation of Contrasting Flow Physics in Different Zones of a High-Lift Low-Pressure Turbine Blade”. In: *Journal of Turbomachinery* 138.1 (2015), pp. 011003 1–10.
- [126] Rogers, S. E., Kwak, D., and Kiris, C. “Steady and unsteady solutions of the incompressible Navier-Stokes equations”. In: *AIAA Journal* 29.4 (1991), pp. 603–610.
- [127] Martinelli, L. “Calculations of viscous flows with a multigrid method”. PhD thesis. Princeton University, 1987.
- [128] Burgess, D. A., Crumpton, P. I., and Giles, M. B. *A parallel framework for unstructured grid solvers*. Tech. rep. 95. Oxford University Computing Laboratory, 1994, pp. 1–13.
- [129] Hills, N. “Achieving high parallel performance for an unstructured unsteady turbomachinery CFD code”. In: *The Aeronautical Journal* 3100 (2007), pp. 185–193.
- [130] Karypis, G. and Kumar, V. “A Fast and High Quality Multilevel Scheme for Partitioning Irregular Graphs”. In: *SIAM Journal on Scientific Computing* 20.1 (1998), pp. 359–392.
- [131] Hasan, K. M. et al. “Analytical Computation of the Eigenvalues and Eigenvectors in DT-MRI”. In: *Journal of Magnetic Resonance* 152.1 (2001), pp. 41–47.
- [132] Nagabhushana Rao, V. et al. “Large eddy simulations in low-pressure turbines: Effect of wakes at elevated free-stream turbulence”. In: *International Journal of Heat and Fluid Flow* (2013).

- [133] Kennel, M. B. “KDTREE 2: Fortran 95 and C++ software to efficiently search for near neighbors in a multi-dimensional Euclidean space”. In: *arXiv Physics repository* 2 (2004), pp. 0408067 1–8. arXiv: [0408067 \[physics\]](#).
- [134] Spalart, P. R. “Direct simulation of a turbulent boundary layer up to $R\theta = 1410$ ”. In: *Journal of Fluid Mechanics* 187 (1988), pp. 61–98.
- [135] Schlichting, H. T. and Gersten, K. *Boundary-layer theory*. Springer-Verlag, 2000.
- [136] Saad, T. et al. “Scalable Tools for Generating Synthetic Isotropic Turbulence with Arbitrary Spectra”. In: *AIAA Journal* 2016-03-J0 (2016), pp. 1–14. arXiv: [NIHMS150003](#).
- [137] Rogallo, R. S. *Numerical experiments in homogeneous turbulence*. en. Tech. rep. NASA Ames Research Center, Moffett Field, CA. Report No. NASA-TM- 81315, 1981.
- [138] Hunt, J. C. R., Wray, A. A., and Moin, P. “Eddies, streams, and convergence zones in turbulent flows”. In: *Center for Turbulence Research, Proceedings of the Summer Program* (1988), pp. 193–208.
- [139] Jeong, J. and Hussain, F. “On the identification of a vortex”. In: *Journal of Fluid Mechanics* 285 (1995), pp. 69–94.
- [140] Gresho, P. M. and Lee, R. L. “Don’t suppress the wiggles—They’re telling you something!” In: *Computers & Fluids* 9.2 (1981), pp. 223–253.
- [141] Rees, W. M. van et al. “A comparison of vortex and pseudo-spectral methods for the simulation of periodic vortical flows at high Reynolds numbers”. In: *Journal of Computational Physics* 230.8 (2011), pp. 2794–2805.
- [142] Boom, P. and Zingg, D. “Time-Accurate Flow Simulations Using an Efficient Newton-Krylov-Schur Approach with High-Order Temporal and Spatial Discretization”. In: *51st AIAA Aerospace Sciences Meeting*. Reston, Virigina: American Institute of Aeronautics and Astronautics, 2013, pp. 0383 1–20.
- [143] Celik, I. B., Klein, M., and Janicka, J. “Assessment Measures for Engineering LES Applications”. In: *Journal of Fluids Engineering* 131.3 (2009), pp. 031102 1–10.
- [144] McMullan, W. A. and Page, G. J. “Large Eddy simulation of a controlled diffusion compressor cascade”. In: *Flow, turbulence and combustion* 86.2 (2011), pp. 207–230.
- [145] McMullan, W. A. and Page, G. J. “Large eddy simulation of a compressor cascade and the influence of spanwise domain”. In: *... Engineers, Part A: Journal of Power and ...* 225.6 (2011), pp. 817–831.

- [146] Ciardi, M. “Large Eddy Simulation for broad-band noise in turbomachinery”. PhD thesis. University of Cambridge, 2005.
- [147] Lundgren, T. S. “Linearly forced isotropic turbulence”. In: *Annual Research Briefs* 2 (2003), pp. 461–473.
- [148] Bassenne, M. et al. “Constant-energetics physical-space forcing methods for improved convergence to homogeneous-isotropic turbulence with application to particle-laden flows”. In: *Physics of Fluids* 28.3 (2016), pp. 035114 1–16.
- [149] Rosales, C. and Meneveau, C. “Linear forcing in numerical simulations of isotropic turbulence: Physical space Implementations and convergence properties”. In: *Physics of Fluids* 17.9 (2005), pp. 095106 1–8.
- [150] Carroll, P. L. and Blanquart, G. “A proposed modification to Lundgren’s physical space velocity forcing method for isotropic turbulence”. In: *Physics of Fluids* 25.10 (2013), pp. 105114 1–9.
- [151] Tavoularis, S., Bennett, J. C., and Corrsin, S. “Velocity-derivative skewness in small Reynolds number, nearly isotropic turbulence”. In: *Journal of Fluid Mechanics* 88.01 (1978), pp. 63–69.
- [152] Hilgenfeld, L. and Pfitzner, M. “Unsteady Boundary Layer Development Due to Wake Passing Effects on a Highly Loaded Linear Compressor Cascade”. In: *Journal of Turbomachinery* 126.4 (2004), pp. 493–500.
- [153] Lieblein, S., Schwenk, F. C., and Broderick, R. L. *Diffusion factor for estimating losses and limiting blade loadings in axial-flow-compressor blade elements*. Tech. rep. NACA Research Memorandum, 1953.
- [154] Saric, W. S. “Gortler Vortices”. In: *Annu. Rev. Fluid Mech* 26 (1994), pp. 379–409.
- [155] Zaki, T. A. and Durbin, P. A. “Continuous mode transition and the effects of pressure gradient”. In: *Journal of Fluid Mechanics* 563.2006 (2006), pp. 357–388.
- [156] Ovchinnikov, V., Choudhari, M. M., and Piomelli, U. “Numerical simulations of boundary-layer bypass transition due to high-amplitude free-stream turbulence”. In: *Journal of Fluid Mechanics* 613 (2008), pp. 135–169.
- [157] Sayadi, T. and Moin, P. “Large eddy simulation of controlled transition to turbulence”. In: *Physics of Fluids* 24.11 (2012), pp. 114103 1–17.
- [158] Piomelli, U. “Large-eddy simulation: Achievements and challenges”. In: *Prog. Aerospace Sciences* 35 (1999), pp. 335–362.

- [159] Scillitoe, A. D., Tucker, P. G., and Adami, P. “Numerical Investigation of Three-Dimensional Separation in an Axial Flow Compressor: The Influence of Freestream Turbulence Intensity and Endwall Boundary Layer State”. In: *Journal of Turbomachinery* 139.2 (2016), pp. 021011 1–10.
- [160] Spalart, P. R. and Rumsey, C. L. “Effective Inflow Conditions for Turbulence Models in Aerodynamic Calculations”. In: *AIAA Journal* 45.10 (2007), pp. 2544–2553.
- [161] Walker, G. J., Hughes, J. D., and Solomon, W. J. “Periodic Transition on an Axial Compressor Stator: Incidence and Clocking Effects: Part I—Experimental Data”. In: *Journal of Turbomachinery* 121.3 (1999), pp. 398–407.
- [162] Cumpsty, N. A., Dong, Y., and Li, Y. S. “Compressor Blade Boundary Layers in the Presence of Wakes”. In: *ASME 1995 International Gas Turbine and Aeroengine Congress and Exposition*. ASME, 1995, pp. 1–16.
- [163] Walker, G. J. et al. “Investigation of the Calmed Region Behind a Turbulent Spot”. In: *Journal of Turbomachinery* 119.4 (1997), pp. 802–809.
- [164] Boudet, J., Monier, J. F., and Gao, F. “Implementation of a roughness element to trip transition in large-eddy simulation”. In: *Journal of Thermal Science* 24.1 (2015), pp. 30–36.
- [165] Zlatinov, M. B. et al. “Turbine Hub and Shroud Sealing Flow Loss Mechanisms”. In: *Journal of Turbomachinery* 134.6 (2012), pp. 061027 1–12.
- [166] Kozulovic, D. and Lapworth, B. L. “An Approach for Inclusion of a Nonlocal Transition Model in a Parallel Unstructured Computational Fluid Dynamics Code”. In: *Journal of Turbomachinery* 131.3 (2009), pp. 031008 1–7.
- [167] Scillitoe, A. D., Tucker, P. G., and Adami, P. “Evaluation of RANS and ZDES Methods for the Prediction of Three-Dimensional Separation in Axial Flow Compressors”. In: *Proc. of ASME Turbo Expo 2015*. Montreal, 2015, pp. 43975 1–15.
- [168] Ma Wei. “Experimental Investigation of Corner Stall in a Linear Compressor Cascade”. PhD thesis. École Centrale de Lyon, 2012.
- [169] Ludwig Prandtl. *Essentials of Fluid Mechanics*. Ed. by Oertel, H. Applied Mathematical Sciences. New York, NY: Springer New York, 1952.
- [170] Gand, F. “Dynamique des écoulements de jonction en régime turbulent”. PhD thesis. Université Pierre et Marie Curie, 2011.
- [171] Meyer, R. et al. “A parameter study on the influence of fillets on the compressor cascade performance”. In: *Journal of theoretical and applied mechanics* 50.1 (2012), pp. 131–145.

- [172] Reutter, O. et al. "Endwall Contouring and Fillet Design for Reducing Losses and Homogenizing the Outflow of a Compressor Cascade". In: *ASME Turbo Expo 2014*. Düsseldorf, Germany: ASME, 2014, pp. 25277 1–10.
- [173] Coull, J. D. and Hodson, H. P. "Predicting the Profile Loss of High-Lift Low Pressure Turbines". In: *Journal of Turbomachinery* 134.2 (2012), pp. 021002 1–14.
- [174] Halstead, D. E. et al. "Boundary Layer Development in Axial Compressors and Turbines: Part 1 of 4—Composite Picture". In: *Journal of Turbomachinery* 119.1 (1997), pp. 114–118.
- [175] Lefas, D., Cui, J., and Tucker, P. G. "A Critical Examination of a Correlation-Based Transition Model for Low Pressure Turbines". In: *55th AIAA Aerospace Sciences Meeting*. Reston, Virginia: American Institute of Aeronautics and Astronautics, 2017, pp. 0782 1–18.
- [176] Medic, G. and Durbin, P. A. "Toward Improved Prediction of Heat Transfer on Turbine Blades". In: *Journal of Turbomachinery* 124.2 (2002), pp. 187–192.
- [177] Kato, M. and Launder, B. E. "The Modelling of Turbulent Flow Around Stationary and Vibrating Square Cylinders". In: *9th Symposium on Turbulent Shear Flows*. Kyoto, 1993, pp. 10.4 1–6.
- [178] Lodefier, K. and Dick, E. "Modelling of unsteady transition in low-pressure turbine blade rows with two dynamic intermittency equations". In: *Flow, Turbulence and Combustion* (2006), pp. 103–132.
- [179] Bradshaw, P. "Effects of streamline curvature on turbulent flow". In: *Advisory Group for Aerospace Research and Development* (1973).
- [180] Speziale, C. G. "Analytical Methods for the Development of Reynolds-Stress Closures in Turbulence". en. In: *Annual Review of Fluid Mechanics* 23.1 (1991), pp. 107–157.
- [181] Launder, B. E. "Second-moment closure: present... and future?" In: *International Journal of Heat and Fluid Flow* 10.4 (1989), pp. 282–300.
- [182] Morsbach, C., Franke, M., and Mare, F. "Towards the application of Reynolds stress transport models to 3D turbomachinery flows". In: *7th International Symposium on Turbulence, Heat and Mass Transfer*. 2012, pp. 10.1615 1–13.
- [183] Lien, F. S. and Leschziner, M. A. "Modelling 2D separation from a high lift aerofoil with a non-linear eddy-viscosity model and second-moment closure". In: *Aeronautical Journal* 99 (1995), pp. 125–144.
- [184] Dacles-Mariani, J. et al. "Numerical/experimental study of a wingtip vortex in the near field". In: *AIAA Journal* 33.9 (1995), pp. 1561–1568.

- [185] Menter, F. R., Kuntz, M, and Langtry, R. “Ten Years of Industrial Experience with the SST Turbulence Model”. In: *Turbulence Heat and Mass Transfer 4* 4 (2003), pp. 625–632.
- [186] Rung, T. et al. “Restatement of the Spalart-Allmaras Eddy-Viscosity Model in Strain-Adaptive Formulation”. en. In: *AIAA Journal* 41.7 (2003), pp. 1396–1399.
- [187] Shur, M. L. et al. “Turbulence modeling in rotating and curved channels - Assessing the Spalart-Shur correction”. In: *AIAA Journal* 38 (2000), pp. 784–792.
- [188] Smirnov, P. E. and Menter, F. R. “Sensitization of the SST Turbulence Model to Rotation and Curvature by Applying the Spalart–Shur Correction Term”. In: *Journal of Turbomachinery* 131.4 (2009), 041010: 1–8.
- [189] Lilly, D. K. “A proposed modification of the Germano subgrid-scale closure method”. In: *Physics of Fluids A: Fluid Dynamics* 4.3 (1992), pp. 633–635.
- [190] Vreman, A. W. “The filtering analog of the variational multiscale method in large-eddy simulation”. In: *Physics of Fluids* 15.8 (2003), pp. 61–64.
- [191] Lévéque, E. et al. “Shear-improved Smagorinsky model for large-eddy simulation of wall-bounded turbulent flows”. In: *Journal of Fluid Mechanics* 570 (2007), pp. 491–502.
- [192] Cahuzac, A. et al. “Smoothing algorithms for mean-flow extraction in large-eddy simulation of complex turbulent flows”. In: *Physics of Fluids American Institute of Physics* 22 (2010), pp. 1–14.